The oxidative reforming of methane to synthesis gas on a commercial steam reforming catalyst

J.N. Theron

Department of Chemical Engineering

University of Cape Town

Rondebosch, Cape Town

South Africa

April 1997

Thesis presented for the Degree of

DOCTOR OF PHILOSOPHY

in the Department of Chemical Engineering

UNIVERSITY OF CAPE TOWN

April 1997

Acknowledgements

Abstract

The oxidative reforming of methane to predominantly carbon monoxide and hydrogen was studied over a commercial steam reforming catalyst (Südchemie G-90B). The said reaction was performed in an integral fixed-bed reactor at temperatures between 575°C and 650°C at a total pressure of 200 kPa(a). The primary objective of the study was the design and construction of equipment to facilitate firstly, the measurement of axial bed temperature profiles, and secondly, the investigation of transport effects during the oxidative reforming of methane.

The absence of external transport resistance was confirmed by measuring the methane conversion at constant temperature (604 °C), reactant partial pressures ($P°_{CH4}$ = 2.69 kPa and $P°_{O2}$ = 1.34 kPa), total pressure (P_T = 201.3 kPa), particle size range (425μm < d_p < 710μm) and contact time (W/$F°_{CH4}$ = 1.9 E4 g s mol^{-1}), but varying the linear velocity between 3 m s^{-1} and 18 m s^{-1}. The absence of internal gradients were confirmed by measuring the methane conversion over different particle size ranges (125μm < d_p < 710μm) with all other parameters being constant (T = 604°C, u_o = 14.1 cm s^{-1}, $P°_{CH4}$ = 2.69 kPa, $P°_{O2}$ = 1.33 kPa, P_T = 201.3 kPa and W = 200 mg).

The absence of internal or external temperature- and concentration gradients were tested by subjecting the experimental results to theoretical criteria that had previously been derived to check for transport limitations. In all cases the correlations confirmed that the experimental system was free of transport resistances.

A kinetic study was performed under these conditions of negligible transport limitations. Methane partial pressures at the bed inlet was varied between 2.75 kPa and 4.82 kPa and that of oxygen between 0.99 kPa and 1.63 kPa. All the reaction products were co-fed at constant (inlet) methane and oxygen partial pressures. The ranges of product partial pressures at the reactor inlet was: $P°_{CO}$ = 1.34 to 6.29 kPa, $P°_{H2}$ = 1.45 to 5.61 kPa, $P°_{CO2}$ = 0.27 to 2.77 kPa and $P°_{H2O}$ = 0.49 to 1.20 kPa.

The integral data thus obtained was first analyzed by the method of initial rates (at zero conversion) by taking the slopes of the X_{CH4} vs. W/$F°_{CH4}$ data at the origin. This indicated that the rate of methane consumption was first-order with respect to methane partial pressure

and independent of oxygen partial pressure. The reaction products were found to inhibit the rate of methane consumption. The activation energy was found to correlate well with the activation energy of methane chemisorption on Ni(111) surfaces. Various curves were fitted to the data to enable the calculation of the slopes of the X_{CH4} vs. $W/F°_{CH4}$ data at different values of $W/F°_{CH4}$. In spite of yielding the lowest deviation in general between measured- and predicted X_{CH4}, the second-order polynomial curves failed to predict the slopes of the curves at high methane conversion because of excessive curvature. A set of ten hand-drawn curves to a model data set also showed a good correlation between predicted X_{CH4} and measured X_{CH4}. Two exponential curves were also fitted to the data, with one of the curves taking account of the methane conversion at thermodynamic equilibrium ($W/F°_{CH4} \rightarrow \infty$). The relative success of these curves were assessed in terms of a selected model data set.

Having obtained differential reaction rates from the integral data, two Langmuir-Hinshelwood models were developed and fitted to the data. The model which was derived from the assumption that methane adsorption on a single active site was the rate-determining step, gave the best fit to the experimental data. Adsorption constants correlated in broad terms with the reaction orders of the species which were previously determined by the method of initial rates. The differential kinetic data that were obtained from the fitting of exponential curves to the integral data gave the best correlation between predicted and measured reaction rates.

Subsequent to the differential treatment of the data, an attempt was made to correlate the integral data by means of an integral reaction model. A combination of the total oxidation-, oxidative reforming- and steam reforming of methane, as well as the water-gas shift reaction, resulted in the best fit between measured- and predicted data. The predicted methane, carbon monoxide- and hydrogen partial pressures correlated well with experimental data, but that of oxygen, carbon dioxide and water were less accurately predicted by the model. The lack of any comparable study in the literature made it impossible to compare adsorption- and rate constants to other work.

X-ray diffraction results showed that the active catalyst bed consisted of a top layer of nickel oxide on alumina and zero-valent nickel on alumina deeper into the bed. Evidence from thermogravimetric experiments revealed that carbon formation was inhibited by H_2 co-feeding and high O_2 inlet partial pressures, but that it was enhanced by CO co-feeding.

TABLE OF CONTENTS

LIST OF FIGURES

LIST OF TABLES

List of Symbols

a_m	External Surface Area Available for Mass Transport	$m^2\ g^{-1}$
C	Concentration	$mol\ m^{-3}$
C_p	Heat Capacity	$J\ mol^{-1}\ K^{-1}$
C_s	Concentration at the Catalyst Surface	$mol\ m^{-3}$
D_e	Effective Diffusivity	
$D_{K,E}$	Knudsen Diffusivity	
E_a	Apparent Activation Energy	$kJ\ mol^{-1}$
F_c	Lack-of-fit F-value	-
$F_{0.95}$	F-value at the 95% Confidence Level	-
F°_{CH4}	Inlet Molar Flow Rate of Methane	$mol\ s^{-1}$
h	Heat Transfer Coefficient	$J\ m^{-2}\ K^{-1}\ s^{-1}$
ΔH	Heat of Reaction	$kJ\ mol^{-1}$
J_A, J_D	Mass and Heat Transport Factors	-
k	Rate Constant	
k_g	Mass Transfer Coefficient	$m\ s^{-1}$
k_s	Rate constant evaluated at Surface Conditions	
K_i	Equilibrium Constant of reaction i	-
M_M	Mean Molecular Mass	$g\ mol^{-1}$
N, n	General Number	-
n_e	Number of Replicate Experiments	-
p	Number of Parameters used in the model fit	-
P_i	Partial Pressure of Compound i	kPa
P°_i	Partial Pressure of Compound i at the reactor inlet	kPa
R	Universal Gas Constant	
S	Catalyst surface area	$m^2\ g^{-1}$
t	Reduced Temperature	-
T	Temperature	K
T_s	Temperature at the Catalyst Surface	K
r	Reaction rate	$mol\ g^{-1}\ s^{-1}$
r_p	Particle Radius	
u_0	Linear Velocity	$m\ s^{-1}$
W	Mass of Catalyst	g
X_{CH4}	Fractional Methane Conversion	-
X_{O2}	Fractional Oxygen conversion	-
X_i	Fractional Conversion of Reaction i	-

Abbreviations and Dimensionless Groups

CSTB	Catalytically-stabilized Thermal Burner
Da	Dahmköhler Number
DEN	Denominator
Le	Lewis Number
LOF - SS	Lack-of-fit sum of squares

NUM	Numerator
Ob	Observable
OCM	Oxidative Coupling of Methane
PE - SS	Pure error sum of squares
Pr	Prandtl Number
PRB	Porous Radiant Burner
Re	Reynolds Number
Re_p	Particle Reynolds Number
RES	Residual sum of squares
Sc	Schmidt Number

Subscripts

Comb	Combustion
Oxref	Oxidative Reforming
SR	Steam Reforming
WGS	Water-gas Shift

Greek symbols

β	Heat-of-Reaction Term	-
γ	Activation Energy Term	-
ϵ_P	Catalyst porosity	-
ρ	Density	g cm^{-3}
ρ_p	Particle Density	g cm^{-3}
η	Effectiveness Factor	-
η_{ext}	External Effectiveness Factor	-
τ	Tortuosity factor	-

Introduction

To him who works and seeks in her, Science gives much pleasure - to him who learns her facts, very little (F. Nietzsche [1])

Volta isolated methane from marsh gas in 1776 [2] and over the next two centuries, methane was utilized in various ways. In the 1890's, for example, Cameron [3] designed a septic tank which supplied the city of Exeter with gas for street lighting. In the present technological environment, the vast resources of natural gas, which is the main source of methane (see Figure A-1), play an important role in the global economy [4].
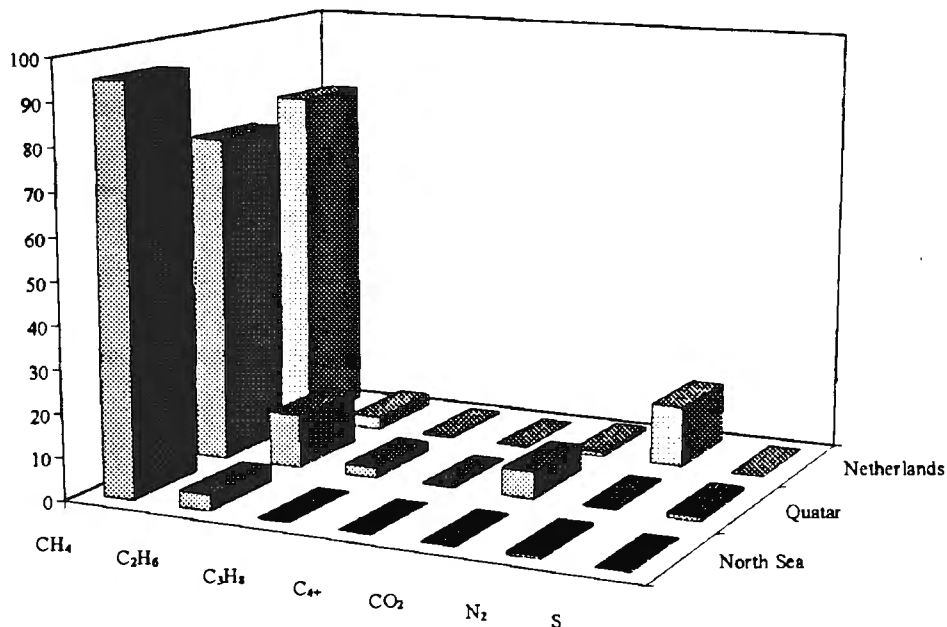
Figure A-1 Typical composition of natural gas (data from ref. 4)

Today, natural gas is widely used for heating purposes in Europe, but the remote location and therefore relatively high transportation costs to the marketplace, has precluded its more widespread use. In the medium term, it is foreseen that oil will be replaced by natural gas as the major source of hydrocarbons, while coal should be regarded as a solution that will

2

be more important in the long term. This is reflected in the ratio of proven reserves to the current rate of production (R/P ratio) of oil, coal and gas given in Table A-1 [5].

Table A-1 Estimated reserves of carbonaceous material

Material	Proven Reserves / Production (Years)	Depletion Date
Oil	34.5	2015
Gas	57.6	2043
Coal	219	2204

The methane in natural gas is also a source of other important products such as hydrogen, hydrogen cyanide (HCN), methyl methacrylate (the monomer used in perspex manufacturing), cellophane, carbon black and a variety of fluorocarbons [6]. In a very recent review article, Peña et al. [7] express the view that heightened environmental awareness will exert pressure on refineries to increase the extent of desulphurization and on the petrochemical industry as a whole to develop technology for the production of more environmentally benign fuels. Increased levels of desulphurization would in turn lead to a higher demand for hydrogen while the direct production of sulphur- and nitrogen-free fuels is already possible by Fischer-Tropsch synthesis (hereafter F-T) of hydrocarbons from synthesis gas [8]. Hence, the conversion of methane to synthesis gas (carbon monoxide and hydrogen) should increase in importance as an industrial process over the next two decades.

The various configurations of the steam reforming of methane (hereafter SRM) are industry standards for the selective conversion of methane to synthesis gas [9].

$$CH_4 + H_2O\ (l) \rightarrow CO + 3\ H_2 \qquad \Delta H\,^{\circ}_{298K} = 250\ kJ\ /\ mol \qquad \text{(A-1)}$$

Steam reforming of methane to synthesis gas, the production of methanol from synthesis gas [10] and the methanol-to gasoline (hereafter MTG) process (reaction (A-2)) over a

ZSM-5 catalyst are well-established and proven technologies.

$$CH_4 \rightarrow CO + H_2 \rightarrow CH_3OH \rightarrow Gasoline \qquad \text{(A-2)}$$

Whether either F-T synthesis or MTG will be preferred in future for the production of clean fuels, will be dictated by the relative economic considerations prevalent at the time.

In a bid to bypass the expensive reforming stage in which up to 30% of the methane fed has to be combusted [11] to provide the heat of reaction, various attempts have been made to **directly** convert methane to methanol and/or ethylene. The catalytic partial oxidation of methane (hereafter **POX**) with the aim of producing formaldehyde and methanol from methane in a single step has, however, been plagued with considerable difficulties. The very low reported oxygenate yields was already pre-empted in 1932 when it was stated that: *(m)ethane is very unreactive and the introduction of the first oxygen atom would require a high temperature level on this account. The introduction of successive oxygen atoms requires successively lower temperature levels....This results in a phenomena similar to the fall of a stone in a vacuum in that the farther it goes the higher the rate of fall becomes [12].*

After substantial efforts that were precipitated by a seminal paper by Keller and Bhasin in 1982 [13], single-pass yields of ethane and ethylene from the oxidative coupling of methane (hereafter **OCM**) were shown to exhibit an upper limit [14]. This limit was attributed to the fact that the product molecules were less stable than methane under reaction conditions. Some progress has been made in overcoming this drawback by ingenious engineering. The yield of higher hydrocarbons from oxidative coupling was significantly improved by utilizing chromatographic reactors and by providing several oxygen injection points along the length of an OCM reactor. To date, neither POX nor OCM has been tested on large scale. A number of extensive reviews have been published that deal with the oxidative coupling of methane [15, 16, 17, 18] and the partial oxidation of methane to oxygenates [19, 20], but interest in these fields have declined substantially over the past three years [21].

As mentioned above, environmental considerations will lead to enhanced demand for synthesis gas and pure hydrogen. It is not surprising that, some time after the peak in the

early 90's in OCM and POX research activity, the attention of researchers involved with methane shifted to processes that offer new ways to produce synthesis gas from methane. Hence, apart from the carbon dioxide reforming or so-called dry reforming of methane (reaction (A-3)),

$$CH_4 + CO_2 \rightleftharpoons 2\ CO + 2\ H_2 \qquad \Delta H°_{298K} = 247\ kJ\ /\ mol \qquad (A-3)$$

the oxidative reforming of methane (OXREF) (reaction (A-4)) has also attracted considerable attention [22].

$$CH_4 + 0.5\ O_2 \rightarrow CO + 2\ H_2 \qquad \Delta H°_{298K} = -56\ kJ/mol \qquad (A-4)$$

The relationship between oxidative reforming and other ways to utilize methane, both directly and indirectly, is shown graphically in Figure A-2.
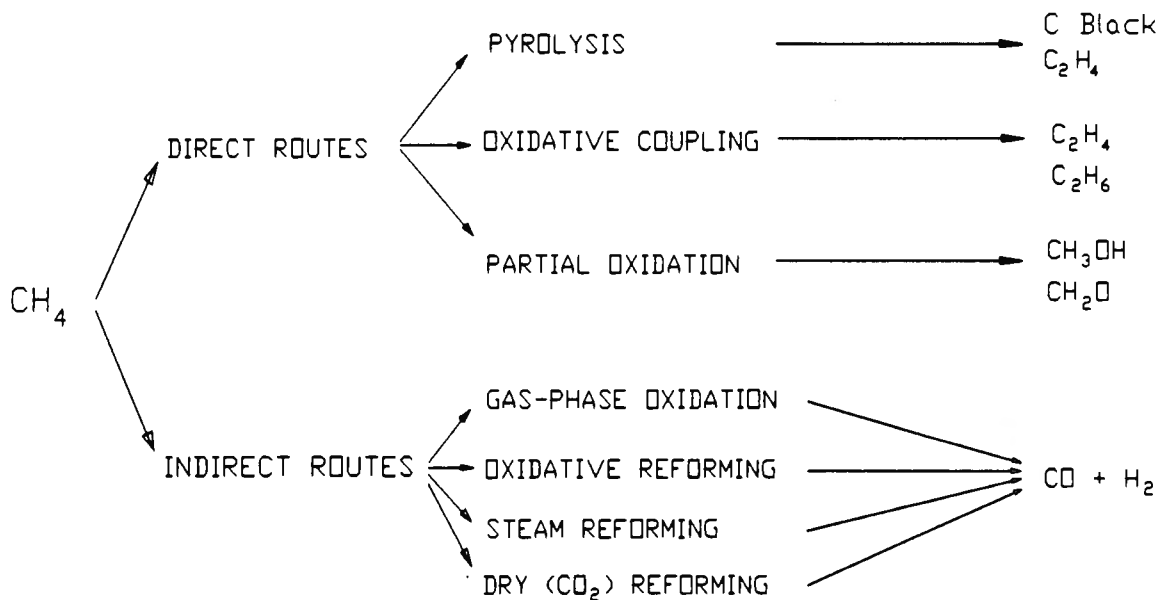
Figure A-2 Oxidative reforming in relation to other routes of methane conversion

Oxidative reforming has to offer a competitive advantage over the well-established process

Oxidative reforming has to offer a competitive advantage over the well-established process of steam reforming of methane if it were to be applied industrially. It could be argued that secondary reforming is in essence identical to oxidative reforming because of the combustion-reforming mechanism and that there is no need for a new name for an existing process. In contrast to this argument, oxidative reforming offers the advantage of *in-situ* water production without the need for an expensive burner design combined with very high space-time yield of synthesis gas. The H_2/CO ratio of 2 resulting from the oxidative reforming of methane is the ideal feed for a methanol reactor. Thus, there is no need for H_2/CO ratio adjustment by water-gas shift reactors as required downstream of a steam reformer. One of the major drawbacks of oxidative reforming, however, is that it requires an expensive oxygen plant. There have been efforts to overcome this by employing membrane reactors that facilitate the selective diffusion of oxygen from a feed stream of air to the catalyst where it reacts with methane. In addition to this, the initial concerns about carbon formation, especially on supported nickel catalysts, have been largely overcome by adding small amounts of platinum-group metals to the nickel catalysts. But perhaps the most condemning aspect of methane oxidative reforming is that it is an unproven technology, a fact that investors never consider lightly.

A great deal has been published on the oxidative reforming of methane and many of the problems that were initially posed have been solved. There is, however, substantial controversy surrounding claims about the reaction pathway and the reaction mechanism. In addition to this, very little information is available about transport effects. Few studies have been conducted in the absence of substantial axial temperature gradients inside the catalyst bed. The present study was undertaken in an attempt to shed some light on these issues.

In order to contextualize the experimental work contained in this study, the first chapter is devoted to a literature review of the aspects of oxidative reforming that have been reported. The thermodynamics of the process, heat and mass transfer and the effect of operating conditions are first dealt with. Thereafter, a review of the reported kinetic studies is presented while also considering theoretical aspects of the activation of methane and oxygen on clean metal surfaces. This first chapter is concluded with a statement of the objectives of the experimental programme.

The second chapter describes the experimental apparatus and the procedures that were followed. Axial bed temperature profiles are shown to indicate the effect of reactant dilution on the bed temperature profile. The last results contained in chapter two are concerned with a demonstration of the absence of heat and mass transport.

Chapter three contains the results of the kinetic experiments. Also considered are a number of methods to calculate reaction rates from integral reactor data. These methods are used throughout this work. The product composition is shown for each of the reaction conditions investigated. The effect of temperature, methane partial pressure and oxygen partial pressure on the product composition and reaction kinetics are first presented. This is followed by the results of co-feeding experiments.

A theoretical treatment of external transport phenomena introduces chapter four. This is followed by a differential treatment of the kinetic data and the results of the modelling of the differential data. Next presented are the results of an integral treatment of the kinetic data and general statements concerning the reaction mechanism. The study is concluded by a summary of the main findings and proposals are made for future work.

Chapter 1

1. LITERATURE REVIEW

Il est regrettable que les traitées modernes négligent l'histoire et présentent comme des monuments achevés des sciences en perpétuelle évolution. (F. Osmond, 1906)

This chapter provides the background against which the present experimental work should be seen. Various aspects of the oxidative reforming of methane that have been reported in the literature will be considered. A discussion of the thermodynamics is followed by a consideration of the effect of operating conditions on the synthesis gas yield, the effect of transport phenomena, reported results of reaction kinetics and aspects of the mechanism of the reaction that have been raised in the literature. After these general aspects of methane oxidative reforming, a more fundamental discussion of the interaction between methane and oxygen with nickel catalysts is presented. Armed with this background information, the present chapter is concluded with a statement of the objectives of the experimental work.

1.1. Early work on the oxidative reforming of methane

Prettre [23] is often cited as the pioneer of the oxidative reforming of methane. He demonstrated the formation of carbon monoxide and hydrogen from methane and oxygen over a supported nickel catalyst as early as 1946. This effort was, however, not the first attempt at the oxidative reforming of methane. As early as 1929, Liander [24] reported a study of oxidative reforming over supported nickel catalysts (see Figure 1-1). The work cited above [24] was most probably influenced by that of Bone and Coward [25] who, twenty years earlier, demonstrated the ability of heated surfaces to dissociate methane. BASF recognised the economic potential of the oxidative reforming of methane very early when they took out the first patent for a process very similar to methane oxidative reforming in 1927 [26].

Recent interest in the field was revived in the late 1980's to the early 1990's. One of the earlier of these studies reported the use of transition metal catalysts to produce synthesis gas from methane and oxygen at 777°C [27]. A great number of publications have appeared since then, including a number of review articles [7, 22].

1.2. Thermodynamics of the oxidative reforming of methane

In this study, unless stated otherwise, the product composition at thermodynamic equilibrium was calculated by performing a Gibbs free energy minimization of all the gaseous species (CH_4, O_2, CO, H_2, CO_2 and H_2O) with the HYSIM software package [28]. It was decided to perform a **total species equilibrium** calculation mainly because the dissociative adsorption of methane and oxygen on metal surfaces lead to the complete breakdown of the molecules to the constituent atoms. Hence, the overall thermodynamic equilibrium is established between all possible gaseous combinations of these atoms (including C_2 hydrocarbons) and it would therefore be erroneous to allow for only selected reactions in the thermodynamic equilibrium calculation. In the case where non-dissociative adsorption is more likely (such as metal oxide catalysts), a more restrictive approach may perhaps be taken, but this falls outside the scope of the present work.

In the earliest reported study of OXREF, Liander showed that both carbon monoxide selectivity (S_{CO}) and methane conversion (X_{CH_4}) **increased** with increasing space velocity.

The conversion in the above work exceeded the methane conversion predicted at thermodynamic equilibrium [28]. Excluding the possibility of an incorrectly-determined mass balance, an inaccurate temperature measurement presents the only remaining possibility for equilibrium to be exceeded. If the reaction mechanism consists of exothermic combustion followed by endothermic reforming reactions and heat transfer limitations exist, a temperature peak may develop in the first part (combustion zone) of the bed. This would, of course depress the methane conversion. If, however, the endothermic methane reforming reactions occur at this higher temperature, the methane conversion will be enhanced. An incorrect assumption, namely that the reactor was isothermal and that the catalyst surface

temperature was identical to the measured temperature, while the abovementioned scenario actually persisted in the catalyst bed, would thus lead to the conclusion that equilibrium was exceeded.
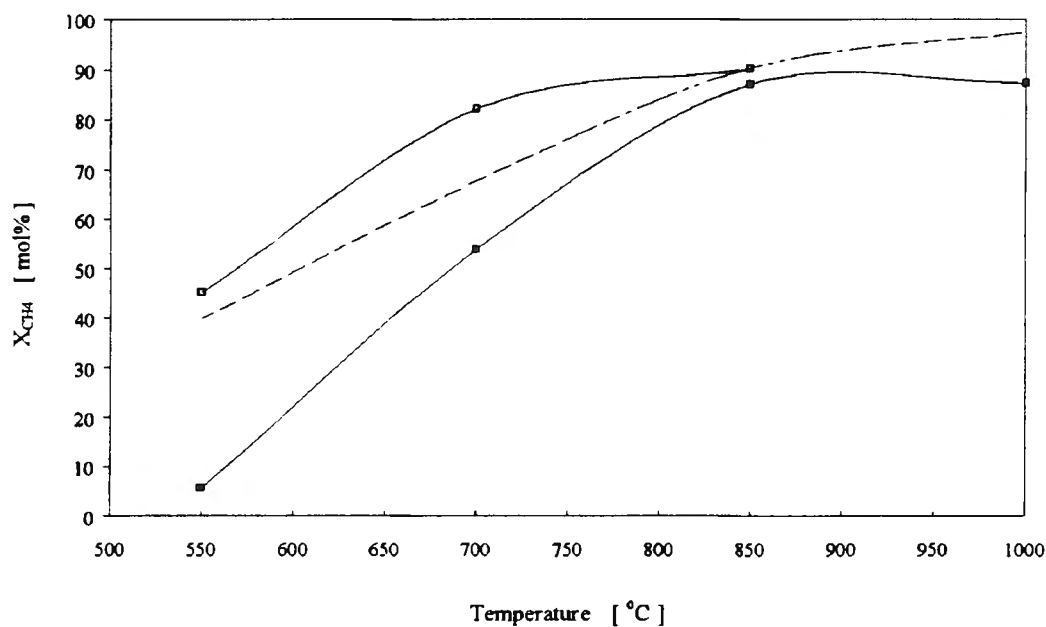
Figure 1-1 Oxidative reforming on a nickel catalyst reported in 1929 [24] (■ = low SV, □ = high SV, The dotted line corresponds to thermodynamic equilibrium)

These observations suggest the possibility that the temperature in the catalyst bed was higher than that reported by the author. Hence, the current debate about temperature measurement in methane oxidative reforming experiments has passed virtually unnoticed for more than **sixty years** only to emerge again in the 1990's as a hotly-disputed topic.

In addition to the cited example [24], there are a number of studies [29, 30] that report carbon monoxide and hydrogen yields higher than the calculated equilibrium values (especially at low measured temperature), but these results have been strongly disputed. It will be shown later that the exceeding of thermodynamic equilibrium is most likely attributable to inaccurate temperature measurements (section 1.4.1).

1.2.1. Possible reactions

Methane may be either oxidized to total oxidation products

$$CH_4 + 2\ O_2 \rightarrow CO_2 + 2\ H_2O\ (l) \qquad \Delta H\ ^\circ_{298K} = -890\ kJ\ /\ mol \qquad \text{(1-1)}$$

or to the partial oxidation products as shown previously in reaction (A-4) (H_2/CO ratio of 2). Both of these reactions are exothermic [31] and thermodynamically permitted over a wide temperature range ($\Delta G^\circ < 0$ for T > 273K).

Apart from the methane oxidation reactions, methane may also react with products of oxidation, namely water and carbon dioxide. In the presence of water and a suitable catalyst, methane may be consumed by the endothermic steam reforming reaction (reaction (A-1)) to produce carbon monoxide and hydrogen (H_2/CO = 3) while the presence of CO_2 will lead to the so-called dry reforming reaction, also resulting in the formation of carbon monoxide and hydrogen (H_2/CO = 1) (reaction (A-3)). In addition to the above reactions, methane dissociation on a metal surface yields hydrogen and surface carbon;

$$CH_4 \rightarrow C + 2\ H_2 \qquad \text{(1-2)}$$

while carbon monoxide is another possible source of surface carbon by the so-called Boudouard reaction:

$$2\ CO \rightarrow C + CO_2 \qquad \text{(1-3)}$$

Carbon may be removed from the catalyst surface by a number of reactions:

$$C + H_2O \rightleftharpoons CO + H_2 \tag{1-4}$$

$$2 C + O_2 \rightleftharpoons 2 CO \tag{1-5}$$

$$C + O_2 \rightleftharpoons CO_2 \tag{1-6}$$
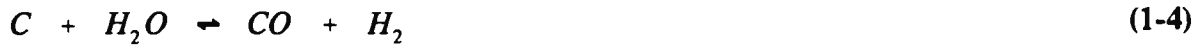
Further possible reactions are the oxidation of CO and hydrogen

$$CO + 0.5 \, O_2 \rightarrow CO_2 \tag{1-7}$$

$$H_2 + 0.5 \, O_2 \rightarrow H_2O \tag{1-8}$$

and the water-gas shift (WGS) reaction

$$CO + H_2O \rightleftharpoons CO_2 + H_2 \tag{1-9}$$

The effect of three operating conditions, namely temperature, pressure and the CH_4/O_2 ratio on the equilibrium values of X_{CH4}, S_{CO} and S_{H2} have been calculated and will be presented next. As stated previously, the calculations allow for all possible reactions; ie. water-gas shift, steam reforming, carbon dioxide reforming and total oxidation in addition to oxidative reforming [32, 28]. Although carbon was not included in our equilibrium calculations, results from other workers are referred to in a discussion on the feasibility of carbon formation (section 1.2.5).

1.2.2. The effect of temperature on equilibrium

Th Gibbs free energy for the oxidative reforming reaction is highly negative (ΔG° = -142 kJ mol^{-1} at 600K) and the equilibrium constant decreases with increasing temperature because of the exothermicity of the reaction. Therefore, if one considers the case where oxidative reforming (reaction (A-4)) is the only reaction taking place, virtually complete methane conversion and pure synthesis gas can be expected over the temperature range from 200°C to 1000°C. Furthermore, since oxidative reforming is slightly exothermic, an increase in temperature should favour the reverse reaction and thus lead to lower conversion. This was confirmed when the calculated equilibrium methane conversion of the pure oxidative reforming reaction was found to decrease from 0.998 at 27°C to 0.966 at 927°C (pure methane and oxygen with CH_4/O_2 = 2) [28].

At temperatures higher than about 650°C, ΔG° for the carbon dioxide reforming and steam reforming reactions are negative (K_p > 1). This implies that the reactions proceed to the right and that the production of synthesis gas (CO and H_2) rather than CO_2 and H_2O (products from exothermic combustion reactions) is favoured at higher temperatures.

The combustion of methane to carbon dioxide and water (ΔG°_{900K} = -800 kJ mol^{-1}) is thermodynamically much more favourable than oxidative reforming to carbon monoxide and hydrogen (ΔG°_{900K} = -200 kJ mol^{-1}). It was argued by Stanley in 1938 [33] that this implies that the reaction products of a feed consisting of $CH_4:O_2$ = 2:1 would consist of unreacted methane and deep oxidation products rather than traces of methane and oxygen in synthesis gas. If a suitable catalyst is employed, the deep oxidation products may be used to reform the unreacted methane to synthesis gas.

The total species equilibrium (excluding carbon but including the C_2 hydrocarbons) of a CH_4 + 0.5 O_2 feed at an absolute reactor pressure of 201.3 kPa was calculated as a function of temperature in order to obtain values for the species mol fractions at thermodynamic equilibrium [28]. Using these mol fractions, the methane conversion and product selectivities were calculated and are shown in Figure 1-2. The amount of higher hydrocarbons were negligible.

An increase in temperature led to an increase in the predicted values of methane conversion as well as carbon monoxide and hydrogen selectivities. Carbon dioxide was the major carbon-containing product at low temperatures, but carbon monoxide became the dominant product at temperatures higher than about 600°C. Complete conversion of methane to pure synthesis gas was predicted only at very high temperatures.
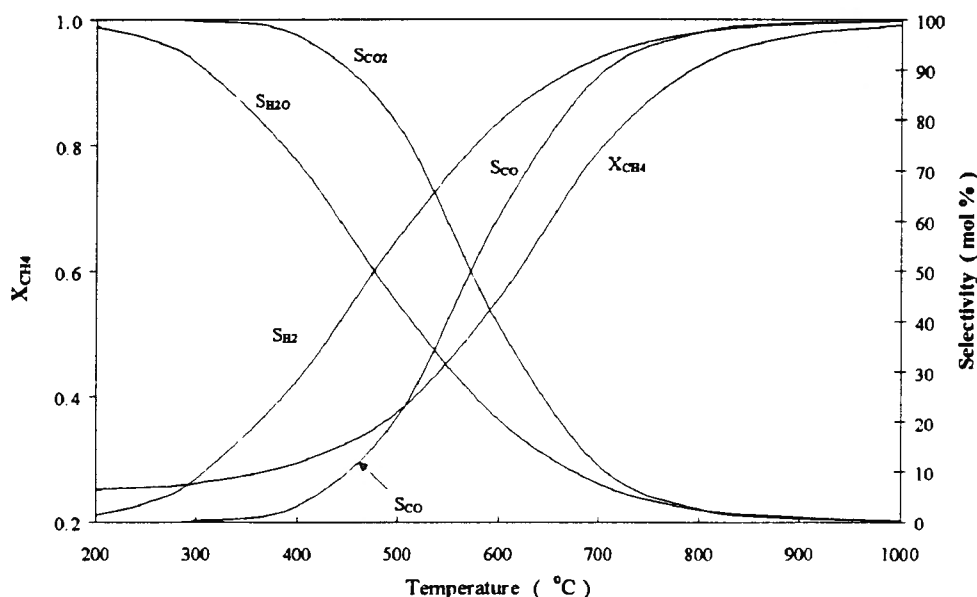
Figure 1-2 Influence of temperature on equilibrium X_{CH_4} and product selectivities (Feed: CH_4 + 0.5 O_2, P_T = 201.3 kPa)

This product distribution is in marked contrast with the predicted product composition for the oxidative reforming reaction only, namely pure syngas and almost complete methane conversion at temperatures as low 200°C.

Pure synthesis gas at low temperatures (around 200°C) has (with the exception of some studies [29] which have since been discredited [80]) never been found experimentally. This suggests that catalytic methane oxidative reforming consists of a network of reactions rather than a single reaction.

1.2.3. The effect of CH_4/O_2 ratio on equilibrium

The total species equilibrium (excluding solid carbon) was calculated at 600°C and 100 kPa(g) as a function of the CH_4/O_2 ratio. The effect of the CH_4/O_2 ratio on methane conversion and CO and H_2 selectivities is shown in Figure 1-3. A higher CH_4/O_2 ratio led to a decrease in the methane conversion (X_{CH4}). As expected, the presence of less oxygen also favoured the production of less total oxidation products and therefore higher carbon monoxide and hydrogen selectivities. The decrease in H_2/CO ratio shown in Figure 1-3 with increasing CH_4/O_2 ratio was mostly due to a drop in the hydrogen mol fraction because the CO mol fraction was more or less constant over the range of CH_4/O_2 considered.
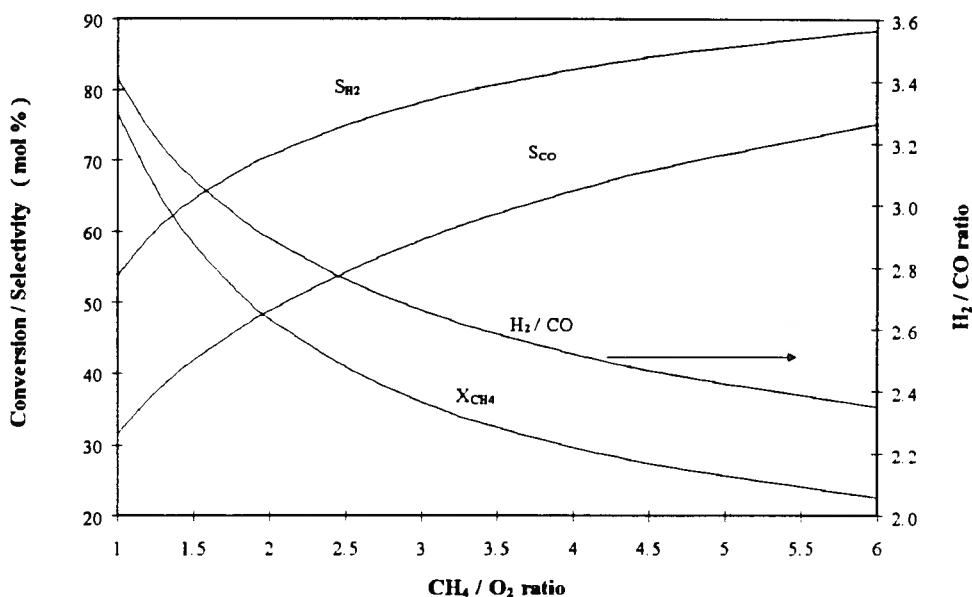
Figure 1-3 Effect of CH_4/O_2 ratio on equilibrium conversion and product selectivities (T = 600°C, P_T = 201.3 kPa)

1.2.4. The effect of pressure on equilibrium

If only the oxidative reforming reaction (as represented by reaction (A-4)) were to take place, an increase in the total pressure would favour the reverse reaction and thus lead to lower values of methane conversion while having no effect on carbon monoxide and hydrogen selectivities. Methane combustion is **not** affected by pressure, but steam reforming and carbon dioxide reforming are both depressed by high pressure.

The effect of pressure on the product composition of a feed containing methane and oxygen was quantified by calculating [28] the total species equilibrium (from atmospheric pressure to 100 atm at 1000°C) and plotting the resulting methane conversion, S_{CO} and S_{H2} as a function of pressure in Figure 1-4. Methane conversion decreased significantly from about 0.98 to less than 0.65. Hydrogen selectivity declined by a greater margin than carbon monoxide selectivity as the operating pressure was increased.
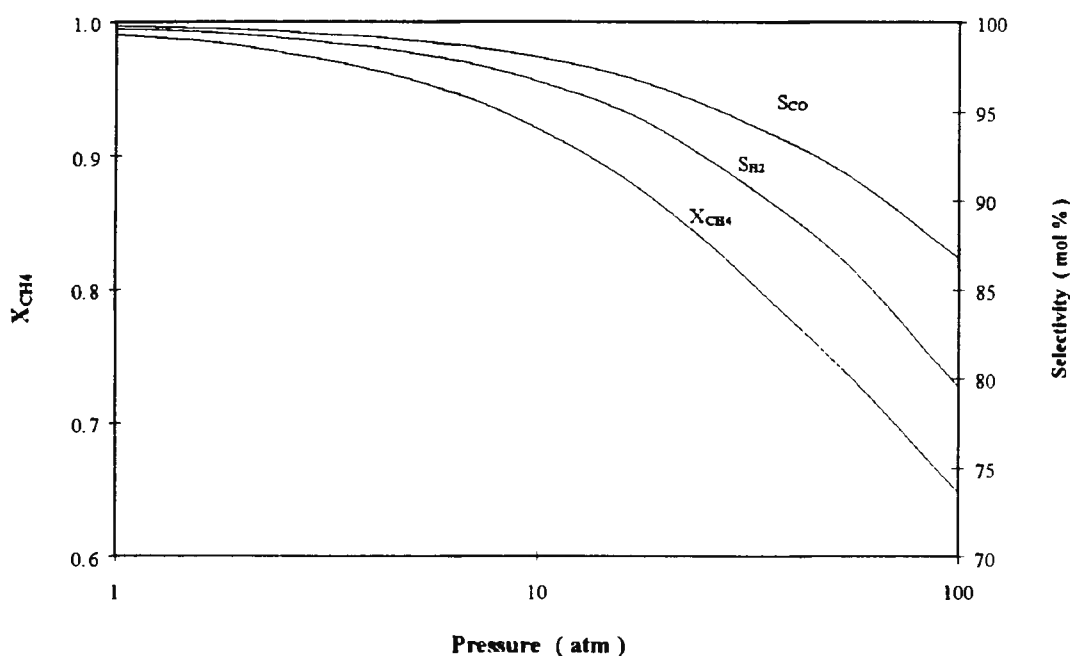
Figure 1-4 The effect of pressure on thermodynamic equilibrium (Feed: CH_4 + 0.5 O_2, T = 1000°C)

The effect of pressure on the H_2/CO ratio at 600°C and 1000°C is depicted in Figure 1-5. At 600°C the H_2/CO ratio increased from 2.5 to about 4.3 as the pressure was increased from 1 atm to 100 atm. At 1000°C, however, the H_2/CO ratio was constant over the same pressure range.

When the water-gas shift reaction (equimolar) is in equilibrium, a constant H_2/CO ratio should prevail, irrespective of the pressure. However, if the water-gas shift reaction does not play a role at a given temperature, the H_2/CO ratio at thermodynamic equilibrium will depend on the pressure. Hence, one may conclude that the water-gas shift reaction is important at 1000°C but not at 600°C.

16
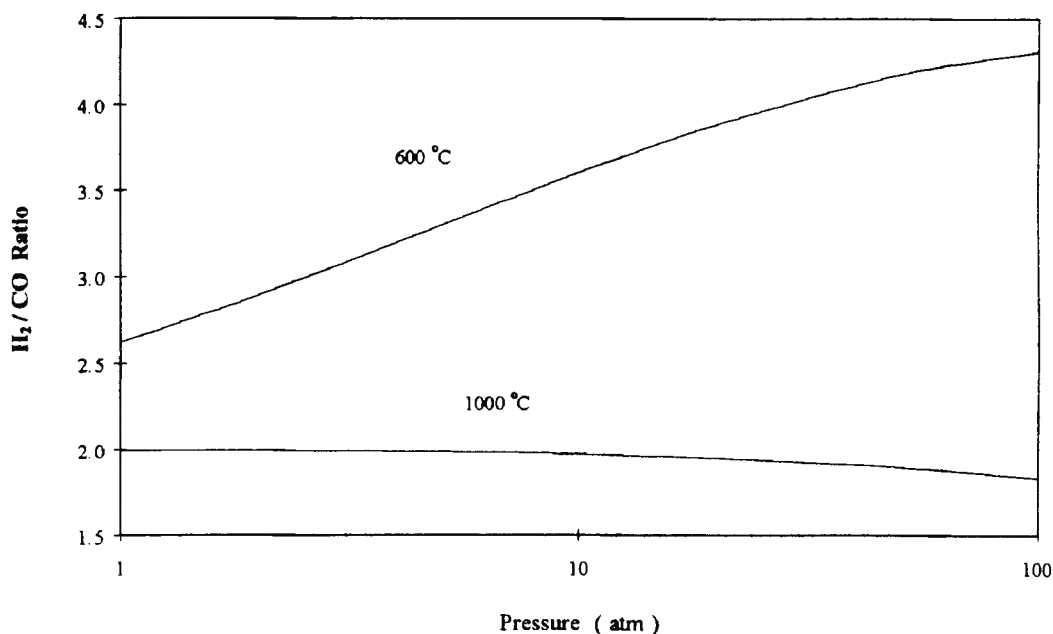
Figure 1-5 The effect of pressure on the equilibrium H_2/CO ratio at two temperatures (Feed: CH_4 + 0.5 O_2, T = 600°C and 1000°C)

1.2.5. Carbon deposition

Torniainen and Schmidt performed equilibrium calculations and predicted that the formation of graphitic carbon is feasible at all temperatures for $CH_4/O_2 \geq 2$ [136]. Vermeiren *et al.* showed for the oxidative reforming of methane on a Ni/Al_2O_3 catalyst that the exit gas composition at 780°C, $CH_4/O_2=2$ and $W/F°_{CH4} = 3.2$ kg(cat).s.mol(total)$^{-1}$ could be represented by considering the overall equilibrium predicted by combustion (reaction (1-1)), steam reforming (reaction (A-1)) and water-gas shift (reaction (1-9)) [34]. When the Boudouard reaction (reaction (1-3)) was included in their reaction scheme, thermodynamics predicted that 3.75% of the methane should be converted to carbon. Since no carbon was found on their catalyst at 780°C, the authors concluded that the Boudouard reaction was not operative under reaction conditions. The Gibbs free energy of the Boudouard reaction increases with increasing temperature and becomes positive at temperatures higher than about 700°C. Thus, the above mentioned observation [34] is consistent with thermodynamics.

1.3. Reactor and reaction engineering

The reactor design that will be selected for the commercial application of oxidative reforming of methane is dependent on the relative importance of the influence of transport phenomena and the reaction kinetics on the synthesis gas yield. Transport phenomena are not only important in industrial reactor selection, but perhaps even more so in studies on laboratory scale. Catalyst comparison and kinetic studies are questionable without first ensuring that the reactor is operated in a regime which is free of transport resistances. The role of mass and heat transfer for oxidative reforming as reported in the literature, will be addressed in the present section. Thereafter, a number of reactor types that have been employed to study oxidative reforming will be analyzed in terms of the effect of operating conditions on the observed methane conversion and product selectivities. Finally the published results of the kinetics of methane oxidative reforming will be considered.

1.3.1. Transport phenomena

Before the kinetics of oxidative reforming may be addressed, the effect of mass and heat transport on the observed reaction rate needs to be quantified. Haynes has proposed a general rule for transport phenomena, namely that:

"external mass transfer can usually be neglected, while internal mass transfer is often important; external heat transfer is more often important than internal heat transfer." [35].

In the light of this comment, it is surprising that most of the reports on oxidative reforming that have considered transport phenomena, have dealt with external transport effects only.

1.3.1.1. Mass Transfer

Berger and Marin [36] have eluded to the possibility that transport limitations can be

minimized by using a bed of diluted catalyst or a reactor which contains a single noble metal gauze. Hickman and Schmidt [37, 38] studied the effect of linear velocity over ten layers of Pt-10%Rh gauze at 1110°C and 1227°C and found that X_{CH4}, S_{CO} and S_{H2} increased with increasing superficial gas velocity (see Figure 1-6). Methane conversion and the product selectivities, however, attained constant values at gas velocities higher than about 15 cms^{-1}. This, in their view indicated the diminishing effect of external mass transfer resistance with increasing superficial gas velocity. It needs to be pointed out, however, that the change in linear velocity in the above mentioned work was not effected at constant contact time between the reactants and the catalyst and was associated with a change in the space velocity (lower contact time).
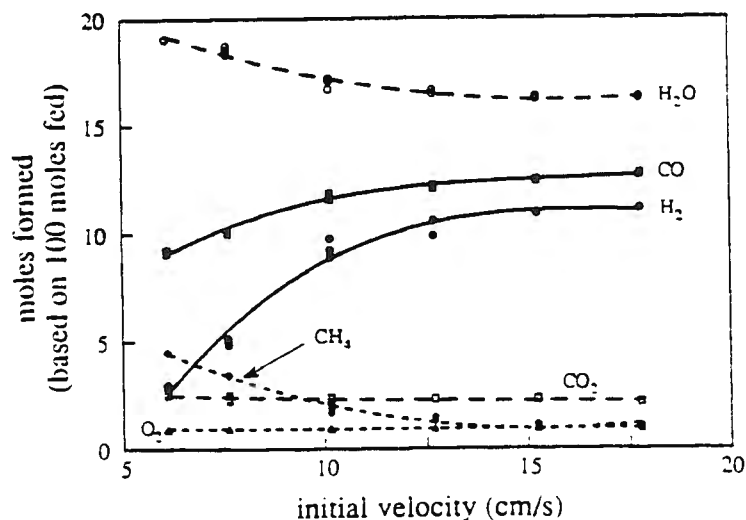
Figure 1-6 The effect of linear velocity over 10 layers of Pt-10%Rh gauze [37] (Feed: 16 mol% CH$_4$ in air, T = 1110°C)

Because shorter contact times (at constant linear velocity) result in lower methane conversion for a catalytic reaction and since the authors observed an increase in conversion (albeit at a higher linear velocity), their data are certainly not conclusive about the absence of transport limitations.

The effect of external transport resistances on the product selectivity is closely linked to

the kinetics and the pathway of a reaction; the faster the intrinsic reaction rate, the higher the superficial gas velocity that is needed to ensure that the mass transfer coefficient (k_m) is much higher than the intrinsic rate constant (k). Furthermore, if, for example, methane oxidation is a series reaction with sequential formation of carbon monoxide and carbon dioxide (*ie.* $CH_4 \rightarrow CO \rightarrow CO_2$), then an observed increase in S_{CO} with increasing linear gas velocity would be strong evidence that carbon monoxide is an intermediate or primary product [37, 38].

The mass-transfer coefficient (k_m) is also a function of the catalyst geometry. An increase in the turbulence (at constant superficial velocity) of gas flowing over a catalyst surface will decrease the film thickness, leading to higher k_m values and higher rates of mass transfer across the film. So, for example, a monolith body with more tortuous channels will have a higher mass transfer coefficient than a straight-channel monolith [94] and the former would be the preferred configuration if the yield of an intermediate product needs to be maximised.

1.3.1.2. Heat Transfer

Due to the exothermicity of the methane oxidative reforming reaction, a temperature gradient is expected to develop between the catalyst surface and the bulk gas if the heat that is generated by the reaction at the catalyst surface is not dissipated at a sufficiently high rate into the gas phase [39]. It was shown by Froment that the maximum temperature difference between the bulk gas and the catalyst surface is directly proportional to the heat of reaction [40]. Therefore, if the total oxidation of methane with a high heat of reaction forms part of the reaction pathway for oxidative reforming, the temperature gradient between the catalyst surface and the gas phase may be severe. Temperature generally has a more significant influence on reaction rate than the concentration of gaseous compounds and therefore a low value of the heat transfer coefficient may be more effective than the mass transfer coefficient in disguising the intrinsic kinetics of oxidative reforming.

Due to the difficulty of measuring actual catalyst temperatures, empirical correlations are normally used to check whether heat transport limitations are significant. There has been

only one report published that shows the absence of temperature gradients under conditions of negligible film diffusion and internal diffusion [96]. The measured reaction rate was used to check whether empirical expressions that have been developed to ensure the absence of temperature gradients, were adhered to.

1.3.2. Reactor Type

1.3.2.1. Fixed Bed Reactor

The majority of the studies on methane oxidative reforming have made use of either a packed bed or a monolith-type reactor configuration. A major advantage of the packed bed reactor is that its performance is well known and that it is easy to model. Disadvantages are, among others, a high pressure drop over the catalyst bed (especially when carbon is formed during the reaction) and a low specific rate of mass and heat transfer compared to fluidized-bed reactors. Carbon formation in a packed bed reactor may lead to particle breakup, blockage of the void spaces between catalyst particles and an increase in the pressure drop across the packed bed; in a fluidized bed reactor, carbon gasification may occur when catalyst particles are recirculated to the oxygen-rich region at the reactor inlet [41]. In spite of the variety of techniques available to determine flow patterns, the degree of backmixing, the thermal behaviour and other fixed-bed reactor characteristics, most of the data on methane oxidative reforming in packed bed reactors have thus far been generated in reactors with unknown or undisclosed hydrodynamic characteristics.

1.3.2.2. Fluidized Bed Reactor

Fluidized bed reactors are being used increasingly for studying the oxidative reforming of methane as for other partial oxidation reactions [42]. These reactors have a number of unique advantages over conventional packed bed reactors. The pressure drop over a fluidized bed is much lower than over a fixed bed reactor of equivalent size and the heat transfer per unit volume of catalyst bed is much higher in a fluidized bed reactor [7].

Bharadwaj and Schmidt observed flames and small explosions when using a fluidized bed reactor and operating at CH_4/O_2 ratios lower than 1.4 [43] which is within the explosive regime of methane-oxygen mixtures [44, 45].

A high degree of isothermicity can be obtained in fluidized reactors as demonstrated by Santos *et al.* who were able to limit temperature differences in the bubbling region of their fluidized bed to less than 5°C [41] and 10°C respectively [46].

A further advantage of the fluidized-bed configuration is that carbon that has been deposited on catalyst particles may be gasified when these particles are circulated to an oxygen-rich region of the bed [41, 46]. On the other hand, deactivation of the catalyst by oxidation of the active metal (Ni to NiO, for example) may be reversed when the deactivated catalyst particles are recirculated from the oxygen-rich inlet region to the hydrogen-rich region near the outlet of a fluidized bed reactor.

Bharadwaj and Schmidt [43] studied oxidative reforming in a fluidized reactor with a contact time between 0.1s and 0.5s using catalysts consisting of nickel, platinum or rhodium deposited on 100 μm α-Al_2O_3 beads. Catalyst particle agglomeration was observed only when the temperatures were higher than 850°C for Ni and Pt and higher than 950°C for Rh on Al_2O_3 beads. The operating temperature was always lower than these stated limits and the catalyst microstructure of the used catalysts was reported to be unchanged (*ie.* no particle agglomeration). Autothermal behaviour of the reactor was observed as the reaction sustained itself by the heat that was generated by the chemical reaction and very little additional heat input was required to maintain the steady-state (autothermal) temperatures. A doubling of the flow rate on the nickel catalyst had no discernable effect on the methane conversion (X_{CH4} = 0.91) and syngas selectivity (S_{CO} and S_{H2} > 90%).

1.3.2.3. Monolith reactor

The major advantage of a monolith type reactor over a packed bed reactor is the low pressure drop and therefore the very high space velocities which may be attained in such

reactors. The group of Hickman and Schmidt [37, 38, 94, etc.] has published some excellent work, mainly using monolith reactors, but with a general feature that the contact time between the gas and the catalyst was in the order of milliseconds. Their work was however preceded by sixty years by that of Fischer and Pichler who used a contact time of about 5 milliseconds and a tube packed with broken pottery (held at between 100 and 1400°C) to convert mixtures of methane and air to acetylene, hydrogen and carbon monoxide [47]. At 120 atm pressure, these authors found that the acetylene disappeared and that the main products were carbon and synthesis gas.

Thermal equilibrium of the support is more easily achieved than with conventional supported catalysts because of the low wall thickness of monoliths as opposed the comparatively large dimensions of catalyst pellets. Monolith bodies are therefore less prone to fracture due to rapid changes in temperature at start-up and shut-down of the reactor. As discussed earlier (cf. Section 1.3.1.1), more efficient film (external) diffusion may be realized by using foam monoliths with highly tortuous channels instead of straight channel monolith bodies as support for the catalytically active material.

1.3.2.4. Metal gauze-type flow reactor

A "packed bed" of a number of Pt-10%Rh gauzes was used to catalyze the methane oxidative reforming reaction and it was shown that essentially all of the reaction occurred on the first three layers of gauze [38]. After the first layer, oxygen consumption was complete and only a slight increase in conversion and selectivity could be measured when more layers of gauze were added.

Heitnes *et al.* [48] studied methane oxidative reforming on platinum gauzes, Ni and Pd-impregnated monoliths and a packed bed of Ni/Al_2O_3 catalyst. Using a single Pt gauze as the catalyst, no reaction was observed with a feed temperature of 700°C, but when the temperature was increased to 750°C, methane conversion jumped from zero to 0.31 ($S_{CO} = 71\%$ and $X_{O2} = 91\%$). At the same time, the temperature at the gauze increased to a level which was up to 150°C higher than the furnace temperature. A doubling of the space

time (decreasing the contact time from 0.4 ms to 0.2 ms) resulted in a decrease of X_{CH4} from 0.31 to only 0.29, S_{CO} increased from 71% to 84% and X_{O2} decreased from 0.91 to 0.85. A significant observation was that there was only a very small amount of H_2 (mostly water) produced on the Pt gauze [48]. This is in agreement with the view of Schmidt *et al.* [94] who showed that there is a larger activation energy barrier to OH formation on rhodium than on platinum and that higher H_2 selectivities may therefore be obtained on a rhodium surface than on a platinum surface.

In the author's view, the high temperatures upstream of the gauze in the work discussed above [48] may be indicative of either the purely radiative heating of the incoming gas, or the presence of exothermic gas-phase reactions; the ignition of the feed and initiation of gas-phase reactions should not be discounted at temperatures of about 900°C. The role of gas phase reactions is discussed later (section 1.6.4). In another study with the same platinum gauze catalyst and a feed which was diluted in helium ($CH_4:O_2:He = 2:1:10$), the temperature difference between the gauze and the furnace was as high as 400°C [49]. It should also be kept in mind that this temperature difference will be even higher when a pure CH_4/O_2 feed is used.

1.3.2.5. Electrochemical cells

Solid oxide fuel cells are well known for their ability to convert the heat of reaction that is liberated during methane combustion and hydrogen oxidation, to electrical energy [50]. Eng and Stoukides [51] also mention the possibility of using solid oxide membranes to facilitate the oxidation of methane. An electrochemical cell may either be used in the so-called fuel cell mode where the liberated heat of reaction is recovered as electrical energy, or the electrochemical cell may be used in conjunction with an external power source to "pump" oxygen across an oxygen-ion conducting membrane. The main advantage of the latter configuration is the fact that the solid electrolyte (O^{2-} conductor) acts as a O_2-N_2 separator. This would enable one to use air as the feed to a OXREF reactor and an expensive oxygen plant would not be required.

1.3.2.6. Membrane reactors

Santos *et al.* [52] packed a 14 cm long bed of NiO/Al_2O_3 catalyst inside an alumina membrane (nominal pore size of 200 nm) in an attempt to selectively remove hydrogen from the product gas by the preferential diffusion of hydrogen through the membrane pores. It was hoped that this approach would therefore force the equilibrium of reaction (A-4) to the right and result in a higher value of methane conversion than in a conventional fixed bed reactor. The feed (CH_4 + 0.5 O_2) flowed over the catalyst which was packed inside the tube and nitrogen was used as sweep gas on the shell side of the membrane. The first 6 cm of the membrane was modified to prevent the premature diffusion of methane and oxygen to the shell side before significant conversion to products could be attained. Methane conversion was found to increase from 0.95 to 0.98 at 775°C as the sweep gas flow rate was increased; the conversion in a plug flow reactor under the same conditions was 0.94. Furthermore, the H_2/CO ratio on the shell side ($H_2/CO > 3.5$) was much higher than the ratio on the tube side ($H_2/CO \approx 1$) and the difference between the two streams increased as the sweep gas flow rate was increased. This hydrogen enrichment was attributed to the preferential permeation of hydrogen through the membrane. When the pressure was increased to 2 bar, methane conversion at a sweep gas flow rate of 200 $cm^3.min^{-1}$ decreased from 0.97 to 0.95, CO selectivity was virtually constant and the hydrogen selectivity dropped from 100% to 98%.

Ioannides and Verykios [53] were very successful in obtaining values of methane conversion higher than the thermodynamic equilibrium by using dense-silica membrane reactors and a Rh/SiO_2 catalyst to selectively remove the reaction products and forcing the reaction to the right. At 600°C, for example, the measured X_{CH4} was 0.86 while the equilibrium value of methane conversion was only 0.43. The enhancement of the conversion was, however, only observed at very low space velocities (SV < 100 h^{-1})

Pei and co-workers [54] fed methane and air on opposite sides of a membrane constructed from a perovskite-like material ($Sr(Co_{0.8}Fe_{0.2})O_x$) which has a high oxygen permeability. Methane was fed to the tube side and oxygen to the shell side and a precious metal reforming catalyst was packed on the tube side of the membrane. Performance data for the oxidative reforming of methane was not given, but the authors focused on the possible

mechanisms for failure (cracking) of the ceramic membranes. The presence of an oxygen gradient in the membrane was shown to lead to phase changes which introduced strain in the membrane; decomposition of the membrane material under reducing conditions was isolated as another cause for cracking of the membranes.

Clearly there is more work to be done before this technology can be applied industrially, but it has great potential for the production of hydrogen-rich synthesis gas.

1.3.2.7. Transient reactors and temporal analysis of products reactors

A number of studies have employed packed bed reactors operated in a transient mode [55, 56, 57, 58, 59, 60, 61, 62]. Three studies reported on the oxidative reforming of methane on platinum and rhodium catalysts, using a temporal analysis of products (hereafter **TAP**) reactor [59, 106, 63]. This experimental setup enables one to obtain the complete product composition by mass spectrometry with submillisecond response times. The results of these studies will be discussed later (section 1.6.3).

1.3.2.8. Porous Radiant Burners / Catalytically Stabilized Thermal Burners

Two interesting characteristics that have been reported for some oxidative reforming reactors are that, firstly, the conversion was either zero or almost complete (close to the equilibrium value) and secondly, that the reaction could sustain itself without any additional heat input (autothermal operation). This behaviour is also exhibited by typical porous radiant burners (hereafter **PRB**) [64, 65] and catalytically-stabilized thermal burners (hereafter **CSTB**) [66, 67].

In a PRB, the fuel-air mixture to be combusted is fed to a packed bed of refractory material without a catalytic function. The feed is ignited and the function of the packed bed is the stabilization of the resulting flame/reaction front by means of radiative heat feedback to the bulk gas. CSTB's consist of empty tubes with the inside walls coated with an agent

(normally a precious metal) with a catalytic function. This facilitates re-ignition of homogeneous (gas phase) reactions which may otherwise be extinguished by small-scale flow perturbations. The range of stable operating conditions is thus extended compared to pure gas-phase oxidation. Heat convection against the direction of flow and back-diffusion of radicals result in autothermal operation of PRB's. In a PRB, the reaction can therefore be sustained without the need for external heating. A similar situation exists for normal industrial reactors such as the oxidation of nitrogen to NO_x on a catalytic gauze. In this instance, autothermal operation is achieved by radiative heating of the feed [68, 69, 70].

At the high temperatures typical of oxidative reforming, gas phase reactions may play an important role in the overall reaction scheme. This opinion was reinforced by Chang and Heinemann who acknowledged the possible role of gas phase reactions in oxidative reforming of methane [81]. Certain products of gas phase reactions may be shared by reactions taking place on the catalyst surface, leading to coupling between the gas phase and the surface reactions. It is in this respect worth considering that gas phase reactions are well known in PRB's and integrally part of CSTB operation.

If oxidative reforming reactors that exhibit autothermal behaviour were to be seen as a type of PRB, the results of methane oxidative reforming could in our opinion be much better modelled by using the approach of hetero-homogeneous reaction coupling as applied in CSTB's and OCM [71].

1.3.3. Modelling of reactors for oxidative reforming

De Groote and Froment [72] developed a kinetic model for the oxidative reforming of methane based on kinetic equations previously developed for the combustion of methane to carbon dioxide and water [73], the steam reforming reaction, water gas shift reaction, coking reactions and carbon oxidation reactions. The kinetic model was combined with a one-dimensional heterogeneous reactor model which neglected temperature gradients over the external film. The problem of the degree of reduction of the nickel catalyst was overcome

by considering two cases; in the one instance, the steam reforming- and combustion reactions were assumed to occur in parallel (the bivalent- or BV model) and in the second case the steam reforming reaction was allowed to occur consecutive to total combustion (the VDR model). The oxidation of methane to synthesis gas with air or oxygen was simulated at an inlet temperature of 535°C, 25 bar and a CH_4/O_2 ratio of about 1.6.

One of their main findings was that the VDR model led to the prediction of a much higher temperature peak than the BV model early in the catalyst bed. This was attributed to the fact that the endothermic steam reforming reaction was assumed in the BV model to occur earlier in the catalyst bed than with the VDR model. It was also observed that when **air** was used instead of oxygen, both the magnitude of the temperature peak was reduced and its position in the bed moved deeper into the bed.

The high rate of coke formation that was calculated when using pure methane and air was successfully suppressed by adding either carbon dioxide or steam. Using pure methane and air as feed, methane cracking was found to be the major carbon producing reaction, both at the bed inlet and after the majority of the oxygen was consumed. The reverse Boudouard reaction was the main consumer of carbon deeper into the bed. When the inlet temperature was raised from 535°C to 635°C at 25 atm pressure with a feed consiting of methane and air, carbon formation was enhanced. This was indicated by the calculated (not measured) gas-phase carbon balance which decreased from 79% to 75%.

Reversed-flow operation of a fixed bed reactor was also simulated. In such a reactor configuration, the catalyst bed is preheated and the reactants introduced at a much lower temperature. The reactants are heated by the hot bed of catalyst particles until the temperature of the gas is high enough for ingition to occur, leading to a temperature rise. The temperature wave or reaction front thus produced is forced towards the bed outlet by convective heat transfer. Before the wave reaches the bed outlet, the flow is reversed so that the hot part of the bed near the outlet (heated by the generated heat of reaction) can act as preheat for the cold incoming gas. The authors considered a reactor preheated to 800°C and operated with $CH_4/O_2=2$ and 10 mol% H_2 at atmospheric pressure; flow was reversed every 350 seconds. The peak temperature was never above 1030°C which would be detrimental

to the nickel catalyst. Methane conversion was about 0.8 and the product selectivities reported were 93.5% for hydrogen and 91.5% for carbon monoxide respectively.

Such a large-scale reversed-flow reactor was built and operated by Blanks *et al.* [95]. The reactor consisted of an insulated, refractory-lined steel tube 4 m long and with an inside diameter of 0.57m. The reactor was operated at 200 kPa with a natural gas feed of 1400m^{3}day^{-1} and an air flow rate of 400m^{3}day^{-1}; the flow direction was reversed every hour. The reactor was operated successfully for more than a year and for weeks without interruption. The authors found hydrocarbon conversion to vary between 0.85 and 0.97 with a CO yield between 75 mol% and 95% mol%. Any carbon deposits were removed by a 4-minute burst of steam after each flow reversal. Breakthrough of oxygen could not be tolerated by downstream operations and consequently the unreacted feed gas was incinerated for two minutes at each flow direction change. To ensure a continuous flow to downstream operations, a number of these units needs to be run in parallel with each other in such a way that the 4 minutes of steam regeneration between flow reversals no not overlap. The control algorithm on such periodic reactors may also prove to be quite complex and hence the overall operation could be very risky.

1.4. The effect of operating conditions

1.4.1. The effect of temperature

Temperature is an important parameter in any catalytic study because of the exponential dependence of the reaction rate on temperature. If the catalyst bed is not isothermal, the temperature profile needs to be given if one were to compare different catalysts. Furthermore, the presence of external heat transfer resistance as discussed in section 3.1.2 may result in a substantial temperature gradient between the catalyst surface and the bulk gas. Therefore even if the bed temperature is given, this may not be an accurate representation of the catalyst surface temperature. Since the catalyst bed temperature is very superficially treated in most studies of methane oxidative reforming with only a handful of studies reporting bed temperature profiles [34, 74 and 75], catalyst comparison is virtually impossible.

Various approaches have been taken to report the temperature datum. One report does not make mention of the thermocouple position [76] while some workers cite the reactor wall temperature [77] and others mount small amounts of catalyst on the tip of a thermocouple. There have also been two reports where optical methods were used for a more direct measurement of the catalyst temperature [80, 81]. Boucouvalas *et al.* [78] claim to have operated under conditions of negligible temperature gradients in their catalyst bed by using a feed diluted to 4 % in He. Unfortunately, only the bed inlet temperature and the bed outlet temperatures were reported. Preliminary experiments by the present authors, however, showed that there may be temperature differences of up to 20°C in a bed of Ni/Al_2O_3 catalyst when using a feed diluted to as low as 5 vol% in He [79].

The high methane flow rates often employed in reported studies of oxidative reforming result in high rates of methane conversion and to high rates of heat generation. If the heat produced by the reaction at the catalyst surface is not removed, the catalyst temperature may rise rapidly and lead to the autothermal operation of the catalyst bed. Both Chang and Heinemann [81] and Dissanayake *et al.* [80] observed that the reaction did not cease when the furnace was switched off. Chang and Heinemann furthermore did an experiment with two loadings of the same batch of catalyst at identical space velocity (constant contact time) with a feed of almost pure methane and oxygen (5 mol% inerts). The low catalyst loading (0.026g) resulted in predominantly deep oxidation products ($S_{CO} = 1\%$) at low methane conversion (0.26 at 673°C) while the high catalyst loading (0.1g) led to mostly partial oxidation products ($S_{CO} = 89\%$) at a higher methane conversion (0.45 at 652°C). The authors attributed the high conversion on 0.1g catalyst to a greater *"amount of heat generated at the same conversion and product selectivity"* than the lower loading of catalyst. This was based on the assumption that the heat loss for the two catalyst loadings were similar. On the other hand, it may also be possible that by increasing the catalyst mass from 0.026g to 0.1g, the change in linear velocity (to maintain the contact time) resulted in a higher mass transfer coefficient and therefore an increase in the methane conversion.

Matsumura and Moffat studied oxidative reforming with an undiluted feed of methane and oxygen ($CH_4/O_2 = 2$) over a Ru/SiO_2 catalyst with the temperature measured outside the reactor [77]. Dissanayake *et al.* [80] used an optical pyrometer to show that the catalyst

surface temperature was more than 300°C hotter than that measured by a thermocouple in contact with the top of the bed. Chang and Heinemann [81] used a similar technique to measure a surface temperature of 1270°C over a Co/MgO catalyst when a thermocouple gave a reading of only 450°C and Hickman *et al.* [37] measured a temperature of about 1200°C at the inlet face of their monolith while the gas inlet temperature was at least 800°C cooler.

Homogeneous ignition has been observed [82] over polycrystalline platinum foils at temperatures higher than about 1200°C. This is very similar to the temperature at which Hickman and Schmidt [37] observed homogeneous reactions and multiple steady states for methane oxidation. Chang and Heinemann [81] measured a dramatic temperature increase over a Co/MgO catalyst with a feed containing only 5% inerts when the feed was introduced to a pre-reduced catalyst. As stated earlier, the authors found that the reaction continued even when the furnace was switched off. The glowing catalyst (*ca.* 1270°C) was cooled by increasing the flow of nitrogen and it was found that the reaction products disappeared when the catalyst surface temperature dropped lower than 1150°C. All of the above observations suggest that gas phase reactions may be initiated by a hot surface from which the heat of reaction is not effectively dissipated, typically if the feed of an oxidative reforming experiment is not diluted. Even though heterogeneous reactions may occur at much lower temperatures than homogenous ignition [81], it has not yet been demonstrated beyond doubt that gas-phase reactions are not essential for sustaining the oxidative reforming of methane at very low contact times.

There is no consensus about the most relevant temperature datum or the method of temperature determination, especially when an undiluted feed is used and autothermal operation of a packed bed reactor becomes feasible. In general, the observed effect of increasing reaction temperature is that it leads to increased methane conversion and increased selectivity to carbon monoxide and hydrogen. This is consistent with predicted equilibrium values as discussed earlier (section 1.2.2).

1.4.2. The effect of the CH_4/O_2 ratio

Vernon and co-workers investigated the effect of the CH_4/O_2 ratio over a $Pr_2Ru_2O_7$ catalyst at 777°C [121]. Methane conversion decreased from 0.98 to 0.90 while the CO and H_2 selectivities increased from 91% and 96% respectively to 98% and 100% as the CH_4/O_2 ratio was increased from 1.72 to 2.15. Since more oxygen in the feed would favour total oxidation reations over partial oxidation reactions, this result is consistent with the thermodynamics. The same trend in S_{H2}, S_{CO} and X_{CH4} was observed over a Rh/Al_2O_3 catalyst in a fluidized-bed reactor, but the extent of the change was less pronounced [43].

Both Hickman and Schmidt [83, 84] and Huff and co-workers [85] studied the effect of increasing the CH_4/O_2 ratio from 1.5 to 2 over monolith catalysts coated with Rh, Ni, Ir and Pt. The authors found that carbon monoxide selectivity increased and that methane conversion decreased with increasing CH_4/O_2 ratio for all catalysts. The hydrogen selectivity, however, was more sensitive to the catalytic material employed. S_{H2} increased over nickel and rhodium catalysts and decreased over platinum catalysts with increasing CH_4/O_2 ratio. Mouaddib et al. [86] studied the influence of CH_4/O_2 over Pd/Al_2O_3 catalysts. Under oxygen-rich ($CH_4/O_2=0.25$) and stoichiometric ($CH_4/O_2=0.5$) mixtures at 500°C, only deep oxidation products (CO_2 and H_2O) were observed while the methane conversion was complete. Carbon monoxide was observed only at CH_4/O_2 ratios higher than 1.

The change in the selectivities to hydrogen and carbon monoxide and the value of methane conversion changes with the CH_4/O_2 ratio in the manner predicted by thermodynamics (see section 1.2.3).

1.4.3. The effect of pressure

Vernon et al. [87] investigated the effect of pressure on syngas yield with an undiluted methane/oxygen feed (CH_4/O_2 = 2) over a $Pr_2Ru_2O_7$ catalyst (Table 1-1).

Table 1-1 The effect of pressure on methane conversion and syngas selectivity [121]

Pressure (atm)	CH_4/O_2	X_{CH4}	S_{CO}	Yield CO	S_{H2}	Yield H_2
1	3.4	58	99	57	100	58
5	3.8	39	91	35	92	36
10	4.1	38	90	34	91	35
15	4.5	33	86	28	88	29
20	4.5	30	85	26	88	26

When the pressure was increased from atmospheric pressure to 20 atm, they found that methane conversion decreased to almost half its initial value. Both carbon monoxide and hydrogen selectivities also decreased with increasing pressure. Unfortunately, the CH_4/O_2 ratio was also increased with the reactor pressure. A high CH_4/O_2 ratio would lead to higher syngas selectivities, but in spite of this, the effect of pressure dominated their results by depressing the syngas yield. These observations are in agreement with the trends predicted by equilibrium calculations (discussed in section 1.2.4).

1.4.4. The effect of space velocity

An increase in the reactant space velocity in some studies of OXREF has been observed to enhance the methane conversion. Various attempts have been made to explain this increase in X_{CH4} in terms of the reaction mechanism, but in non-isothermal experiments and in the absence of a discussion of transport effects, mechanistic explanations are dubious.

1.4.4.1. Observed decrease in X_{CH4} with $F^°_{CH4}/W$

In a study of oxidative reforming over $Pr_2Ru_2O_7$, it was found that the methane conversion

approached the thermodynamic equilbrium when the methane flow rate was lowered to about 0.028 mol(kg$_{cat}$)$^{-1}$s^{-1} [121]. At higher flow rates, there was a significant departure from equilibrium as shown in Table 1-2.

Table 1-2 The effect of methane flow rate on the approach to thermodynamic equilibrium over a $Pr_2Ru_2O_7$ catalyst [121].

F°$_{CH4}$/W mol(CH$_4$)kg^{-1}s^{-1}	X$_{CH4}$	S$_{CO}$	S$_{H2}$
0.925	68	76	87
0.370	73	82	90
0.278	81	89	94
0.185	88	93	97
0.028	90	95	98
Equilibrium	90	95	98

Dissanayake and co-workers measured the equilibrium methane conversion over a commercial steam reforming catalyst and a methane flow rate (F°$_{CH4}$/W) of 0.048 mol(CH$_4$)kg^{-1}s^{-1} [88]. The methane conversion and synthesis gas selectivity were significantly reduced when the contact time in the catalyst bed was lowered (by increasing the flow rate of He diluent) at constant temperature. The reactants were diluted to less than about 10% of the total flow and one could expect the actual bed temperature between experiments to be comparable.

In a similar experiment, a pure CH_4-O_2 mixture was diluted with nitrogen in order to decrease the contact time. When the contact time was more than halved, methane conversion decreased from about 0.4 to about 0.35 [77].

1.4.4.2. Observed increase in X$_{CH4}$ with F°$_{CH4}$/W

If the reactant flow rate and superficial gas velocity is increased without ensuring the

effective removal of the heat generated at the catalyst surface, there will be an increase in the catalyst surface temperature which in turn will increase the reaction rate. The equilibrium methane conversion, S_{H2} and S_{CO} all increase with temperature as previously discussed (section 1.2.2). Undissipated heat will therefore enhance the measured syngas yield to the yield that would be expected if the bulk temperature were equal to the elevated surface temperature. In this section, a number of examples from the literature are discussed to demonstrate this point [29, 30].

Matsumura and Moffat observed an increase in X_{CH4} from 0.3 to 0.5 when the methane flow rate was increased ten-fold from 1.24E-3 to 1.24E-2 $mol(CH_4).g^{-1}.s^{-1}$ [77]. The only temperature that was reported was the temperature outside the reactor furnace. Choudhary has reported extensively on the effect of space velocity on syngas yield. All the catalysts were tested between 650 and 700°C and exhibited a characteristic methane flow rate at which either S_{CO} or X_{CH4} reached a maximum value (F°_{CH4}/W at the maximum varied between 4 and 7 $mol(CH_4)kg^{-1}s^{-1}$). This behaviour is unexpected and a convincing effort was not made by the authors to explain the maxima.

Boucouvalas *et al.* [78] demonstrated the effect of reactant dilution on the difference between the bed inlet- and outlet temperatures as well as on the X_{CH4} vs. space time behaviour of a packed bed of Rh/Al_2O_3 catalyst. At $P_{CH4} = 50$ kPa, the methane conversion was found to increase with increasing flow rate, but when the methane was diluted to $P_{CH4} = 4$ kPa, the expected behaviour, namely a decrease in methane conversion with increasing flow rate, was observed. The CO yield was much higher than the equilibrium value when using an undiluted feed, but as the helium content of the feed was increased to 96%, the CO yield coincided with that expected from equilibrium. In spite of the absence of complete axial bed temperature profiles, this study therefore clearly showed that claims of higher-than-equilibrium CO yield are unfounded until it can be proven that the cited temperature coincides with the actual catalyst surface temperature.

Vermeiren *et al.* [34] also showed that X_{CH4} and S_{CO} increased with F°_{CH4}/W at 600°C when the methane flow rate was increased from 0.0286 to 0.143 $mol_{CH4}kg^{-1}s^{-1}$.
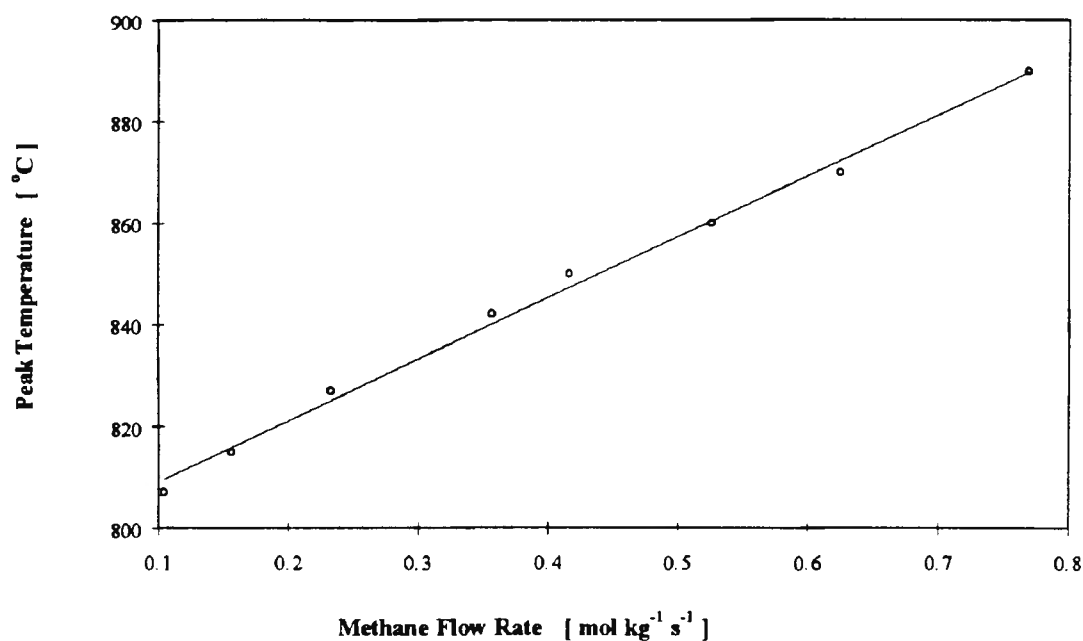
Figure 1-7 The relationship between maximum temperature and methane flow rate [34]

From bed temperature profile measurements, these authors demonstrated that the hot spot or maximum temperature in the bed increased with space velocity at constant inlet temperature. The hot spot temperature was read from their bed temperature profiles (Figure 3 in ref. 34) and plotted as a function of flowrate; this is shown in Figure 1-7. Even though the observed increase in conversion and selectivity may therefore also be assigned to a thermal effect, an attempt was made to measure the true catalyst temperature and hence their data enables one to explain the phenomenon.

From the above mentioned information it is clear that there are only a limited number of earlier reports in which the thermal effect has been decoupled from the space velocity effect. Three of these [78, 88, 101] used dilute mixtures (less than 10%) of methane and oxygen in helium to minimize heat build-up in the catalyst bed and the fourth [34] measured bed temperature profiles at different values of space velocity. The latter approach enables one to compare values of X_{CH4} and selectivities at comparable bed temperatures. In the past year, however, a number of kinetic studies have appeared that show excellent isothermicity of the catalyst bed and consequently enables the decoupling of a thermal effect from the flow rate [89, 98].

1.4.5. Co-feeding of reaction products

Oh *et al.* [90] co-fed carbon dioxide with a reaction mixture with $CH_4/O_2 = 1.33$ over catalysts consisting of Pt, Pd or Rh supported on Al_2O_3 to investigate the effect on carbon monoxide production. Methane conversion on all three catalysts, and carbon monoxide production on Pt and Pd, was not affected by CO_2 co-feeding. However, carbon monoxide production was found to increase markedly when carbon dioxide was co-fed over the Rh catalyst. The authors attributed this to the fact that Rh enabled the WGS reaction to play a more significant role in determining the overall product selectivity than the Pt and Pd catalysts. The authors explained the absence of any significant effect of co-fed carbon dioxide on X_{CH4} by postulating a rate-determining step (dissociation of adsorbed methane) and then stating that this step was insensitive to the presence of carbon dioxide. Matsumura and Moffat also co-fed carbon dioxide and observed virtually no change in methane conversion over 10 wt% Ru/SiO_2 [77]. A substantial increase in carbon monoxide selectivity and a decrease in hydrogen selectivity was observed, however, and this was ascribed to the participation of the reverse WGS reaction.

Choudhary *et al.* [29] co-fed water to a feedstream with $CH_4/O_2=2$ over a NiO/CaO catalyst. As the water content was raised from nil to $H_2O/CH_4=2$, both the methane conversion and carbon monoxide selectivity dropped substantially. X_{CH4} decreased from ca. 0.64 to less than 0.5 and S_{CO} from ca. 84% to less than 40%. The authors ascribed the decrease in CO selectivity to the WGS reaction, but did not address the possibility that the decrease in methane conversion could have been acribed to a decrease in the methane partial pressure (as the H_2O/CH_4 ratio was increased at constant total flowrate). The occurrence of both the reverse WGS and methanation reactions were confirmed by passing an equimolar H_2/CO_2 mixture over the catalyst under operating conditions which were identical to the oxidative reforming runs. A similar set of experiments was performed on a MgO-supported nickel catalyst [62].

Vernon *et al.* [87] co-fed varying amounts of CO_2 to a $CH_4 + O_2$ mixture over an Ir/Al_2O_3 catalyst at 777°C, but unfortunately the oxygen and carbon dioxide partial pressures were not changed independently to allow the interpretation of their results.

1.5. Kinetics

1.5.1. Results of combustion studies and models used

Very little is known about the kinetics of the methane oxidative reforming. This may perhaps be ascribed to the difficulty of minimizing transport resistances and of measuring the true catalyst surface temperatures under experimental conditions. While looking at the results of oxidative reforming that are available, it might be instructive to also consider the findings of some kinetic studies of methane combustion over supported metal catalysts under fuel lean conditions since methane combustion is often assumed to form part of the reaction pathway for oxidative reforming [73, 91, 92, 93].

Hickman and Schmidt [94] used low-pressure rate data that was previously collected over single-crystal and polycrystalline foils, to model the oxidative reforming of methane on Pt and Rh-coated monolith catalysts. In spite of the difference in catalyst microstructure, species coverage values and pressure between their experiments and the sources from which their model parameters were obtained, they were able to model their experimental results successfully.

Blanks *et al.* [95] used kinetic expressions for total combustion, carbon dioxide reforming and steam reforming to model the temperature profiles in a pilot plant scale reversed-flow reactor. The rate constants and activation energy that these authors used were, however, not reported. Slaa *et al.* [89] studied the kinetics of methane oxidative reforming over Rh/Al_2O_3 catalysts at 1012°C. These workers used diluted mixtures (10% in helium) and high flow rates to enable them to observe incomplete oxygen conversion. This led them to draw more general conclusions about the reaction mechanism than was previously possible with studies that reported only near-complete oxygen conversion.

1.5.2. Measured reaction orders for methane and oxygen

Trimm and Lam [73] varied the CH_4/O_2 ratio between 0.33 and 2 and measured a reaction order of 1 for methane and between 0.75 and 1 for oxygen on supported Pt catalysts.

Veldsink and co-workers [96] studied the effect of methane partial pressure in excess oxygen as well as that of the oxygen partial pressure on the rate of methane oxidation over a CuO/Al_2O_3 catalyst. The reaction order for oxygen was determined over a wide range of oxygen partial pressures and at two different temperatures. They observed a reaction order of one for methane at 660°C and a value of 0.07 for oxygen at 480°C. When the temperature was raised to 600°C, the oxygen reaction order assumed a value of 0.5 at low oxygen partial pressure and was zero at high oxygen partial pressure. The authors interpreted the reaction order with respect to oxygen of 0.5 as being indicative of dissociative chemisorption of oxygen.

Slaa *et al.* [89] found that the reaction order for oxygen was 0.4 and that of methane was 0.5 over a Rh/Al_2O_3 catalyst at 1012°C and a total pressure of 400 kPa. At constant oxygen partial pressure, an increase in the methane partial pressure led to increased values of X_{O2} and X_{CH4}. When P_{CH4} was kept constant and the oxygen partial pressure increased, however, methane conversion increased and the oxygen conversion decreased.

1.5.3. The effect of reaction products on the rate of methane oxidation

Reaction products may inhibit the rate of methane consumption by decreasing the number of sites available for methane chemisorption. Furthermore, some reaction products may re-adsorb dissociatively and thus provide additional routes to other products.

Trimm and Lam [73] found that carbon dioxide and water did not affect the kinetics of methane combustion over supported platinum catalysts at temperatures between 500°C and 600°C. Ribeiro *et al.* [90] also studied the effect of carbon dioxide and water on the rate of methane oxidation on a $Pd/Si-Al_2O_3$ catalyst, but had slightly different results. When the carbon dioxide content was varied while maintaining a constant water partial pressure ($CH_4 = 1\%$ and $H_2O = 0.05\%$ in air), no inhibition of the reaction rate was observed at carbon dioxide partial pressures lower than 0.5%. When the carbon dioxide content was higher than 0.5%, however, the rate of methane oxidation was inhibited severely and a reaction order of -2 with respect to carbon dioxide was measured. When carbon dioxide content was kept

constant and the water concentration varied, the reaction order for water was -1.

Veldsink and co-workers [96] found carbon dioxide to have a reaction order of only -0.1 while water had a greater influence on the reaction rate with the reaction order assuming a value between -0.5 and -0.6; these results were obtained in excess oxygen and on a CuO/Al_2O_3 catalyst.

1.5.4. Activation energy

Veldsink *et al.* [96] calculated a value of 135 kJ mol^{-1} for the activation energy of methane oxidation in excess oxygen on a CuO/Al_2O_3 catalyst. While the authors conducted a number of experiments using high CH_4/O_2 ratios typical of the conditions at which oxidative reforming of methane is conducted, the activation energy was not determined under these conditions. By using a very dilute feed and a diluted catalyst bed, Boucouvalas *et al.* [97] showed that the activation energy for carbon monoxide formation (85-109 kJ mol^{-1}) was much higher than that for carbon dioxide formation (ca. 34 kJ mol^{-1}), and of the same order of magnitude as that of carbon monoxide formation during carbon dioxide - and steam reforming.

1.5.5. Rate multiplicity and oscillations

König and co-workers used in-situ ellipsometry to study the catalyst surface during the oxidation of methane on a palladium film that was sputtered onto sapphire substrates [117]. When the authors passed a mixture of methane and oxygen (4% CH_4 and 2% O_2 in Ar) over the catalyst at 500°C, they observed that the carbon dioxide concentration initially rose steadily, but that it started to oscillate spontaneously after about 12 minutes on-stream; the carbon monoxide signal was found to oscillate 180° out of phase with that of carbon dioxide. The observed oscillations in the gas phase concentration were correlated with measured changes in the oxidation state of the palladium film. The presence of Pd metal was related to the formation of carbon monoxide and was found to be less active than PdO which, in

40

turn, was related to the formation of carbon dioxide. An attempt was made to explain the oscillations in terms of the roughness of the palladium film and the formation, growth and decomposition of oxide nuclei.

1.6. Mechanism/pathway

In the oxidative reforming of methane, carbon monoxide may be formed in in the presence of oxygen as a primary product [29, 122]. Alternatively, it has been suggested that a fraction of the methane is first combusted to give carbon dioxide and water, and that the carbon monoxide is formed deeper into the bed by carbon dioxide reforming and steam reforming of the remaining methane (scheme II). These two reaction schemes can be represented by:

$$CH_4 \xrightarrow{O_2} CO \qquad\qquad \textbf{SCHEME I}$$

$$CH_4 \xrightarrow{O_2} CO_2, H_2O \xrightarrow{CH_4} CO \qquad\qquad \textbf{SCHEME II}$$

1.6.1. The indirect formation of carbon monoxide (Scheme II)

Prettre and co-workers [23] were the first to observe that the bed inlet temperature is higher than the temperature deeper into the bed. Ever since then, the existence of a hot spot has frequently been used as evidence for the indirect mechanism (scheme II). The reasoning behind this is that the first combustion reaction is exothermic (with the evolved heat causing the temperature to rise) and that the reforming reactions, which take place in the latter part of the bed, are endothermic and consume the energy evolved in the combustion step, thus resulting in a drop in temperature. A measure of temperature alone, however, does not constitute sufficient evidence that the second (or any other) mechanism is valid since a hot spot may also exist in a nonadiabatic reactor, even when a **purely exothermic** reaction is

taking place. The hot spot may in such a case develop by virtue of heat losses through the reactor wall.

The existence of different solid phases in the catalyst bed has also been used as evidence for the indirect formation of carbon monoxide [88]. NiO/Al_2O_3 was observed at the front end of the packed bed while Ni/Al_2O_3 was found deeper in the catalyst bed. It was suggested that the oxide was active for the total combustion of methane to carbon dioxide and water and that the Ni^0 in the latter part of the bed catalysed the steam- and carbon dioxide reforming of methane.

Van Looij *et al.* [98] used a very dilute feed to overcome the heating problems encountered by other workers and showed that the carbon monoxide selectivity decreased with increasing space velocity which is a clear indication that carbon monoxide is not a primary reaction product. A further experiment revealed that the methane conversion that was obtained when using a catalyst bed comprised of a manganese oxide combustion catalyst followed by a nickel reforming catalyst, was identical to the methane conversion when using only the nickel catalyst. The authors thus concluded that the mechanism consists of combustion followed by reforming, as in scheme II. The same conclusion was reached when van Looij used a silica-supported palladium catalyst and a MnO_x combustion catalyst [75]. Although the effect of diffusion was not explicitly stated, the difference in the measured conversion and selectivities when using identical catalysts (which differed only with respect to the palladium particle size), suggested that diffusion did not play a role in their work.

Buyevskaya *et al.* [59] and Walter and co-workers [108] concluded from the results of transient and infrared studies of oxidative reforming and adsorption on a Rh/Al_2O_3 catalyst that carbon dioxide is the primary reaction product and that the majority of the carbon monoxide is formed by the reverse Boudouard reaction (reaction (1-3)).

In terms of activity on the catalyst surface, carbon dioxide can be formed as a primary product only by the reaction of gaseous oxygen with absorbed carbon. It may be **observed** as a primary product by one additional route, ie. when the desorption of carbon monoxide is slower than carbon dioxide desorption and slower than the rate of carbon monoxide

oxidation. The kinetics of carbon monoxide oxidation and desorption is predominantly a function of the surface material. The first two means of direct carbon dioxide formation is most likely to occur in the early part of the bed, firstly, because gaseous oxygen is still present there and secondly, because oxygen is less likely to dissociate upon adsorption onto an oxidized surface (which also predominates in the region of high gaseous concentration of oxygen, ie. the early part of the bed) than on a transition metal surface. The strength with which oxygen is adsorbed onto the surface, and whether it is dissociatively adsorbed or not, is a function of the surface. It is important to know which metal is used and whether the oxide or the metal is stable at the oxygen partial pressure and temperature in the early part of the bed ie. before oxygen consumption is complete. Hickman and Schmidt [94] assumed oxygen to be adsorbed non-competitively on Pt and Rh with all the other gaseous compounds in formulating their surface reaction model. This may be valid for most metal catalysts and as shown for Ni by Au et al. [58], one would expect oxygen to be adsorbed dissociatively by a material and at conditions that would enable the dissociation of methane. In view of the evidence suggesting the presence of multiple Ni phases in the catalyst bed, a surface reaction model for oxidative reforming should also contain information about the effect of temperature and gas phase composition on the formation and stability of oxide nuclei and their subsequent growth into a continuous oxide layer [99]. The effect that changes in the chemical and physical properties of this layer have on the surface chemistry of oxidative reforming needs to be studied in greater detail.

Inui et al. [100] approached the problem of methane oxidative reforming from the perspective of applications for catalytic combustors and regarded oxidative reforming as a two-step reaction. The first step (combustion of methane) was regarded as essential in providing the heat supply and reaction products needed in the second step (rapid steam reforming and CO_2 reforming) deeper into the catalyst bed.

1.6.2. The direct formation of carbon monoxide

Hickman and Schmidt [94] used a surface reaction model in conjunction with oxidative reforming experiments conducted at very short contact times to show that CO was a primary

product of the oxidative reforming reaction. They considered the observed increase in carbon monoxide selectivity with increasing space velocity as direct evidence that CO is a primary product. While it may be argued that the observed rise in carbon monoxide selectivity with increasing space velocity (cf. also Section 3.2.4) supports the postulate of carbon monoxide as a primary product, it should first be demonstrated that the increase in surface temperature that accompanies an increase in space velocity is negligible, that the reaction rate is not controlled by the rate of external mass transfer and that gas phase reactions are negligible. The same provision holds for the work of the Choudhary group who also observed an increase in carbon monoxide selectivity at higher space velocity [29, 122].

In spite of the fact that Buyevskaya et al. [59] and Walter and co-workers [108] showed carbon dioxide to be the major primary product, the reaction of CH_x fragments with surface oxygen could not be excluded from their findings as a source of primary carbon monoxide:

$$CH_x + O \rightarrow HCHO \rightarrow CO + H_2 \qquad \text{(1-12)}$$
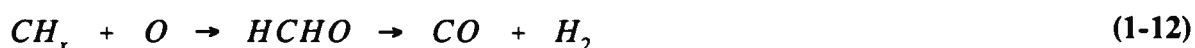
An interesting approach was followed by Matsumoto [101] who performed transient experiments on an Pd ion-exchanged zeolite to elucidate the mechanism of carbon monoxide formation. By switching from O_2/He (first sequence of a 20 minute exposure) to CH_4/He (second sequence), he found at 527°C that carbon monoxide and hydrogen were the main products. Upon switching back to O_2/He (third sequence) after a further 20 minutes, only deep oxidation products were, however, produced. Almost total oxygen consumption was furthermore measured in independent co-feed experiments. Matsumoto subsequently argued that the absence of gaseous oxygen during co-feed experiments is analogous to the second sequence of the transient experiment where primarily CO and H_2 was observed and concluded that carbon monoxide and hydrogen were the primary reaction products. It is known that PdO rather than Pd° is the stable phase of palladium at low temperatures [118]; thus one may assume that methane in the second sequence of Matsumoto's experiment is exposed to PdO rather than Pd. This situation would correspond to the catalyst state at the O_2-rich bed inlet (where primary products indeed originate) of a working oxidative reforming catalyst, and

adds some weight to the conclusions reached by Matsumoto.

Hu and Ruckenstein [61] investigated the effect of the carrier gas space velocity while pulsing CH_4/O_2 mixtures to a Ni/La_2O_3 catalyst and found that CO selectivity increased when the space velocity was raised. This data supports the mechanism of direct CO formation because an increase in space velocity (low contact time) can only result in enhanced CO production if CO is a primary product.

Choudhary et al. [30] observed selectivities to CO and H_2 close to, and even slightly above, the equilibrium values at 500-800°C over a Ni/Al_2O_3 catalyst. The space velocity was very high (4.5 $mol(CH_4)kg^{-1}s^{-1}$) and the mixture consisted of pure methane and oxygen ($CH_4/O_2=2$). When the authors passed equimolar mixtures of CH_4/H_2O and CH_4/CO_2 over the same catalyst at the same methane flowrate, the methane conversion at 700°C was only 0.104 and 0.134 respectively. This data led them to the conclusion that carbon dioxide and water are not primary reaction products of the reaction and that carbon monoxide is formed directly from methane. A similar conclusion was arrived at for a NiO/CaO catalyst [29]. However, major reservations based on the temperature that was reported, have been expressed about these results [80, 81] and not too much weight should therefore be attached to the mechanistic conclusions of the Choudhary group.

Steghuis et al. [112] varied the contact time over an order of magnitude at 600°C over a Y_2O_3/ZrO_2 catalyst to demonstrate the direct formation of both carbon monoxide and carbon dioxide (Figure 1-8).

A reaction mechanism that included the direct formation of CO from methane via adsorbed OCH_3 and OHCH species, was proposed (see Figure 1-9).
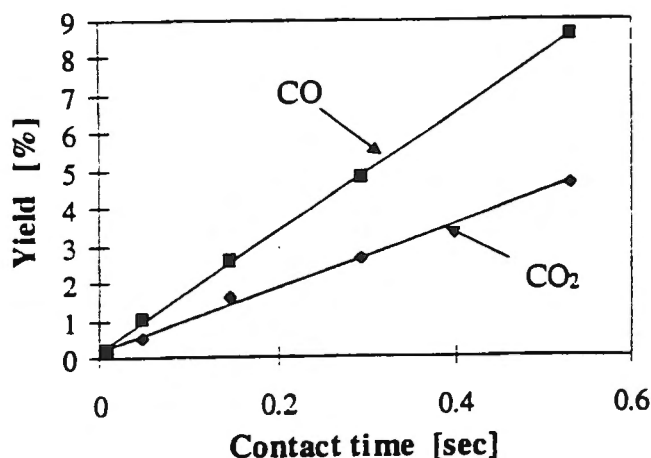
Figure 1-8 Direct formation of both CO and CO_2 [112] (Y_2O_3/ZrO_2 catalyst at 600°C)

$$O_2 + 2\square \longrightarrow 2O_{(latt.)} \qquad\qquad CO_2 + H_2O + 2OH_{(ad.)} + \square$$

$$O_2 \nearrow O_{(latt.)}$$

$$O_2 + 2\square \longrightarrow OCH_{3(ad.)} + OH_{(ad.)}$$

$$\searrow O_{(latt.)}$$

$$OHCH_{(ad.)} + 2OH_{(ad.)}$$

$$2OH_{(ad.)} \longrightarrow H_2O + O_{(latt.)} + \square \qquad\qquad CO + H_2 + 2OH_{(ad.)} + \square$$
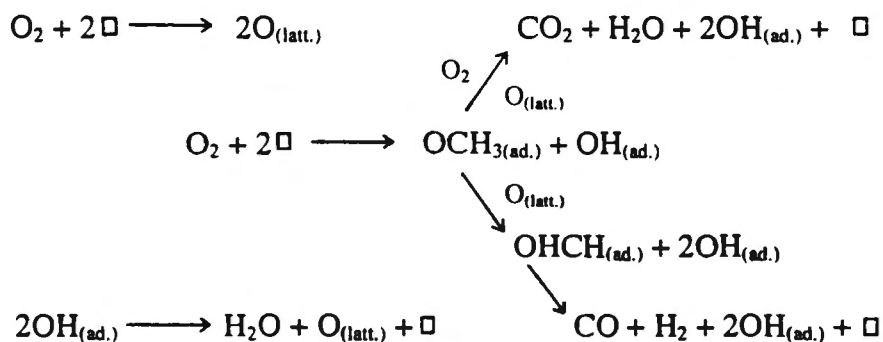
Figure 1-9 Mechanism for CO_x formation [112] ($\square$ = vacant site, Y_2O_3/ZrO_2 at 600°C)

Ruckenstein and Hu [102] used a transient technique to study the mechanism of methane oxidative reforming on a reduced NiO/La_2O_3 catalyst. They found that the peak of the dynamic CO response curve occurred at longer residence times when pure CO was pulsed over a Ni/La_2O_3 catalyst than when a CH_4/O_2 pulse was passed over the same catalyst. The authors concluded from this data that the CO formation reaction (reaction (1-15)) was much slower than the CO adsorption/desorption (reaction (1-16)) and that reaction (1-15) is the rate-determining step (hereafter RDS) in the following proposed reaction mechanism:

$$CH_4 \rightarrow \ldots \rightarrow C_s + 4 H_s \qquad\qquad (1\text{-}13)$$

$$O_2 \rightarrow 2 O_s \qquad\qquad (1\text{-}14)$$

$$C_s + O_s \rightarrow CO_s \qquad\qquad RDS \qquad\qquad (1\text{-}15)$$

$$CO_s \rightarrow CO_g \qquad\qquad (1\text{-}16)$$

$$CO_s + O_s \rightarrow CO_{2(s)} \rightarrow CO_2 \qquad\qquad (1\text{-}17)$$

$$2 H_s \rightarrow H_{2(s)} \rightarrow H_{2(g)} \qquad\qquad (1\text{-}18)$$

1.6.3. Other pathways and the role of the support in the reaction mechanism

The actual reaction pathway of methane oxidative reforming most probably involves both direct and indirect routes to carbon monoxide formation with their respective contributions to the total carbon monoxide flux being determined by the temperature, reaction kinetics and adsorption/desorption/re-adsorption phenomena. The situation is compounded by the possible existence of more than one type of active site and there may therefore be a change in rate-determining step along the catalyst bed.

Chu et al. [103] studied the oxidative reforming of methane on $NiO/La_2O_3/\gamma\text{-}Al_2O_3$ catalysts and concluded that CO, H_2, CO_2 and H_2O are all primary products of the reaction. Experiments at high space velocity showed that steam reforming and CO_2 reforming occur only to a limited extent, with direct CO and H_2 formation from methane therefore being the major source of syngas. The authors used a pure CH_4/O_2 feed, and did not report temperature measurements along the length of the catalyst bed. Consequently one should not discount the possibility that the reaction might have been self-sustaining under conditions of high space velocity and that the catalyst temperature was much higher than the cited temperature of 750°C. The activity of the catalyst for the steam reforming- and CO_2 reforming reactions needs to be tested at the true catalyst temperature, which in this case is

not available, in order to ensure the cogency of the conclusion that CO and H_2 are primary products of methane oxidative reforming.

Bhattacharya *et al.* [104] proposed that carbon monoxide formation from CH_x species occurs on the surface in parallel to the gas-phase formation of carbon dioxide from the oxidation and decomposition of desorbed CH_3 fragments. The increase in CO selectivity with increasing temperature was explained by the rate of the CO-producing surface reaction increasing beyond the rate of gas-phase carbon dioxide production. This effect was also proposed to be assisted by the re-adsorption of carbon dioxide at high temperature, reacting with CH_x fragments to form more carbon monoxide. Lapszewicz *et al.* [105] showed that **completely** dissociated CH_x fragments ($x \rightarrow 0$) are the surface precursors for carbon monoxide formation. They demonstrated by means of CH_4-D_2 exchange experiments that the catalysts resulting in the most completely-exchanged methyl fragments exhibited the highest methane conversion in independent oxidative reforming experiments. It was suggested that surface carbon is the precursor for CO_x formation while adsorbed methyl groups are responsible for the formation of amorphous carbon.

Choudhary *et al.* [126] briefly mentioned the possibility of methane heterolytic cleavage, followed by oxidation to form OCH_3^-. In their scheme, this would lead to hydrogen, carbon monoxide, water and carbon dioxide, but they gave no supporting evidence for these suggestions.

Mallens *et al.* [106] used the temporal analysis of products (TAP) reactor to study the oxidative reforming of methane over platinum sponge between 700 and 800°C. They found that carbon dioxide may be both a primary and a secondary reaction product and that the oxygen species present on the catalyst surface determines whether CO or CO_2 is formed. The reaction mechanism that was proposed is shown in Figure 1-10. Methane was found to be directly converted to CO_2 and water by dissolved (subsurface) oxygen while chemisorbed oxygen led primarily to carbon monoxide and hydrogen.
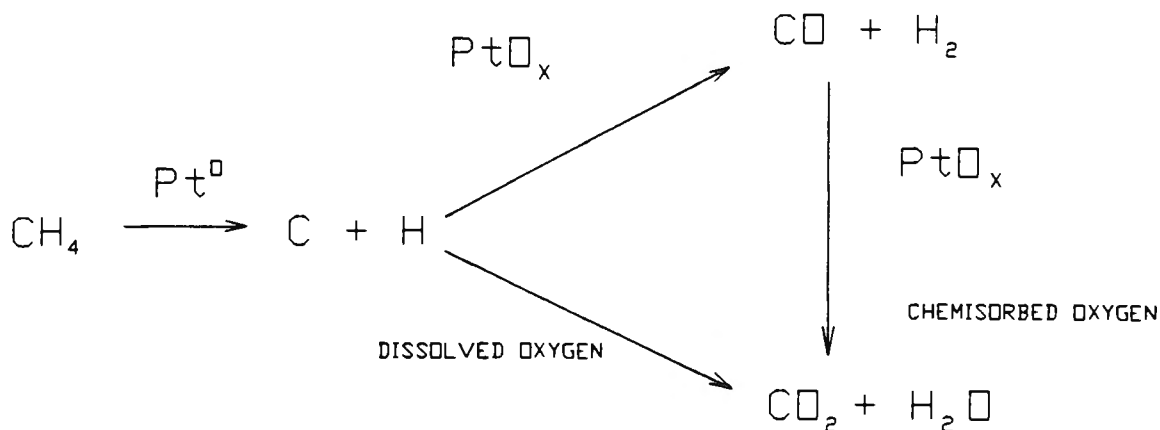
Figure 1-10   Reaction network for CO_x formation on platinum sponge

Hayakawa *et al.* [107] observed the incorporation of ^{18}O, adsorbed on the SiO_2 support, into the reaction products (*i.e.* carbon monoxide and CO_2) when performing oxidative reforming with a Rh/SiO_2 catalyst. They concluded that oxygen spillover therefore forms part of the reaction pathway. Using in-situ infrared techniques, Walter *et al.* [108] showed that support OH^- groups of a Rh/Al_2O_3 catalyst take part in the conversion of methane to syngas, but their contention was that this step is slow compared to the total combustion of methane on oxygen sites. H-bridged bonding between surface OH^- groups and methane during oxyreforming over Ir/Al_2O_3 was also suggested by Solymosi and Cserényi [109] on the basis of infrared evidence. Baerns *et al.* [110] suggested that hydroxyl groups and possibly a "loosely bound surface carbonate" on a MgO support may aid in the conversion of CH_x fragments on supported metal sites. The redox properties of CeO_2 was used by Otsuka, *et al.* [120] to convert methane to syngas in a two-step process with the overall reaction corresponding to steam reforming and carbon dioxide reforming respectively. The possible use of ceria as an oxygen sink in the early part of a bed of oxidative reforming catalyst and its role in thus preventing the oxidation of the active metal when it is exposed to high partial pressures of oxygen, is an option that needs careful examination.

The role of the support in determining the state of oxygen in supported metal particles and

the influence that this might have on the reaction mechanism needs to be examined in more detail.

1.6.4. Gas phase reactions

A study of methane combustion on MgO showed that gas phase reactions contribute to the conversion of methane above about 650°C [111]. This finding may indicate that other supports normally used in oxyreforming may also contribute to the overall reaction scheme by the production of methyl radicals or by acting as radical scavengers. Chang and Heinemann [81] expressed the opinion that the catalyst may act merely as an initiator for the reaction, with the result that the temperature would rise rapidly and that homogeneous reactions would consequently make the most dominant contribution to the overall product spectrum. Bharadwaj and Schmidt [43] argued against the presence of homogeneous reactions, stating that the absence of C_2 products ruled out the occurrence of gas phase reactions. Schmidt *et al.* [22] put forward a comprehensive argument against the presence of homogeneous reactions. They argued that homogeneous reactions may be avoided by adhering to the following guidelines:

i) reactant mixtures should be outside the flammability regime,

ii) flow velocity should be higher than the flame velocity and

iii) the temperature should be lower than the ignition temperature.

From their extensive work done in this field, they concluded from the absence of visible flames, the simplicity of the product spectrum and from the fact that their products are not at the thermodynamic equilibrium (which, as was stated, would not be the case with free radical reactions), that homogeneous reactions play a negligible role in determining their product composition. Direct evidence for the absence of gas phase reactions by, for example, co-feeding a radical-quenching species, has not been presented.

The fact that both Heitnes *et al.* [48] and Slaa *et al.* [89] detected C_2 hydrocarbons in the product stream supports the contrary argument that gas-phase radical reactions may not be

negligible. Slaa *et al.* [89] detected both ethane and ethylene in their product spectrum over a Rh/Al_2O_3 catalyst at 1012°C and 400 kPa total pressure. While the presence of pure gas-phase reactions was ruled out by the authors, they concluded that the gas-phase coupling of methyl radicals which are produced on the catalyst surface and subsequently desorbs into the gas-phase, may account for the presence of C_2 hydrocarbons in their product. A reaction network was proposed which accounts for both surface reactions and gas-phase reactions when oxygen conversion is lower than 1.0.

1.7. The Catalyst

1.7.1. Supported metal catalysts

Most catalysts tested for oxidative reforming are supported metal catalysts. Steghuis and co-workers suggested that the high activity and the associated heat transfer problems of supported metal catalysts used for the oxidative reforming of methane will pose scale-up problems [112]. In their view, a catalyst is needed that is able to facilitate the **direct** and more mildly exothermic oxidation of methane to carbon monoxide rather than having to cope with a catalyst that operates with the two-step combustion/reforming mechanism. These authors presented an example of a class of irreducible metal oxide catalysts that was active for the direct formation of CO from methane and oxygen (Y_2O_3/ZrO_2).

Most of the active catalysts consist of a supported group VIIIB metal. It is generally accepted that the active species is the reduced or zero-valent state of these metals. Temperature-programmed experiments of unreduced supported metal catalysts show that methane conversion is low below a characteristic temperature for each catalyst, and that there is a sudden increase in X_{CH4} as the temperature is increased; this jump in conversion roughly coincides with the temperature at which the metal oxide is reduced to the metallic state. This is the point of ignition that was elegantly shown by Choudhary *et al.* [132] for supported nickel catalysts. Jones *et al.* [113] found that the temperature at which the reaction was initiated when a $Eu_2Ir_2O_7$ catalyst was exposed to a CH_4-O_2 mixture, corresponded to the temperature of collapse of the pyrochlore structure and the segregation of iridium from the lattice to form Ir/Eu_2O_3. Poirier *et al.* [31] showed the light-off temperature to coincide with

the temperature at which the reduction of RuO_2 to Ru metal takes place. Poirier *et al.* [114] concluded from the catalyst mass loss, evolved gas analysis and thermal events registered in a TG-DTA apparatus, that the reduction of $Pr_2Ru_2O_7$ to Ru metal and Pr_2O_3 corresponded to the onset of O_2 consumption and the activation of the catalyst. Hayakawa *et al.* [115] observed a marked increase in the methane conversion when a number of titanes-based perovskite oxides containing reducible metals were first exposed to methane for 1 hour at 775°C. Methane is thought to decompose to hydrogen which may facilitate the in-situ reduction of the metal.

Subsequent to the formation of the metallic form of the catalyst, oxidative reforming can be sustained at much lower temperatures than the ignition temperature but re-oxidation of the metal with a subsequent decrease in X_{CH4} (extinction) takes place when incomplete oxygen conversion occurs [132]. Methane conversion consequently exhibits hysteresis and the area under the curve is clearly then a function of the redox properties of the catalyst. Such ignition-extinction behaviour is also understood on a theoretical level and has been described successfully by Deutschmann *et al.* [116] for methane oxidation on Pt by using a surface reaction model combined with a stagnation-point flow model.

Au *et al.* [58] used a pulsing technique to demonstrate that a NiO catalyst led to the formation of predominantly carbon dioxide while a pre-reduced nickel catalyst exhibited a higher selectivity for carbon monoxide formation. Choudhary and co-workers pulsed pure methane over a packed bed of unreduced $NiO-Al_2O_3$ catalyst at 600°C [132]. The methane conversion rose from 0.01 at the first pulse to a maximum of 0.26 at the third pulse and then declined to 0.16 at the sixth pulse. Carbon monoxide selectivity also exhibited a maximum, but the highest value of 63% was attained after five pulses. When the authors pulsed pure methane over a reduced (used) catalyst, the conversion was, however, only 0.002 From this evidence they concluded that lattice oxygen was responsible for CO_x formation and since CO_2 was almost exclusively formed on the unreduced catalyst, that a certain degree of reduction was necessary to ensure CO formation.

D. König *et al.* [117] used in-situ ellipsometry to show that methane conversion and selectivity to carbon monoxide exhibited oscillations on a palladium surface at temperatures

higher than about 500°C when the CH_4/O_2 ratio was higher than 1.25 (rich mixtures). They also demonstrated that the state of high S_{CO} corresponded to the existence of Pd metal (low activity for methane oxidation) and that the presence of PdO lead mostly to the formation of deep oxidation products. McCarty studied the combustion of methane on a supported palladium catalyst and also observed that PdO was more active (lower activation energy for combustion) than Pd for the conversion of CH_4/O_2 mixtures ($CH_4:O_2=1:2$) [118]. PdO was the predominant phase at temperatures below about 550°C while the metal was the stable phase at temperatures above 700°C.

Hu and Ruckenstein [61] studied the oxidative reforming of methane on a Ni/La_2O_3 catalyst by pulsing mixtures of methane and oxygen to a packed bed of catalyst. They found that over the prereduced catalyst, methane conversion slowly declined and reached a constant value after about nine pulses. When the unreduced catalyst was exposed to pulses of CH_4/O_2, the methane conversion slowly increased and reached the same constant value as that of the pre-reduced catalyst after about nine pulses. This led them to conclude that nickel in the working catalyst was in a semi-reduced state.

Clearly the state of reduction of supported metal catalysts influences the activity of a catalyst for the oxidative reforming of methane and the oxidation state which would ensure optimal performance of a catalyst differs from one catalytic material to the next.

1.7.2. Metal oxide catalysts

There are only a small number of workers who have reported oxidative reforming of methane on metal oxide catalysts. Veldsink and co-workers studied methane oxidative reforming (rich mixtures) as well as methane combustion (lean mixtures) on a CuO/Al_2O_3 catalyst [96]. Otsuka *et al.* [119, 120] used the redox properties of CeO_2 in a two-step process to convert methane to syngas. In the first step, methane was used to reduce the ceria (resulting in a H_2/CO ratio of 2), and water or carbon dioxide was used in the second step to re-oxidize the catalyst. The corresponding reactions are:

$$CeO_2 + x\,CH_4 \rightarrow CeO_{2-x} + x\,CO + 2x\,H_2 \qquad\qquad \text{(1-19)}$$

$$CeO_{2-x} + x\,CO_2 \rightarrow CeO_2 + x\,CO \qquad\qquad\qquad \text{(1-20)}$$

$$CeO_{2-x} + x\,H_2O \rightarrow CeO_2 + x\,H_2 \qquad\qquad\qquad \text{(1-21)}$$
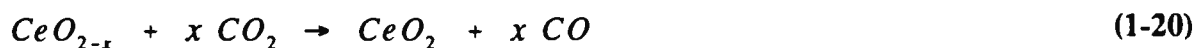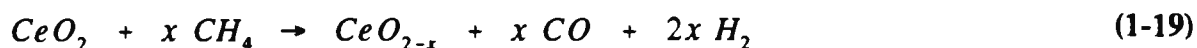
Problems were experienced with carbon deposition if more than an optimum 10% of the ceria was reduced in the first step. A number of compounds were added to the ceria in an attempt to enhance the rate of methane dissociation to synthesis gas and of the compounds tested, Pt black led to the greatest increase in syngas yield.

Matsumura and Moffat [121] studied the partial oxidation of methane to syngas over a number of hydroxyapatite catalysts with the general formula $Ca_{10\text{-}z}(HPO_4)_z(PO_4)_{6\text{-}z}(OH)_{2\text{-}z}$ $(0 \le z \le 1)$. The methane conversion was about 0.26 and carbon monoxide selectivity 76.8% at 600°C. The rate of methane conversion compares well with supported metal catalysts (Table 1-5).

Due to either the presence of external mass transfer resistance, which is a strong function of hydrodynamic flow patterns around catalyst particles, or of long residence times, which enable the attainment of equilibrium, different metals are often perceived to have similar activity. In the next section, a qualitative assessment of reported activity sequences for oxidative reforming catalysts will first be presented with the comparison of catalysts based on a very loose definition of activity, namely CO yield.

1.7.3. Metal type - qualitative assessment of catalyst activity

Vernon and co-workers [121] presented results to show that the yield of syngas for a series of Al_2O_3 supported catalysts with 1% metal loadings of Ru, Rh, Pd, Ir, Pt or Ni was the same for all the metals tested. In a different experiment, the authors studied the effect of methane flow rate on the attainment of equilibrium over a $Pr_2Ru_2O_7$ catalyst (see Table 1-2).

They found that X_{CH4}, S_{CO} and S_{H2} corresponded to the expected equilibrium values at a specific flow rate of about 0.028 $mol_{CH4}kg^{-1}s^{-1}$ and that the products deviated from equilibrium at higher flow rates. If the methane flow rate that is required to attain equilibrium is similar for all the catalysts tested, then, under the conditions used to compare the catalysts, one would expect equilibrium to be approached and the metals to become indistinguishable in terms of the values of X_{CH4} and of the syngas selectivity measured.

Bharadwaj and Schmidt [43] found that Ni/Al_2O_3 and Rh/Al_2O_3 gave approximately equilibrium values of S_{CO} and X_{CH4} at 850°C but that Pt/Al_2O_3 was much less active. For MgO-supported catalysts, Choudhary et al. [122] reported better performances for Ni than for Co at both 500 and 700°C. Lapszewicz et al. [105] found that the methane conversion activity decreased for 0.5 wt% metal supported on MgO in the order Rh > Ru > Pt > > Pd throughout the temperature range 550 - 900°C.

Hickman and Schmidt [83] also reported the superiority of Rh over Pt supported on alumina and Poirier and co-workers [31] showed that ruthenium exhibited substantially higher activity than did nickel. Torniainen et al. [136] showed Re to be highly active, giving a rapid temperature increase upon introduction of methane and oxygen but most of the metal was subsequently lost from the support, probably by evaporation. These authors reported that the overall activity decreased in the sequence Rh > Ni > Ir > Pt > Pd > Co. They also found that Ru and Fe was unable to sustain the oxyreforming reaction in their autothermal reactor. Slagtern and Olsbye [76] confirmed the superiority of Rh over Ni; they also showed that Cr produced almost exclusively carbon dioxide with a methane conversion of 0.26, thus having poorer performance than Co. Oh and co-workers reported the activity sequence (in terms of the methane consumed) Rh > Pt > Pd for a $CH_4/O_2 = 1.33$ mixture at 520°C [90]. In contrast to the findings of Torniainen et al. [136], Claridge et al. [123] found Re to be very active for the oxidative reforming of methane at temperatures higher than 1000 K. At temperatures as low as 873 K, however, very little activity was measured. This was attributed to the oxidation of the metal.

Nakamura et al. [133] observed a slightly altered activity sequence for metals supported on silica at 650°C, viz. Pt > Rh > Ru > Pd > Ni, Fe > Co, when the reaction was

initiated at 400°C and the temperature then increased stepwise. This sequence contains the only two inconsistencies in all of the above activity sequences, namely the position of platinum and that of nickel. Nickel was much higher in the reported activity sequence if the initial catalyst activity was measured at 700°C and the catalyst was then cooled incrementally rather than starting at low temperature. Platinum was found by no less than four other groups to be less active than Rh, Ru and Ni [83, 105, 43 and 136].

Hence, a tentative assignment of the activity of some Group VIIIB and VIA metals for oxidative reforming is:

$$Rh > Ru > Ni > Ir > Pt > Pd > Fe > Co > Cr.$$

This is valid for non-acidic supports and for temperatures close to 700°C. In order to determine the relative activities of the different metals beyond doubt, one needs to compare catalysts by conducting experiments under strictly comparable operating conditions while ensuring that transport resistances are negligible. The work on which the above sequence is based, was done by a great number of workers under widely varying operating conditions, and it is therefore likely to be inaccurate; an attempt will nevertheless be made in the following section to correlate the activity sequence with other known properties of the metals.

The catalytic activity of metals for the steam reforming of methane as reported by Dowden [124] may be compared with the above sequence:

$$Ru > Rh > Ni > Co > Pt > Fe > Pd$$

There is quite substantial agreement between these two sequences, and especially interesting is the high activity of nickel for both reactions. If one considers the sequence of metal activity for methane combustion in excess air that was cited by Marek and Hahn [142]

$$Os > Pd > Pt > Ru > Ir > Rb > Au$$

there is less of a correlation with the sequence for methane oxidative reforming. The order

Ir > Pt > Pd (obtained for oxidative reforming at low oxygen content) is an exact mirror image of the way these three elements are arranged in the sequence obtained for combustion (using excess oxygen). This may be indicative that the reaction mechanism for methane combustion is very different from the mechanism of oxidative reforming and perhaps more comparable to that of steam reforming, but the urge to come to such insightful conclusions should be resisted until such time as workers in the field of oxidative reforming produce results which allow one to compare catalysts on a more solid basis.

1.7.4. Multicomponent catalysts

Inui *et al.* [100] studied the effect of the addition of noble metals to a supported nickel catalyst for the oxidative reforming of methane, steam reforming, CO_2 reforming and a combination of all three reactions. The authors concluded that the noble metal acted as a hydrogen sink in the sense that it caused the dissociation of hydrogen produced in the reaction and thus aided the nickel to remain in a more reduced (active) state. A Rh-modified Ni-CeO_2-Pt active component supported on an alumina-washcoated ceramic fibre carrier was the most active catalyst.

Choudhary *et al.* [125] observed a lowering of the temperature at which the production of syngas started when Pt, Pd and Ru was added to the Ni catalyst. The lowering of the reaction start temperature was ascribed to the role of the noble metals in hydrogen dissociation and the concomitant lowering of the temperature at which $NiAl_2O_4$ can be reduced to $Ni°$.

Oh and Mitchell [126] studied the effect of rhodium addition to a number of composite supported noble metal catalysts (used as automotive exhaust catalysts) on methane oxidation under fuel lean conditions. While the onset temperature of methane oxidation was not affected by adding Rh to a $Pt/Pd/Ce/Al_2O_3$ catalyst, the methane conversion to carbon monoxide was significantly enhanced under reducing conditions (fuel-rich feed). This is in agreement with the reported activity sequence (section 4.1.1) where rhodium was found to be more active for methane oxidative reforming than either platinum or palladium.

1.7.5. Metal Loading

The range of metal loadings that have been used vary between 0.015 wt% Ru/Al_2O_3 [31] and almost pure cobalt in a 94 wt% Co/MgO catalyst [122]. The amount of heat of reaction evolved per unit mass of catalyst is directly related to the amount of exposed metal. If mass transport or heat transport resistances are present at low metal loadings, the heat transport problem will incease as the metal loading is increased (at comparative values of metal dispersion) and as the reaction rate per unit mass of catalyst is effectively increased.

Virtually identical values of X_{CH4} (about 0.85) and total activity (expressed per gram of catalyst) were obtained at 800°C on a Ru/Al_2O_3 catalyst with metal loadings between 0.029 wt% and 1 wt% (see Table 1-3) [31].

Table 1-3 The effect of metal loading on the performance of a Ru/Al_2O_3 catalyst [31]

Metal loading wt%	Temp °C	F_{CH4}/W $mol.kg^{-1}.s^{-1}$	X_{CH4} mol%	Activity $\mu mol.g(cat)^{-1}.s^{-1}$	TON[a] s^{-1}
1	800	0.893	88.1	787	7.95
0.1	800	0.893	85.3	760	76.11
0.029	800	0.893	85.5	760	264.87
0.015	800	0.893	66.3	592	398.89

a $mol(CH_4).mol(Ru\text{-}total)^{-1}.s^{-1}$

A further decrease in ruthenium content to 0.015 wt%, however, resulted in a decrease in methane conversion to 0.66. In spite of the decrease in conversion and total activity brought about by lowering the metal loading, the activity in terms of metal content of the catalyst increased drastically. The similar values of methane conversion and specific acticity for the first three catalysts may be ascribed to similar metal dispersion in the three cases, and the decrease in conversion and activity on the catalyst with the lowest Ru loading to a decrease in the amount of available metal. This opinion needs to be backed up by evidence of metal dispersion from independent measurements which was *not supplied*. Therefore is it impossible to conclude with more confidence than the above speculation, what the effect of

58

metal loading was on catalyst performance.

The same effect of increasing activity was also observed for supported nickel catalysts [34, 31]. Vermeiren *et al.* [34] measured similar total activities for different metal loadings in terms of catalyst mass, but again the activity expressed per gram of metal present increased substantially when the metal loading was lowered. The highest activity reported for the above mentioned Ru catalysts was 400 mol(CH$_4$).mol$_{metal}^{-1}$.s^{-1} at 800°C [31]. Activity was calculated from $X_{CH4} * F^{\circ}_{CH4}/W = 0.663 * 0.893$ mol(CH$_4$).kg^{-1}.s^{-1} and assuming that all metal atoms were exposed. This is a conservative estimate, since the selection of a lower dispersion value will result in an even higher activity per mol of metal. This value far exceeds that of any other catalyst reported in the literature (see Table 1-5). The observed increase in specific activity with decreasing metal loading may be explained in terms of metal-support interaction; however, more information about the degree of metal dispersion and the nature of the interaction between metal and support is needed before one can come to any meaningful conclusions.

With a methane flow rate ten times lower than that of Poirier and co-workers [31], Ashcroft *et al.* [27] found that a similar 0.1 wt% Ru/Al$_2$O$_3$ catalyst was unable to yield equilibrium syngas selectivity or X_{CH4}. The group of Poirier and co-workers [31] repeated this experiment carefully under comparable conditions over a catalyst with the same metal loading and showed that it could indeed produce approximately equilibrium gas yields.

Choudhary *et al.* [62] showed that X_{CH4}, S_{CO}, S_{H2} and H$_2$/CO ratio varies with respect to Ni loading on a Ni/MgO catalyst. Both at 500 and 700°C, X_{CH4} and H$_2$/CO ratio exhibited a maximum at a Ni/Mg ratio between 1 and 3. However, S_{CO} increased initially with increasing Ni/Mg ratio and reached a constant level at about Ni/Mg = 0.1. The same effect was observed for NiO-CaO [29]. The initial increase in conversion and selectivity with increased metal content may be attributed to an increase in the number of exposed metal atoms/active sites at which reaction may occur, but more information about the catalyst surface area and metal dispersion is needed to make any further conclusions. The decrease in methane conversion and S_{H2} at high Ni/Mg ratio might be due to low dispersion of the nickel, but again no information on the catalyst properties was provided by the authors.

Lapszewicz *et al.* [105] showed that X_{CH4} and S_{CO} is a strong function of the metal content; they studied the effect of the Rh content on a Sm_2O_3 support and found that oxygen conversion was complete at Rh loadings higher than 0.07 wt% but that methane conversion and carbon monoxide selectivity remained constant for metal loadings higher than 0.5 wt%.

1.7.6. Structure sensitivity

It has been reported that palladium [90, 127] and Pt/Al_2O_3 catalysts [128] used in the combustion of methane to deep oxidation products become more active with time on stream. This has been attributed to the preferential exposure of less dense, but more active, $Pt(110)$ and $Pd(200)$ planes that grow epitaxially on the corresponding low index planes of the Al_2O_3 support material. The higher reactivity of low index planes of transition-metal oxides is well-known [129]. Such behaviour however, is not limited to mixtures containing more than the stoichiometric amount of oxygen needed for total combustion $(CH_4/O_2 \leq 1)$; indeed Mouaddib *et al.* [86] observed a Pd/Al_2O_3 catalyst exposed to a mixture of $CH_4/O_2 = 1.52$ for 12 hours to be more active than a fresh catalyst. A similar effect has been observed for Ni/CaO in which it was necessary to decrease the furnace temperature consistently over a period of 60 hours in order to keep the bed inlet temperature constant [130]. Methane conversion on a pre-reduced CoO/MgO catalyst increased from 0.7 to 0.75 in the first three hours on-stream, but remained constant at 0.75 after this period of initial "activation" [122]. The authors attributed this to a restructuring of the catalyst surface or the creation of additional active sites but no information on metal dispersion and the metal surface area was given as substantiation for their claim. The possibility that the observed increase in conversion may be due to the gradual heating of the catalyst bed towards a thermal equilibrium (autothermal operation) cannot not be excluded at this stage.

More work needs to be done to elucidate this phenomenon. If meaningful results were to be obtained, it should again be stressed that better control of the temperature of the catalyst bed is essential.

1.7.7. Support Material

For a reaction which proceeds at very high catalyst surface temperatures, a support is needed that will not sinter under reaction conditions and which is structurally stable when rapid changes in temperature occur. Furthermore, the support may also play a role in the reaction mechanism by, for example, supplying oxygen [107]. Such a function is unlikely to be supplied by the monoliths coated with metal such as that used by Schmidt's group, but traditional supports such as Al_2O_3 may exhibit spillover phenomena. If there are gas phase free radical reactions taking place simultaneously with the surface reactions, the catalyst surface may act either as a sink or as a source for radicals. Very few of these questions have thus far been addressed.

Vermeiren *et al.* [34] attributed the low values of X_{CH4} and S_{CO}, which they measured using low metal loadings (1 %) of Ni on SiO_2-Al_2O_3 and H-Y zeolite, to the stabilization of metal cations on acidic sites, thus rendering the metal unreducible and unable to catalyze the oxidative reforming reaction. At 5 % metal loading, the above mentioned two supports as well as Al_2O_3 and SiO_2-ZrO_2 exhibited more or less the same values of X_{CH4} (approaching thermodynamic equilibrium) and S_{CO}. If there is more nickel present than the ion-exchangeable amount, Ni would be more readily reducible and thus able to act as a catalyst for the oxidative reforming of methane.

Bhattacharya *et al.* [104] conducted a study of partial oxidation of rich methane/oxygen mixtures (4 < CH_4/O_2 < 8) on catalysts consisting of 1 wt% Pd supported on nine different oxides. At the low flow rates used, one would expect all catalysts to result in the same (equilibrium) conversion. It is therefore surprising to note that the support in this study had a strong influence on methane conversion while the carbon monoxide selectivity was almost 100% and, with the exception of SiO_2, virtually unaffected by changing the support. Pd/Y_2O_3 had the highest activity for methane conversion (0.022 $mol(CH_4)kg^{-1}s^{-1}$). Even though it might be tempting to find an explanation in terms of the support BET surface area and the percentage of exposed metal atoms, the absence of more information on metal dispersion precludes the drawing of any further conclusions from the data of these authors. Working at much higher flow rates (F°_{CH4}/W = 4.3 $molkg^{-1}s^{-1}$), Choudhary *et al.* [131]

also observed a strong support effect for Co on some exotic catalyst supports, in this case both on X_{CH4} and S_{CO}. They found the activity in terms of CO space-time yield at 700°C to decrease in the order

$$Yb_2O_3 > Nd_2O_3 > Eu_2O_3 > Sm_2O_3 > CeO_2$$
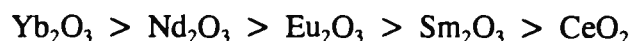
A number of Ni catalysts were tested at the same flow rate and in this case the carbon monoxide productivity was higher than that of the corresponding cobalt catalysts. There was, however, very little effect of changing the supports of the nickel catalysts [132]. Solymosi and Cserényi [48] showed the support to have an influence on the reactivity of CH_x fragments on supported Ir catalysts.

Nakamura and co-workers [133] could not observe any significant production of hydrogen and carbon monoxide at temperatures between 300°C and 700°C on their barren SiO_2 support, but Poirier et al. [31] reported methane conversion of 0.05 and oxygen conversion of 0.13 over Al_2O_3 at 800°C.

1.8. Poisoning and Deactivation

1.8.1. Carbon formation

Equilibrium calculations predict the formation of graphitic carbon at all temperatures for $CH_4/O_2 \geq 2$ [136]. The range of operating conditions in which carbon build-up is prevented, is consequently limited and if one is required to operate within these limits, a catalyst should be used that places a kinetic limitation on the rate of carbon formation. Closely linked to this is the concept of the minimum number of adjacent active sites (ensemble) needed for carbon formation as defined for steam reforming, as opposed to the number needed for, in this case, oxyreforming [9].

Claridge et al. [134] ranked six transition metals in decreasing rate of carbon deposition over 24 hours at 777°C: Ni > Pd > > Ru, Rh > Pt, Ir. Upon further testing for over 200 hours, iridium was still free of any carbon. This is consistent with the observation that

iridium is an effective coke limiting agent by virtue of its properties as a spillover promoter (which promotes coke gasification) and an ensemble size control material [135]. As previously proposed by Vermeiren *et al.* [34], Claridge *et al.* [134] demonstrated that methane decomposition (reaction (1-2)) and not carbon monoxide disproportionation by the Boudouard reaction (reaction (1-3)) was the main source of deposited carbon. These observations are in line with the simulation results of de Groote and Froment [72] who found methane cracking to be the major source of carbon, both at the bed inlet and in the region of almost complete oxygen consumption. From their modelling results, the authors concluded that the reverse Boudouard reaction was responsible for the removal of the majority of the gasified carbon deeper into the catalyst bed.

Four times less carbon was deposited on the surface under oxidative reforming conditions than when pure methane was passed over the catalyst at the same temperature [134]. Electron micrographs showed that both whisker and encapsulate forms of carbon were present on the Ni catalyst after exposure to a CH_4-O_2 stream. Torniainen and co-workers [136] substantiated these results by also reporting coke-free operation of a supported iridium catalyst. Contrary to the above findings by Claridge and co-workers, however, Torniainen *et al.* [136] found that Pd supported on α-Al_2O_3 foam monoliths coked severely and also deactivated; in their study Pt, Rh and Ir sintered without deactivation and coke was only formed on the platinum catalyst. This may be an effect of the support but further data is necessary to settle the discrepancy between these two sets of data.

In order to limit the number of adjacent active sites available for coke formation, Slagtern and Olsbye [76] attempted to prepare a supported Rh catalyst with particle size smaller than about 70 Å by decomposition of a $LaRhO_3$ perovskite but were unable to obtain the required metal cluster size distribution (12-16 atoms). In spite of this apparent failure, they found that the coke content was very low, viz. 0.25 wt% after 17 hours on stream. A nickel catalyst was found to have 2.98 wt% carbon after reaction under comparable conditions. This indicated clearly that carbon formation is kinetically inhibited by using Rh and can be limited even in a regime where its formation is thermodynamically favoured. The size of the metal clusters increased with increasing reduction time; this suggested that the particle size also increased during oxyreforming. In spite of this reduction in exposed surface area, no

deactivation could be detected over a 120 h period.

While it has therefore not yet clearly been demonstrated that coking during oxyreforming may be inhibited by limiting the number of adjacent active sites, the correct choice of metal could prevent or minimize carbon formation. No special precautions, however, seem to have been taken in the above work to avoid the formation of "hot spots" in the reactor. Considering the fact that Rh is more active than Ni (as discussed earlier), the effective surface temperature of the Rh catalyst may be much higher than that of the nickel catalyst and this may increase the rate of carbon gasification reactions more than it would increase the rate of carbon depostion deposition reactions. This, however, needs to be checked experimentally in an isothermal reactor.

Choudhary et al. [126] studied the influence of the supports of a number of rare-earth supported Ni catalysts on the extent of carbon deposition using a methane flow rate of 4.3 mol.kg^{-1}.s^{-1}. The amount of carbon deposited varied from 9 wt% (after six hours) on the NiO/Al$_2$O$_3$ catalyst to 56 wt% (after only four hours) on the NiO/Er$_2$O$_3$ catalyst. The maximum rate of carbon deposition of 52 g(C).g(cat)$^{-1}$h^{-1} was measured when a Tb$_4$O$_7$ support was used. In spite of the large amounts of carbon deposited and the ensuing rise in the pressure drop across the catalyst bed (from 0.03 bar to 0.32 bar over a period of six hours), the methane conversion and product selectivities remained virtually unchanged from their respective initial values. This suggests that filamentous carbon which in may break up the nickel particles and result in a higher nickel surface area, rather than encapsulate carbon which leads to a decrease in the amount of available nickel, was formed.

Vernon et al. [87] observed no carbon on a 1 wt% Ir/Al$_2$O$_3$ catalyst operated at 777°C and with up to 48% carbon dioxide in the feed.

1.8.2. Other causes for loss of activity

Metal may be lost from the support with time on stream by means of volatilization due to high surface temperatures. It was reported that cobalt was lost in this way from its MgO

support [81], and Torniainen *et al.* [136] observed the same effect for Co and Re on an α-Al$_2$O$_3$ support. Heitnes *et al.* [137] showed that the dispersion of nickel and platinum catalysts decreased by up to 57 % and 63 %, respectively. The surprising fact is that this decrease in available catalytic surface had hardly any effect on the methane conversion and selectivity to carbon monoxide. Bharadwaj and Schmidt found that the catalyst particles used in a fluidized bed agglomerated above a threshhold temperature; this phenomenon needs to be avoided if flow patterns in the reactor is not to be disturbed and catalyst performance to be maintained over a long period of time [43].

1.9. Applications for methane oxidative reforming

Dave and Foulds used a process simulator to compare the oxidative reforming of methane with combined reforming, ICI's gas-heated reforming and Exxon's all-in-one combined reforming process as a potential source of syngas for a methanol-producing plant [138]. The study indicated that, whereas the energy requirements of oxidative reforming was comparable to that of the other technologies and methane conversion was the highest for oxidative reforming, the oxygen demand per ton of methanol produced was the highest. If it is taken into account that the oxygen source would contribute significantly to the overall cost of the process, oxidative reforming might not be able to compete with established technologies. However, in spite of all the difficulties that the oxidative reforming poses, it has already been shown that, within the bounds of the assumptions that were made, it may be economically competitive with traditional routes such as steam reforming and autothermal reforming [139]. Even though the study is based on a hypothetical production unit, the result certainly encourages further work in this field.

If oxidative reforming is to be used successfully for the upgrading of natural gas, the effect of other constituents of natural gas, such as ethane, on the performance of oxidative reforming catalysts need to be considered as well. Battle *et al.* [140] demonstrated that a perovskite catalyst that was active for the oxidative reforming of methane was also a successful catalyst for ethane conversion. The CO yield from ethane steadily increased from 37% at 600°C to 91% at 900°C. Battle and co-workers also studied a complex feed

consisting of methane, ethane and oxygen (CH_4:C_2H_6:O_2 = 2:1:1) over $Ba_3NiRuTaO_9$ in the temperature range 600-900°C and at 1 atm pressure [140]. Methane content remained constant to within 5% (the consumed methane was probably compensated for by methane produced from ethane), but up to 98% of the ethane was converted at 900°C. CO was the major product, but there was also ethylene (up to 14% at 900°C) and C_{2+} species present (about 2%). When the pressure was increased to 10 atm, more carbon dioxide was formed and a smaller amount of higher hydrocarbons was produced; CO still remained the major product. At high temperature and still at 10 atm, ethane hydrogenolysis to methane was enhanced.

Najbar *et al.* [141] studied the oxidation of natural gas (95.2% CH_4, 1.2% C_2H_6, 0.7% C_3H_8, 2.1% N_2 and trace amounts of butane and CO_2) over silica-supported Pd and Pt catalysts. At temperatures up to 500°C and using a natural gas/oxygen ratio of 9, oxygen consumption was complete and all the higher hydrocarbons was converted to CO, CO_2, H_2 and water.

Marek and Hahn [142] reviewed the available literature on methane oxidation to synthesis gas as long ago as 1932. They considered the possibility of using the product gas of a reactor in which air was used to oxidize methane to carbon monoxide and hydrogen for the subsequent synthesis of both methanol and ammonia, and from the resulting hydrogen/nitrogen ratio, concluded that a considerably higher pressure than normal would be needed for methanol synthesis due to the effect of nitrogen dilution. For ammonia synthesis, the authors proposed the partial oxidation of methane-containing coke-oven gas to carbon monoxide and hydrogen and the subsequent shift of CO with water to produce the required amount of hydrogen. Marek and Hahn reached the following conclusion [142]:

"For utilization in ammonia synthesis, however, the combination of oxidation by steam and oxygen at temperatures of about 1000°C is better adapted for the production of hydrogen since better conversion to hydrogen alone is possible."

This is to a degree still the prevailing opinion and it will be some time before methane oxidative reforming is accepted as a competitive process.

1.10. The interaction of methane and oxygen with nickel catalysts

The first section deals with the mechanism of methane chemisorption on nickel surfaces and the effect of pre-adsorbed species on methane chemisorption. In the following section, oxygen chemisorption will be considered.

1.10.1. Methane chemisorption

It has been postulated that CH_4 dissociative chemisorption on metal surfaces proceeds by a direct mechanism and not via an activated intermediate [143, 144, 145, 146]. The only effect of the presence of adsorbed oxygen atoms on the chemisorption of methane is that it supposedly decreases the number of vacant sites [147]. Yang and Whitten [152] mention that the Ni $3d$ orbitals contribute to bonding by directly mixing with $4s$ orbitals and CH_3 orbitals. This is in contrast to oxygen adsorption where it was found that the $3d$ orbitals of nickel remain passive on a Ni(100) surface with the $4s$ orbitals contributing to O_2 dissociative chemisorption [148]. This supports the previous finding [147] that the presence of adsorbed oxygen atoms have little effect on the chemisorption of methane.

Wright et al. [149] measured the initial rate of hydrogen liberation when methane was exposed to a nickel film to obtain an activation energy for dissociative chemisorption. Beebe et al. [150], on the other hand, used Auger electron spectroscopy to follow the rate of change in the C/Ni Auger ratio. This ratio was used to calculate the rate of methane decomposition on different Ni planes and was found to decrease in the order

$$Ni(110) > Ni(100) > Ni(111)$$
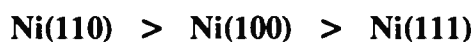
The corresponding activation energies of methane chemisorption on each crystal face are given in Table 1-4.

Table 1-4   Activation energy for methane chemisorption on nickel

Nickel plane	Method[A]	E_a kJ.mol⁻¹	Notes	Reference
111	Calc	69.9	CH₃-* and H-* on separated 3-fold sites	152
111	Calc	64		151
111	Meas	52.7±5.0		150
111	Meas	51.5	Data re-evaluated in Ref. [150]	143
110	Meas	55.6±6.3		150
100	Calc	29		151
100	Meas	26.8±4.6		150
100	Meas	59±1.5		146
Film		41.8	Rapid adsorption above 140 °C	149

A   "Meas" if the E_a was determined from experimental data and "Calc" if it was obtained from a simulation of a theoretical surface.

A similar method was used by Nielsen *et al.* [146] to probe the dissociative chemisorption of methane on a Ni(100) surface. The disagreement between the results obtained in these types of experiments and that obtained in beam studies was considered in some detail by Beebe *et al.* [150]. They concluded that the most plausible explanation for the discrepancy was that

"the vast majority of the thermal impingement flux has normal kinetic energies well below the range probed by the molecular beam techniques".

Anderson and Maloney [151] used ASED (atomic superposition, electron delocalization) molecular orbital theory and various cluster models to study the interaction of methane with simulated nickel surfaces. The activation energy for methane adsorption on Ni(100) was 29 kJ mol⁻¹ and for the Ni(111) crystal face the activation energy was 64 kJ mol⁻¹. Yang and Whitten [152] concentrated on the Ni(111) surface by using a 41-atom three-layer cluster and found the activation energy barrier to be overcome for C-H bond breakage to be 69.9 kJ mol⁻¹.

68

The disagreement between cluster model predictions and measured data may be due to a number of reasons, not the least of which is the differences in metal-metal bond strength (152 and 106 kJ mol^{-1} for the Ni$_7$ and Ni$_{13}$ clusters [153], respectively, compared to 71 kJ mol^{-1} for bulk nickel [153]).

1.10.2. Oxygen chemisorption

With the exception of gold, silver and the (111) and (100) planes of platinum, oxygen is readily adsorbed on the surfaces of transition-metal catalysts with a high initial sticking probability at room temperature [154]. This implies that the activation energy for adsorption is very low. Adsorbed oxygen atoms are believed to form island-like structures on some metals due to interaction between adsorbed O$_s$ species. Reaction of O$_s$ with the reactant that is being oxidized occurs either at the edges of these islands (if the reactant is also adsorbed) or on the islands themselves in the case an Eley-Rideal or impact type of mechanism. The island-like character of adsorbed oxygen is thought to lead to oscillatory behaviour in the rate of CO and H$_2$ oxidation. Au et al. [58] showed that adsorption of methane and oxygen at 500°C is a competitive process and that oxygen is adsorbed preferentially. Schmidt et al., however, assumed non-competitive adsorption of oxygen with all other species in their model of methane oxidative reforming to synthesis gas [94].

Hu and Ruckenstein [61] used the bond-order conservation morse potential (BOC-MP) approach to study the effect of chemisorbed oxygen on methane dissociation on Ni(111) and Ni(100) crystal faces. The authors considered three different oxygen adsorption sites, namely on-top, bridge and hollow sites and they found that for both crystal faces considered, the activation energy for reaction (1-22) was lowered only when the oxygen was located at the on-top sites.

$$CH_4 + O_{(s)} \rightarrow CH_{3(s)} + OH_{(s)} \tag{1-22}$$

They concluded that only the oxygen species present in weak bonding sites (at on-top sites

in this case) could facilitate the dehydrogenation of methane and that such species may either take part in the reaction or migrate to more stable sites such as hollow sites.

Discussing the partial oxidation of hydrocarbons, Boreskov expressed the opinion that a catalyst with weakly-bound oxygen species would lead to deep oxidation products [154]. On the other hand, there exists an inverse relationship between the metal-O bond strength and the reactivity of an O_s species. Therefore there should be an optimum in the metal-O bond strength which will ensure a maximum in the rate of methane conversion.

At low coverage, the chemisorbed oxygen atoms are covalently bound to the metal surface with a symmetry which is determined by the underlying metal structure; this layer may undergo disordering or dissolve in the bulk metal at elevated temperatures, or it may be transformed to a two-dimensional metal oxide layer with concomitant metal-metal bond rupture at increased oxygen coverage. If bulk NiO is formed in a Ni/Al_2O_3 catalyst, for example, continued exposure to O_2 at high temperature may lead to the formation of catalytically inactive $NiAl_2O_4$. It has been suggested that the addition of a noble metal to Ni/Al_2O_3 catalysts increases the reducibility of such aluminate species [125]. It may also be possible that the formation of nickel aluminate may be prevented by the hydrogen dissociation ability of noble metals; this would prevent the growth of bulk NiO and the formation of $NiAl_2O_4$.

It has not been determined whether methane reacts with adsorbed oxygen by the impact (Eley-Rideal) mechanism or whether methane is first dissociatively chemisorbed to form adsorbed CH_x and H which then react with adsorbed oxygen species.

A more rigorous assessment was also attempted to compare the activity of metals for methane oxidative reforming. The activity of a number of catalysts were calculated and the values are given in Table 1-5.

Activity in this sense is defined either as $X_{CH4} * F°_{CH4}/W$ or as the measured reaction rate, whichever of the two is provided. The rate at the given temperature was converted to a turnover number (molecules converted per exposed site per second) if the metal dispersion

was given. In cases where the dispersion was unavilable, the turnover numbers were calculated by assuming that 1% of the metal atoms were exposed. All rates and turnover numbers were corrected to 630°C by assuming an apparent activation energy of 100 kJ mol^{-1} if a value for E_a was not supplied. It was also assumed that the pre-exponential factor is not a function of temperature and that a general rate expression is valid for a very wide temperature range.

Table 1-5 Attempt to compare the activity of oxidative reforming catalysts

Catalyst	Ref	Temp °C	CH$_4$/O$_2$	Rate at Temp mol/g$_{cat}$/s	k^c m^3/s
25% Ni/Al$_2$O$_3$	88	800	1.78	5.09E-6	0.02^b
5% Ni/SiO$_2$	31	800	2	4.16E-4	2.2^b
18.7% Ni/Al$_2$O$_3$	125	800	2	5.83E-3	2.5^b
1% Ni/Al$_2$O$_3$	31	800	2	1.67E-4	4.4^b
5% Ni/Al$_2$O$_3$	34	800	2	7.1E-5 to 5.3E-4	3 to 23^b
10% Ni/Al$_2$O$_3$	79	625	2	1.63E-4	158

a Methane conversion expressed as a fraction of the equilibrium conversion; if $X_{CH_4}/X^-_{CH_4} < 0.1$, the data is more likely to be kinetically-controlled and if $X_{CH_4}/X^-_{CH_4} > 0.5$, equilibrium is approached.

b Turnover number (TON) in mol(CH$_4$).mol(surface atoms)$^{-1}$.s^{-1} was calculated at 630°C with $E_a = 100$ kJ.mol^{-1} if E_a was not given. If metal dispersion was also not given, a value of 1% was assumed to calculate the TON.

c A pseudo first-order rate constant was calculated at 630°C (k = TON / C°$_{CH_4}$); the rate is assumed to be independent of O$_2$

The rate at the given temperature and the rate at 630°C were related by the expression:

$$\frac{Rate^{T_1}}{Rate^{T_2}} = exp \left[\frac{E_a}{R} \left(\frac{1}{T_2} - \frac{1}{T_1} \right) \right] \tag{1-23}$$

The turnover numbers were corrected for the effect of concentration and a pseudo first-order rate constant was arrived at by calculating k = TON / C°$_{CH_4}$. While considering the data in Table 1-5 it should be kept in mind that sweeping assumptions were made in order to calculate the turnover numbers. As stated previously, there is little sense in comparing catalytic activity when catalysts are operated close to equilibrium and in many of the cases

considered in Table 1-5, the ratio of the actual conversion to the conversion at equilibrium $(X_{CH_4}/X^=_{CH_4})$ is close to unity. As equilibrium is approached the reaction rate and the turnover number should decrease; firstly because of product inhibition of the rate and secondly due to the fact that reactants are depleted. Therefore the highest observed turnover numbers should be used in comparing catalysts.

1.11. Summary of the main findings from the literature

Oxidative reforming is an exothermic reaction and is therefore likely to exhibit autothermal behaviour. When a reaction sustains itself in such a way, especially when the reaction mixture has significant catalytic interaction with a solid surface, the effect of conditions such as the surrounding temperature and the nature of the solid material on conversion and selectivity is not always immediately apparent. Since most studies report only limited measurement of temperature, little is known about the thermal behaviour of this reaction. There is thus great scope for further research.

Many of the reported results have not been decoupled from secondary heat effects and are therefore difficult to draw conclusions from. Another fundamental question about which very little is known and which may substantially influence the approach to oxidative reforming research is the extent to which homogeneous reactions occur in conjunction with the catalytic surface reaction. Coupled with this is the determination of the actual working temperature of the catalyst and the development of methods to measure it.

The dynamic nature of catalytic surfaces at the ignition temperature is not well documented but investigations of the effect that changes in gas composition have on the metal/metal oxide equilibrium and of the effect of temperature on the on the overall equilibrium is needed to improve the level of understanding of the oxidative reforming of methane.

Davis stated that "...science partly driven by economics will not always show an orderly progression of activity..." [155]. This is especially true of oxidative reforming. As with all research, new results often lead to diversification rather than a more focused viewpoint

and the unanswered questions will increase in number. However, as with the oxidative coupling of methane, the urgency will surely dissipate as the economic impact becomes clear, thus allowing more systematic research to be conducted.

1.12. Objectives of this research

Based on the state of knowledge of the oxidative reforming of methane presented above, the present research had a number of objectives.

- In the first instance it was necessary to develop an experimental approach and to construct the necessary equipment to allow the measurement of axial bed temperature profiles during oxidative reforming experiments.

- Using the equipment described above, the **primary** objective was to find experimental confirmation of the absence of heat and mass transport limitations. As shown in the preceding discussion, the absence, or at least the negligible effect of, mass and heat transfer limitations has never been shown under isothermal conditions and at constant contact time, in the open literature.

- The **secondary** experimental objective was to perform a series of kinetic experiments in the absence of transport phenomena in order to gain some insight into the rate, and hopefully into the reaction pathway, of the oxidative reforming of methane.

- While the above two objectives were considered as crucial to this study, it was decided in the third instance that an attempt at the development of a kinetic model to account for the measured kinetic data might add more depth to the experimental data by providing a quantitative framework for the experimental data and allowing for an interpretation of the reaction pathway.

- The fourth objective was to perform a study of the catalyst and to determine how it was affected by the reaction.

Chapter 2

2. EXPERIMENTAL

I often say that if you can measure that of which you speak, and can express it by a number, you know something of your subject; but if you cannot measure it, your knowledge is meagre and unsatisfactory. (Lord Kelvin)

The experimental apparatus and operating procedures for kinetic experiments are described in the first section of the present chapter. Also included are the results of some blank runs that were used to characterize the system. This is followed by a description of the techniques and apparatus that were used for catalyst characterization, as well as the properties of the unused catalyst. The chapter is concluded with an account of all the experiments that were conducted.

2.1. Experimental apparatus

2.1.1. Flowsheet of the kinetic testing apparatus

The kinetic experiments as well as diagnostic tests for the presence of film- and internal diffusion were conducted in a flow system that incorporated a fixed-bed microreactor. The flowsheet of the experimental apparatus, which includes the reactor, mass flow controllers, valves and tubing, is shown below in Figure 2-1.

2.1.1.1. The reactor

Catalytic testing was performed in a single-pass fixed-bed tubular downflow reactor (Figure 2-2). Quartz was chosen as the material of construction because stainless steel has

Figure 2-1 Flowsheet of experimental setup
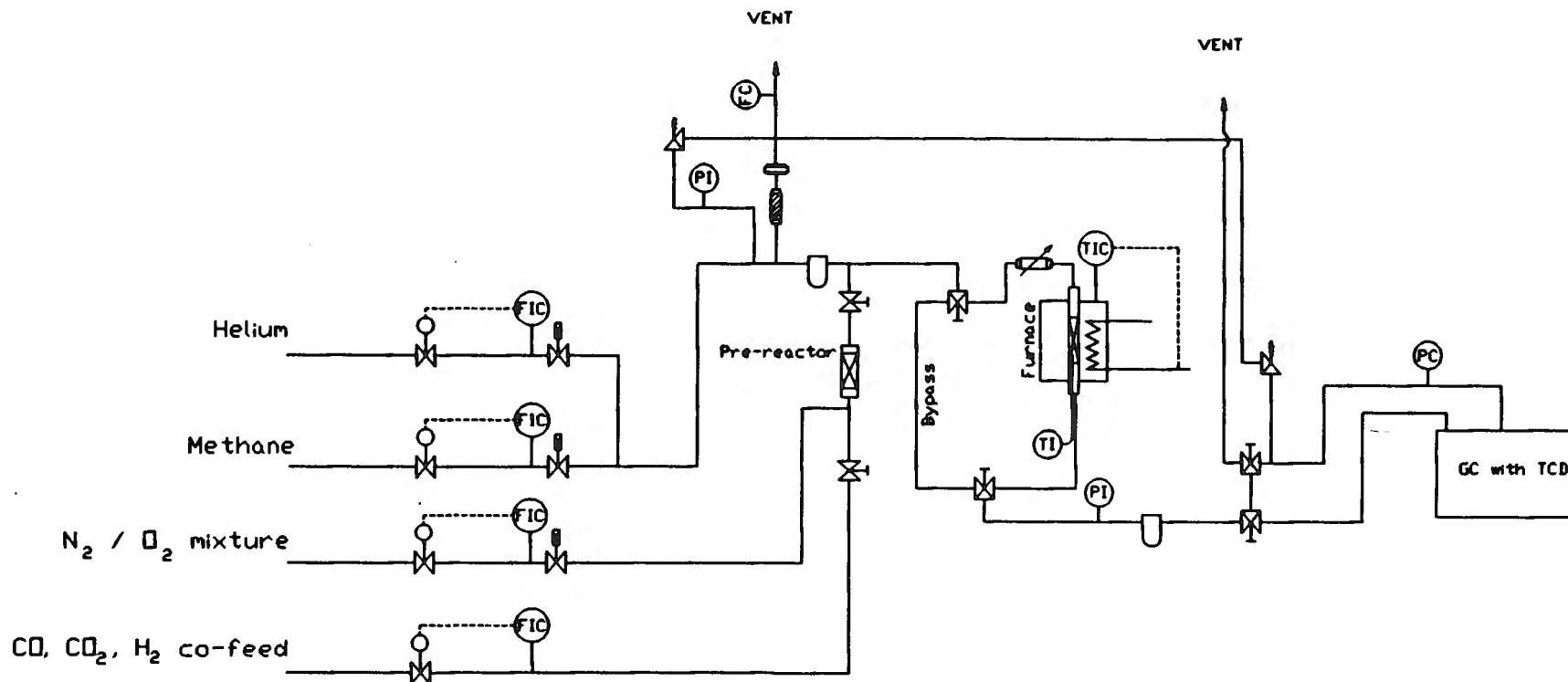
PI	Analogue pressure gauge		Pressure relief valve		
TI	K-type thermocouple		Air operated valve		HPLC pump
FC	Flow sensor for emergency shutoff		3-way valve		Jetloop mixer
FIC	Mass flow controller		Control valve		Packed bed reactor
TIC	Temperature controller		Hand operated valve		Flashback arrestor
PC	Pressure sensor for emergency shutoff		Bursting Disk		Line filter

been shown to catalyze the formation of carbon oxides [13]. Anderson and Pratt [158] furthermore suggested that pyrex reactors should not be used at temperatures exceeding 500°C.
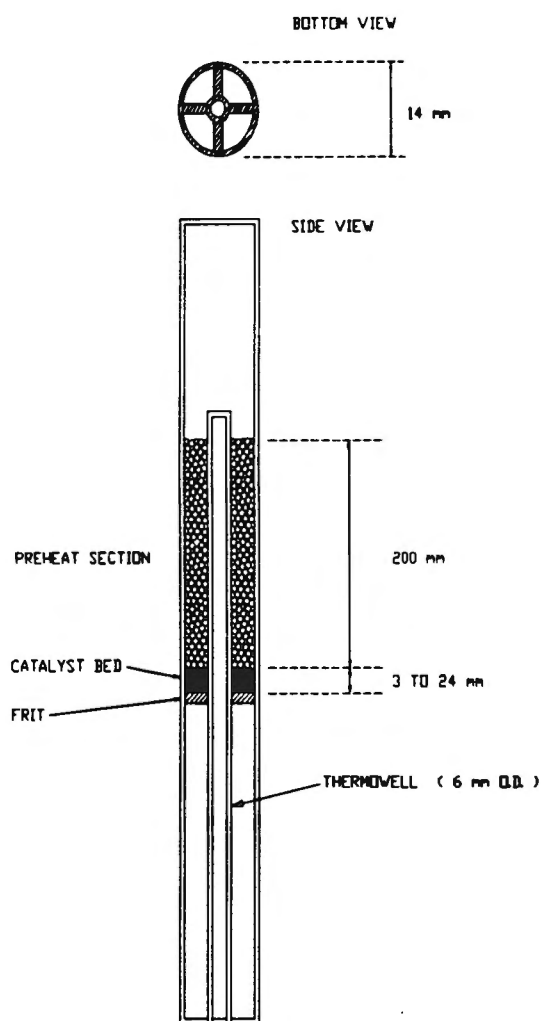
Figure 2-2 Cross-sectional view of the quartz reactor
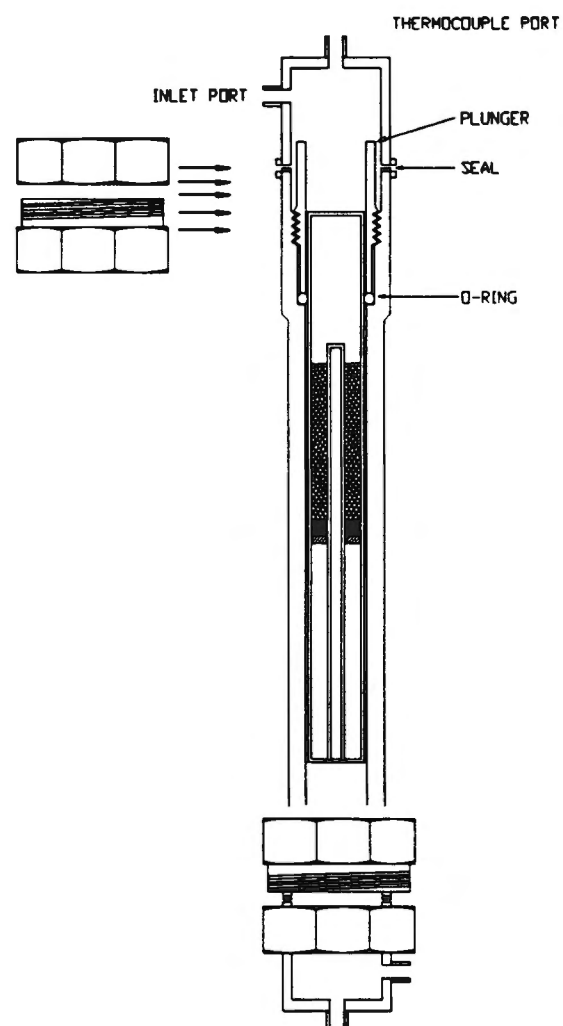
Figure 2-3 Reactor and steel sheath

The reactor was constructed from two quartz tubes of 14mm ID and 6mm OD respectively in an annular arrangement. The inner tube was sealed at the top and joined to the outer tube at the bottom in a configuration that allowed gas to exit through four holes at the bottom of the reactor. A view from the bottom of the reactor which is included in Figure 2-2 shows this feature. The annular tube was open at the bottom to accommodate a thermocouple for the determination of the axial bed temperature profile. A frit with a thickness of 2mm was

fused into the annular space at a height of 185mm from the bottom of the reactor to act as support for the catalyst particles. The frit had a porosity grade of 0. A stainless steel sheath (ID = 17mm) was furthermore constructed to act as a shield for the quartz reactor in the case of explosions and for experiments at elevated pressure. The space between the quartz tube and stainless steel sheath surrounding the quartz tube was sealed with a viton o-ring to prevent the feed from bypassing the catalyst bed in the quartz reactor. The o-ring was compressed with a steel plunger which could be screwed down onto it, thus squeezing the viton o-ring tightly to form a good seal between the quartz and steel. The whole unit (steel sheath with the quartz reactor mounted inside) was enclosed in an electrically-heated furnace which consisted of a split brass heating block. Each half of the brass block was heated by two cartridge heaters, each rated at 400W. A cross-sectional view of the quartz reactor inside the stainless steel sheath is shown in Figure 2-3.

2.1.1.2. Mass flow controllers

All the gases except for water were fed to the reactor from high-pressure cylinders and the flow rates were controlled by means of mass flow controllers (Brooks, model 5850TR). These units measure the increase in the temperature of a gas stream after passing a constant heat flux into the gas stream. The temperature increase, which is proportional to the gas mass flow rate, is used as a signal to control the flow of gas by means of electromagnetic valve. Since the thermal properties of gases vary from one compound to the next, the mass flow controllers had to be calibrated for each compound. The calibration procedure is discussed in more detail in the appendix (section B.1) and the results of the mass flow controller calibration are summarized in Table 2-1. The data is given in the form of two constants which were calculated from a linear least-squares regression to the calibration data:

$$F_i = A * SP_i + B \qquad \qquad (2\text{-}1)$$

where SP_i is the mass flow controller set point as a percentage of the maximum flow rate and F_i the flow rate in units of cm^3/min (at STP).

When steam was co-fed to the catalyst, water was generated in-situ to prevent the pulsing behaviour which often occurs when a positive-displacement pump is used to feed the water as a liquid to an evaporator. The water was formed upstream of the reactor inlet by passing hydrogen and oxygen over an oxidation catalyst (Südchemie catalyst EX-1621). The catalyst was packed into a ¼" tube which was heated with a mantle heater to 275°C. The ability of the oxidation catalyst to sustain the hydrogen oxidation reaction for the duration of an experiment was tested for H_2/O_2 ratios between 1.4 and 4.3. Even at a much higher oxygen concentration than were used during kinetic experiments, the oxygen concentration at the outlet of the H_2 oxidation reactor was unchanged for two hours. The normal feed during water co-feeding kinetic experiments consisted of water in oxygen (all hydrogen consumed during the pre-oxidation). More details of water production is included in the appendix (section B.1).

Table 2-1 Calibration constants for the mass flow controllers

Compound	A ml/min.SP(%)	B ml/min	R^2
Helium	35.8074191	-10.9951027	0.99950
N_2	1.0656083	-0.9600875	0.99981
O_2/N_2 mix	1.1588401	-0.5904647	0.99900
CH_4	0.3487715	0.5831179	0.99973
O_2	0.4253740	-0.3589538	0.99907
CO	0.4118485	-0.0221599	0.99930
CO_2	0.3171720	-0.1963370	0.99801
H_2	0.4900969	-1.4739731	0.99852

2.1.1.3. Temperature measurement

The K-type thermocouple that was used to measure the axial bed temperature profile was calibrated with an electronic calibration device. The response was found to be linear and the difference between the indicated temperature and true temperature was less than 5°C. A plot of the calibration results of the thermocouple that was used to measure the bed temperature profile is shown in Figure B-2 (Appendix B.3). The calibration curve was used to convert

all temperature data from the indicated values to true temperatures.

The actual position of the couple in the sheathed thermocouple was determined by comparing the axial bed temperature profile (of an active catalyst bed) that was measured with an unsheathed thermocouple on which the couple was visible, to the profile that was measured with the sheathed thermocouple. In addition to this, a soldering iron with a thin tip was passed along the thermocouple sheath to determine the maximum temperature reading. Using both these techniques, the actual position of the thermocouple was found to be 3 mm behind the physical tip of the stainless steel sheath.

2.1.1.4. Auxiliary equipment and tubing

The gases were metered from 50 dm^3 cylinders which were filled to a pressure of about 20MPa. Double-stage regulators were used to ensure a smooth outlet pressure. The outlet of the regulators which were connected to the mass flow controllers were maintained at a gauge pressure of 400kPa while the pressure in the reactor was maintained at 100kPa above atmospheric pressure. The pressure drop over the mass flow controllers was therefore about 300kPa. The atmospheric pressure was 100.5 ± 1.4 kPa (average-, not maximum-, deviation from the mean atmospheric pressure).

A jet loop mixer was installed upstream of the reactor to ensure thorough mixing of the gas streams prior to entering the reactor. The vessel was constructed from $^1/_4$" tubing and Swagelok fittings and is shown in Figure 2-4. The jet loop mixer operates on the principle of momentum transfer - the momentum of the gas leaving the jet at high velocity is transferred to the gas in the loop, thus causing it to be swept with the fast-flowing gas rather than flowing towards the outlet. This results in the gas recycling through the loop a number of times before it exits the vessel. The recycle ratio of the unit was determined by a transient technique during which the dispersion of a propane pulse by the mixer in Figure 2-4 was measured by an FID (see appendix B.2). The recycle ratio was found to be between 2.2 and 2.3 with a flow rate of 230 cm^3/min.

The recycle ratio of these type of mixers increase with flow rate. Therefore it may be concluded that the recycle ratio of the mixer will exceed 2.3 at the flow rates used during kinetic experiments (about 1000 cm³/min). While such a recycle ratio is not high enough to ensure CSTR behaviour, the presence of the jet loop mixer upstream of the reactor inlet, combined with the α-Al_2O_3 balls directly upstream of the catalyst bed should be sufficient to ensure adequate for pre-mixing of the reactor feed.
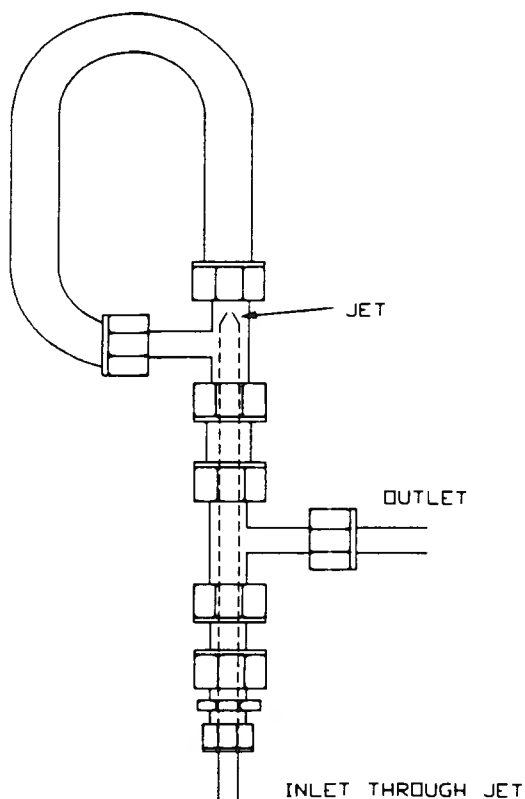
Figure 2-4 Jetloop mixer

2.1.1.5. Safety Features

Since the feed composition was at times within the explosive regime of methane-oxygen mixtures, the experimental apparatus was equipped with a number of safety features. A porous metal filter was located upstream of the reactor to quench possible flames and thus prevent back-propagation of a flame front towards the methane mass flow controller- and cylinder. A bursting disk rated at 80bar was also located upstream of the reactor to vent the feed in case of an uncontrolled pressure rise in the system and if the pressure relief valve failed to open. Since most of the kinetic experiments were conducted with a very dilute feed stream (less than 3% reactants in helium), flame propagation by means of free radical chain branching was unlikely and the above safety precautions of little need. In the case of autothermal experiments, the feed consisted of about 28% methane in air. A mixture with such a composition is above the upper flammability limit (UFL) of 15% CH_4 in air and therefore not explosive [156]. In spite of the fact that operating conditions for this work fell outside of the flammable regime of CH_4-O_2 mixtures, the safety features were considered important in the case of mass flow controller failure or modified operating conditions.

2.1.2. Gas analysis and calibration

Gas analysis was performed by means of an on-line gas chromatograph. The gas from the outlet of the reactor was allowed to pass through a sample loop with an internal volume of 0.25ml which was mounted on a six-port switching valve. The gas chromatograph (Varian 3300) was equipped with a thermal conductivity detector. Gas separation was achieved by means of a Carbosieve SII column (Supelco.). The column packing consists of a mixture of activated carbon and a molecular sieve and was able to separate the permanent gases (H_2, CO, CO_2, O_2, N_2 and CH_4) as well as all C_2 hydrocarbons. No C_2 hydrocarbons were detected in any of the experiments. Water could be separated on the column, but the peak area could not be evaluated quantitatively due to excessive tailing. Operating conditions of the GC is shown in Table 2-2.

Table 2-2   Operating conditions of the gas chromatograph

Column	Carbosieve SII (Supelco)
	length = 3.069 m, d_i = 3.175E-3 m
Carrier gas	Helium (99.995%)
Carrier gas flow rate	35 $cm^3.min^{-1}$ (at STP)
Injector temperature	150°C
Detector temperature	250°C
Filament temperature	285°C
Temperature program	5 minutes @ 45°C, then ramp to 225°C at 32°C/min, then maintain at 225°C for 14 minutes
Internal standard	Nitrogen co-fed with reactants

A sample chromatogram with the peak assignments is shown in Figure 2-5 and further calibration details of the gas chromatograph are given in appendix B.4.

CHANNEL A   INJECT 21-08-26 14:09:35 STORED TO BIN #   1

1 12   H₂

AT 3C

O₂   N₂

5 93

AT-0
11 0
7 96   CO
AT 16

19 18   CH₄
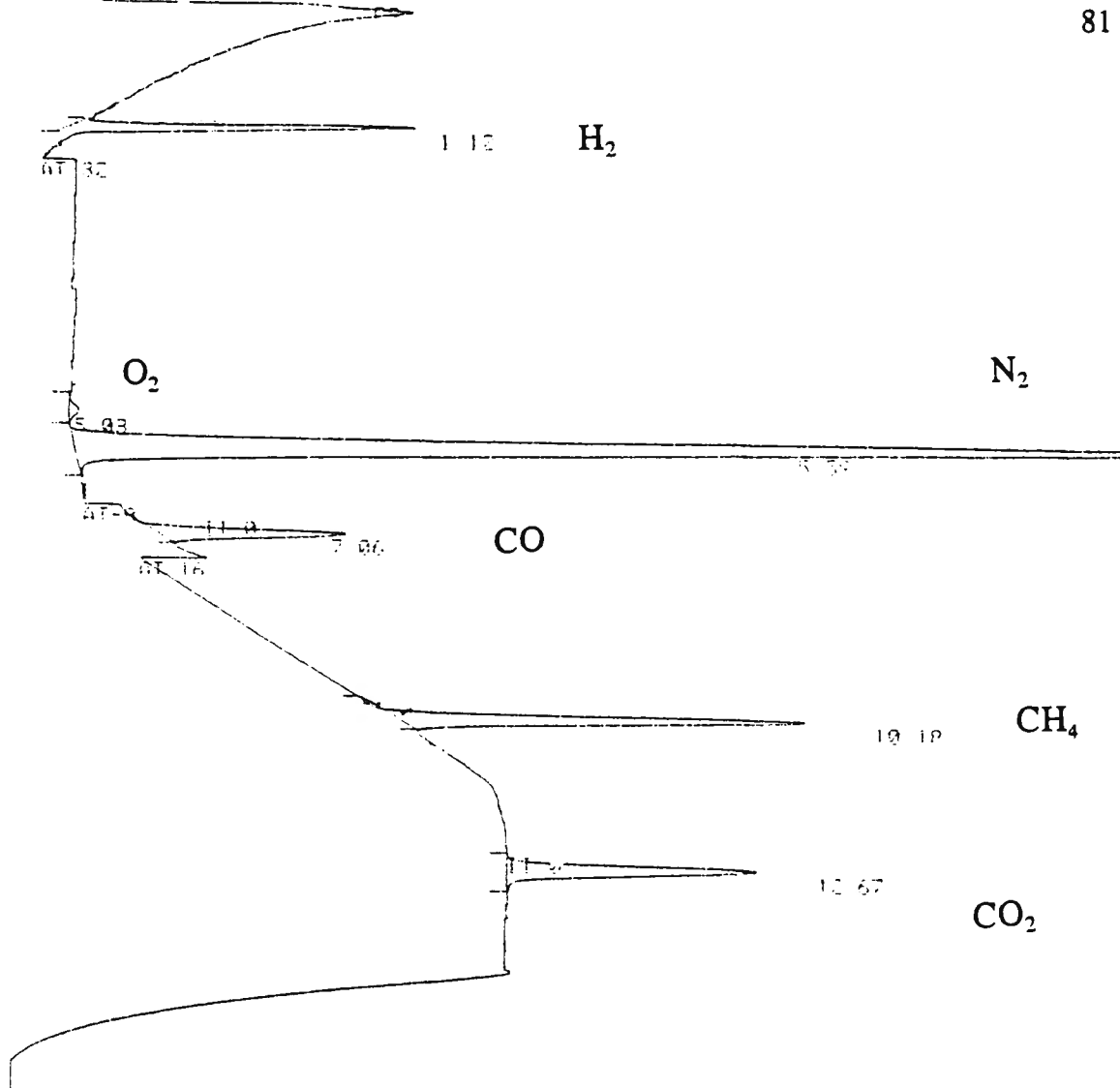
12 67
CO₂

DATA SAVED TO BIN #   4

Jan   21-08-96 14:09:35   CH= "A" PS= 1

FILE 1   METHOD 0   RUN 40   INDEX 10   BIN 4

PEAK#	AREA%	RT	AREA BC
1	0 15	1 12	1688 01
2	0 627	5 03	7071 02
3	81 721	5 59	921677 03
4	2 173	7 06	24596 03
5	8 737	10 18	98423 03
6	6 599	12 67	74427 01

Figure 2-5 Sample gas chromatogram with peak assignments

2.1.2.1. Response factor determination

Due to its inert nature, nitrogen was used as the internal standard. After careful calibration by feeding the required combinations of pure gases and performing a gas analysis of each feed composition, the response factors of all the permanent gases relative to N_2 were calculated. Further details of the calibration procedure are included in the appendix and the results are given in Table 2-3. Due to excessive tailing of the water peak on the chromatographic column, only the response factors of H_2, O_2, CO, CO_2 and CH_4 could be calculated. Linearity of the TCD response was confirmed by the very high correlation coefficients of the response factor plots. The values of the response factors were found to change slightly during the course of the experiments. This is most likely due to particle breakup in the column and the concomitant change in the carrier gas velocity through column at constant head pressure. The response factors never changed by more than 5% over the period of the experiments, but as a precautionary measure, they were periodically re-evaluated to ensure good mass balances.

2.2. The catalyst

A commercially-prepared steam reforming catalyst (Südchemie catalyst code G-90B) was used in all experiments. The catalyst was prepared by Südchemie for laboratory testing and consisted of nickel supported on irregular α-Al_2O_3 chips in the size fraction 500μm to 1mm. Prior to use, the catalyst was crushed in an agate mortar and pestle and sieved to yield particles in the ranges 150 - 250μm, 250 - 425μm, 425 - 500μm and 500 - 710μm. Further catalyst pretreatment will be discussed in the following section.

2.3. Experimental procedure and blank tests

The purity as well as the suppliers of the gases that were used to test catalytic activity are given in appendix B.6. This section is devoted to a discussion of the experimental procedure that was followed and the presentation of the results of some blank experiments. This is

followed by a complete sample calculation (section 2.3.5) which shows how GC traces of the product stream was converted to species partial pressures.

2.3.1. Loading the reactor

After weighing off and mixing the required amount of a given size fraction of catalyst and α-Al_2O_3 diluent, the diluted catalyst was poured into the reactor and allowed to rest on the quartz frit. The ratio of the mass of catalyst to the mass of α-Al_2O_3 chips were kept constant at 1:10 and the same size fraction of alumina and catalyst particles were used to make up the bed. The reactor was lightly tapped on its sides to ensure a homogeneous bed depth. The alumina balls (average d_p = 1.5 mm) were then loaded on top of the catalyst bed and the height of the bed and the preheat section measured. The viton o-ring was fitted to the quartz reactor which was then slid into the stainless steel sheath. After screwing down the steel plunger onto the o-ring to ensure it was squeezed tight against the quartz and the steel to form a good seal, the steel seal was inserted and the top of the steel sheath bolted down.

2.3.2. Reduction and catalyst pretreatment

After sealing the stainless steel reactor, the valve in the helium line was opened and the helium mass flow controller adjusted to a flow of about 150 cm^3/min (STP). With helium passing through the catalyst bed at atmospheric pressure, the reactor was heated to 400°C. As soon as the temperature was stable at 400°C, the valve in the hydrogen line was opened and the mass flow controller adjusted to a hydrogen flow of 20 cm^3/min. The reactor was kept under a He/H_2 atmosphere for one hour at 400°C after which the hydrogen valve was closed and the reactor heated to the required reaction temperature in a helium stream with a flow rate of 180 cm^3/min. About ten minutes prior to the introduction of the reactants, helium flow was increased to the level that would be required during reaction (about 900 cm^3/min) and the reactor pressure increased to 100 kPa gauge pressure. As soon as a stable reactor pressure and catalyst bed inlet temperature was obtained, the reactor was bypassed and the reactant flow rates adjusted to the required levels while maintaining the

reactor under a helium atmosphere of 100 kPa gauge pressure at the reaction temperature.

2.3.3. Startup

After allowing the inlet stream to stabilize for at least five minutes, the reactor bypass was closed, thus replacing the helium in the reactor with the premixed stream of reactants. Upon introducing the reactants to the reactor, the pressure fluctuation was always less than 5 kPa. The bed inlet temperature as well as the time at which the reactants were introduced to the reduced catalyst were noted. The furnace temperature was adjusted from time to time to ensure that the bed inlet temperature remained constant. For most experiments, the axial bed temperature profile was determined within ten minutes of introducing the reactants and for some experiments the temperature profile was determined a number of times during the experiment. The first outlet gas sample was analyzed three to five minutes after introducing the reactants.

2.3.4. Blank experiments

The reactor was loaded with preheat material and catalyst bed diluent, both consisting of α-Al_2O_3. The reactor was then heated stepwise from room temperature to 700°C and the X_{CH4} and product selectivities calculated from the gas analysis at the reactor outlet.

2.3.5. Data evaluation

The procedure is outlined to convert GC analysis data to outlet partial pressures, conversions, product yield, and elemental balances. The assumptions that were made are explained as far as possible.

2.3.5.1. Calculation of the inlet partial pressure

The molar flow rates of all species at the inlet were calculated from calibration constants of the mass flow controllers (see Table 2-1). The oxygen/nitrogen mixture contained 9.27 mol% O_2. The O_2 content was determined by injecting a number of pulses of the mixture into the GC column and calculating the area ratio of O_2 to N_2. The O_2 response factor was known from previous calibration results using pure oxygen and therefore a value for the oxygen content could be guessed and then tested using the known response factor. An iterative procedure was followed until convergence was reached. The molar flow rates of all the species were converted to mole fractions and using the measured absolute reactor pressure, to species partial pressures.

2.3.5.2. Calculation of the product composition

The amount of each product and residual reactants were determined from GC analysis of the reactor outlet. The integrated peak areas were converted to molar flows by applying the definition of the relative response factor and the molar flow rate of nitrogen. The relative response factors (as defined in appendix B.5) of CH_4, O_2, CO, CO_2 and H_2 were evaluated from independent experiments and the values are included in Table 2-3.

Table 2-3 Relative response factors of the analyzed species

Compound	Relative Response Factor
N_2	1.00000
CH_4	1.30573
O_2	0.96031
CO	1.10855
H_2	0.01618
CO_2	2.10873
H_2O	n.a.

All the carbon-containing products (CH_4, CO and CO_2) are directly measured by the GC, which enables one to calculate the carbon balance:

$$C_{Balance} = \frac{F^{OUT}_{CO} + F^{OUT}_{CO_2} + F^{OUT}_{CH_4}}{F^{IN}_{CO} + F^{IN}_{CO_2} + F^{IN}_{CH_4}} * 100 \qquad (2\text{-}2)$$

2.3.5.3. Determination of the water content

Since water was not directly quantifiable due to excessive tailing on the GC column, the water content at the reactor outlet had to be calculated.

The three possible methods to do this are given in Table 2-4. The first method involves the use of the measured hydrogen (H_2) and the assumption that all the oxygen atoms that were not included in the measured carbon oxides and unreacted oxygen was contained in water ($O_{Bal} = 100\%$).

Table 2-4 Possible pathways for determining mass balances and the water partial pressure

Species / Action	Method of determination		
CH_4, CO, CO_2, O_2	Measured	Measured	Measured
H_2	Measured	Measured	Calculated
H_2O	Calculated	Calculated	Calculated
Assumption	O_{Bal} = 100%	H_{Bal} = 100%	O_{Bal} and H_{Bal} = 100%
Parameters evaluated	C and H Balance	C and O Balance	C Balance only

Using the first assumption, it follows that:

$$F^{OUT}_{H_2O} = 2 * (F^{IN}_{O_2} + F^{IN}_{CO_2}) + F^{IN}_{H_2O} + F^{IN}_{CO}$$
$$- 2 * (F^{OUT}_{O_2} + F^{OUT}_{CO_2}) - F^{OUT}_{CO} \qquad (2\text{-}3)$$

This value of the water flow rate can be used to evaluate the hydrogen balance since all the other hydrogen-containing products were directly measured by the GC:

$$H_{Balance} = \frac{4 * F^{OUT}_{CH_4} + 2 * (F^{OUT}_{H_2} + F^{OUT}_{H_2O})}{4 * F^{IN}_{CH_4} + 2 * (F^{IN}_{H_2O} + F^{IN}_{H_2})} * 100 \qquad (2\text{-}4)$$

In the second method one could use the measured hydrogen flow rate and the amount of unreacted methane to calculate the water content at the outlet from a hydrogen balance:

$$F^{OUT}_{H_2O} = 2 * F^{IN}_{CH_4} + F^{IN}_{H_2O} + F^{IN}_{H_2}$$
$$- 2 * F^{OUT}_{CH_4} - F^{OUT}_{H_2} \qquad (2\text{-}5)$$

These values enables one to evaluate the oxygen balance

88

$$O_{Balance} = \frac{2 * F^{OUT}_{CO_2} + F^{OUT}_{H_2O} + F^{OUT}_{CO} + 2 * F^{OUT}_{O_2}}{2 * F^{IN}_{CO_2} + F^{IN}_{H_2O} + F^{IN}_{CO} + 2 * F^{IN}_{O_2}} * 100 \qquad (2\text{-}6)$$

Since the hydrogen measurement by TCD was not always reliable due to signal inversion at high hydrogen concentration, a third alternative would be to first calculate the molar flow rate of water and hydrogen by assuming a 100 % oxygen balance to determine the water flow rate and then calculate the hydrogen by assuming that the remaining hydrogen atoms are contained in H_2. This approach does not enable one to assess either the oxygen or hydrogen balance since both are assumed to be 100 % and thus it was not used in this work.

2.4. Experiment design

A number of experiments were conducted to probe the region of operating conditions within which isothermal operation of the packed-bed reactor would be allowed. These operating conditions were then applied to a number of experiments to test for the presence of film diffusion and internal diffusion. The results from these experiments were in turn used to establish operating conditions for kinetic experiments, ie. the absence of transport phenomena.

2.4.1. Initial isothermal experiments
2.4.1.1. Isothermicity of the catalyst bed

The first experiments in this set were designed to test the level of isothermicity that could be attained in the reactor. In order to quantify the effect of reactant partial pressure on the axial bed temperature profile, the reactant partial pressure ($P^\circ_{CH4} + P^\circ_{O2}$) was varied between 3 kPa and 73 kPa (absolute pressure). The helium flow rate was adjusted to maintain a constant total flow rate and reactor pressure. The temperature profile was measured at six settings of the reactant partial pressure (see Figure 2-6). The y-axis represents the difference between the temperature profile under reaction conditions and the

temperature profile with only helium flowing through the reactor. With a reactant partial pressure of 73 kPa, the maximum temperature difference between the active catalyst bed and the catalyst bed with a feed of pure helium was more than 180°C. The maximum temperature difference always occurred at, or close to, the bed inlet. It was, however, not only inside the catalyst bed that the temperatures recorded earlier during the blank run were exceeded in the presence of reactants. The temperature "peak" extended upstream of the bed inlet.
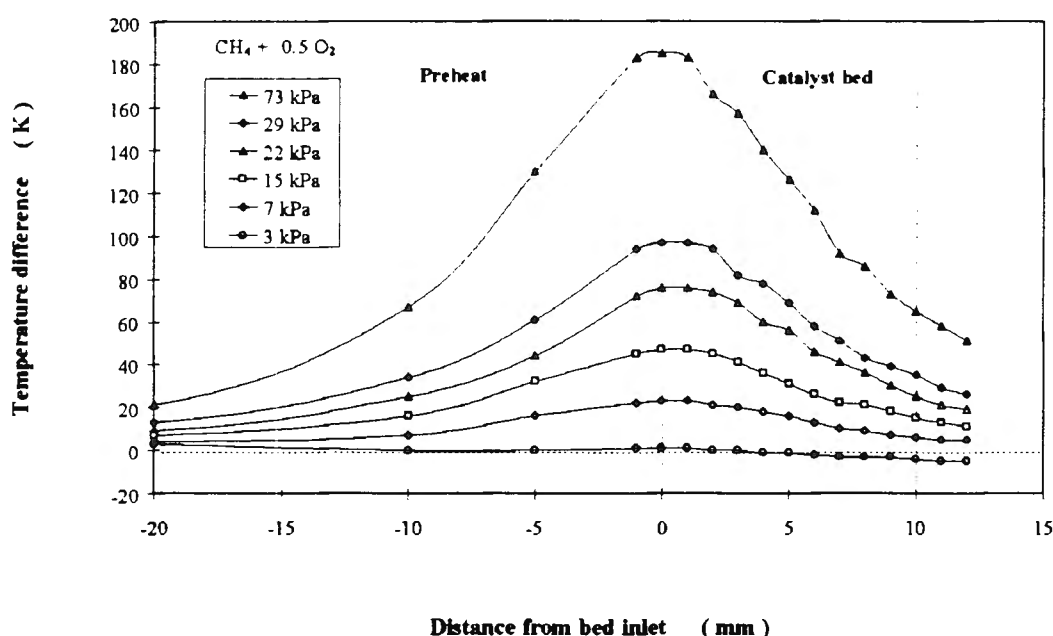
Figure 2-6 The effect of reactant $(CH_4 + \frac{1}{2}O_2)$ partial pressure on axial temperature profile $(V^{\circ}_T = 600 \text{ cm}^3/\text{min}, P_T = 145 \text{ kPa}, CH_4/O_2 = 2)$

In order to probe the possibility that the peak upstream of the catalyst bed was caused by radiative heating of the incoming gas by hot catalyst particles, an experiment was conducted in which helium was substituted by nitrogen as carrier gas. The magnitude of the peak maximum was reduced and the peak was moved slightly deeper into the catalyst bed (see Figure 2-7).

The nitrogen experiment was performed with a catalyst that had been used in prior runs and had therefore been slightly deactivated. The difference in methane conversion between the two experiments $(X_{CH4} = 0.52$ and 0.327 for He and N_2 respectively) testify to this.
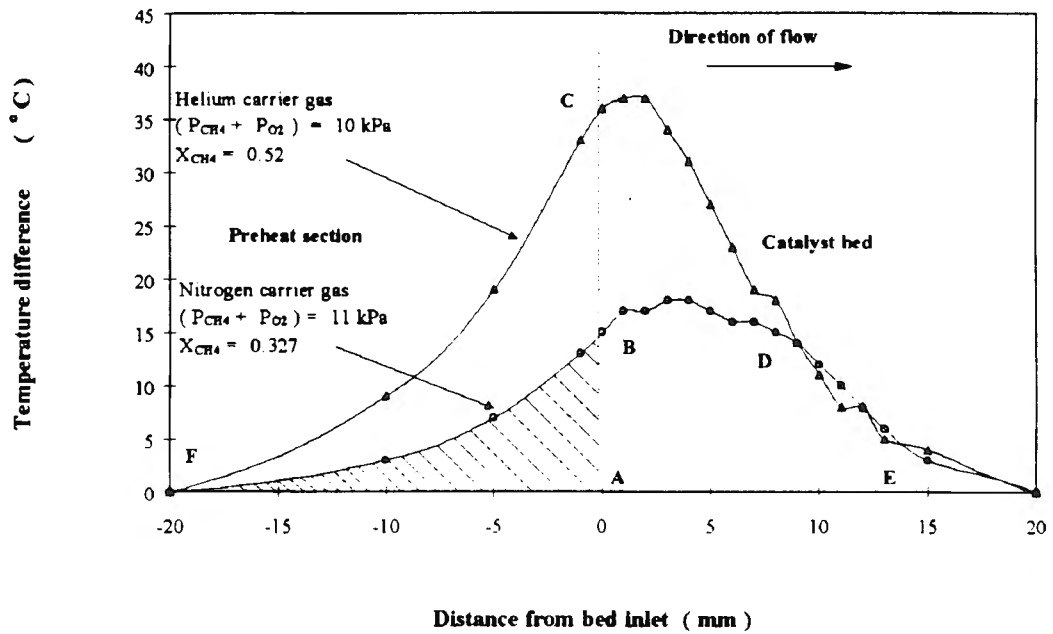
Figure 2-7 Difference between catalyst bed temperature profiles using helium and nitrogen as carrier gas (Setpoint = 625°C, $V°_T$ = 1200 cm³/min, P_T = 150 kPa)

Because of its superior **thermal conductivity** (κ_{He} = 0.25 W m⁻¹ K⁻¹ and κ_{N2} = 0.04 W m⁻¹ K⁻¹ at 600K - see Table 3-309 in ref. 157), helium is more frequently used than nitrogen as carrier gas in catalytic experiments when isothermal behaviour is desired. Because of the decrease in the ability of a carrier gas with low thermal conductivity to conduct reaction heat out of a reactor, a more exaggerated temperature profile should be expected when helium is replaced with nitrogen. In the experimental data shown in Figure 2-7, however, this was not the case.

If the ratio of the area under the two respective curves is compared to the ratio of methane conversion between the two experiments, the values are virtually the same ($Area^{N2}$ / $Area^{He}$ = 0.5 and X^{N2}_{CH4} / X^{He}_{CH4} = 0.6). Therefore the two curves should describe the same area and therefore virtually coincide - if the methane conversions were the same. Radiative heat transfer is independent of the carrier gas, while convective- and conductive heat transport are not. Hence, the conclusion that the temperature profiles for N_2 and He experiments would be coincident in the case of identical methane conversion, provides strong evidence for the presence of radiative heat transport.

The shaded area upstream of the catalyst bed (ABF in the case of nitrogen and ABCF in the case of helium) is an indication of the extent to which radiative heat transport, particle-to-particle conductive heat transport and backmixing, which are the only heat transport phenomena which can lead to heat transport in a direction opposite to the direction of flow, contribute to the development of the temperature profile upstream of the catalyst bed.

In conclusion it may therefore be stated that the catalyst bed approached isothermal behaviour at a high value of reactant dilution (below 7 mol% in inerts). A consideration of the thermal conductivities of the nitrogen and helium led to the conclusion that radiative heat transport may account for the temperature rise upstream of the catalyst bed inlet. The maximum temperature difference of 180°C that was measured at a reactants partial pressure of 73 kPa in helium (Figure 2-6) was significantly reduced by decreasing the reactant partial pressure. At a reactant partial pressure of 3 kPa, the axial bed temperature profile was virtually flat and the temperature varied by less than 5°C along the length of the bed. Since an isothermal catalyst bed is crucial for kinetic studies, all kinetic experiments in the present work were conducted with a feed that contained less than 3 mol% reactants diluted in helium.

2.4.1.2. Rate of attainment of constant bed inlet temperature

The bed inlet temperature was measured as a function of time after starting an experiment. It was found that the temperature increased from an initial value of 497°C with no flow in the reactor (static helium) to a steady state value of 532°C within three minutes of exposing the catalyst bed to a feed stream containing 7 kPa of methane and oxygen. The attainment of thermal steady state is shown in Figure 2-8.

The CH_4/O_2 ratio was increased from 2 to 4 after the catalyst bed had attained a constant inlet temperature and the corresponding change in bed inlet temperature is also shown above. In spite of the fact that the mass flow controllers took some time to adjust the reactant flows to the new values during the change from $CH_4/O_2 = 2$ to $CH_4/O_2 = 4$, the temperature reached a steady state value at a much faster rate (within less than two minutes after the change) than when the experiment was started with the reactor under static helium.
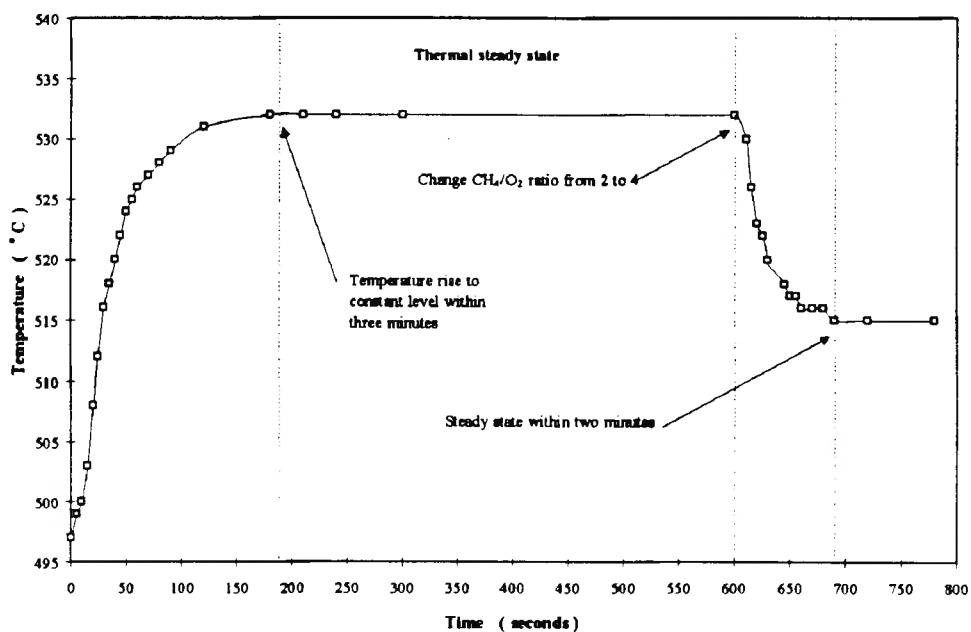
Figure 2-8 The attainment of thermal steady state ($P_{reactants}$ = 7kPa, CH_4/O_2 = 2 and 4, $V°_T$ = 1200 cm³/min and P_T = 145 kPa)

The slow attainment of thermal steady state from start-up (only helium in the reactor) could be ascribed to a number of factors, all of which are speculative until further evidence is forthcoming. Firstly, reconstruction of the catalyst surface into its active state may be slow. Secondly, it is possible that, at the relatively high reactant partial pressures used to generate the data in Figure 2-8, the reaction rate is high enough for transport phenomena to be rate-limiting and that the establishment of steady-state temperatures take longer because of slow heat and mass transfer between the catalyst surface and the bulk gas. Since more reaction heat is evolved per unit volume of the catalyst bed for a feed stream containing 7 kPa of reactants than when a more dilute feed stream is used, the time to reach thermal steady state during kinetic experiments (during which less than 5 kPa of reactants were used) should be even less than three minutes. In all subsequent experiments, the first GC analysis of the product stream was never conducted at a time on-stream that was shorter than three minutes.

2.4.1.3. Film diffusion

The effect of film diffusion on methane conversion was investigated by increasing the linear

flow rate of the feed at a constant contact time in the catalyst bed. This was achieved by increasing the catalyst mass (at constant dilution of 1:10 in alumina) while simultaneously increasing flow rates of all the species proportionally. The experiments were therefore all conducted at constant reactant partial pressure and total reactor pressure. The linear velocity was varied between 1.8 and 8.3 cm/s (based on an empty tube). The results of these experiments are included in chapter 4 and a further discussion follows in chapter 5.

2.4.1.4. Internal diffusion

After studying the effect of film diffusion, the catalyst particle size was varied between the fractions (125-250 μm) and (425-710 μm) while keeping all other variables constant and at the same time ensuring that the linear velocity was in the range where the effect of film diffusion was insignificant. Two sets of experiments were conducted at 600°C and 650°C.

2.4.1.5. Determination of catalyst performance

The catalyst deactivated steadily with time on-stream and steady state was never attained. Furthermore, it was found that the catalyst could not be regenerated. One example of an attempt to regenerate a charge of catalyst used for three hours at 629°C is shown in Figure 2-9. After three hours on-stream, methane flow was stopped and the catalyst allowed to remain at 629°C for thirty minutes under an oxygen atmosphere (P°_{O2} = 1.4 kPa in He) before oxygen flow was also stopped and the catalyst cooled to room temperature in flowing helium. The next day, the experiment was re-started in the normal procedure, ie. the reactor was heated to 400°C and the catalyst then reduced for an hour before heating to 629°C and introducing the reactants. Upon introducing the reactants after the regeneration procedure, the methane conversion did not return to the level that it exhibited with a fresh charge of catalyst, but continued downwards on the same curve as before the regeneration cycle.
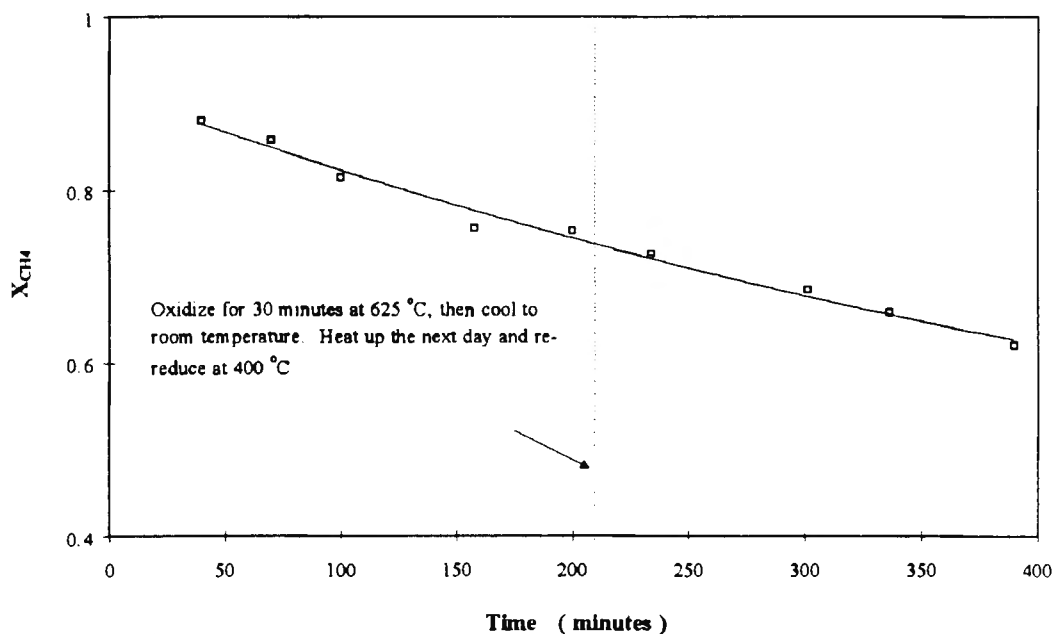
Figure 2-9 Regeneration of a charge of catalyst (T = 629°C, P_T = 201.3 kPa, $P°_i$ in kPa: CH_4 = 2.75, O_2 = 1.38, W = 201 mg)

Neither an oxidizing nor a reducing atmosphere was able to regenerate the catalyst activity. Given the possibility that the oxygen partial pressure could have been too low to ensure efficient carbon burn-off, this hints at the conclusion that neither carbon deposition nor nickel oxidation was responsible for catalyst deactivation.

The deactivation of the catalyst and the fact that steady state was never attained, led to the approach of extrapolating the P_i vs time plots to zero time on-stream in order to calculate the species partial pressures for the kinetic study. An example of this is shown in Figure 2-10. As the catalyst deactivated, the furnace setpoint had to be adjusted slightly to compensate for the loss in catalytic activity and to maintain a constant bed inlet temperature. The magnitude of the change in inlet temperature was therefore not determined at constant furnace temperature, but the difference between the furnace setpoint at the start and at the end of an experiment was never higher than 4°C. Since the kinetic data were determined from best straight-line fits to the first three data points of an experiment, the temperature may be considered as constant. The procedure that was followed to calculate the partial pressure data from the results of gas analyses is outlined in section 2.3.5 and described in detail in appendix B.7.
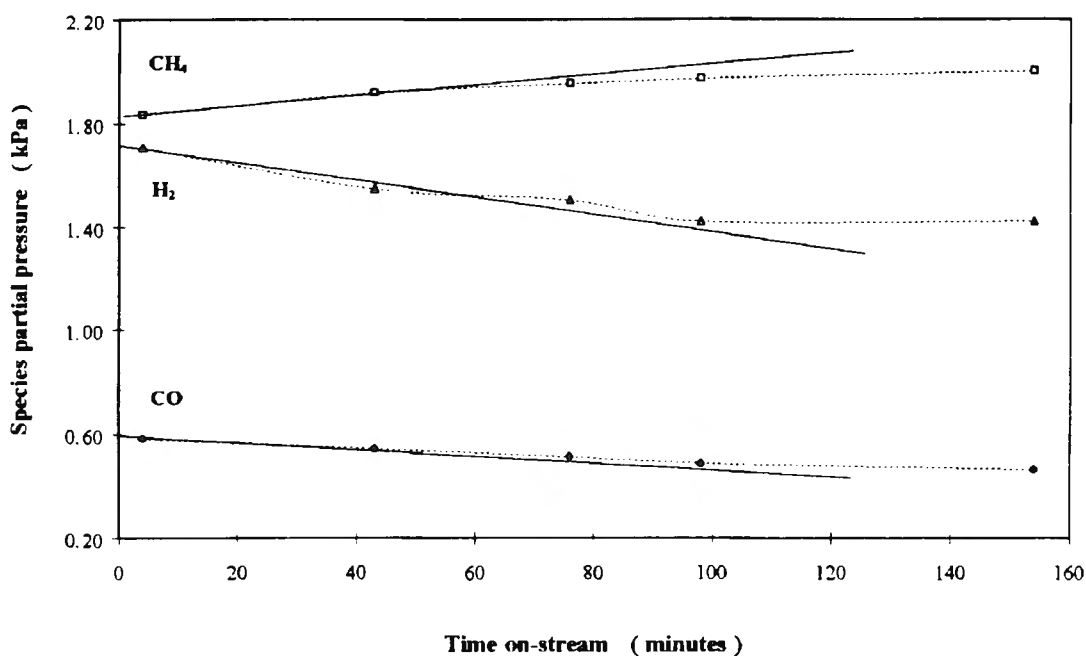
Figure 2-10   Time on-stream behaviour and the extrapolation of species partial pressure to zero time on-stream.

2.4.2. Kinetic study

After establishing that film diffusion as well as internal diffusion was absent in the laboratory reactor, it was decided to conduct a kinetic study of the oxidative reforming of methane. The parameter ranges that were investigated are given in Table 2-5. For each value of partial pressure or temperature, three or more experiments were conducted. Each experiment was conducted with a **fresh catalyst charge**. Since the methane conversion often exceeded 0.25, the reactor was treated as an integral reactor. All experiments were conducted at 100 kPa above atmospheric pressure or 201.3 kPa absolute pressure.

2.4.2.1. The effect of temperature on reaction kinetics

The inlet temperature of the catalyst was varied between 579 and 654°C at 25°C increments and with a constant feed composition. Since the catalyst bed inlet temperature and outlet temperatures differed by up to 6°C in some cases, the bed inlet temperature was used as the temperature datum. The results from these experiments would give an indication

of the temperature dependence of the reaction rate and therefore enable one to calculate the apparent activation energy.

2.4.2.2. Reactant partial pressure

A set of experiments was conducted at constant oxygen partial pressure (P°_{O2} = 1.34 kPa) with the methane partial pressure (P°_{CH4}) being varied. This would enable one to obtain a measure of the dependence of the reaction rate on methane partial pressure. Another set of experiments, designed to test the dependence of the reaction rate on oxygen partial pressure, involved a constant value of P°_{CH4} while varying the value of the oxygen partial pressure. In all cases, the helium flow rate was adjusted to ensure that the overall gas-hourly space velocity and therefore the total contact time, remained constant.

2.4.2.3. Product partial pressure

At constant methane and oxygen inlet partial pressures of, respectively, 2.96 and 1.34 kPa, one of the products was introduced to the reactor feed. As the flow rate of the co-fed product was increased, helium flow rate was decreased to compensate for the change in flow rate, thus ensuring that the total flow rate was constant for all experiments. As indicated in Table 2-5, three values of the inlet partial pressure of each product were studied, with the exception of CO_2 for which four values were studied.

2.4.2.4. Experiment labelling

All the kinetic experiments that were performed as well as the operating conditions (inlet species partial pressure and bed temperature) are listed in Table 2-5. The balance consists of helium and nitrogen which were present as inerts. The catalyst performance of at least three different amounts of catalyst were tested for each combination of P°_i and temperature. A total of 83 experiments were conducted, each with a fresh charge of catalyst.

Table 2-5 Labelling of experiments and reaction conditions

Entity	Label	T (°C)	Inlet species partial pressure (kPa)					
			CH_4	O_2	CO	H_2	CO_2	H_2O
$P°_{O2}$	ppo2_x5	604	2.964	0.991	-	-	-	-
varied	ppo2_x4	604	2.970	1.202	-	-	-	-
	ppo2_x1	604	2.977	1.343	-	-	-	-
	ppo2_x2	604	2.969	1.626	-	-	-	-
$P°_{CH4}$	ppc_x5	604	2.752	1.375	-	-	-	-
varied	ppc_x2	604	3.442	1.375	-	-	-	-
	ppc_x3	604	4.132	1.375	-	-	-	-
	ppc_x4	604	4.816	1.375	-	-	-	-
$P°_{H2}$	pph_x3	604	2.963	1.342	-	1.449	-	-
varied	pph_x4	604	2.963	1.342	-	2.836	-	-
	pph_x5	604	2.963	1.342	-	5.609	-	-
$P°_{CO}$	ppcm_x2	604	2.963	1.343	1.417	-	-	-
varied	ppcm_x3	604	2.963	1.342	2.837	-	-	-
	ppcm_x4	604	2.952	1.338	6.294	-	-	-
$P°_{CO2}$	ppcd_x1	604	2.960	1.341	-	-	0.269	-
varied	ppcd_x2	604	2.955	1.339	-	-	0.551	-
	ppcd_x3	604	2.954	1.338	-	-	1.371	-
	ppcd_x4	604	2.953	1.338	-	-	2.768	-
$P°_{H2O}$	ppw_x1	604	2.954	1.330	-	-	-	1.339
varied	ppw_x2	·604	2.965	1.344	-	-	-	2.678
	ppw_x3	604	2.963	1.343	-	-	-	5.586
Temp	T575_x	579	2.964	1.343	-	-	-	-
varied	ppo_x1	604	2.964	1.343	-	-	-	-
	T625_x	629	2.964	1.343	-	-	-	-
	T650_x	654	2.964	1.343	-	-	-	-

2.5. Characterization techniques and procedures

The unused catalysts were subjected to characterization techniques for the determination of nickel content, BET surface area and exposed nickel surface area (unused but reduced catalyst). The X-ray diffraction pattern was also determined. Due to the small amount of catalyst that was used for each kinetic experiment, it was difficult to perform all these characterization techniques on all the used samples. Where deemed necessary, a number of samples were combined in order to compare its properties with that of the unused catalyst. A more detailed description of the characterization techniques and equipment is included in Appendix D.

2.5.1. BET surface area and Hydrogen chemisorption

BET surface area analysis was performed using a standard N_2 adsorption in a Micrometrics apparatus (ASAP 2000) equipped with two Edwards vacuum pumps (E2M-0.7).

Chemisorption was done in the same apparatus according to the procedure described next. The powdered sample was heated to 100 °C in flowing nitrogen to remove adsorbed water.
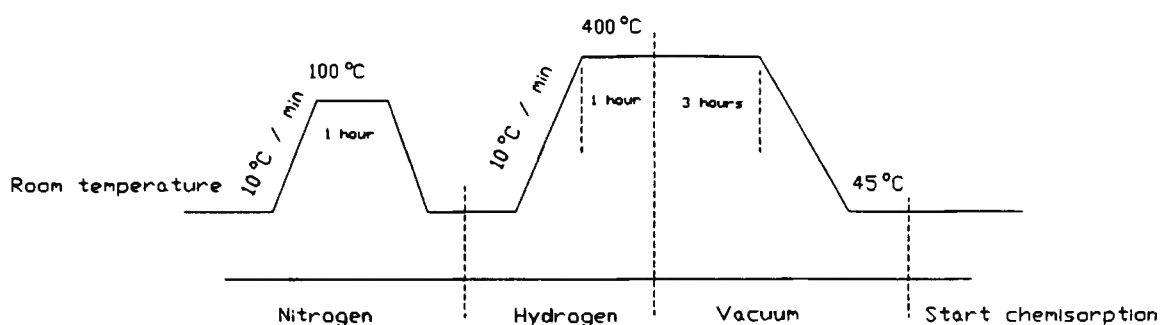
Figure 2-11 Temperature program for chemisorption

Flow was then switched to hydrogen and the temperature increased to 400°C at 10°C/min. The temperature was maintained at 400 °C for one hour, after which the hydrogen flow was stopped and the sample chamber evacuated to 5 μmHg for **three hours**. The temperature

was then lowered overnight to 45 °C at which chemisorption was performed. The temperature profile of the procedure as well as the chamber contents at each temperature is shown in Figure 2-11. Further details of the experimental procedure are given in Appendix D.1 and the BET catalyst surface area as well as the results from chemisorption experiments are contained in Table 3-1.

2.5.2. The use of X-ray diffraction for probing solid state phase changes

XRD spectra were collected on a Philips X-ray diffraction apparatus fitted with a Cu tube (K_α radiation with $\lambda = 1.542$ Å) and an automatic divergence slit (PW 1386/55). The X-ray generator (PW 1130/90/96) was operated with 40kV potential and a 25mA current and was controlled by an automatic unit (PW 1390). The detector was a PW 1050/70 goniometer and data logging was done on a personal computer. Powdered samples were placed in an aluminium sample cup and the scanning angle was increased at a rate of $0.05°.min^{-1}$ from a starting angle of 10° 2θ to the final value of 90° 2θ.

The mean nickel crystallite diameter was calculated by the Scherrer equation [158]:

$$d = \frac{K \lambda}{B_d \cos \theta_o} \tag{2-7}$$

where K is the Scherrer constant, θ_o the Bragg angle, λ the X-ray wavelength and B_d determined by

$$B^2_d = B^2_{obs} - B^2_{inst} \tag{2-8}$$

with B_{obs} the measured line width and B_{inst} the instrumental line width. The Scherrer constant (K) was assigned a value of 0.9 because the line width was measured at half the maximum peak height. The peak corresponding to the Ni(hkl) plane was selected because it was well separated from any of the alumina peaks.

2.5.3. Thermogravimetric analysis for carbon analysis and Ni oxidation

Thermogravimetric experiments were performed in a Stanton Redcroft STA-780 apparatus. A personal computer (PC) was used as the data logging device. The PC also controlled the mass flow controllers and electrically-activated valves.

The sample to be tested was weighed off (about 25mg) and placed in a platinum crucible. The reference cup (also a Pt crucible) contained 25mg of α-Al_2O_3. After stabilizing the balance, it was zeroed and air was introduced to the reaction chamber at 30 cm^3/min. The sample was heated in the air stream at 50°C for one hour to remove adsorbed moisture from the catalyst and the weight loss was noted.

After re-zeroing the balance, the flow was adjusted to 27 cm^3/min of nitrogen and 3 cm^3/min of air. With this feed stream ($P°_{o2} \approx 3$ kPa), the temperature of the reaction vessel was increased to 600°C at a rate of 1°C/min while logging the change in mass of the sample onto a floppy disk. After the designated run time had elapsed (normally 950 minutes), the sample was cooled down to room temperature in the air/nitrogen mixture.

2.5.4. Changes in catalyst morphology probed by scanning electron microscopy (SEM)

A Cambridge Instruments microscope with a 40 kV electron beam was used to obtain surface images of the catalyst. For normal SEM operating mode, the samples were dusted onto an aluminium stub and covered with a thin layer of gold.

2.5.5. Transmission electron microscopy (TEM)

A JEOL (JEM-200CX) instrument was used that allowed one to work with a 80 kV to 200 kV electron beam. The catalyst samples were crushed in an agate mortar and pestle, dried in acetone and then embedded in a clear resin. Thin slices were prepared which were supported on copper grids for TEM analysis. Contact prints were made of the resulting

TEM plates which allowed one to calculate the actual particle size of an object directly from the size on the photographic print.

2.5.6. Determination of the catalyst nickel content by atomic absorption (AA)

Atomic absorption was used to determine the nickel content of unused catalysts. A Varian SpectrAA-30 atomic absorption spectrophotometer was used with an oxidizing acetylene-air flame. The catalyst particles were dissolved by a standard solid-state fusion procedure.

Chapter 3

3. RESULTS

Nature abhors the straight line (R. Ross, 1914)

The results from the integral kinetic experiments as well as the findings from characterization studies of the fresh catalyst are presented and discussed at some length in the present chapter. Also included in this chapter is the description of a number of curve-fitting techniques that were used to calculate (differential) reaction rates from integral kinetic data. A model data set was chosen to demonstrate the application of the selected techniques. The applicability of the various curve-fitting techniques were evaluated with reference to the model data set.

3.1. Properties of the unused catalyst

The catalyst was received without any information regarding its physicochemical properties. It was therefore decided to subject the unused catalyst to a number of characterization procedures. Some properties of the unused catalyst thus obtained are summarized in Table 3-1. Nitrogen physisorption was used to probe the pore structure at low pore diameters while mercury porosimetry was used to study the wider pores of the catalyst. The results from the two studies were combined to calculate the overall surface area (7.8 m^{-2} g^{-1}) and pore volume. The high surface area of 7.8 m^{-2} g^{-1} may perhaps be attributed to high surface area NiO since the catalyst was not pre-reduced prior to nitrogen adsorption. A pore diameter of 1000 Å was used as the cut-off point below which the results of nitrogen adsorption and above which the results of mercury porosimetry was used. The incremental pore volume and cumulative surface area (A) are shown in Figure 3-1. The transition between the surface area results from Hg penetration and N_2 adsorption is quite smooth and it was therefore decided to combine the results of the two experiments in order to calculate

the total surface area and the total pore volume of the catalyst. In the case of Hg penetration, the surface area was determined by assuming cylindrical pores.

Table 3-1 Properties of the unused catalyst (G-90B)

Property	Value	Units
Nickel loading[a]	10.6	wt %
BET surface area[e] $(19\text{Å} < d_p < 975\text{Å})$	4.9	$m^2\ g^{-1}$
"Hg" surface area[b] $(1079\text{Å} < d_p < 2.1\ \mu m)$	2.9	$m^2\ g^{-1}$
Total surface area (BET + "Hg")	7.8	$m^2\ g^{-1}$
Porosity[b]	54	%
Average pore diameter $(4V/A)$[g]	152	nm
Pore volume[e] $(19\text{Å} < d_{pore} < 975\text{Å})$	0.014	$cm^3\ g^{-1}$
"Hg" pore volume[b] $(1079\text{Å} < d_p < 2.1\ \mu m)$	0.282	$cm^3\ g^{-1}$
Metal surface area[f]	1.02	$m^2\ g^{-1}$
Dispersion[f]	1.5	%
Average nickel particle size[f]	69	nm
Average nickel particle size[c]	25?	nm
Solid density[d]	4.6	$g\ cm^{-3}$
Particle density[b]	1.8	$g\ cm^{-3}$

a Determined by atomic absorption spectrometry
b Determined by mercury porosimetry - catalyst unreduced
c Determined by X-ray line broadening of the Ni(111) peak
d Determined by helium pycnometry
e Determined from nitrogen adsorption (BET plot) - catalyst unreduced
f Calculated from hydrogen chemisorption results on a pre-reduced catalyst
g Combined pore volume and surface area values from Hg penetration and N_2 adsorption were used

The results from Figure 3-1 suggests that most of the pore volume resides (V) in the wider pores of the catalyst $(d_p > 1000\ \text{Å})$ and that the surface area is spread between the two regions with about 60% of the surface area in the micropore region $(d_p < 1000\ \text{Å})$. The metal surface area and dispersion was determined by means of hydrogen chemisorption and the nickel loading of the catalyst was measured by atomic adsorption spectrophotometry. The nickel particle size was determined by both applying the Scherrer equation to the measured X-ray diffraction line broadening and by calculating the number of exposed nickel atoms from the hydrogen chemisorption results.
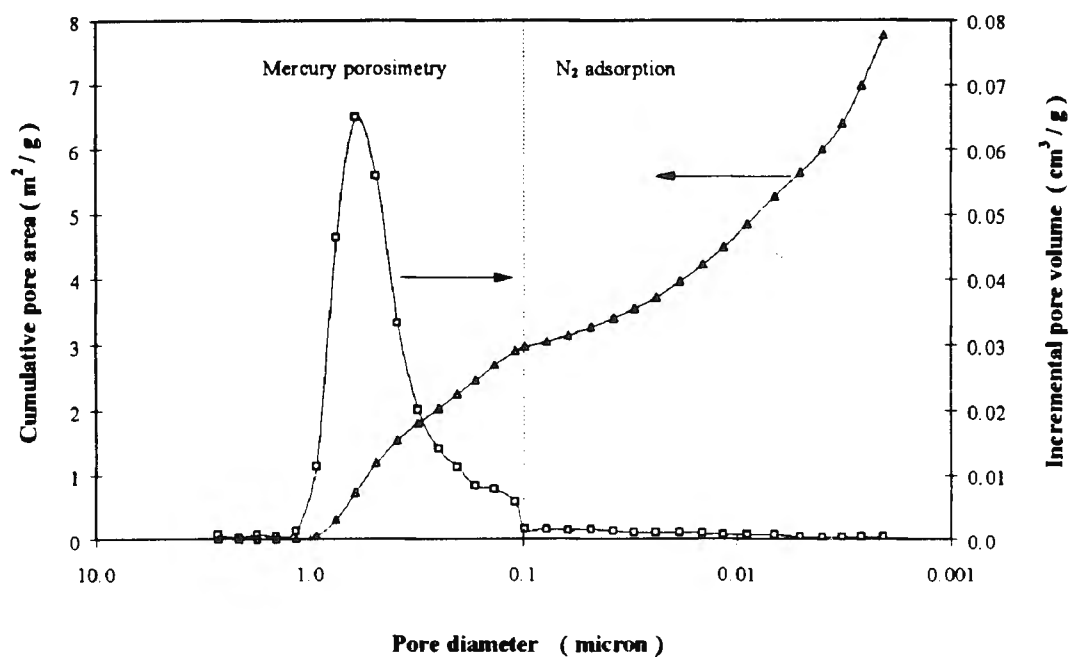
Figure 3-1 Pore volume distribution and cumulative surface area of the unused, unreduced G-90B catalyst

The above results indicate, as expected, that the G-90B catalyst consists of fairly large nickel particles supported on a low surface-area alumina body.

3.2. Preliminary catalytic testing

The present section is divided into two parts. The results of initial system checks to ensure the reproducibility of results, isothermicity of the catalyst bed and inertness of the preheating section and of the material used to dilute the catalyst bed are presented first. These results are followed by the results of a series of experiments which were conducted to check for the absence of external and internal transport phenomena.

3.2.1. Reproducibility of results

In order to determine the reproducibility of the complete procedure for catalytic testing, a number of runs were repeated, each time with a fresh charge of catalyst, under identical

operating conditions. These experiments were performed over a period of several weeks and the results are tabulated in Table 3-2. Because of its importance in the kinetic study, methane conversion (X_{CH4}) was the most significant measure of reproducibility in the above table. The average methane conversion ($X_{CH4,M}$) and the standard deviation (S_y defined in equation (3-1)) was calculated for each catalyst mass.

Table 3-2 Reproducibility of the catalytic testing procedure ($P°_{CH4}$ = 2.96 kPa, $P°_{O2}$ = 1.34 kPa, P_T = 201.33 kPa, Inlet T = 604°C)

Run	$W/F°_{CH4}$ [a]	W [b]	X_{CH4}	X_{O2}	S_{CO}	S_{H2}	S_{CO2}	S_{H2O}
	g.s.mol^{-1}	mg			mol %			
ppo2_71	1347.34	15.4	0.176	0.459	25.8	47.9	74.2	52.1
ppcm_60	2201.54	25.0	0.229	0.610	42.6	57.6	57.4	42.4
ppcd_10	4394.27	49.9	0.469	0.924	53.7	73.1	46.3	26.9
ppo2_01	6604.61	75.0	0.579	1.000	69.9	84.8	30.1	15.2
pph_70	1356.15	15.3	0.158	0.513	25.4	47.8	74.6	52.2
ppo2_61	2201.54	25.0	0.238	0.584	38.4	53.4	61.6	46.6
ppo2_11	4455.91	50.6	0.448	0.910	56.0	74.8	44.0	25.2
ppcd_00	6604.61	75.0	0.627	0.997	71.6	89.4	28.4	10.6

a   Methane flow rate was maintained constant at 1.136E-5 mol.s^{-1} for all experiments.
b   Mass of catalyst used. The catalyst was diluted 1:10 in α-Al$_2$O$_3$.

$$S_y = \sqrt{\frac{\sum_{i=1}^{n}(X_{CH4,i} - X_{CH4,M})^2}{n - 1}}$$

(3-1)

The coefficient of variation (c.v.) was defined as c.v. = $S_y/X_{CH4.M}$. The results of the calculations shown in Table 3-3 indicate that the coefficient of variation of the methane conversion varied between 2.5 and 7.5% with an average value of 4.8% which is very close to the error of the gas analysis. The implications of the error in the measured methane conversion on the calculation of the reaction rate will be discussed later.

Table 3-3 Standard deviation and coefficient of variation with respect to X_{CH4} (The conditions are the same as Table 3-3)

W (mg)	$X_{CH4,M}$ [a]	S_y [b]	c.v.[c] (%)
15.4	0.167	0.486	7.6
25.0	0.234	0.597	2.7
50.3	0.459	0.917	3.2
75.0	0.603	0.999	5.6

a   Mean value of methane conversion
b   Standard deviation
c   Coefficient of variation

3.2.2. Inertness of the reactor and packing material

A catalyst bed which consisted of preheating material and bed diluent only was tested for catalytic activity at a number of temperatures.
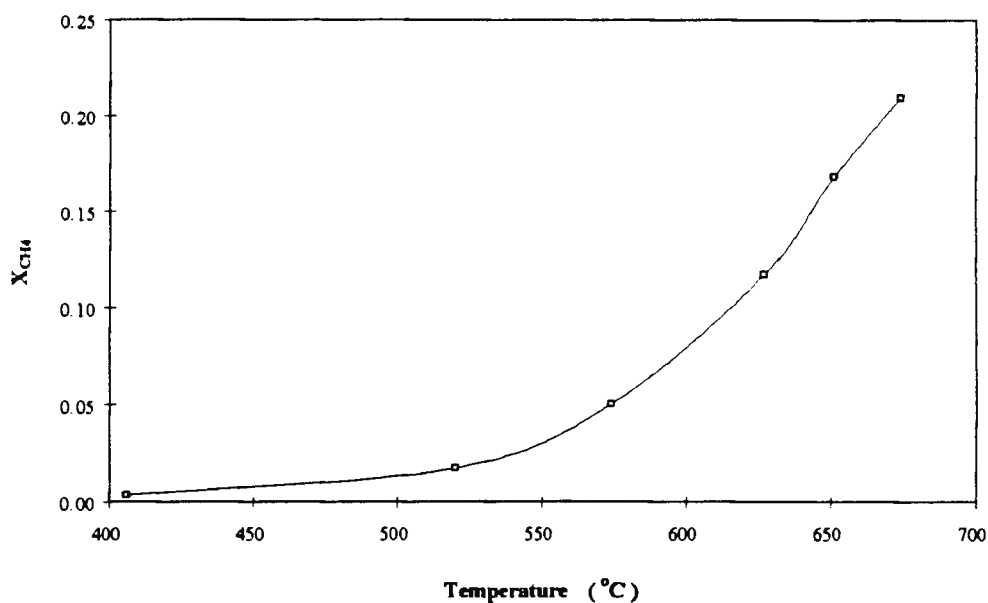
Figure 3-2 Activity of α-Al$_2$O$_3$ (P°_{CH4} = 2.93 kPa, P°_{O2} = 1.33 kPa, P_T = 201.33 kPa, W = 14.61 g, W/F°_{CH4} = 1.286E6 g.s.mol^{-1})

The resulting methane conversion is shown in Figure 3-2. Clearly the preheat section and catalyst bed diluent exhibited some activity for methane oxidation with X_{CH4} = 0.21 at 675°C. Carbon dioxide was the only carbon-containing product in detectable quantities at

temperatures below 650°C, but carbon monoxide was detected in trace quantities above 650°C. In spite of the high conversion resulting from the alumina packing material, the rate of methane consumption (r_{CH4}) on α-Al_2O_3 was, however, significantly lower than the rate that was measured later on either the unreduced or the pre-reduced steam reforming catalyst. This is indicated in Figure 3-3 which contains a comparison between the initial rate of methane consumption on the pre-reduced catalyst (G-90B), unreduced catalyst (G-90B) and α-Al_2O_3.
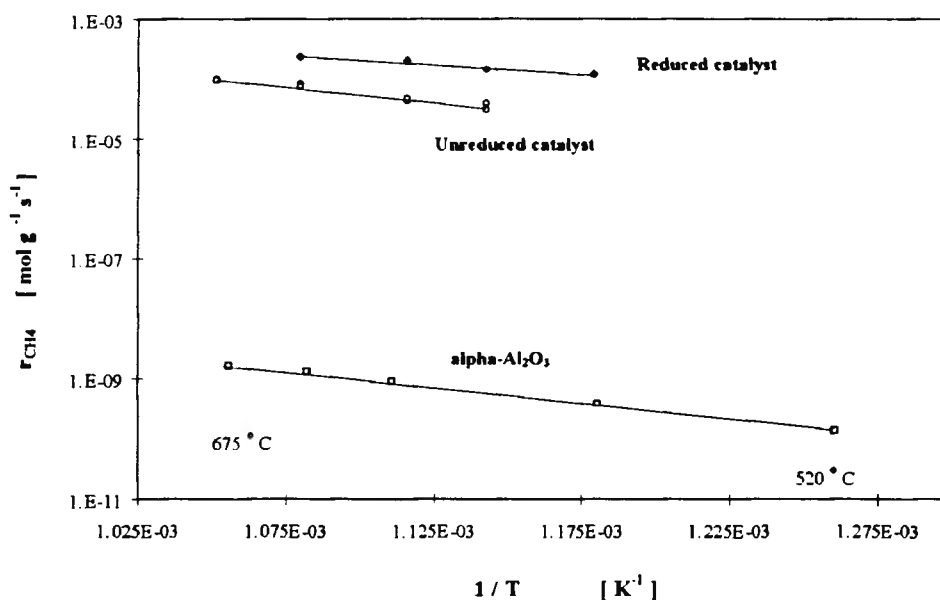
Figure 3-3 Comparison of the rate of methane consumption on various forms of the catalyst

In the case of reaction over α-Al_2O_3, the low conversion ($X_{CH4} < 0.25$) allowed the rate of methane consumption to be calculated from the following expression:

$$r_{CH_4} = X_{CH_4} \cdot \frac{F^o_{CH_4}}{W} \tag{3-2}$$

The measured reaction rate was plotted as a function of the inverse temperature (in units of K^{-1}) and the slope of the best linear fit to the data enabled one to calculate an apparent activation energy of 102 kJ mol^{-1}. The arrhenius-type plot of the rate data which was calculated from equation (3-2) is shown in Figure 3-4.
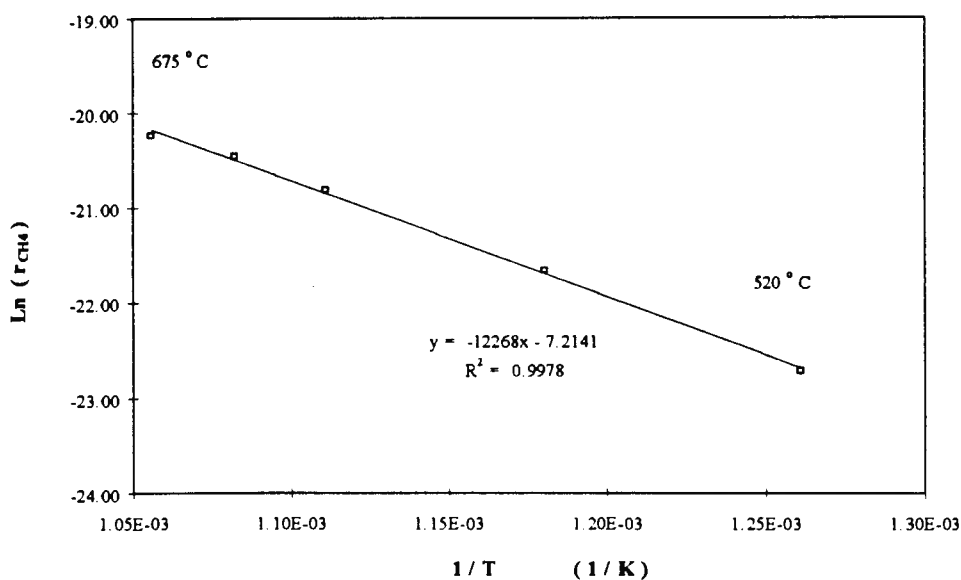
Figure 3-4 Arrhenius-type plots of methane oxidation on α-Al$_2$O$_3$ diluent material (Conditions the same as in Figure 3-3)

3.2.3. Performance of the unreduced catalyst

A catalyst charge of 0.11g and 1.64g of α-Al$_2$O$_3$ diluent was placed in the reactor and the temperature raised from 600°C to 675°C at 100 kPa(g).
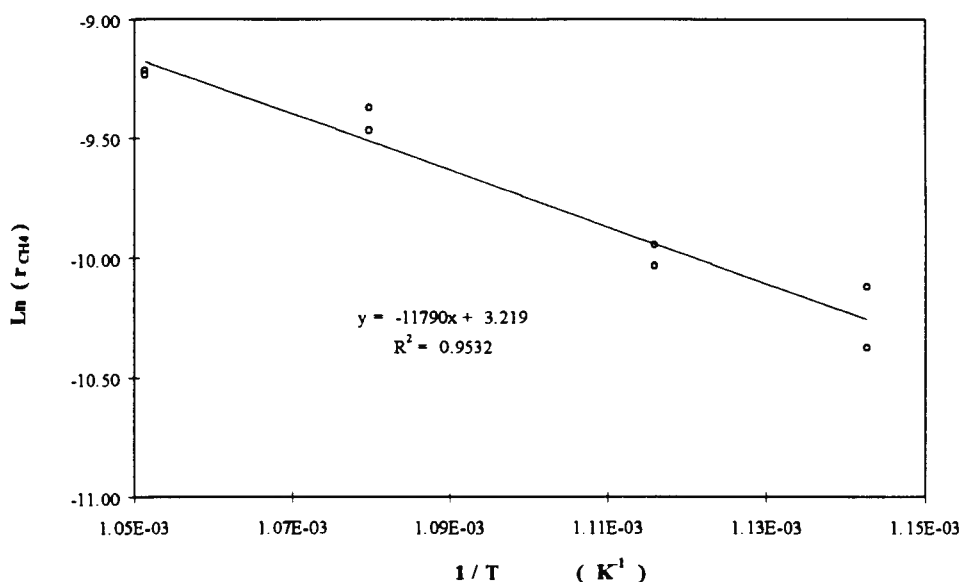
Figure 3-5 Arrhenius-type plot of methane oxidation on the unreduced catalyst (G-90B) (Conditions the same as in Table 3-2)

A feed stream containing 6.67 kPa methane and 3.33 kPa oxygen was passed over the

catalyst and the conversion of the reactants measured. The pseudo-arrhenius plot of the rate data obtained from the methane conversion is shown in Figure 3-5. Although the rate of methane conversion was much higher for the unreduced catalyst than for the α-Al_2O_3, the activation energy for the unreduced catalyst (98.0 kJ mol^{-1}) was only marginally lower than that of the α-Al_2O_3 (102.0 kJ mol^{-1}).

3.2.4. Activation energy of the pre-reduced catalyst

The pre-reduced catalyst exhibited a much lower apparent activation energy than either the unreduced catalyst or the α-Al_2O_3 (see Figure 3-6).
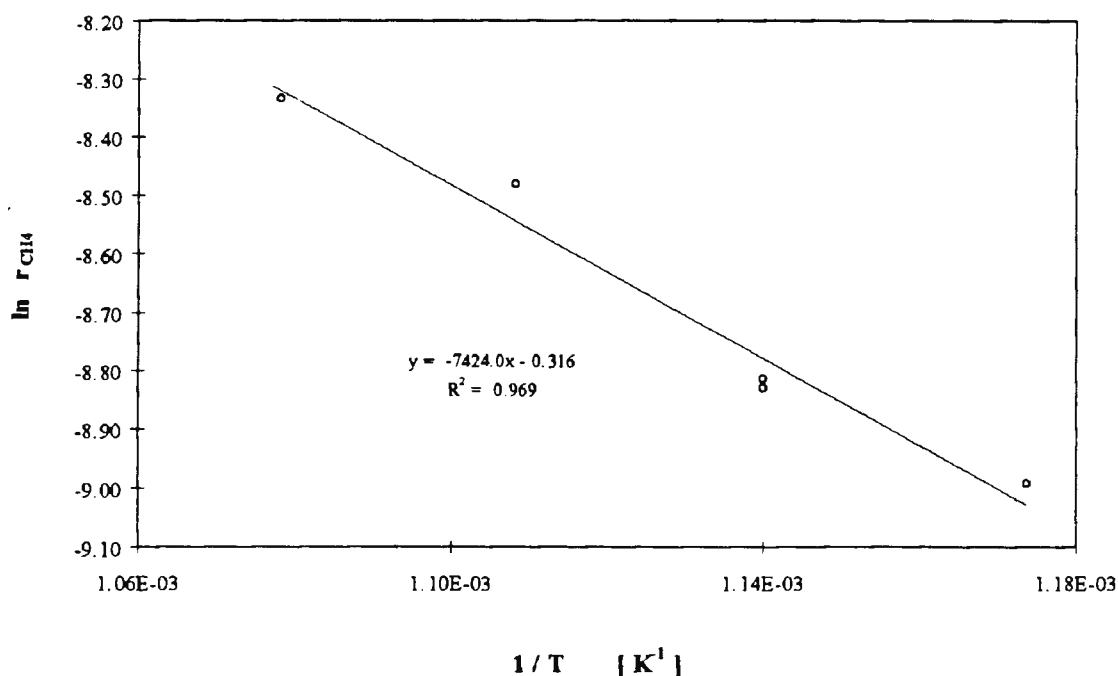
Figure 3-6 Arrhenius-type plot of methane oxidation on the pre-reduced catalyst (G-90B) - slope of an exponential curve fit to $W/F°_{CH_4}$ vs. X_{CH_4} data

As discussed in more detail later (section 3.3.6.1.b), the apparent activation energy of the pre-reduced catalyst was found to lie between 60 kJ mol^{-1} and 70 kJ mol^{-1} which is much lower than the values of about 100 kJ mol^{-1} for the unreduced catalyst and α-Al_2O_3. Not only was the apparent activation energy lower over the pre-reduced catalyst, but the rate of

methane consumption was also higher than over the unreduced catalyst (see Figure 3-3).

3.2.5. Heat and mass transport

The effect of transport phenomena were studied at conditions which ensured an isothermal catalyst bed. The feed that was used in all tests for transport phenomena contained 2% reactants (methane and oxygen) in a mixture of helium and nitrogen. The catalyst bed consisted of a mixture of 10 wt% catalyst particles and 90 wt% α-Al_2O_3 chips which had previously been fired in air at 1000°C. Plug flow behaviour of the feed at the entrance to the catalyst bed was ensured by packing a long bed of α-Al_2O_3 balls (d_p = 1.5mm) directly upstream of the catalyst bed. The L/d_p ratio of this bed was 113. Therefore the condition that L/d_p > 30 to ensure plug flow behaviour is satisfied [159].

3.2.5.1. Film diffusion experiments

The extent of the influence of film diffusion on the measured methane conversion was investigated by measuring X_{CH4} as a function of the linear velocity (based on an empty tube). All of these experiments were conducted at constant residence time in the catalyst bed ($W/F°_{CH4}$ = 1.9 E4 g.s.mol^{-1}). The linear velocity was changed by increasing the volumetric flow rate (at constant gas composition and total pressure) while at the same time increasing the bed depth. The only manipulated variable was the turbulence around the catalyst particles and therefore the thickness of the boundary layer which in turn affects the mass transfer coefficient. The results of these experiments are shown in Figure 3-7. The indicated error bars are for 2% of the measured values of X_{CH4} and the horizontal line was drawn arbitrarily. The fact that the line intersects the 2% error bars of all the data points shows that methane conversion is independent of linear velocities higher than 3 cm.s^{-1} with a certainty of 98%. Therefore it may be concluded that the rate of methane consumption is independent of film diffusion at linear velocities higher than 3 cm/s.
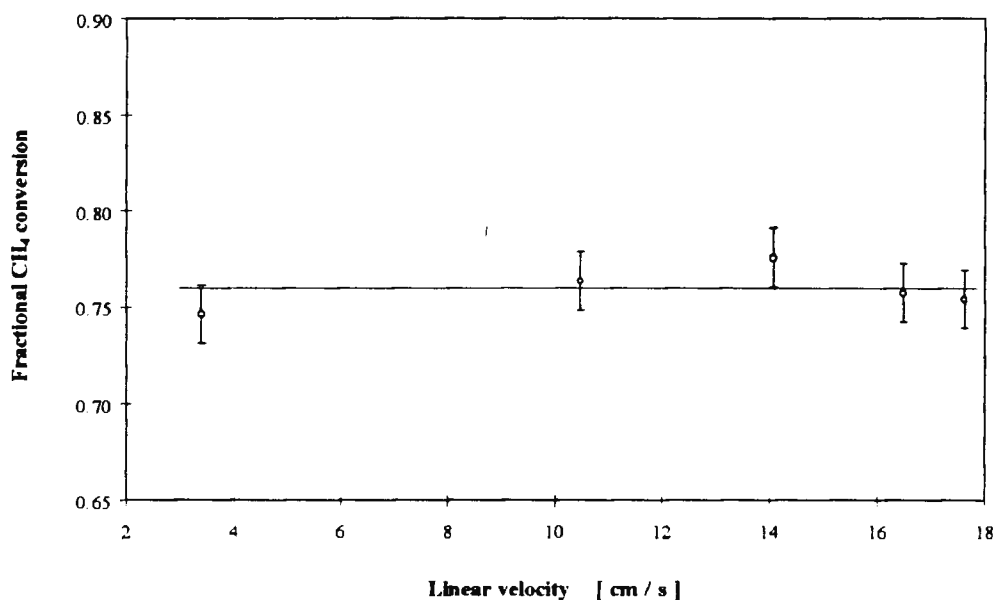
Figure 3-7 The effect of linear velocity on X_{CH_4} (T = 604°C, P°_i in kPa: CH_4 = 2.69, O_2 = 1.34, P_T = 201.3 kPa, 425μm < d_p < 710μm)

3.2.5.2. Internal (pore) diffusion

The effect of particle size on fractional methane conversion was investigated at constant linear velocity and catalyst loading. A linear velocity was selected (14 cm/s) that was in the high range of the values previously used to determine the effect of film diffusion. A plot of the methane conversion as a function of catalyst particle size is shown in Figure 3-8.

The error bars are for deviations smaller than about 2% of the indicated values. It may therefore be concluded with 98% certainty that the catalyst particle size (in the range between 125 micron and 710 micron) has no effect on methane conversion and therefore that pore diffusion does not influence the overall rate significantly. In order to check whether the above conclusions from experimental data may have been predicted by theoretically-derived criteria to check gradientless conditions, a number of correlations were taken from the literature and applied to our data. This will be discussed in section 4.1.1.

112
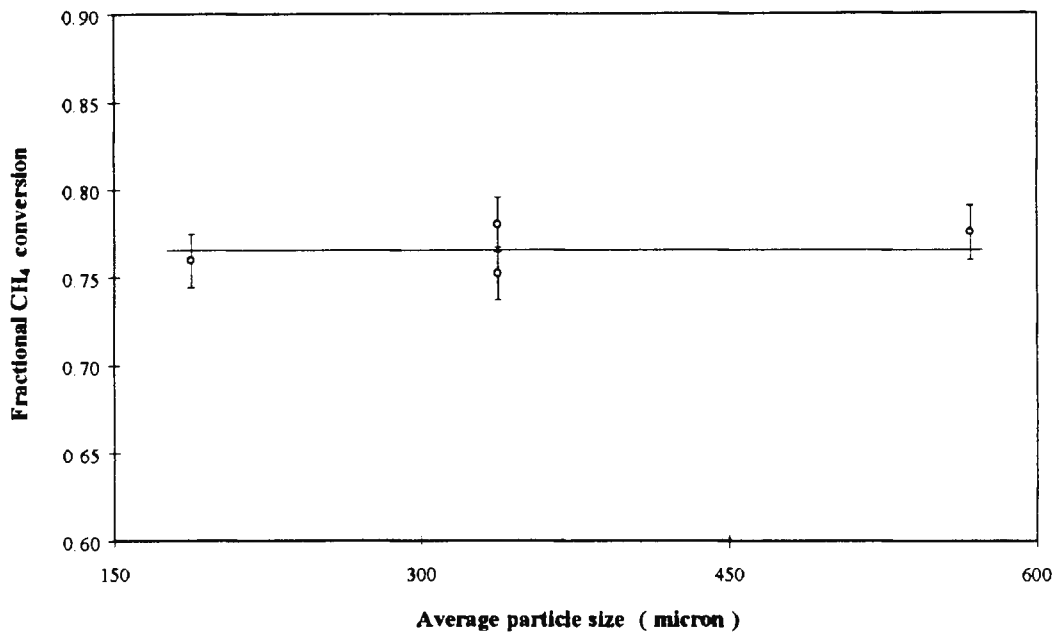
Figure 3-8 The effect of d_p on X_{CH_4} (T = 604°C, u_o = 14.07 cm.s^{-1}, P°$_i$ in kPa: CH$_4$ = 2.69, O$_2$ = 1.33, P$_T$ = 201.3 kPa, W = 200 mg)

3.3. Reaction kinetics

Rate measurements were made with u_0 in the region of negligible film diffusion (u_0 = 14.1 cm/s) and particles in the size range where internal gradients were shown to be absent (425-710 μm). The reactor pressure was maintained constant at 100 $\pm$ 2 kPa (gauge). It was decided to use the integral mode of operation because more accurate values for the methane conversion could be obtained at the high X_{CH_4} typical of integral reactors. A further consideration for this decision was the observation in preliminary experiments that the catalyst deactivated in the presence of oxygen. Small changes in methane conversion due to catalyst deactivation does not make a large impact on X_{CH_4} if the methane conversion and thus also the accuracy of the measurement is high. At low methane conversion, the accuracy of the X_{CH_4} values are lower due to analytical constraints and catalyst deactivation will therefore have a greater impact on the accuracy of the kinetic data. The integral mode of operation also allows one to study the product spectrum at high methane conversion and to gain insight into the reaction pathway.

It should be emphasized that W/F°$_{CH_4}$ was varied by changing the weight of catalyst and not the methane flow rate. Both F°$_{CH_4}$ and the total flow rate (therefore also the linear

velocity u_o) was constant for all experiments, except where the effect of methane partial pressure on the reaction rate was investigated. This procedure was followed because the catalyst could not be regenerated to its original activity and deactivated steadily (as discussed at some length in section 2.4.1.5), thus necessitating the use of a fresh batch of catalyst for each set of operating conditions.

The decision to use an integral reactor implied that the reaction rate could not be obtained directly from the conversion data. A number of mathematical operations were tested to extract kinetic data from the integral (X_{CH4} vs. W/F_{CH4}) data. A model data set was selected to illustrate the mathematical manipulations of the integral reactor data (see Table 3-4). All the results contained in the selected set were obtained at constant linear velocity ($u_o = 14.1$ cm.s^{-1}), methane partial pressure ($P^{\circ}_{CH4} = 2.96$ kPa), oxygen partial pressure ($P^{\circ}_{O2} = 1.34$ kPa) and bed inlet temperature ($T = 604°C$).

Table 3-4 Integral kinetic results used in comparing the methods that were used to obtain differential data

W/F°_{CH4} g.s/mol	X_{CH4}	X_{O2}	P_{CO}	P_{H2}	P_{CO2}	P_{H2O}
			kPa			
1347.341	0.158	0.513	0.115	0.535	0.338	0.584
1356.147	0.177	0.461	0.108	0.463	0.311	0.504
2201.538	0.230	0.611	0.272	0.858	0.366	0.632
2227.957	0.278	0.702	0.239	0.735	0.454	0.729
2201.538	0.239	0.585	0.217	0.747	0.348	0.653
4394.270	0.469	0.924	0.653	1.855	0.564	0.683
4455.913	0.449	0.910	0.691	1.934	0.543	0.651
6604.614	0.579	1.000	1.146	2.840	0.494	0.510
8806.152	0.621	1.000	1.352	3.179	0.404	0.497
13226.841	0.761	1.000	2.051	4.309	0.194	0.205

$P^{\circ}_{CH4} = 2.96$ kPa, $P^{\circ}_{O2} = 1.34$ kPa, $P_T = 201.3$ kPa, $F^{\circ}_{CH4} = 1.14E-6$ mol.s^{-1}, $u_o = 14.1$ cm.s^{-1} and $T = 604°C$

3.3.1. Determination of the rate of methane consumption from experimental data

Integral reactor data (X_{CH4} vs. W/F°_{CH4}) may be converted to reaction rates (r_{CH4}) by

114

converting the data to a differential form. This involves the fitting of an analytical curve such as equation (3-3) to the integral data

$$X_{CH_4} = f_i \left(\frac{W}{F^o_{CH_4}} \right)$$

(3-3)

where f_i may represent any arbitrary function (exponential or polynomial type of expression). The slope of the curve at any value of W/F^o_{CH4} is the first derivative of equation (3-3). If one considers a reactor with no axial dispersion (plug flow reactor), the first derivative (slope) of the curve directly gives the required reaction rate. This follows from the mass conservation equation that governs plug flow behaviour:

$$\frac{W}{F^o_{CH_4}} = \int_{X_{CH_4} = 0}^{X_{CH_4} = 1} \frac{dX_{CH_4}}{-r_{CH_4}}$$

(3-4)

and its differential form:

$$-r_{CH_4} = \frac{dX_{CH_4}}{d\frac{W}{F^o_{CH_4}}} = \frac{df_i}{d \cdot \frac{W}{F^o_{CH_4}}} = f^1_i \left(\frac{W}{F^o_{CH_4}} \right)$$

(3-5)

The term $f^1(W/F^o_{CH4})$ is the analytical expression for the first derivative (with respect to W/F^o_{CH4}) of the fitted curve (equation (3-3)).

A number of analytical functions (f_i) may be fitted to the data, but the merits and drawbacks of each selection may not be immediately apparent. A study of a number of possible curves was therefore made and the rate obtained from each expression was compared in order to demonstrate the dependence of the reaction rate on the form of the curve that was used. The results of this comparison will be discussed in the next section. The data set that

was used for the comparison is given in Table 3-4.

3.3.1.1. Using hand-drawn curves

The set of kinetic data (X_{CH4} vs. W/F°_{CH4}) given in Table 3-4 was plotted on graph paper and a number of people were requested to draw smooth curves through the data points and the origin. The same person was also asked to construct a tangent line to the curve at the origin. This tangent which represents the slope of the curve was used to calculate the initial reaction rate (r°_{CH4}). The results of the initial reaction rate that was obtained in this manner are tabulated in Table 3-5.

Table 3-5 r_{CH4} calculated from hand-drawn tangents to kinetic data

Worker	Rate g.s/mol	Deviation from mean value %
Michael	1.48E-4	12.7
Rein	1.45E-4	9.96
Linda	1.23E-4	-6.84
Sarah	1.38E-4	4.87
Peter	1.19E-4	-9.66
Frank	1.20E-4	-8.75
Dr. van Steen	1.25E-4	-4.94
Prof. O'Connor	1.29E-4	-1.90
Gunther	1.38E-4	4.89
Mean value	**1.32E-4**	**8.31** [a]

a   The standard deviation according to equation (3-1) was 1.09E-5 mol/g/s and the coefficient of variation (c.v.) = 8.31%.

The coefficient of variation was found to be higher than the 5% experimental error of the gas analysis, but surprisingly small if one considers the arbitrary nature of the technique.

3.3.1.2. Fitting analytical expressions to X_{CH4} vs. W/F°_{CH4} data

A number of analytical expressions were fitted to the same set of data that was used in the hand calculation (see Table 3-4). In all cases the minimum of the sum of the square of the errors between the experimental X_{CH4} and the predicted X_{CH4} values were used as a curve-fitting criterion.

3.3.1.3. Fitting a second-order polynomial to the data

A polynomial expression was fitted to the data in Table 3-4. The resulting curve and the analytical expression is shown in Figure 3-9. The rate (r_{CH4}) at zero conversion was evaluated by taking the derivative $W/F^{\circ}_{CH4} = 0$ and the reaction rate determined by this method included in Table 3-6.

$$y = -4.8974E\text{-}09x^2 + 1.2058E\text{-}04x$$
$$R^2 = 0.98178$$

W / F°$_{CH4}$ (g . s / mol)
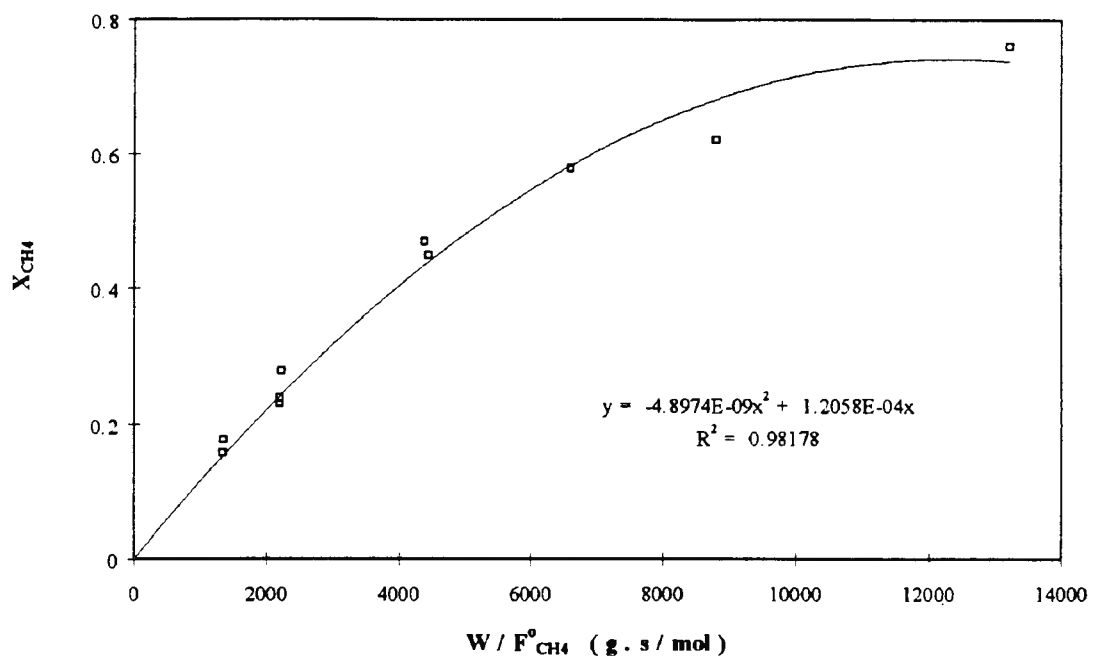
Figure 3-9 The fit of a second-order polynomial to the model data set

3.3.1.4. Fitting exponential curves to the data

3.3.1.4.a. Best fit without considering equilibrium

A simple exponential expression (equation (3-6)) with one constant (A) was fitted to the same set of experimental data (Table 3-4).

$$X_{CH_4} = 1 - exp\left(-A \frac{W}{F^o_{CH_4}}\right)$$ (3-6)

The value of A was determined by minimizing the square of the error between the experimental conversion (X_{CH4} in Table 3-4) and that predicted by equation (3-6). The nonlinear solver routine in Microsoft Excel [160] was used to obtain an estimate of the constant.

3.3.1.4.b. Taking account of equilibrium conversion

The expression that was used to incorporate the overall equilibrium methane conversion took the form:

$$X_{CH_4} = X^{eq}_{CH_4}\left[1 - exp\left(-A \frac{W}{F^o_{CH_4}}\right)\right]$$ (3-7)

The equilibrium methane conversion (X^{eq}_{CH4}) was calculated by a Gibbs free energy minimization technique [28]. Carbon (graphite) was not included in the calculation. Six species were considered to be present, namely CH_4, O_2, CO, H_2, CO_2 and H_2O. The value of the constant A was determined by minimizing the square of the error between the experimental value for X_{CH4} (Table 3-4) and that predicted by the expression. At $W/F^o_{CH4} = 0$, equation (3-7) predicts that $X_{CH4} = 0$ (as it should be) and at very long contact times ($W/F^o_{CH4} \rightarrow \infty$), it predicts the correct value of methane conversion, namely $X_{CH4} = X^{eq}_{CH4}$. Equation (3-7) thus satisfies both of the physical boundary conditions at the

118

bed inlet and at the outlet of a very long bed. The reaction rate is obtained from the fitted function by taking the first derivative of equation (3-7):

$$d \ \frac{X_{CH_4}}{\frac{W}{F^o_{CH_4}}} = -r_{CH_4} = X^{eq}_{CH_4} \ A \ exp \left(-A \ \frac{W}{F^o_{CH_4}} \right)$$

(3-8)

The curves that were obtained after fitting equations (3-6) and equation (3-7) to the selected data set, is shown in Figure 3-10.
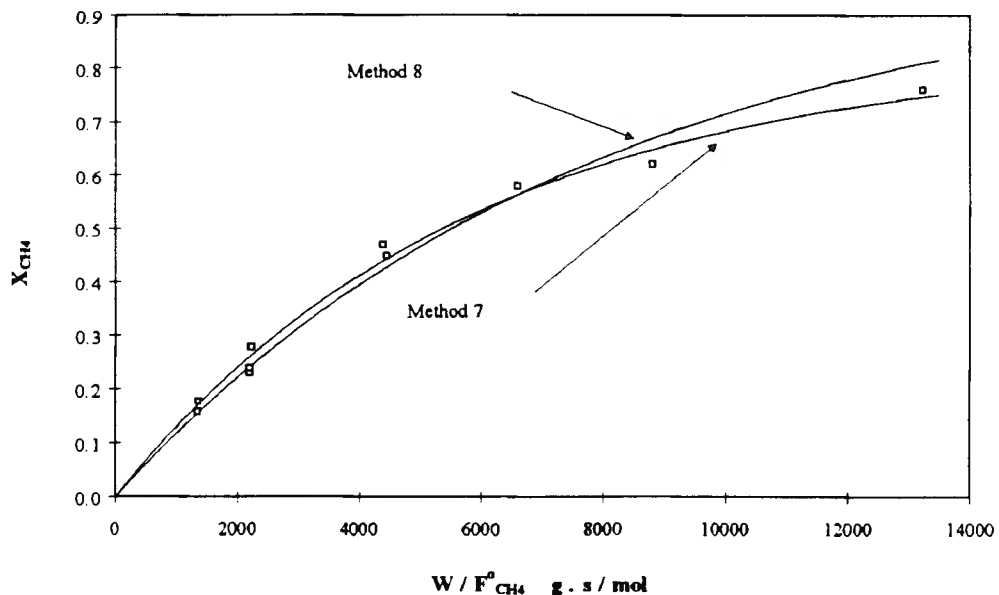
Figure 3-10 Exponential fit with and without equilibrium X_{CH_4} taken into account (Method 7 - equation (3-7) and method 8 - equation (3-6))

3.3.2. Comparison of the curves used to obtain differential r_{CH4} data

The results of the curve-fitting procedures described above are summarized in Table 3-6. The hand-drawn curve gave a result which was very close to the overall average of all the techniques. The initial reaction rates calculated by the second-order polynomial- and one of the exponential curve-fitting functions (method 8) were within 5% of the average. The only two outliers were the linear fit and the rate derived by method 7.

Table 3-6 Comparison of r_{CH4} obtained by various curve fitting techniques to X_{CH4} vs. W/F°_{CH4} data $(T = 604^{\circ}C, P^{\circ}_{CH4} = 2.964, P^{\circ}_{O2} = 1.343)$

Method no.	Description	Slope at $W/F^{\circ}_{CH4} = 0$	R^2	% Deviation from mean value
1	Hand-drawn	1.32E-4	-	3.9
2	Linear fit[a]	1.15E-4	0.8284	-9.4
3	2nd order fit	1.21E-4	0.9818	4.7
7[b]	Exponential with X^{eq}_{CH4}	1.42E-4		11.8
8	Exponential without X^{eq}_{CH4}	1.26E-4		-0.8
	Mean value[c]	**1.27E-4**		**0.00**

a Straight line fit through the origin and the first two data points by means of linear regression.
b Fractional methane conversion at thermodynamic equilibrium $(X^{eq}_{CH4}) = 0.841$
c The standard deviation and coefficient of variation of the above data was calculated to be 1.04E-5 mol/g/s and 8.2% respectively

The exponential fit with equilibrium taken into account (method 7) is the only curve fitting technique of those considered above, which predicts both the correct X_{CH4} value of zero at $W/F^{\circ}_{CH4} = 0$, as well as the expected equilibrium value of X_{CH4} at $W/F^{\circ}_{CH4} \to \infty$. Since this method should therefore provide a good representation of the conversion vs. W/F°_{CH4} data over a wide range of methane conversion, the reaction rates calculated by method 7 should also be accurate over a wide range of reaction conditions.

While the model data set is useful in demonstrating the various methods, the applicability of a technique should be evaluated over the complete data set. The calculated methane conversion was plotted as a function of the measured X_{CH4} for methods 3, 7 and 8 (Figure 3-11, Figure 3-13 and Figure 3-15). In all three cases good agreement was found between the measured and predicted X_{CH4} over the entire range of methane conversion.

The residuals for methods 3, 7 and 8 were also plotted as a function of the measured conversion (Figure 3-12, Figure 3-14 and Figure 3-16). In this case the residuals were defined as:

$$Residual = X_{CH_4}^{Predicted} - X_{CH_4}^{Measured} \tag{3-9}$$

The residuals did not show a discernable trend for any of the three methods, indicating that, if there was an error inherent in any of the methods, then the error was not systematic.
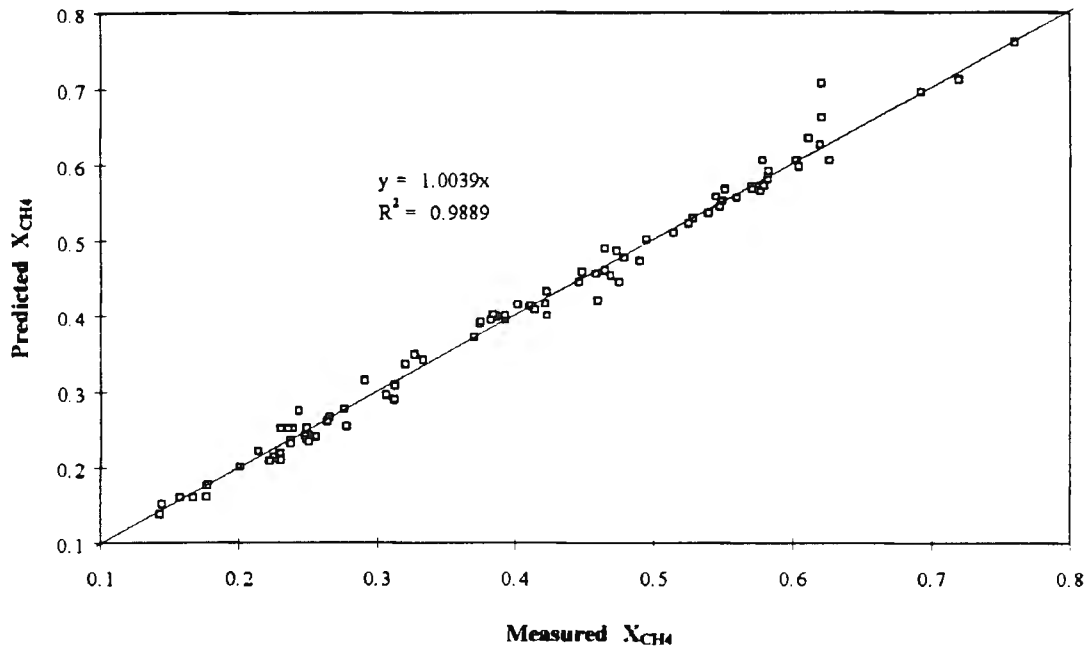
Figure 3-11 Predicted vs. measured X_{CH_4} (Method 3 - second order fit)
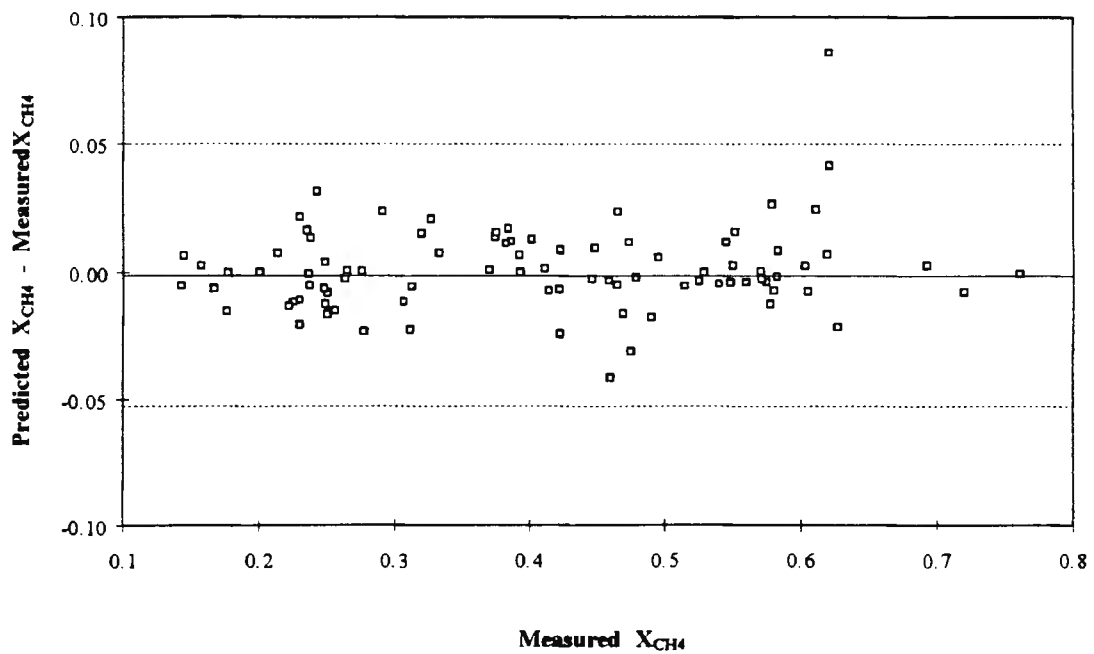
Figure 3-12 Residuals for method 3 (second order fit)
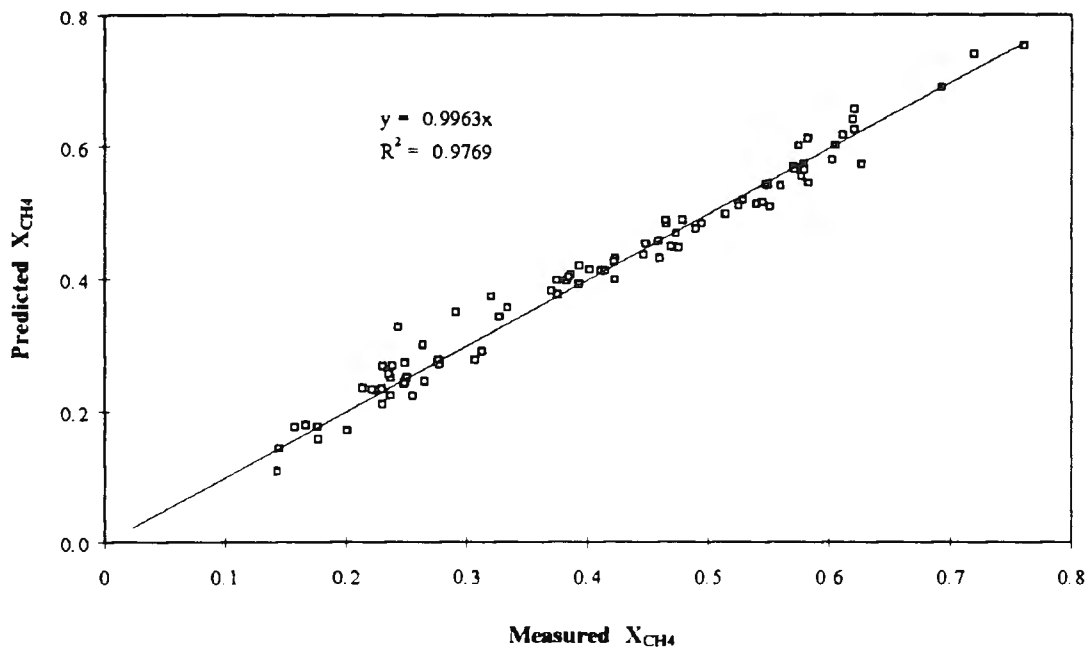
Figure 3-13 Predicted vs. measured X_{CH4} (Method 7 - exponential with equilibrium)
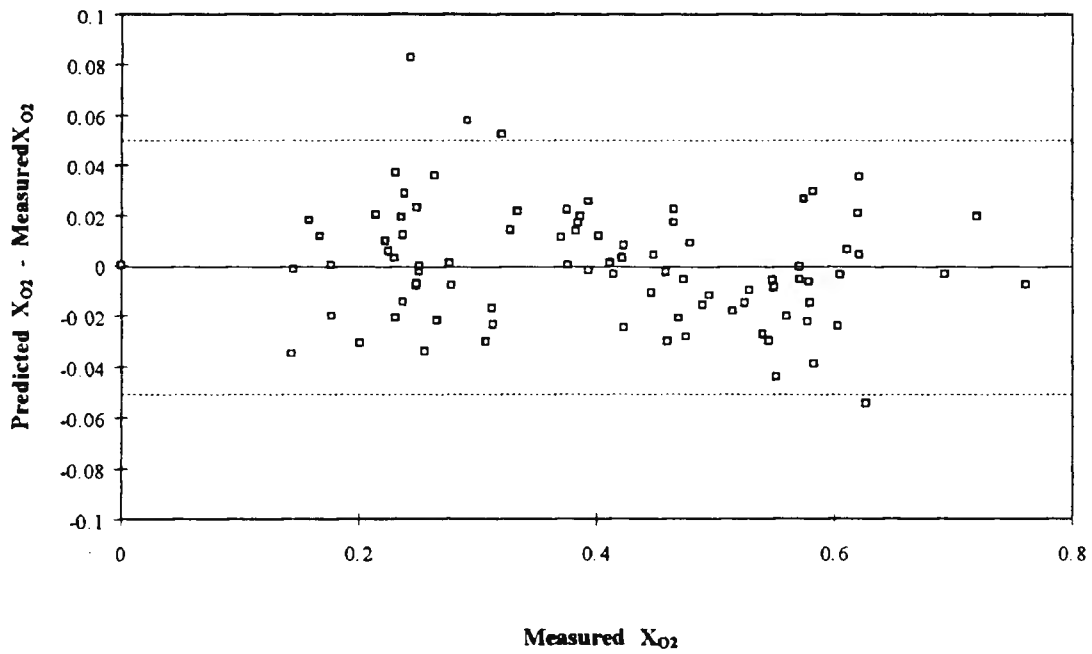
Figure 3-14 Residuals for method 7 (Exponential fit with equilibrium)
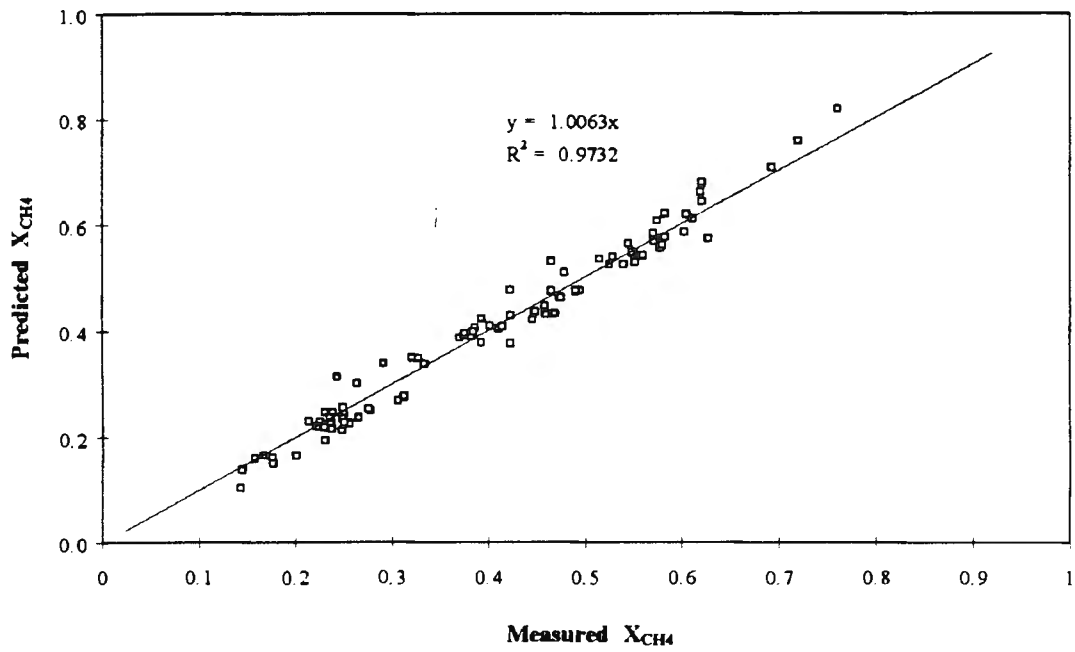
Figure 3-15 Predicted vs. measured X_{CH4} (Method 8 - exponential fit without equilibrium)
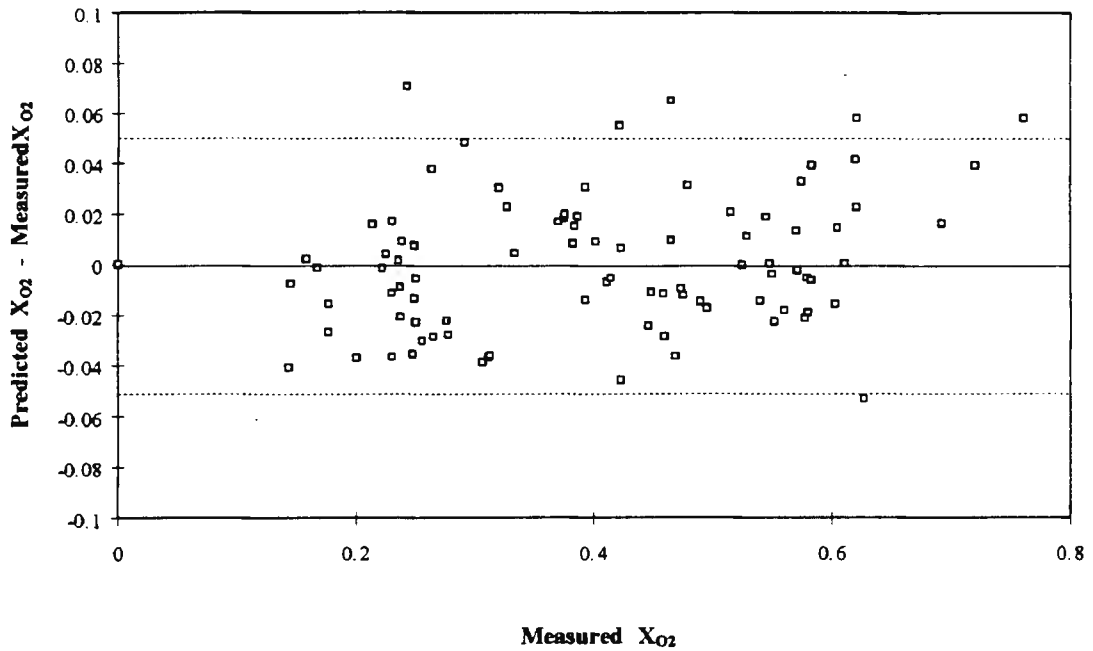
Figure 3-16 Residuals for method 8 (Exponential fit without equilibrium)

The standard deviation and coefficient of variation of methods 3, 7 and 8 with respect to their ability to predict methane conversion is tabulated in Table 3-7.

Table 3-7   Standard deviation of three curve-fitting methods with respect to their ability to accurately predict X_{CH4}

Method number	Standard deviation (S_y)	Coefficient of variation (%)
3	0.016	1.85
7	0.023	2.65
8	0.027	3.07

Of the three analytical fitting functions considered, the second-order polynomial expression (method 3) resulted in the lowest error with respect to X_{CH4}. This, however, does not necessarily imply that it will also be the most successful in predicting accurate values of the **rate** of methane consumption. In fact, at high $W/F°_{CH4}$ values, method 3 sometimes predicted a negative rate of methane consumption when the shape of the X_{CH4} vs. $W/F°_{CH4}$ suggested otherwise. Rather than selecting only one of the methods at this stage to do a complete differential analysis of the integral kinetic data, all three methods shown in Table 3-7 were used. **Method 3** was selected to account for curvature of the X_{CH4} vs. $W/F°_{CH4}$ data which a straight line fit would not be able to do. **Method 7** was selected because of its ability to predict the equilibrium methane conversion at very high values of $W/F°_{CH4}$ and **method 8** was chosen because of its very close approximation of the average $r°_{CH4}$ in the model data set. Polynomials with an order higher than 2 were not considered because most of the kinetic data sets contained less than four data points at any given combination of operating conditions.

The differential kinetic data obtained by the above-mentioned methods are used in this chapter to determine the activation energy and reaction orders. In the following chapter, use will again be made of the differential data when reaction rate models are proposed and evaluated for their ability to accurately predict the rate determined by the above-mentioned methods.

124

3.3.3. Determination of the rate of oxygen consumption

The rate of oxygen consumption was calculated by method 7. This method was chosen because the second-order polynomial was unable to account for the extreme curvature in the X_{O2} vs. W/F°_{O2} data. The equilibrium conversion of oxygen was in all cases 1.00, which led to the the modification of method 7 to a form which is identical to method 8. The resulting expression given by equation (3-10) was fitted to the experimental X_{O2} vs. W/F°_{O2} data and the first derivative used to calculate the rate of oxygen consumption.

$$X_{O_2} = 1 - exp \left(- A \cdot \frac{W}{F^{o}_{O_2}} \right) \hspace{3cm} \text{(3-10)}$$

A plot of the predicted oxygen conversion as a function of the measured conversion shows that the correlation is reasonable:
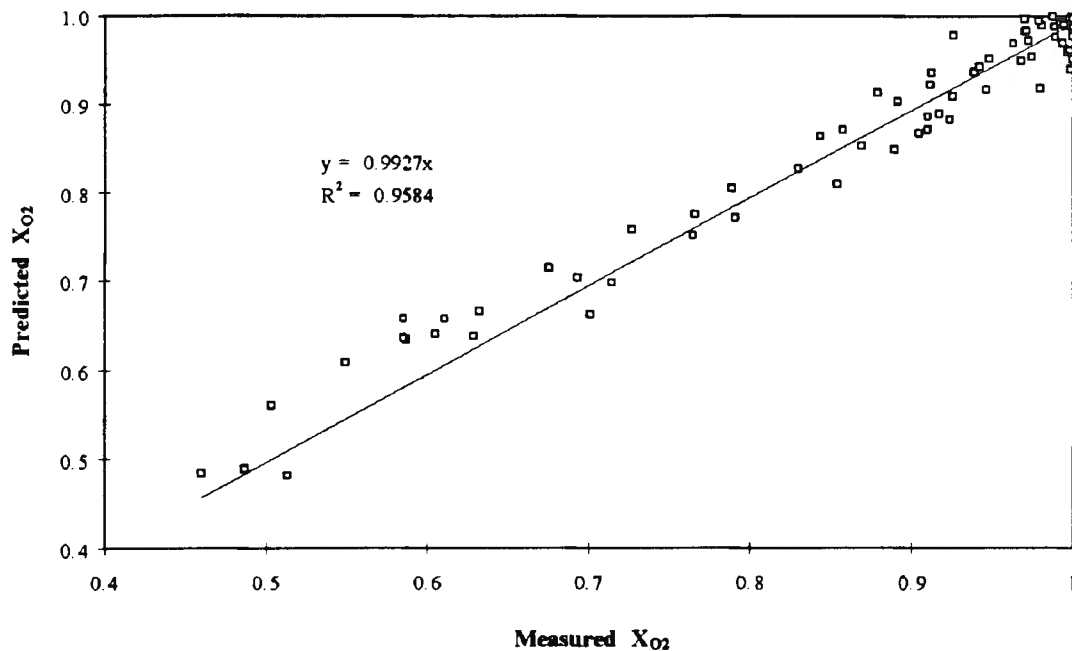
Figure 3-17   Predicted vs. measured X_{O2}

The residuals of the curves that were fitted to the measured oxygen conversion shown in Figure 3-18, however, highlight the fact that the curves overestimate the conversion at low

X_{O2} and that X_{O2} values are underestimated at high X_{O2}.
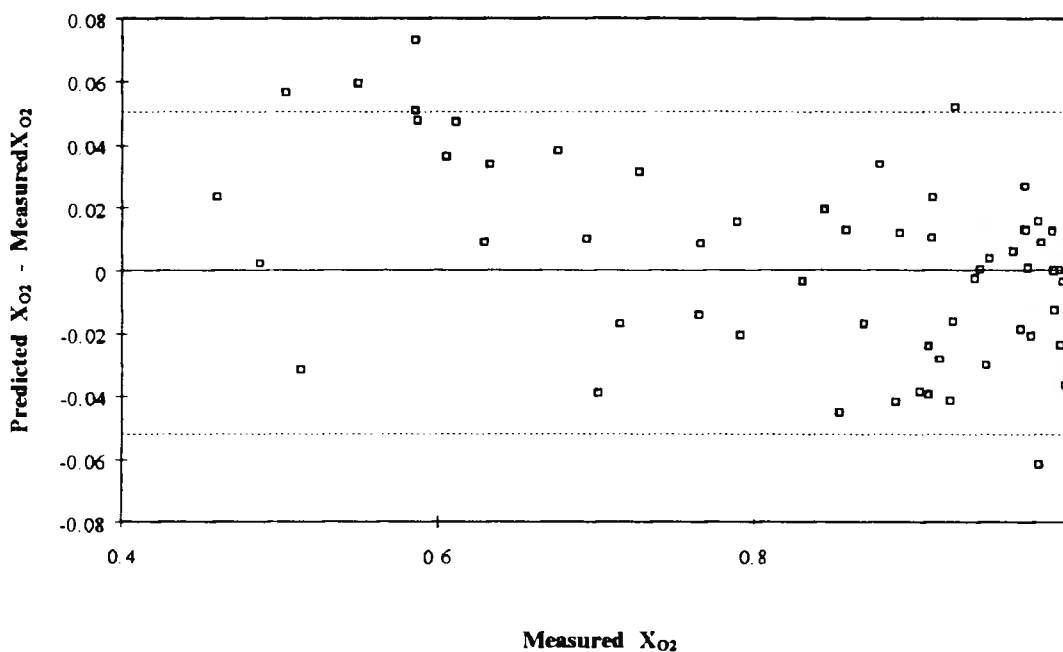
Figure 3-18   Residuals for exponential curves fit to X_{O2} data

This deviation should have an impact on the reaction rate (slope of the curve) that is calculated by this method. Since the exponential curve fit was found to best represent the X_{O2} data, it was used in spite of the drawback highlighted above. Rates of oxygen consumption should therefore be treated with some caution.

3.3.4. Determination of the rates of product formation

The often complex nature of the product partial pressure vs. W/F°_{CH4} curves made it very difficult to fit with an arbitrary analytical expression. The rates of product formation and/or consumption were therefore calculated from the slopes of tangent lines which were drawn to smooth curves through P_i vs. W/F°_{CH4} data. The slopes of the curves were related to the rate of product formation in the following way. A species balance was constructed over a differential section of catalyst bed (In - Out + Produced = 0):

126

$$\frac{V_T \cdot P_i}{R \cdot T}\bigg|_W - \frac{V_T \cdot P_i}{R \cdot T}\bigg|_{W + \Delta W} + r_{co} \cdot \Delta W = 0 \qquad (3\text{-}11)$$

where V_T represents the total volumetric flow rate ($m^3.s^{-1}$), R the universal gas constant T the bed temperature and W the mass of catalyst. This equation may be rewritten to yield the rate of product formation.

$$r_{co} = \frac{V_T}{R \cdot T} \cdot \frac{dP_i}{dW} \qquad (3\text{-}12)$$

Multiplying by $P^{\circ}_{CH4}/P^{\circ}_{CH4}$ (for mathematical convenience) and re-arranging leads to

$$r_i = \frac{1}{P^{\circ}_{CH_4}} \cdot \frac{V_T \cdot P^{\circ}_{CH_4}}{R \cdot T} \cdot \frac{dP_i}{dW} = \frac{1}{P^{\circ}_{CH_4}} \cdot \frac{d\,P_i}{d\,\dfrac{W}{F^{\circ}_{CH_4}}} \qquad (3\text{-}13)$$

The results of the product formation rates are not included explicitly in the present chapter, except when the calculation of reaction orders necessitated it. The next chapter will deal more extensively with the rates of product formation deeper into the bed while the remainder of the present chapter is devoted to initial reaction rates.

3.3.5. The integral approach

The second method to exploit integral reactor data is to propose a rate expression and to integrate this expression:

$$X_{CH_4} = - \int\limits_{\frac{W}{F'_{CH_4}} = 0}^{\frac{W}{F'_{CH_4}} @ \, outlet} r_{CH_4} \cdot d \frac{W}{F^o_{CH_4}}$$

(3-14)

The success or failure of such a rate expression may then be evaluated by comparing the experimentally-obtained conversion to that which was arrived at by means of numerical integration of the rate expressions. This approach was used in the analysis of the experimental data and the results of the integral analysis are given in chapter 4.

3.3.6. Results of the kinetic experiments

The full product composition as a function of W/F^o_{CH4} is shown in Figure 3-19.
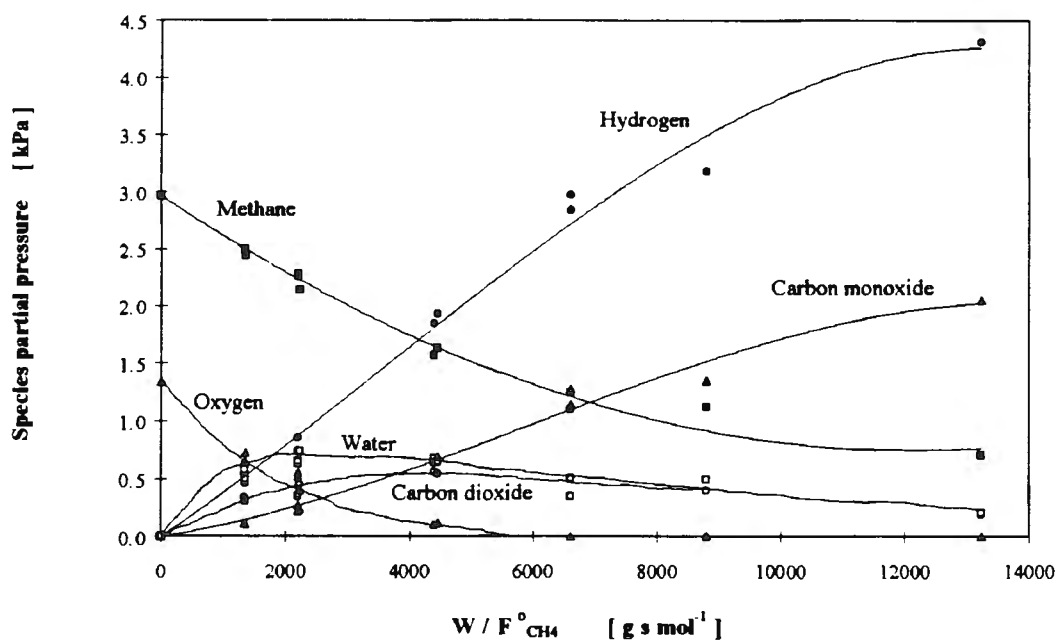
Figure 3-19 The full product composition as a function of W/F^o_{CH4} (T = 604°C, P^o_{CH4} = 2.96 kPa, P^o_{O2} = 1.34 kPa)

The data in this figure were obtained from a replicate set of experiments and are frequently referred to in later sections. These are the same data that were used previously in an

investigation of the reproducibility of the experimental procedure (see Table 3-4) and was then referred to as the "model data set".

3.3.6.1. The effect of temperature

The effect of temperature on the rate of methane consumption and the product composition was investigated at a fixed feed composition of $P°_{CH4}$ = 2.96 kPa and $P°_{O2}$ = 1.34 kPa with a methane flow rate of 1.14E-6 $mol.g^{-1}.s^{-1}$ in the temperature range 575°C to 650°C. The total reactor pressure was 201.3 kPa.

3.3.6.1.a. The effect of temperature on reactants and reaction products

Both X_{CH4} and X_{O2} (shown in Figure 3-20) increased as the temperature was raised from 575 to 650°C.
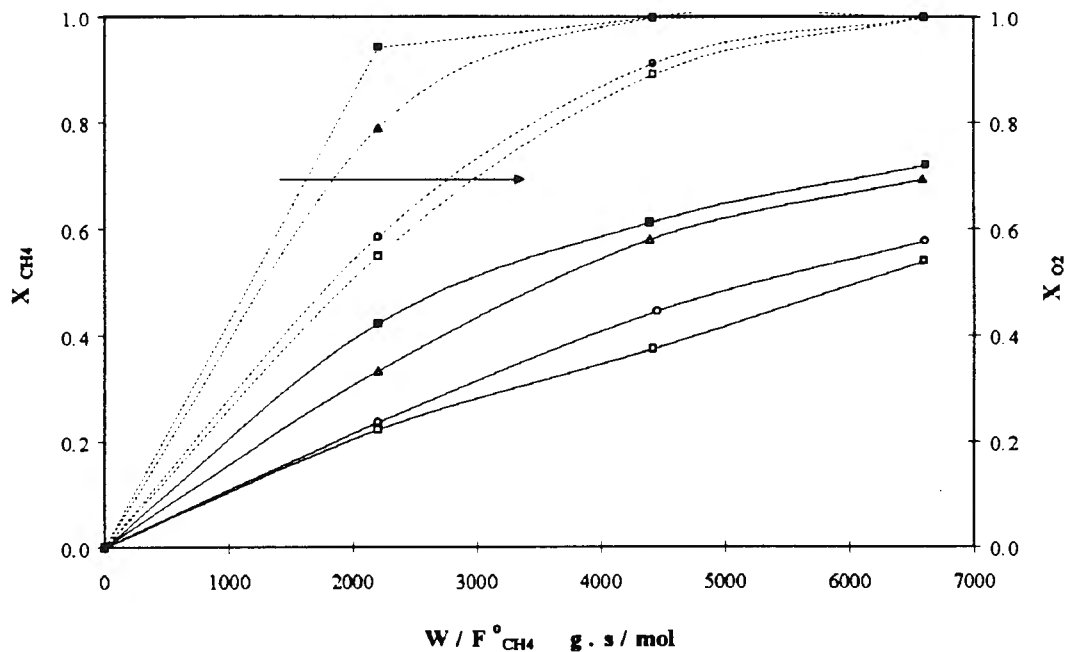
Figure 3-20 The effect of temperature on X_{CH4} and X_{O2} ($P°_{CH4}$ = 2.96, $P°_{O2}$ = 1.34, T (°C):□ = 579, ○ = 604, △ = 629, ■ = 654)

At the third value of W/F°_{CH4} investigated, oxygen consumption was virtually complete at all temperatures, but methane conversion was incomplete and rising.

An increase in temperature led to the production of more partial oxidation products (hydrogen and carbon monoxide) and (at high W/F°_{CH4} values) less deep oxidation products (water and carbon dioxide). This is demonstrated in the next four figures of P_i vs. W/F°_{CH4}. (Note the different scales on the y-axes.)
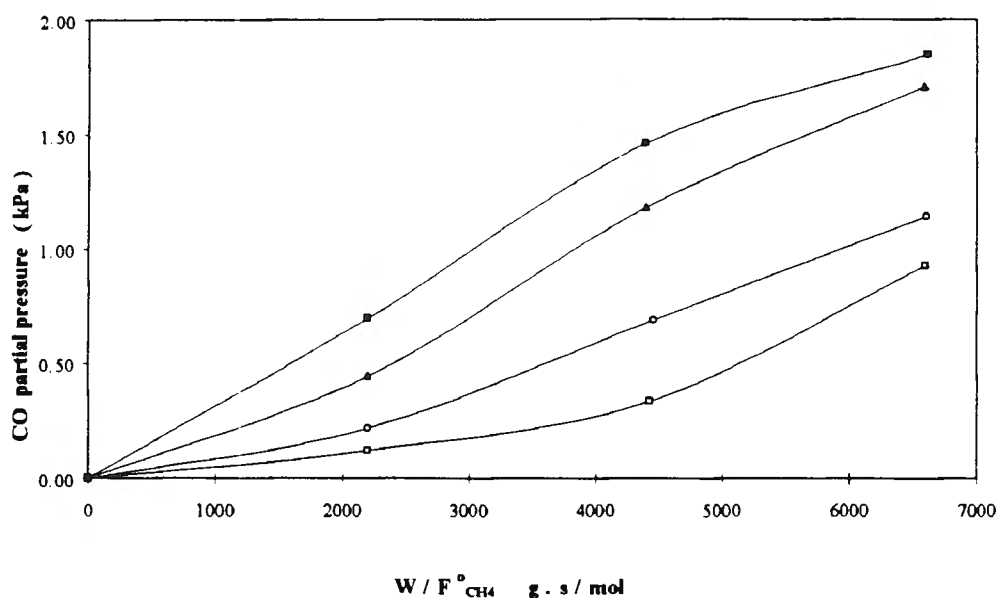
Figure 3-21 The effect of temperature on P_{CO} (P°_{CH4} = 2.96 kPa, P°_{O2} = 1.34 kPa, T (°C):□ = 579, ○ = 604, ▲ = 629, ■ = 654)

The P_{CO} vs. W/F°_{CH4} curves exhibited inflection points. This feature indicates the secondary formation of CO and was also evident in the P_{H2} vs. W/F°_{CH4} plot (Figure 3-22). The inflection point for both carbon monoxide and hydrogen became less apparent, however, as the temperature was increased. At the same time, the slope of the P_{CO} line at the origin increased with increasing temperature, indicating as expected that it was being produced at a higher rate as the bed temperature was increased. Carbon dioxide partial pressure increased initially with increasing W/F°_{CH4}, then passed through a maximum and started to decrease as W/F°_{CH4} was increased beyond the point of maximum P_{CO2}. This trend was apparent at all temperatures.
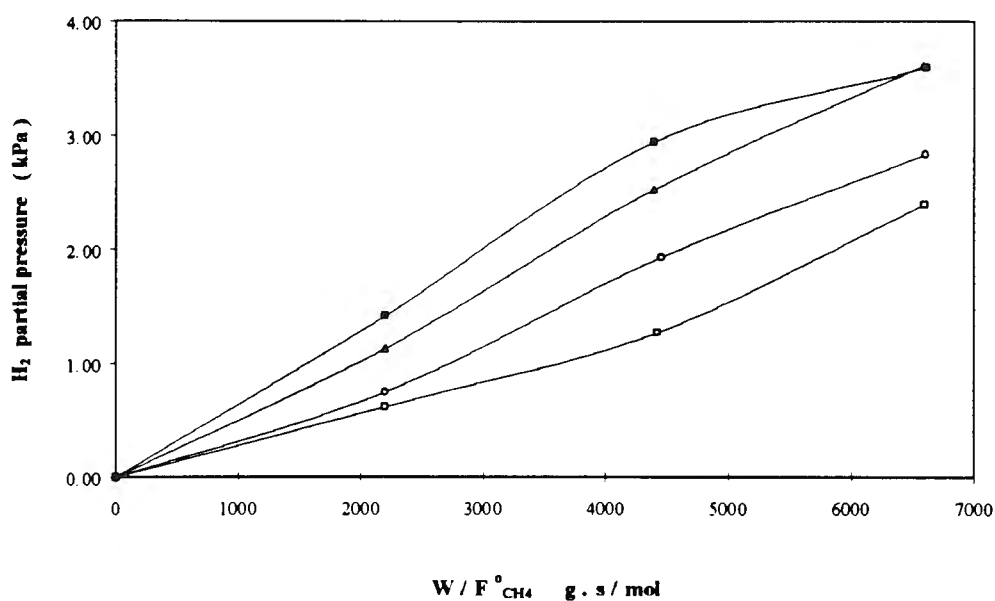
Figure 3-22 The effect of temperature on P_{H2} (P°_{CH4} = 2.96 kPa, P°_{O2} = 1.34 kPa, T in °C:□ = 579, ○ = 604, ▲ = 629, ■ = 654)
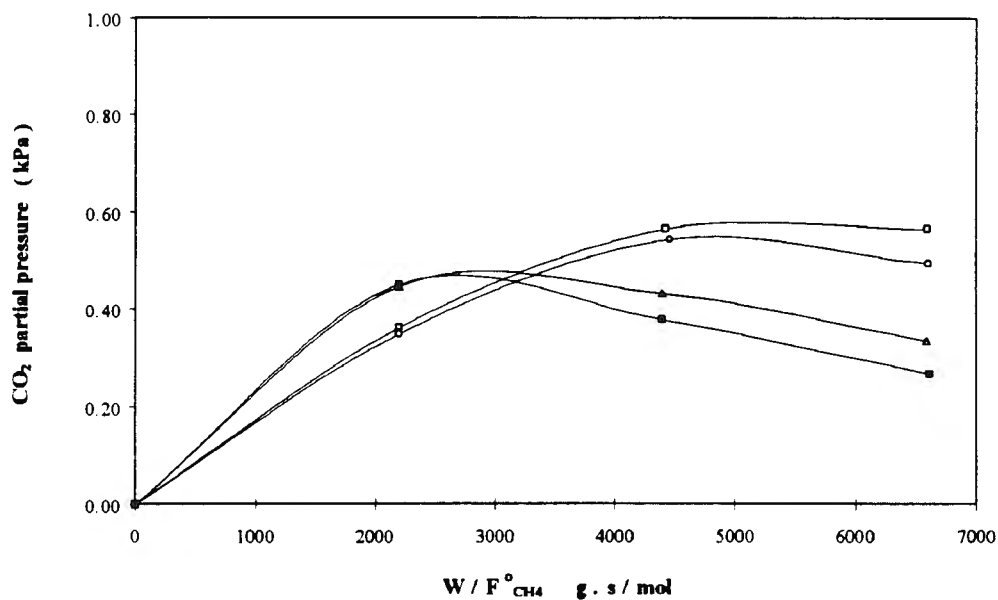
Figure 3-23 The effect of temperature on P_{CO2} (P°_{CH4} = 2.96 kPa, P°_{O2} = 1.34 kPa, T in °C:□ = 579, ○ = 604, ▲ = 629, ■ = 654)

The slope of the P_{CO2} vs. W/F°_{CH4} line at the origin increased slightly with increasing temperature, indicating that the initial rate of CO_2 formation was enhanced at higher temperatures. The decrease in carbon dioxide partial pressure deeper into the bed could only

be ascribed to the presence of a CO_2-consuming reaction. The fact that the (negative) slope of the P_{CO2} curves increased with increasing temperature indicated that the rate of carbon dioxide consumption increased as the temperature was raised. Note also that the peak in total oxidation product formation is frequently described by a single point. This allows the viewer to draw a number of possible curves through the data and could in that instance lead to large errors in the calculation of the rate of product formation. If this fact is not acknowledged, it could be potentially misleading with respect to qualitative interpretations of the data.

The P_{H2O} vs. W/F°_{CH4} plot exhibited the same general features as that of carbon dioxide (Figure 3-24). This suggests that CO_2 and water are both formed as primary products and then consumed deeper into the catalyst bed. The peaks in the case of water were, however, more pronounced than for carbon dioxide. This could be seen as evidence that CO_2 reforming of methane occured to a lesser extent than steam reforming of methane.

Presumably due to the fact that the water content at the bed outlet was calculated from elemental balances and not directly measured, there was more scatter in the water partial pressure data.
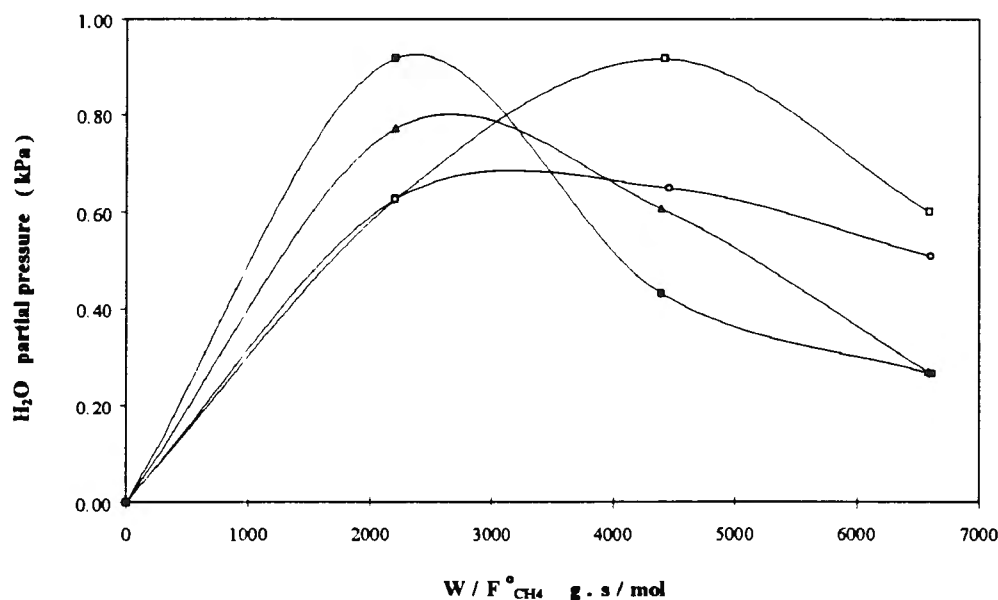
Figure 3-24 The effect of temperature on P_{H2O} ($P^{\circ}_{CH4} = 2.96\ kPa$, $P^{\circ}_{O2} = 1.34\ kPa$, T in °C: □ = 579, ○ = 604, ▲ = 629, ■ = 654)

At or close to the maximum in P_{H2O}, the water partial pressure increased with an increase in temperature. Deeper into the bed, however, the order was reversed. This is a similar finding to the previously discussed trend of respect to carbon dioxide partial pressure with temperature.

The above results may be summarized by the following general statements:

i)   All products are present as primary products.

ii)   Partial oxidation products (CO and H_2) appear, however, to be formed as a secondary product as well.

iii)   Water and carbon dioxide are formed as primary products and are consumed deeper into the bed.

iv)   The formation of all products increase with increasing temperature and the consumption of water and carbon dioxide are also enhanced by increasing temperature.

v)   The CO_2-reforming of methane occurs to a lesser extent than steam reforming.

3.3.6.1.b.   The effect of temperature on the reaction rate

The natural logarithm of the initial rate of methane consumption was plotted against the inverse temperature (Figure 3-25) in order to obtain an estimate of E_a and the pre-exponential factor. The **apparent** activation energy was calculated by means of a linear least-squares fit to the data represented in Figure 3-25 and the results are summarized in Table 3-8. The effect of the curve-fitting technique that was used to obtain r_{CH4} was also studied. The rate of methane consumption calculated from a second-order polynomial fit (method 3), a simple exponential fit (method 8) and an exponential fit which included a term to account for the attainment of thermodynamic equilibrium (method 7) were used to generate the data for Figure 3-25. Since a number of possible reactions are occurring at the same time at the bed inlet (ie. total oxidation, oxidative reforming, CO oxidation etc.), the activation energy values given in Table 3-8 does not refer to a particular reaction, but are very much **apparent** activation energy values of the overall reaction network.
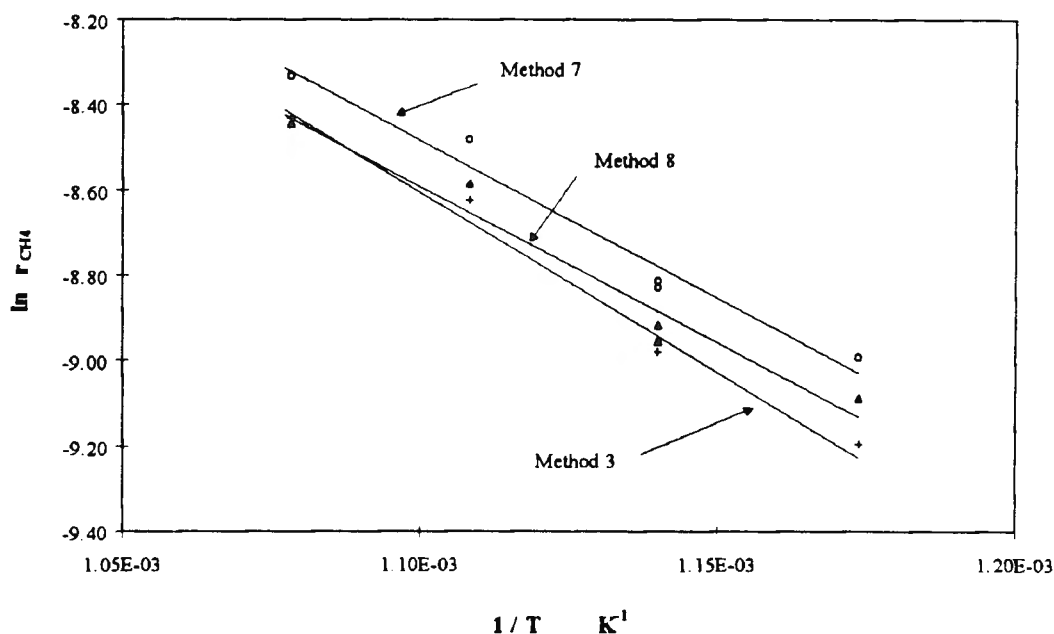
Figure 3-25 Arrhenius-type plot of r_{CH_4} calculated by three methods ($P^\circ_{CH_4}$ = 2.96 kPa, $P^\circ_{O_2}$ = 1.34 kPa, Curve-fit method: + = 3, $\circ$ = 7, $\triangle$ = 8)

Table 3-8 Apparent activation energy from Arrhenius plot

Curve fitting procedure	Activation energy kJ mol^{-1}	Pre-exponential mol g^{-1} s^{-1}	R^2
Method 3	70	0.7	0.9825
Method 7	62	0.6	0.9691
Method 8	61	2.0	0.9567

The activation energy values shown above agree remarkably well with the activation energy of methane chemisorption on Ni(111) surfaces (See Table 3-8).

The effect of temperature on the rates of product formation was also studied. A plot of ln r°_i for all the products as a function of 1/T enabled one to calculate the apparent activation energy barrier to product formation for each of the products. It was found that the E_a sequence followed the order:

$$CO > H_2 > H_2O > CO_2$$

as indicated in Table 3-9.

Table 3-9 E_a of reactant disappearance and product formation from Arrhenius-type plots ($P°_{CH4}$ = 2.96 kPa, $P°_{O2}$ = 1.34 kPa)

Product	Activation energy kJ mol^{-1}	Pre-exponential mol g^{-1} s^{-1}	R^2
CH$_4$	62	0.7	0.9691
O$_2$	93	87.9	0.9551
CO$_2$	32	5.1E-3	0.7861
H$_2$O	44	4.9E-2	0.9848
H$_2$	72	2.3	0.9430
CO	166	2.2E+5	0.9918

$r°_{CH4}$ and $r°_{O2}$ calculated by method 7
The initial rates of product formation were calculated by constructing tangent lines to smooth curves drawn through P_i vs. $W/F°_{CH4}$ data

3.3.6.2. The effect of reactant partial pressure on the oxidative reforming of methane

3.3.6.2.a. The influence of methane partial pressure

$P°_{CH4}$ was varied between 2.75 kPa and 4.82 kPa while keeping $P°_{O2}$ constant at 1.38 kPa. A number of data points from Table C-3 in appendix C.2 were used to illustrate the effect of $P°_{CH4}$ on the product composition and the disappearance of reactants (CH$_4$ and O$_2$). In these experiments, the methane flow rate ($F°_{CH4}$) was constant for a particular $P°_{CH4}$ value and the catalyst mass was varied to obtain different values of $W/F°_{CH4}$ for each methane inlet partial pressure.

3.3.6.2.a.i. The effect of $P°_{CH4}$ on reactants and reaction products

The effect of methane partial pressure on X_{CH4} and X_{O2} at 604°C is shown in Figure 3-26. The lines are drawn as a guide to the eye and are not model fits. Both methane and oxygen conversion were enhanced by an increase in methane partial pressure at low $W/F°_{CH4}$, but the effect on oxygen conversion was more pronounced than on methane conversion.
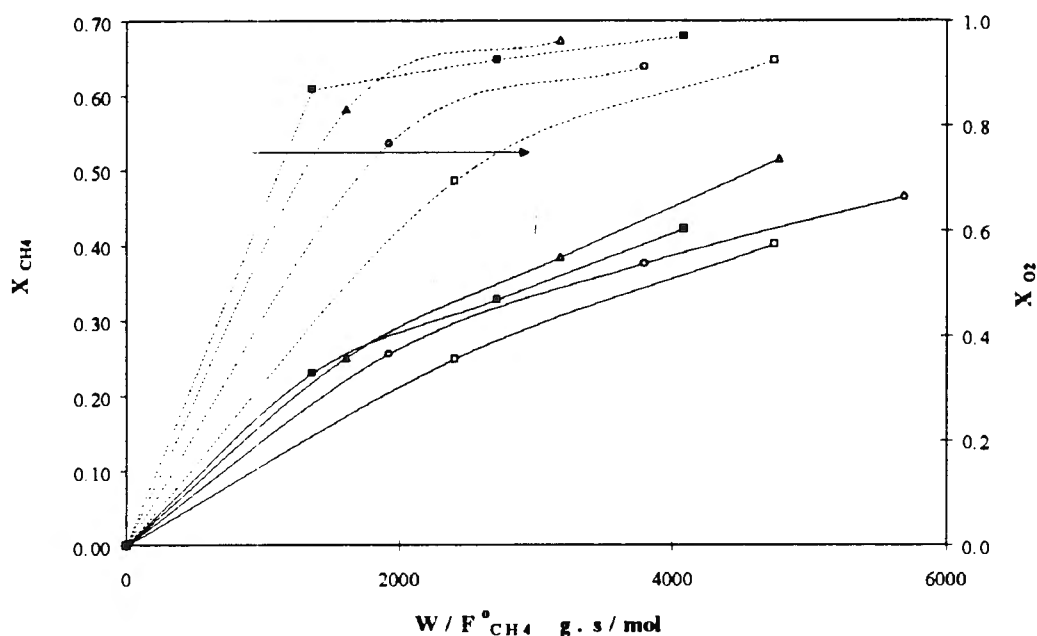
Figure 3-26 The effect of P°_{CH4} on X_{CH4} and X_{O2} (P°_{O2} = 1.38 kPa, T = 604°C, P°_{CH4} in kPa:□ = 2.75, ○ = 3.44, △ = 4.13, ■ = 4.82)

At the highest P°_{CH4} investigated, however, the extent of the increase in conversion of both methane and oxygen was lower than for the other P°_{CH4} experiments at similar W/F°_{CH4} values. Oxygen conversion exceeded 0.9 in that region and the catalyst surface was therefore starved of oxygen. In the absence of other reactants that could react with methane, a less pronounced increase in X_{CH4} was therefore to be expected. This finding also indicates that the rate of the steam- or carbon dioxide reforming of methane reactions were not high enough to ensure the continued increase in X_{CH4} in the absence of oxygen. Alternatively, the levelling off of the methane conversion could be attributed to the enhanced inihibition of products. This issue will be pursued further in the next chapter.

As expected, an increase in methane partial pressure also led to more partial oxidation products. This is demonstrated for CO in Figure 3-27 and for H_2 in Figure 3-28. The curvature in the P_{CO} curve which is present at low P°_{CH4} became less pronounced as the methane partial pressure at the bed inlet was increased, indicating the possibility of a shift in the reaction mechanism. In all the experiments, carbon monoxide was detected. This indicates that, in the range of P°_{CH4} and W/F°_{CH4} investigated, CO was formed as a primary reaction product. At high methane partial pressure, the primary formation of CO appeared

136

to be enhanced.
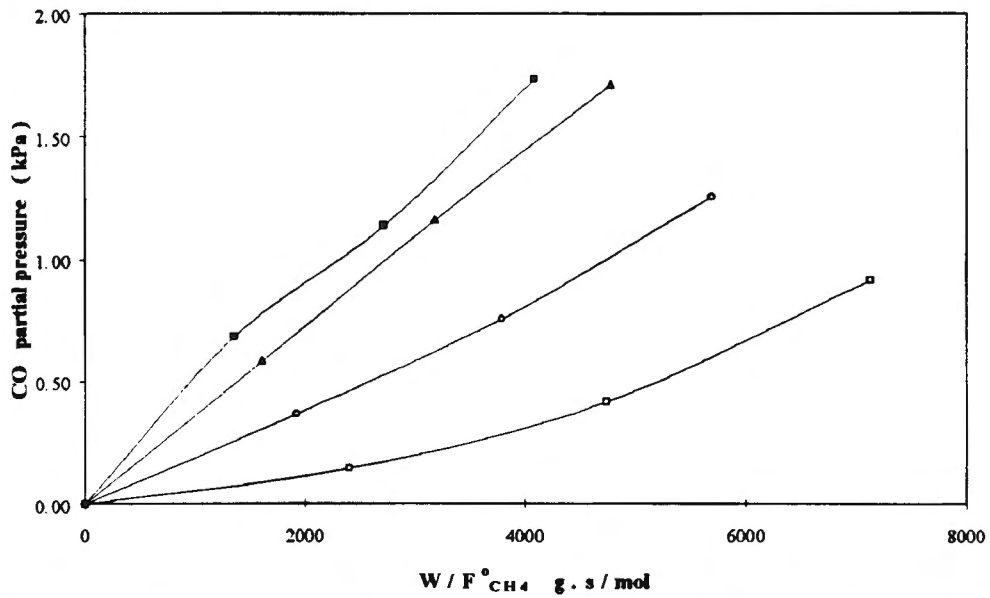
Figure 3-27 The effect of P°_{CH4} on P_{CO} (T = 604°C, P°_{O2} = 1.38 kPa, P°_{CH4} in kPa:□ = 2.75, ○ = 3.44, △ = 4.13, ■ = 4.82)
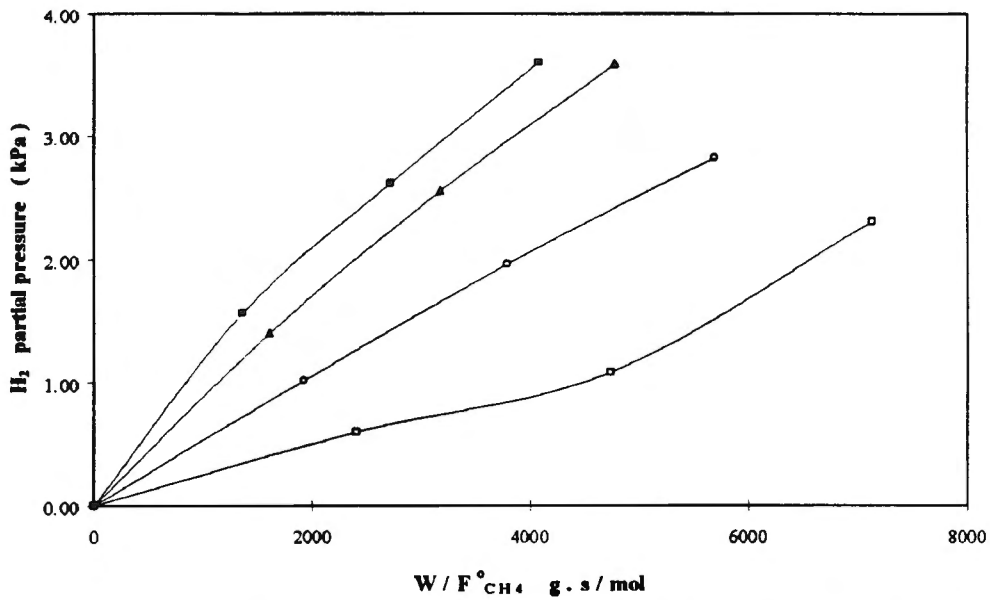
Figure 3-28 The effect of P°_{CH4} on P_{H2} (T = 604°C, P°_{O2} = 1.38 kPa, P°_{CH4} in kPa:□ = 2.75, ○ = 3.44, △ = 4.13, ■ = 4.82)

Hydrogen formation followed exactly the same trends as CO formation and one may

conclude that the formation of the two partial oxidation products are somehow mechanistically linked.

Carbon dioxide partial pressure passed through a maximum and then decreased towards the bed outlet (note the different scale on the y-axis). An increase in $P°_{CH4}$ led to an increase in carbon dioxide production at low $W/F°_{CH4}$ (Figure 3-29) and to the shifting of the position of the peak in P_{CO2} towards the bed inlet. This indicates the earlier onset of CO_2 consumption due to the earlier depletion of oxygen. Downstream of the peak, the slope of the P_{CO2} line became more negative with increasing $P°_{CH4}$, indicating that the rate of carbon dioxide consumption increased at high $P°_{CH4}$. This resulted in the observation that the CO_2 partial pressure at the bed outlet exhibited a net decrease with increasing $P°_{CH4}$.
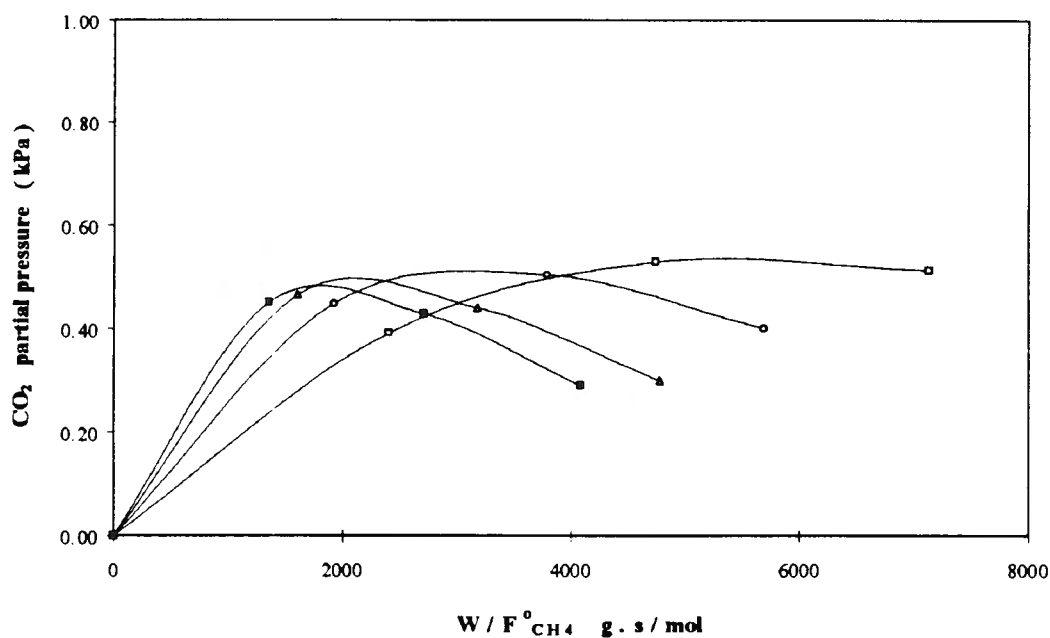
Figure 3-29 The effect of $P°_{CH4}$ on P_{CO2} (T = 604°C, $P°_{O2}$ = 1.38 kPa, $P°_{CH4}$ in kPa:□ = 2.75, ○ = 3.44, △ = 4.13, ■ = 4.82)

As with carbon dioxide, the water partial pressure also passed through a maximum and the position of the peak was also moved towards the bed inlet with increasing $P°_{CH4}$ (Figure 3-30). This is, as in the case of carbon dioxide, an indication of the earlier onset of methane steam reforming due to earlier depletion of oxygen.

The peak in water partial pressure was more pronounced than the peak in carbon dioxide partial pressure. i.e. water consumption occurred more readily than CO_2 consumption.
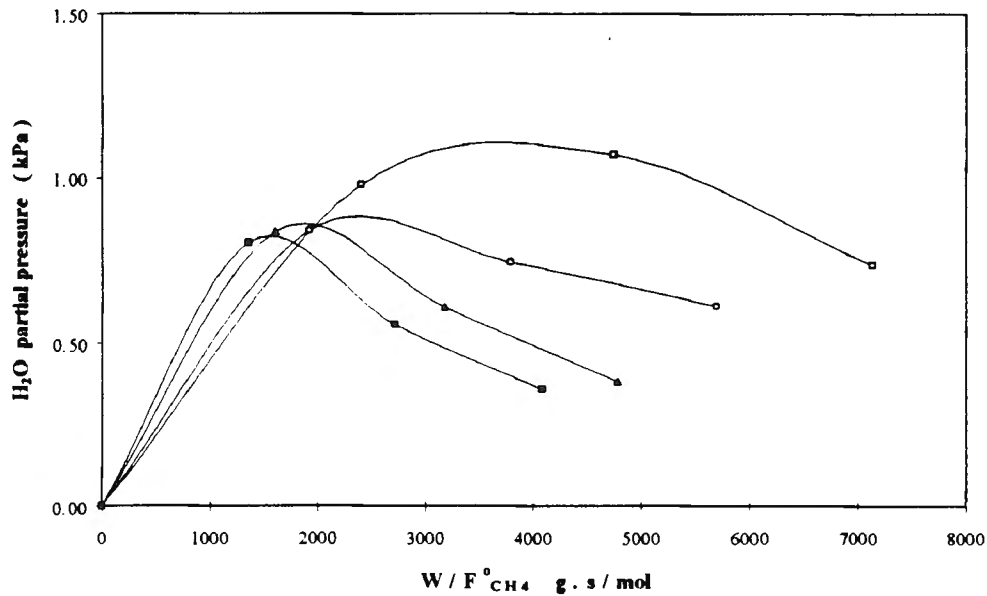
Figure 3-30 The effect of $P^°_{CH4}$ on P_{H2O} (T = 604°C, $P^°_{O2}$ = 1.38 kPa, $P^°_{CH4}$ in kPa:□ = 2.75, ○ = 3.44, ▲ = 4.13, ■ = 4.82)

The expansion due to reaction, expressed as a percentage of the total moles of gas (including inerts) fed to the reactor, was less than 1%. Therefore the trends which were referred to in the above plots of P_i vs. $W/F^°_{CH4}$ are true reflections of the change in moles due to reaction and are not due to dilution because of the formation of products.

3.3.6.2.a.ii. The effect of $P^°_{CH4}$ on reaction kinetics

The initial rate of methane conversion ($r^°_{CH4}$) was plotted as a function of $P^°_{CH4}$ in order to determine the reaction order with respect to methane (see Figure 3-31 and Table 3-10). The reaction order with respect to methane was calculated to be 1.01 when method 7 was used to derive $r^°_{CH4}$ from integral kinetic data and 0.88 when method 3 was used. In both cases the 95% confidence interval included a reaction order of one.

Table 3-10 Reaction order with respect to methane

Curve fitting procedure	Reaction order[a]	R^2
Method 3	0.88 ± 0.14	0.9535
Method 7	1.01 ± 0.25	0.8929
Method 8	0.68 ± 0.14	0.9184

a   95% confidence interval
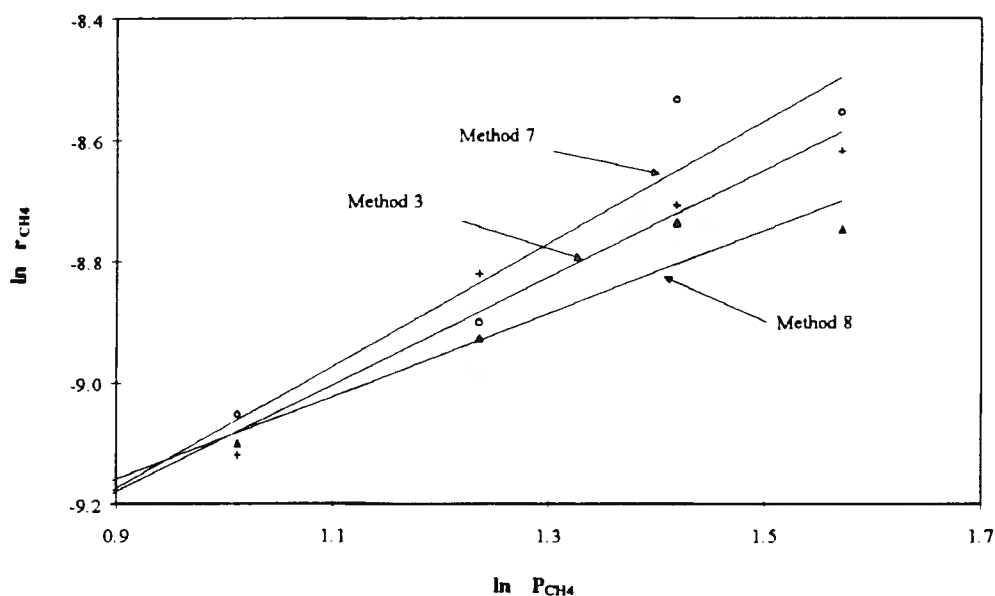
Figure 3-31   Reaction order with respect to methane using three curve-fitting techniques to calculate r_{CH_4} (Method number: + = 3, ○ = 7, ▲ = 8)

However, when method 8 was used, a methane reaction order of only 0.68 ± 0.14 was calculated at the 95% confidence level, thus excluding a methane reaction order of 1.0.

The effect of the inlet methane partial pressure on the initial rate of oxygen consumption was quantified by plotting ln $r°_{O_2}$ as a function of $P°_{CH_4}$ and calculating the slope of the best fit straight line through the data. The effect of $P°_{CH_4}$ on the rates of product formation has also been investigated. In the same manner as for oxygen, the rate of formation of each of the products (CO, H_2, CO_2 and H_2O) was plotted as a function of the inlet methane partial pressure on log-log scales and the slopes were again calculated from best fit straight lines through the data. The results of these calculations are given in Table 3-11. The "reaction orders" thus obtained are not in any way indicative of specific elementary reactions and orders greater than 2, for example, do not imply tri- or termolecular collisions. These

"pseudo-reaction orders" of the products should rather be seen as an indication of the general influence of methane partial pressure on the rates of product formation. Positive values indicate that an increase in inlet methane partial pressure enhanced the rate of product formation (or oxygen consumption) and negative values imply that P°_{CH4} inhibited the rate of formation of a specific product or the rate of consumption of oxygen.

Table 3-11 Pseudo-reaction orders of all the species with respect to methane partial pressure

Compound	Reaction order[a]	R^2
CH_4	1.01 ± 0.25	0.8929
O_2	0.87 ± 0.09	0.9786
CO	3.56 ± 0.66	0.9357
H_2	1.83 ± 0.22	0.9729
CO_2	0.42 ± 0.10	0.8982
H_2O	-0.35 ± 0.27	0.4625

a r°_{CH4} and r°_{O2} were calculated with method 7
    The rates of product formation were calculated from tangents to hand-drawn curves through the P_i vs. W/F°_{CH4} data.
    Intervals are at the 95% confidence level

Using this line of reasoning, an increase in methane partial pressure enhanced the rate of formation of all products except water as well as enhancing the rate of oxygen consumption. The effect on partial oxidation products were more pronounced than on the deep oxidation products, as expected of a more fuel-rich mixture. The negative pseudo-reaction order of water has a very wide 95% confidence interval and consequently the conclusions based on this data point are not very firm.
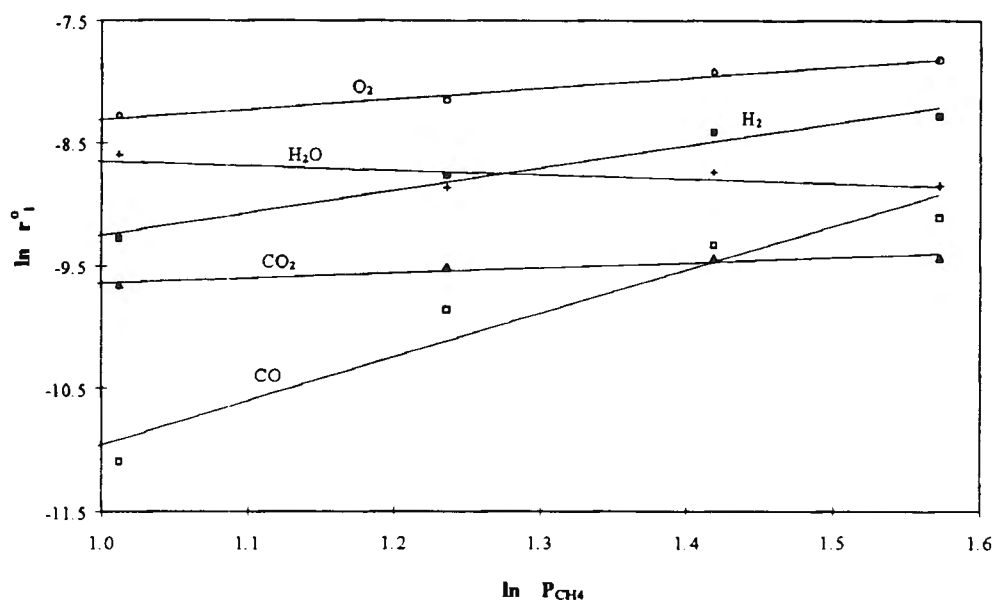
Figure 31-1   Pseudo-reaction orders of the rate of oxygen consumption and product formation with respect to P°_{CH4}

3.3.6.2.b.   Oxygen partial pressure

3.3.6.2.b.i.   The effect of P°_{O2} on reactants and reaction products

P°_{O2} was varied between 0.79 kPa and 1.63 kPa at constant methane partial pressure of 3.0 kPa. The effect of oxygen partial pressure on methane and oxygen conversion is shown in Figure 31-2. As the oxygen partial pressure was increased, oxygen conversion decreased. Methane conversion also decreased with increasing P°_{O2} at low W/F°_{CH4}. Thus, the overall reaction (methane and oxygen) was slowed down at high oxygen partial pressure. This is indicative of a greater abundance of an inactive (or less active) oxygen species at high P°_{O2}.

The flattening out of the X_{CH4} curve at low P°_{O2} and high W/F°_{CH4} follows from a limited amount of oxygen or deep oxidation products available to react with methane.

As expected, an increase in the inlet concentration of oxygen enhanced the formation of total oxidation products (carbon dioxide and water) at the expense of carbon monoxide and hydrogen. The effect of P°_{O2} on CO formation is illustrated in Figure 31-3.
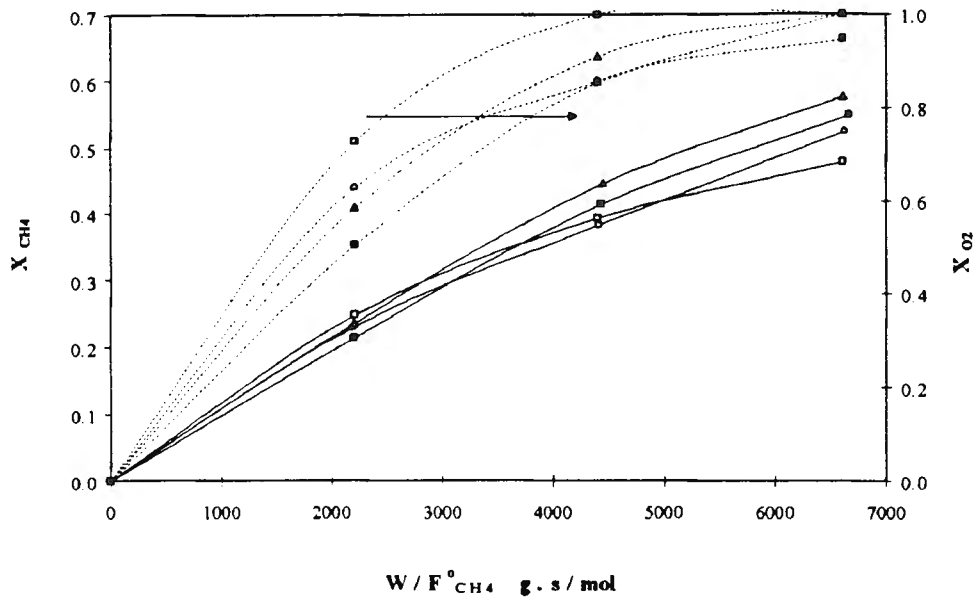
Figure 31-2 The effect of P_{O_2} on X_{CH_4} (solid lines) and X_{O_2} (T = 604°C, $P°_{CH_4}$ = 3.0 kPa, $P°_{O_2}$ in kPa: □ = 0.99, ○ = 1.20, ▲ = 1.34, ■ = 1.63)
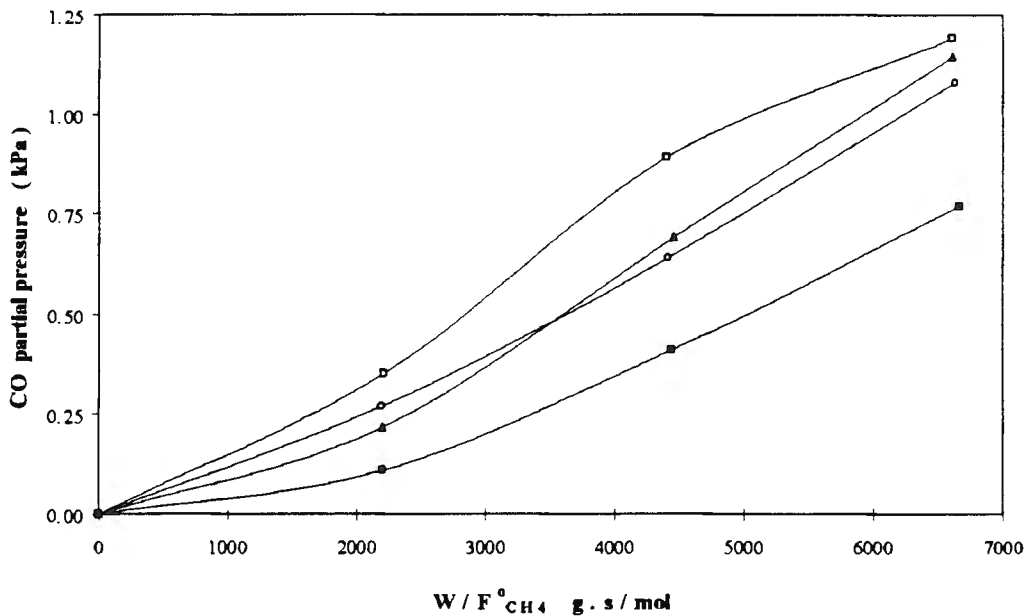
Figure 31-3 The effect of $P°_{O_2}$ on P_{CO} (T = 604°C, $P°_{CH_4}$ = 2.96 kPa, $P°_{O_2}$ in kPa: □ = 0.99, ○ = 1.20, ▲ = 1.34, ■ = 1.63)

The shape of the P_{CO} vs. $W/F°_{CH_4}$ curve at $P°_{O_2}$ = 0.99 kPa is typical of a secondary product in that it exhibits an inflection point. At higher $P°_{O_2}$ values, this feature became less pronounced as the CO formation was suppressed. Within the range of $P°_{O_2}$ and $W/F°_{CH_4}$ studied, carbon monoxide was always present and the inevitable conclusion follows that carbon monoxide is a product of both primary and secondary reactions. While the decrease in P_{CO} was directly related to an increase in oxygen partial pressure at low $W/F°_{CH_4}$ values,

the trend was somewhat obscured at higher values of $W/F°_{CH4}$.

Hydrogen formation was also depressed at high $P°_{O2}$ (Figure 31-4) and the same general trends observed with CO partial pressure was also seen with respect to hydrogen.
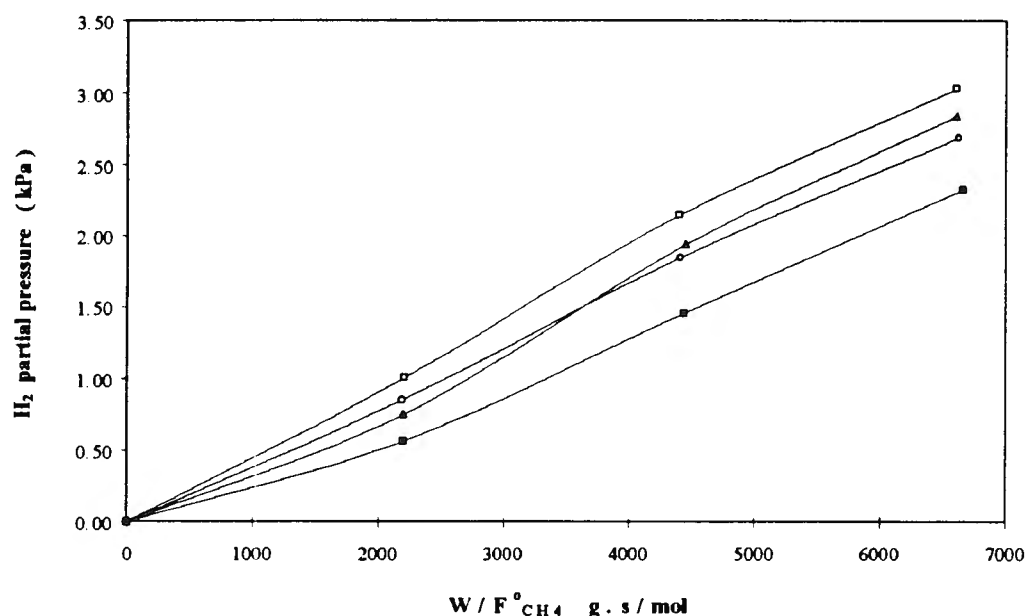
Figure 31-4   The effect of $P°_{O2}$ on P_{H2} (T = 604°C, $P°_{CH4}$ = 2.96 kPa, $P°_{O2}$ in kPa: □ = 0.99, ○ = 1.20, ▲ = 1.34, ■ = 1.63)

The inflection point observed in Figure 31-3 was, however, less pronounced in Figure 31-4.   The effect of $P°_{O2}$ on the formation of carbon dioxide is shown in Figure 31-5.

As previously observed, P_{CO2} passed through a maximum and then either decreased slightly or remained constant deeper into the bed.   Carbon dioxide was enhanced by the presence of more oxygen in the feed.   The effect was more pronounced towards the bed outlet.

The effect of $P°_{O2}$ on water partial pressure is shown in Figure 31-6.   As with carbon dioxide, water formation was enhanced by the presence of more oxygen in the feed and the behaviour of P_{H2O} downstream of the peak was hardly affected by $P°_{O2}$.   The presence of oxygen had little effect on the position of the peak in either water or carbon dioxide formation.
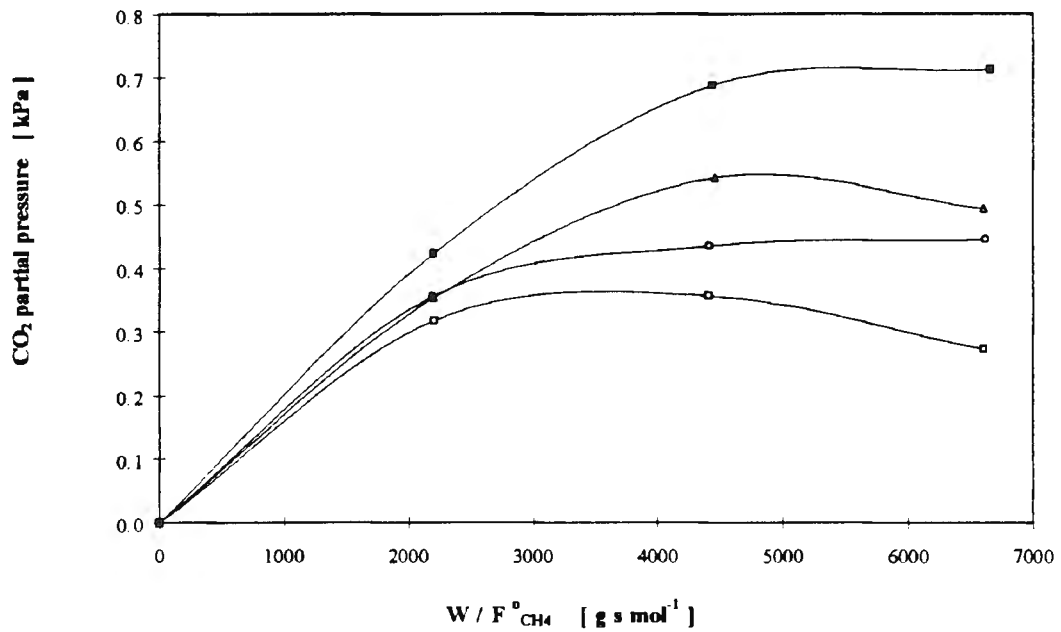
Figure 31-5 The effect of P°_{O2} on P_{CO2} (T = 604°C, P°_{CH4} = 2.96 kPa, P°_{O2} in kPa: □ = 0.99, ○ = 1.20, △ = 1.34, ■ = 1.63)
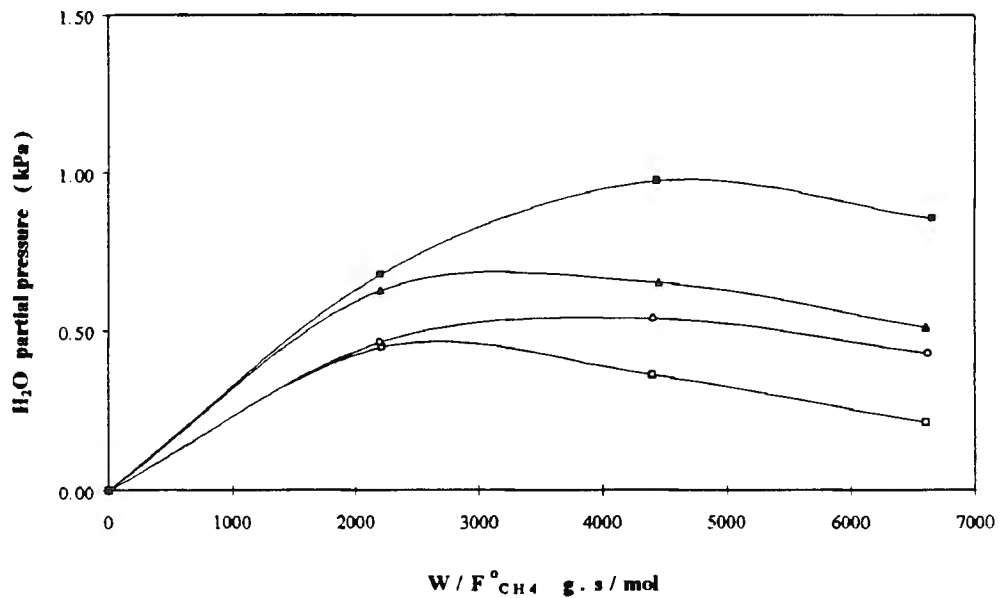
Figure 31-6 The effect of P°_{O2} on P_{H2O} (T = 604°C, P°_{CH4} = 2.96 kPa, P°_{O2} in kPa: □ = 0.99, ○ = 1.20, △ = 1.34, ■ = 1.63)

The effect of P°_{O2} of the H_2/CO ratio as a function of W/F°_{CH4} is shown in Figure 31-7. At the bed inlet, P°_{O2} had a significant enhancing effect on the H_2/CO ratio, but the ratio steadily declined deeper into the catalyst bed for all P°_{O2}. Towards the bed outlet, the H_2/CO ratio of the various experiments approached a common value of about 2.5.
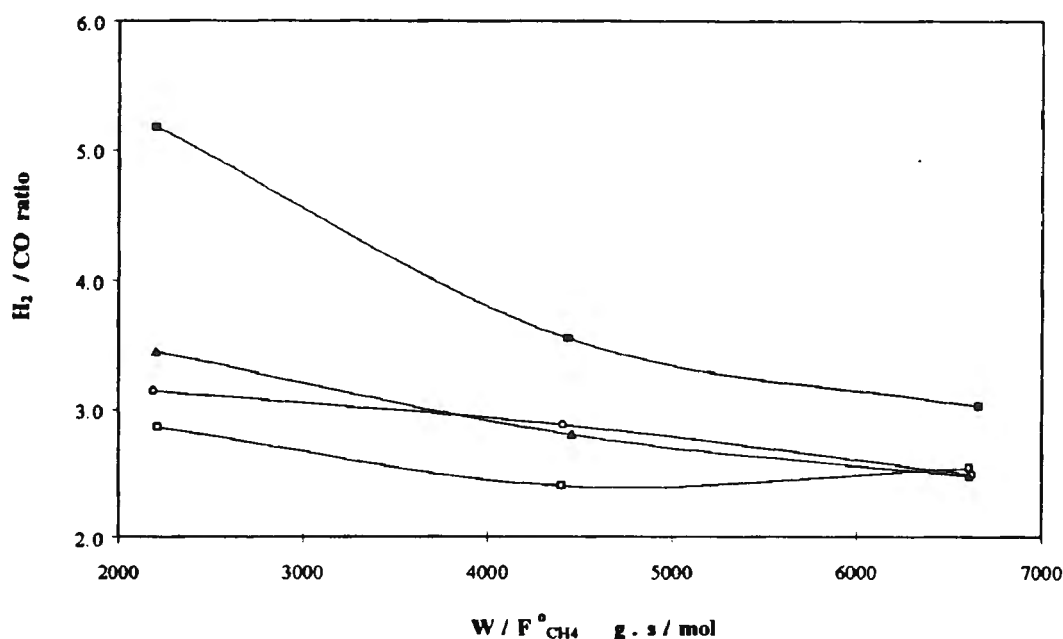
Figure 31-7 The effect of $P°_{O2}$ on the H_2/CO ratio (T = 604°C, $P°_{CH4}$ = 2.96 kPa, $P°_{O2}$ in kPa: □ = 0.99, ○ = 1.20, ▲ = 1.34, ■ = 1.63)

3.3.6.2.b.ii. The effect of $P°_{O2}$ on reaction kinetics

The reaction order with respect to oxygen was obtained by plotting $\ln(r_{CH4})$ as a function of $\ln(P°_{O2})$ and the results are summarized in Table 3-12.

Table 3-12 Reaction order of the rate of methane consumption with respect to oxygen (T = 604°C, $P°_{CH4}$ = 2.96 kPa)

Curve fitting procedure	Reaction order[a]	R^2
Method 3	-0.24 ± 0.26	0.2731
Method 7	-0.14 ± 0.16	0.2462
Method 8	0.22 ± 0.12	0.5828

a   95% Confidence interval

With the exception of method 8, a zero-order dependence of the rate of methane consumption on the oxygen partial pressure falls inside the 95% confidence interval, suggesting that the rate of methane consumption was independent of oxygen partial pressure.

Table 3-13 Pseudo-reaction orders of all species with respect to oxygen partial pressure

Product	Reaction order[c]	R^2
CH_4	-0.14 ± 0.16[a]	0.2801
O_2	0.14 ± 0.01[a]	0.9858
CO	-2.75 ± 0.54[b]	0.9291
H_2	-1.29 ± 0.12[b]	0.9838
CO_2	0.37 ± 0.28[b]	0.4674
H_2O	0.87 ± 0.32[b]	0.7880

a r°_{CH4} and r°_{O2} values were calculated by method 7
b   The rates that were used to calculate the reaction orders were calculated from tangents that were constructed to hand-drawn smooth curves through the P_i vs. W/F°_{CH4} data.
c   95% Confidence interval

The influence of oxygen on the rate of formation of the products and the rate of reactant consumption were quantified as before by plotting ln r°_i as a function of ln P°_{O2} and taking the slope of the best-fit line through the data (Table 3-13).   The highly negative reaction orders of the partial oxidation products indicates that the rate of hydrogen and carbon monoxide production (r°_{H2} and r°_{CO}) was depressed by high oxygen partial pressure. The rate of formation of the total oxidation products were, on the other hand, enhanced by the presence of an excess of oxygen. None of the reaction orders changed sign because of the magnitude of the 95% confidence interval. This is indicative of the fact that the direction of change in the rate of compound formation or disappearance as a function of P°_{O2} was within the experimental error.

3.3.6.3. Co-feeding of products

3.3.6.3.a.   Carbon monoxide partial pressure

3.3.6.3.a.i. The effect of P_{CO} on reaction products and reactants

The effect of carbon monoxide co-feeding on the methane and oxygen conversion is shown in Figure 31-8. At the bed inlet, a small amount of carbon monoxide (P°_{CO} = 1.42 kPa) appeared to enhance the methane conversion, but higher values of carbon monoxide in the inlet caused a decrease in X_{CH4}.

$$W / F^{\circ}_{CH_4} \quad g . s / mol$$
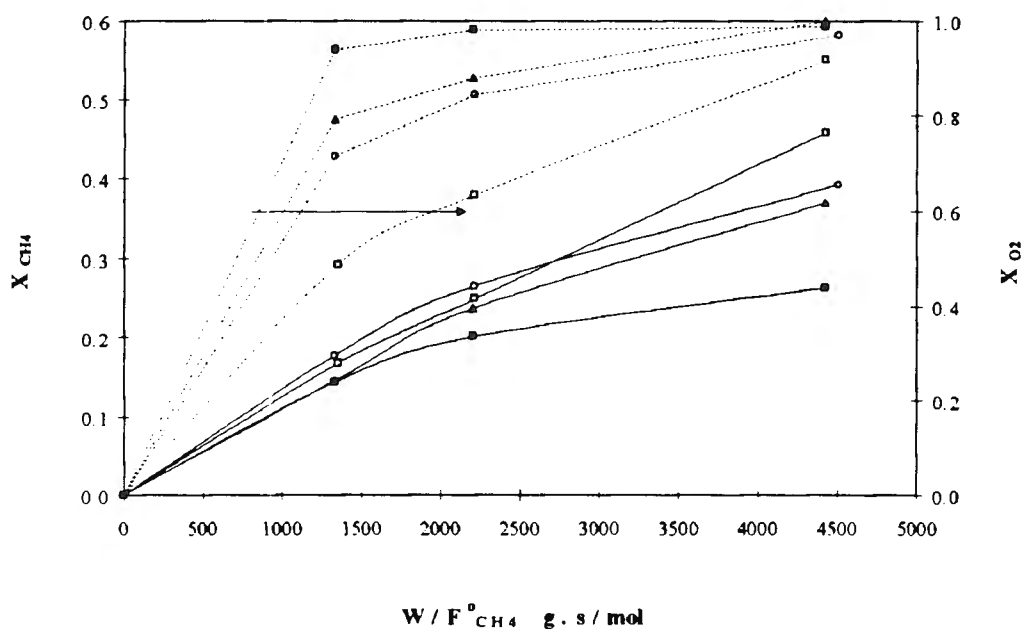
Figure 31-8 The effect of P°_{CO} on X_{CH_4} and X_{O_2} (T = 604°C, P°_i in kPa: CH_4 = 2.96, O_2 = 1.34, CO: □ = 0.00, ○ = 1.42, ▲ = 2.84, ■ = 6.30)

The substantial increase in oxygen conversion suggests that oxygen reacted preferentially with carbon monoxide and that there was thus less oxygen available to react with methane, thus depressing the methane conversion. The fact that methane conversion was enhanced at low carbon monoxide partial pressure (P°_{CO} = 1.42 kPa) may on the one hand be due to experimental error. However, the data corresponding to no CO in the feed (□ data points) are the average of two replicate sets of experiments and the enhanced methane conversion at low P°_{CO} may perhaps be ascribed to some other peculiarity of the reaction pathway. The present data, however, prevents one from drawing any further conclusions about this phenomenon.

The complete product composition when carbon monoxide was present at the reactor inlet is shown in Figure 31-9. This may be compared with the product spectrum in the absence of any co-fed products shown in Figure 3-19. The main feature of the data shown in Figure 31-9 is that the partial pressure of CO passed through a minimum at $W/F^{\circ}_{CH_4}$ = 1500 g.s.mol^{-1} and subsequently increased as the $W/F^{\circ}_{CH_4}$ was increased. This finding, taken in conjunction with the enhanced oxygen conversion (see Figure 31-8) and enhanced carbon dioxide production shown in Figure 31-12, provides conclusive evidence that the oxidation of carbon monoxide was responsible for the enhanced oxygen conversion.
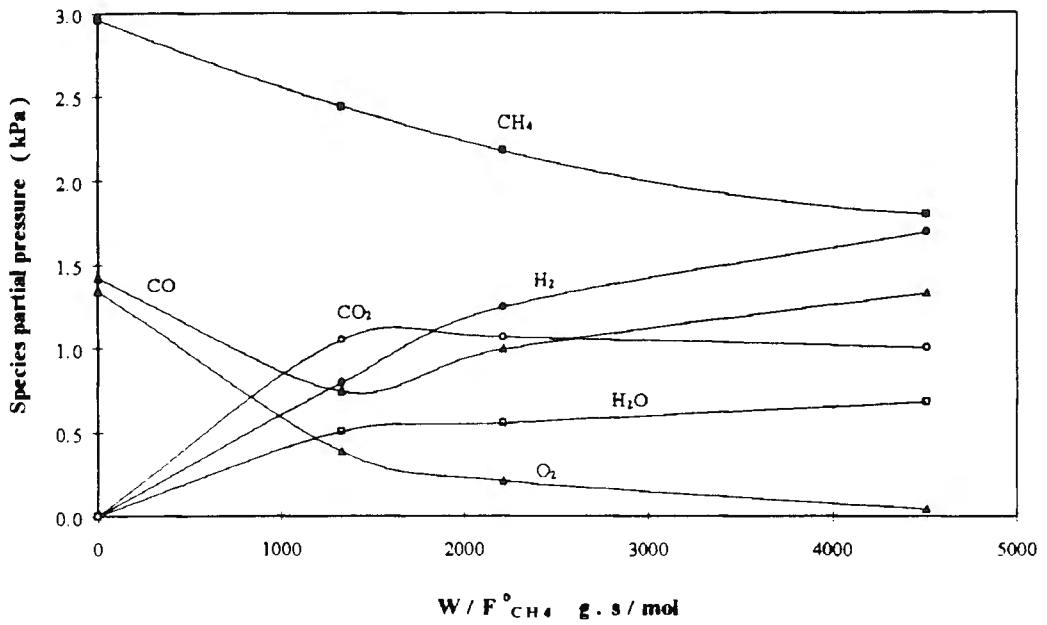
Figure 31-9 The effect of CO co-feeding on the product composition (T = 604°C, $P°_1$ in kPa: CH_4 = 2.96, O_2 = 1.34 and CO = 1.42)

The carbon monoxide partial pressure measured at the reactor outlet never exceeded the corresponding inlet partial pressure ($P°_{CO}$). This is shown in Figure 31-10.
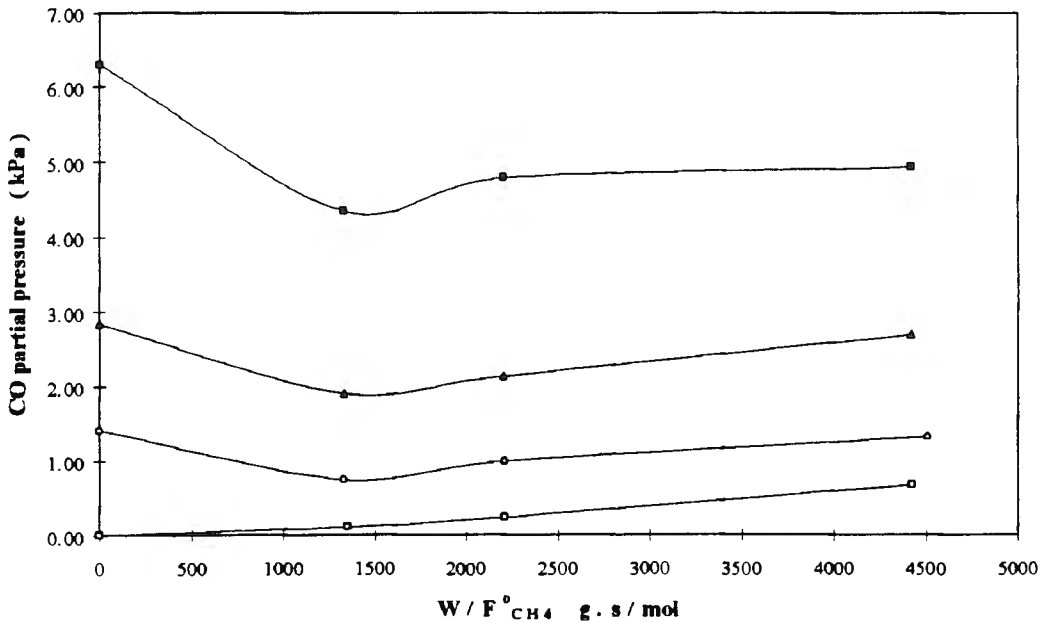
Figure 31-10 The effect of $P°_{CO}$ on P_{CO} (T = 604°C, $P°_1$ in kPa:CH_4 = 2.96, O_2 = 1.34, CO: □ = 0.00, ○ = 1.42, △ = 2.84, ■ = 6.30)

As P°_{CO} was increased, the extent of the carbon monoxide consumption increased and the difference between the inlet and outlet partial pressure of carbon monoxide increased. The suggests that the rate of the reaction repsonsible for CO consumption was directly proportional to CO partial pressure.

Hydrogen formation (Figure 31-11) was enhanced by the co-feeding of carbon monoxide at low W/F°_{CH4}, but this effect diminished as the W/F°_{CH4} was increased. Furthermore, the experiment with the highest inlet partial pressure of CO did not follow the trend of ever-increasing P_{H2} values with increasing P°_{CO}.
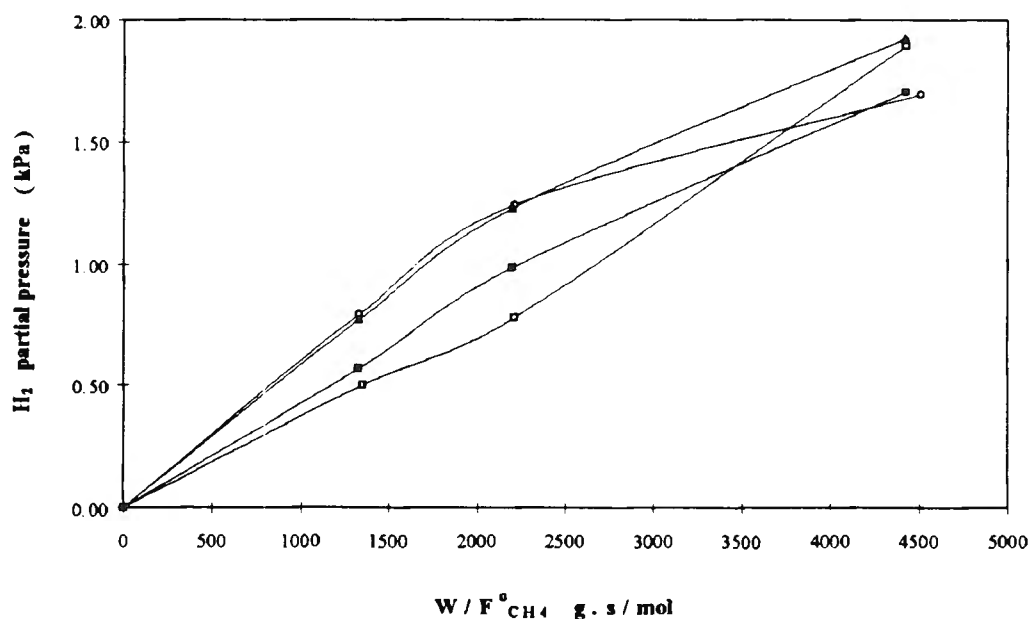
Figure 31-11 The effect of P°_{CO} on P_{H2} (T = 604°C, P°_1 in kPa:CH$_4$ = 2.96, O$_2$ = 1.34, CO: □ = 0.00, O = 1.42, ▲ = 2.84, ■ = 6.30)

With oxygen reacting with both CO and methane, the oxygen partial pressure was effectively lowered compared to a feed of pure methane and oxygen. It was previously shown (Table 3-13) that a decrease in oxygen partial pressure led to the enhanced formation of partial oxidation products. This would offer one explanation for the enhanced hydrogen formation at low W/F°_{CH4} in Figure 31-11. An alternative explanation would be that with more carbon monoxide present, the water-gas shift reaction would be forced to the right, thus leading to the formation of more hydrogen.

150

The experiment with no carbon monoxide in the feed exhibited a steady increase in the formation of CO_2 along the catalyst bed. In the presence of carbon monoxide, however, CO_2 passed through a maximum (Figure 31-12). As P°_{CO} was increased, the maximum became more apparent and the slope of the P_{CO2} vs. W/F°_{CH4} line downstream of the peak, and thus the rate of carbon dioxide consumption, increased slightly. This indicates, as expected, that the rate of dry reforming is directly proportional to CO_2 partial pressure. P_{CO2} was higher than P_{H2O} at all values of W/F°_{CH4}.
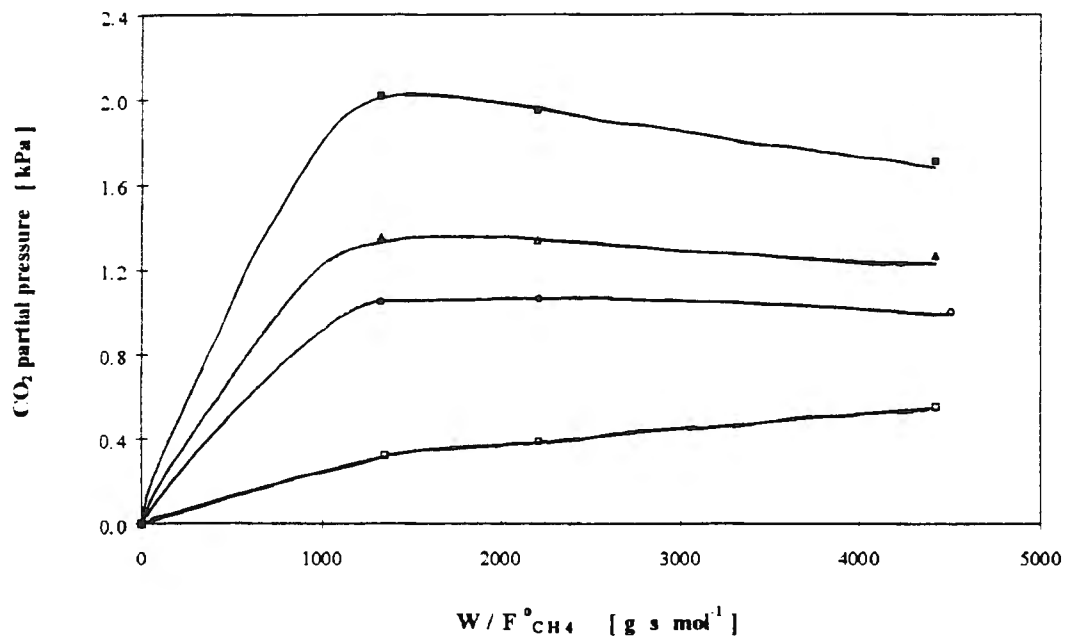
Figure 31-12 The effect of P°_{CO} on P_{CO2} (T = 604°C, P°_i in kPa, CH_4 = 2.96, O_2 = 1.34, CO: □ = 0.00, ○ = 1.42, ▲ = 2.84, ■ = 6.30)

The effect of P°_{CO} on the outlet partial pressure of water is shown in Figure 31-13. There is considerable spread in the data, most probably due to the fact that P_{H2O} was calculated and not directly measured. In spite of this uncertainty, the data indicate that water partial pressure with CO in the reactor feed was lower than without carbon monoxide in the reactor feed (□ data points). The lower P_{H2O} in the presence of carbon monoxide in the feed is most likely due to the fact that oxygen reacted preferentially with carbon monoxide and therefore inhibited the total oxidation of methane to water.
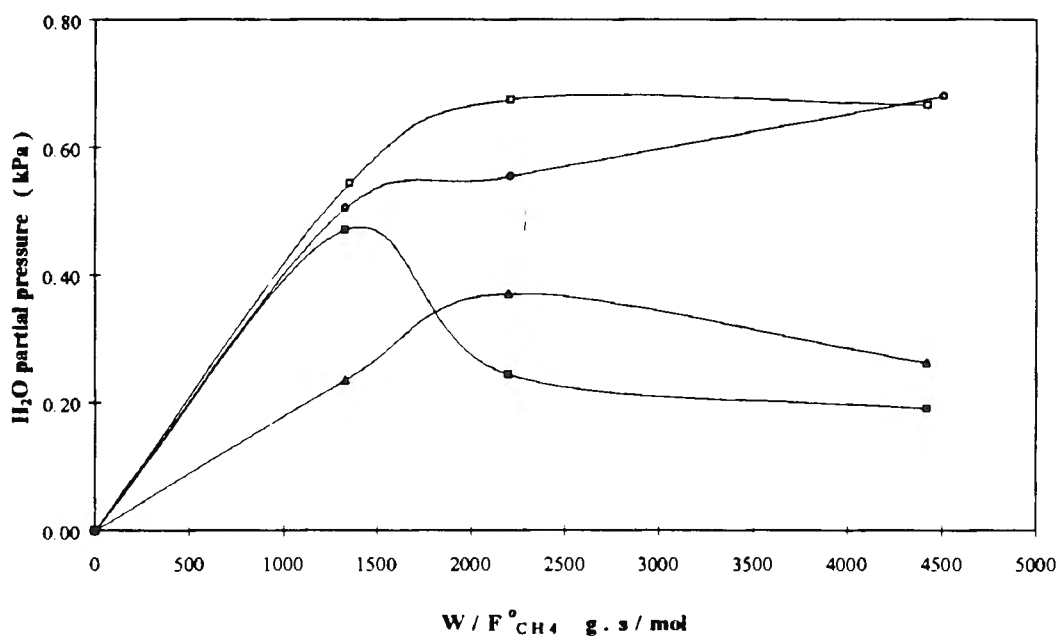
Figure 31-13 The effect of P°_{CO} on P_{H2O} (T = 604°C, P°_1 in kPa, CH_4 = 2.96, O_2 = 1.34, CO: □ = 0.00, ○ = 1.42, △ = 2.84, ■ = 6.30)

If the steam reforming of methane was the major source of carbon monoxide when oxygen had been depleted and less water was formed early in the catalyst bed when CO was co-fed, it could conceivably follow that the carbon monoxide partial pressure at the outlet never exceeded the inlet values. In addition to this, the presence of excess carbon monoxide would force the water-gas shift reaction to the right and thus consume more water in the process than when no CO was present in the feed. This would lead to low P_{H2O} values.

A graph was compiled to show the effect of P°_{CO} on the H_2/CO ratio (see Figure 31-14). The H_2/CO ratio which was a weak function of W/F°_{CH4} decreased sharply as the carbon monoxide partial pressure at the inlet was increased. The H_2/CO ratio decreased with increasing P°_{CO} and seemed to level out to a constant value at high W/F°_{CH4}. The second feature of the H_2/CO data is the direction of change in H_2/CO with increasing W/F°_{CH4}. At low values of P°_{CO} the H_2/CO ratio decreased and then stabilized with increasing W/F°_{CH4} while an increase in P°_{CO} caused H_2/CO to increase with W/F°_{CH4}. These observations suggest that the gas composition was approaching an equilibrium value at increasing W/F°_{CH4}.
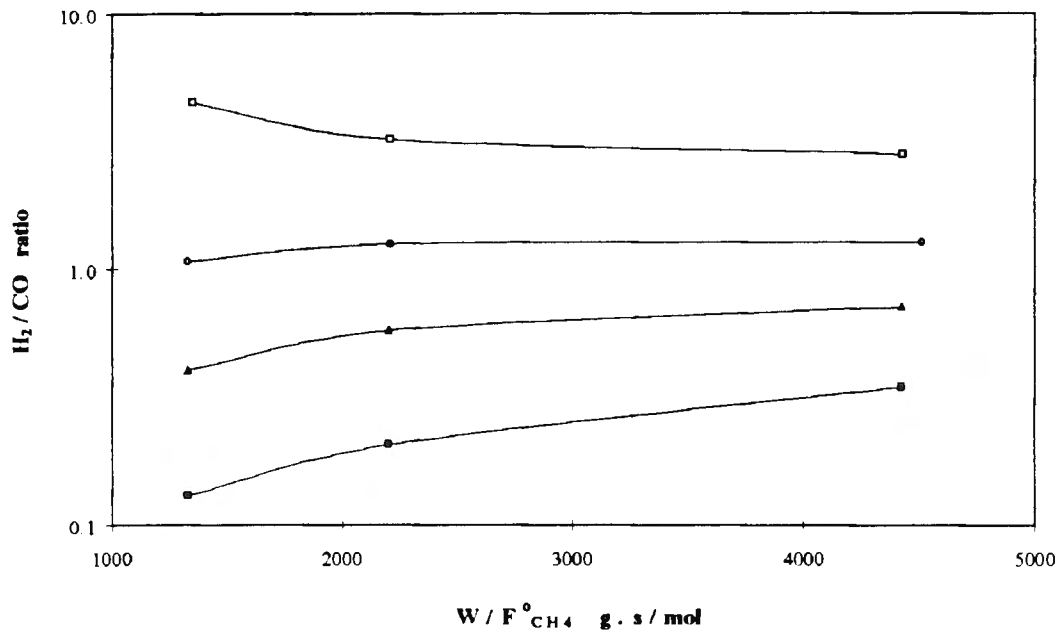
Figure 31-14 The effect of P°_{CO} on the H_2/CO ratio (T = 604°C, P°_1 in kPa: CH_4 = 2.96, O_2 = 1.34, CO: □ = 0.00, ○ = 1.42, ▲ = 2.84, ■ = 6.30)

3.3.6.3.a.ii.   The effect of P_{CO} on reaction kinetics

The reaction order of the rate of methane consumption with respect to carbon monoxide partial pressure was determined by three curve-fitting methods and the results are summarized in Table 3-14.

Table 3-14 Reaction order of the rate of methane consumption with respect to carbon monoxide partial pressure

Curve fitting procedure	Reaction order[a]	R^2
Method 3	-0.14 ± 0.06	0.8266
Method 7	-0.27 ± 0.07	0.9389
Method 8	-0.28 ± 0.07	0.9388

a   95% Confidence interval

All three curve-fitting methods led to a negative reaction order, implying that the presence of carbon monoxide depressed the rate of methane consumption at the 95% confidence level.

Whether this is the result of adsorption phenomena or the fact that the CO oxidation reaction preferentially consumes oxygen which would otherwise have reacted with methane, is not clear at this point. The dependence of the rate of oxygen consumption and the rate of formation of other products on the carbon monoxide inlet partial pressure is presented in Table 3-15.

In addition to the effect of carbon monoxide co-feeding on the rate of methane consumption, the effect of CO co-feeding on the rate of formation of various products were quantified as before by plotting the rate of formation as a function of P°_{CO} and calculating the slope of the best-fit straight lines through the data. All the rates of product formation were determined from tangents that were constructed to hand-drawn curves through P_i vs. W/F°_{CH4} data. The rate of oxygen consumption was calculated by method 7.

A poor correlation was found with respect to the rate of water formation. This is not surprising when the considerable spread in experimental data shown in Figure 31-13 is taken into account. The 95% confidence interval gives an indication of the lack of confidence in this data point. The low correlation coefficient of the rate of CO consumption also led to a wide confidence interval, although the sign of the pseudo-reaction order for CO consumption did not change because of the lack of fit. This precludes any meaningful conclusions about the effect of P°_{CO} on the rate of CO consumption.

154

Table 3-15 Pseudo-reaction orders with respect to carbon monoxide partial pressure
(T = 604°C, $P°_{CH4}$ = 2.96 kPa, $P°_{O2}$ = 1.34 kPa)

Compound	Reaction order	R^2
CH_4	-0.27 ± 0.07	0.9389
O_2	0.56 ± 0.14	0.9423
CO	-1.10 ± 0.81[a]	0.6513
H_2	-0.25 ± 0.09	0.8936
CO_2	0.45 ± 0.06	0.9848
H_2O	0.03 ± 0.65	0.0002

a   The reaction order refers to the rate of CO consumption and not the rate of CO formation.

As far as the formation of other products are concerned, the data in Table 3-15 confirms the finding that an increase in $P°_{CO}$ led to both enhanced carbon dioxide formation and a higher rate of oxygen consumption. The negative reaction order of hydrogen does not contradict the finding that the presence of CO in the feed enhanced the formation of hydrogen when compared to a feed containing no hydrogen. It is rather a finding that gives information about the magnitude of the influence of $P°_{CO}$ on $r°_{H2}$ when comparing a number of experiments where CO was present at the bed inlet.

3.3.6.3.b. Hydrogen partial pressure

3.3.6.3.b.i. The effect of P_{H2} on reactant consumption and product formation

The effect of $P°_{H2}$ on the product composition is summarized in Table C-11 in the appendix. The data contained therein was used to generate plots of the complete product spectrum as a function of $W/F°_{CH4}$. An example of the product spectrum of an experiment during which hydrogen was co-fed to the reactor is shown in Figure 31-15. As before, hydrogen partial pressure exhibited an inflection point. The oxygen line is dotted to indicate that its position was uncertain due to the early consumption of oxygen. The P_{H2O} line which was calculated from an oxygen balance, had the same inherent uncertainty and was therefore also denoted by a dotted line.
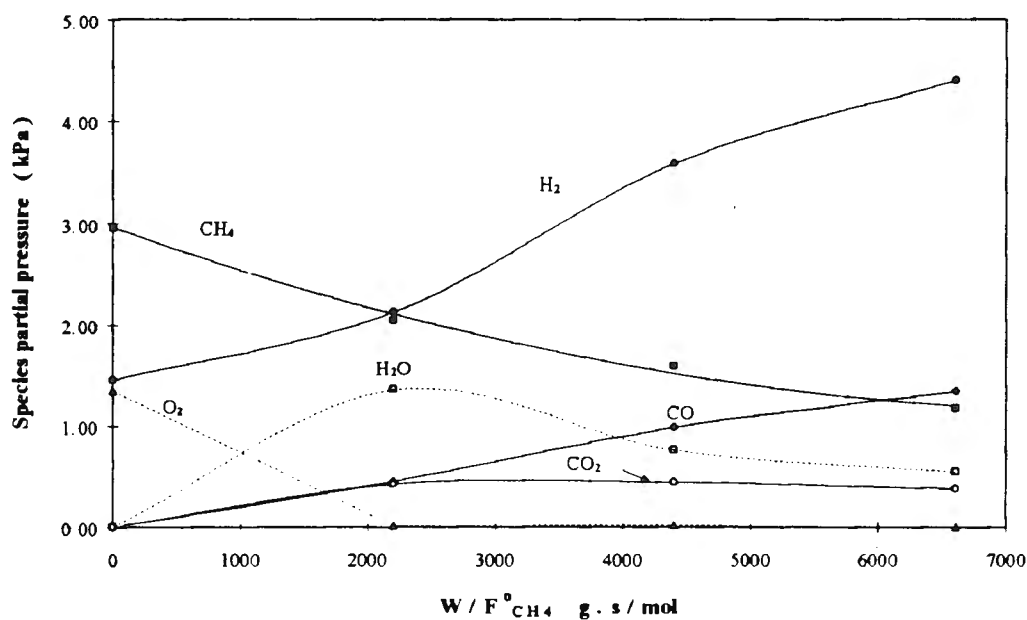
Figure 31-15 The effect of H_2 co-feeding on the product composition (T = 604°C, $P°_{CH4}$ = 2.96 kPa, $P°_{O2}$ = 1.34 kPa, $P°_{H2}$ = 1.45 kPa)

One of the outstanding features of all the experiments during which hydrogen was co-fed was that the oxygen was completely converted at even the lowest value of $W/F°_{CH4}$.
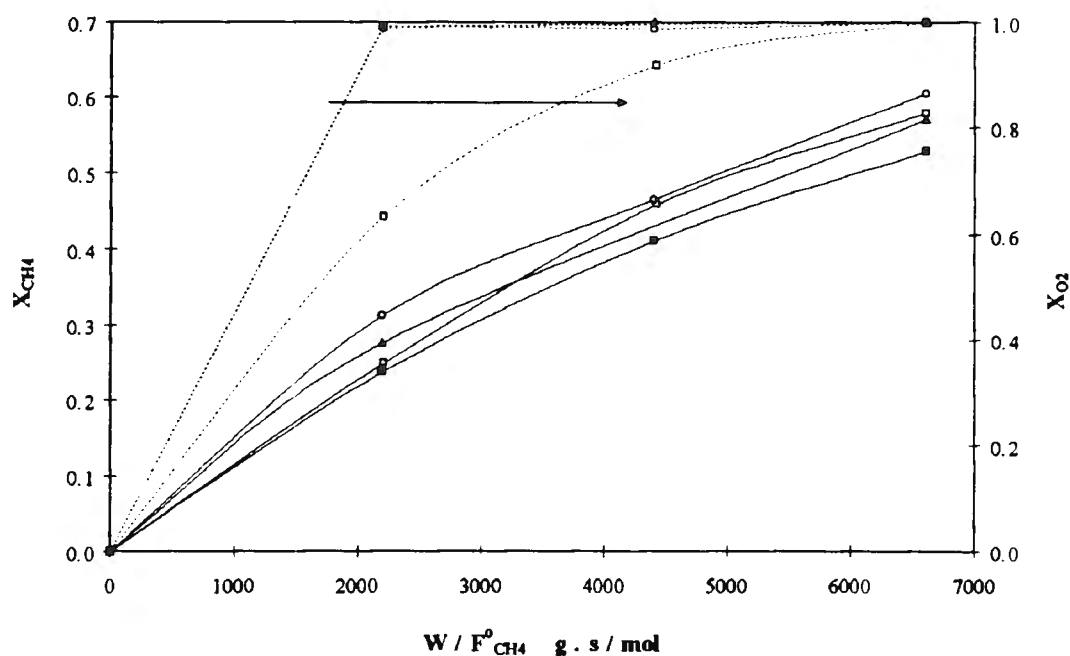
Figure 31-16 The effect of $P°_{H2}$ on conversion (T = 604°C, $P°_i$ in kPa: CH_4 = 2.96, O_2 = 1.34, H_2: □ = 0.00, ○ = 1.45, ▲ = 2.84, ■ = 5.61)

At the lowest amount of co-fed hydrogen ($P°_{H2}$ = 1.45 kPa), methane conversion was enhanced at all $W/F°_{CH4}$ investigated (Figure 31-16) when compared to the methane conversion in the absence of co-fed hydrogen. When the hydrogen content of the feed was increased to 5.61 kPa, methane conversion was lower than the case without any hydrogen in the feed at all $W/F°_{CH4}$ investigated. However, when the hydrogen inlet partial pressure was between these two values ($P°_{H2}$ = 2.84 kPa), methane conversion was enhanced at low $W/F°_{CH4}$ and depressed at high $W/F°_{CH4}$.

As shown later, the presence of hydrogen at the inlet led to an increase in water production (Figure 31-19). The rate of the steam reforming reaction will depend on the concentration of the water with respect to methane and the forward rate constant of the steam reforming reaction at the temperature investigated. Hence, if the rate of the steam reforming reaction was higher than the rate of other phenomena that affect the methane conversion, the increase in methane conversion, if indeed occurring, should be directly proportional to the hydrogen partial pressure.

On the other hand, it may be argued that by reacting with oxygen to form water, hydrogen led to a "cleaning" of the nickel surface, thus lowering the oxygen coverage and exposing more active sites for methane adsorption. The implication of this scenario is two-fold. In the first instance one may argue that a lower oxygen surface coverage will lead to a lowering in methane conversion rate (if surface reaction between methane fragments and surface oxygen is the rate-determining step). Alternatively it may be said that the exposure of more vacant sites would enhance the methane conversion if methane adsorption is the rate-determining step. In the absence of more information on the reaction mechanism, it is impossible to use the above argument to explain the trends in the methane conversion as a function of hydrogen inlet partial pressure.

A third argument was put forward by Pyatnitsky [161] who found that hydrogen inhibited the rate of methane oxidation on a Pd/SiO_2 catalyst when 0.2 vol% H_2 was introduced to a feed containing 0.5 vol% CH_4 and 0.25 vol% O_2. In their case, the inhibition effect was ascribed to preferential adsorption of H_2 onto sites that favour the dissociative adsorption of methane, thus forcing reaction (3-15) to the left.

$$CH_4 + z \rightarrow CH_3 - z + H - z \qquad\qquad\text{(3-15)}$$

The author did not, however, present quantitative results on the effect of hydrogen partial pressure on the lowering of r_{CH4}.

Considered on its own, none of the arguments set out above allows one to fully explain the enhancement of X_{CH4} at low P°_{H2} and the decrease in X_{CH4} at high P°_{H2}. While it may be possible that the rates of the various surface phenomena considered above, i.e. steam reforming, methane adsorption and surface reaction between adsorbed O- and C- fragments, may change from one feed condition to another, it is impossible to quantify at this stage.

The effect of hydrogen co-feeding on carbon monoxide formation is shown in Figure 31-17.
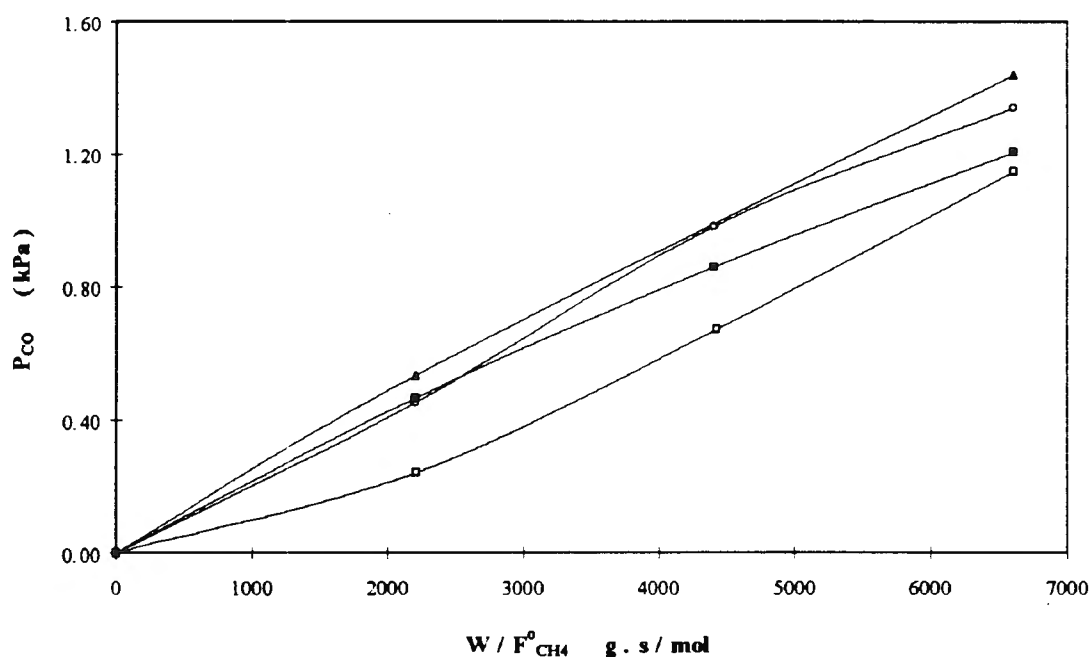
Figure 31-17 The effect of P°_{H2} on P_{CO} (T = 604°C, P°_i in kPa: CH_4 = 2.96, O_2 = 1.34, H_2: □ = 0.00, ○ = 1.45, ▲ = 2.84, ■ = 5.61)

It was found that the presence of any amount of hydrogen in the reactor feed enhanced the production of carbon monoxide. There was, however, no discernable trend with respect to

the degree to which P_{CO} was enhanced as a function of $P°_{H2}$. The increase in carbon monoxide partial pressure may be ascribed to the water-gas shift reaction being pushed to the left. The corollary of this would be that the CO_2 level would be depressed. This was indeed observed as shown in Figure 31-18. It was shown in Table 3-13 that a reduced oxygen partial pressure enhanced the formation of carbon monoxide. In addition to the argument concerning the water-gas shift reaction mentioned above, the enhancement of carbon monoxide could therefore also be ascribed to the fact that oxygen reacted preferentially with hydrogen. This presumably led to a decrease in the oxygen partial pressure and a proportional increase in partial oxidation products.

A small amount of hydrogen in the feed led to a slight increase in carbon dioxide production at low $W/F°_{CH4}$ and a subsequent lowering of P_{CO2} at high $W/F°_{CH4}$.
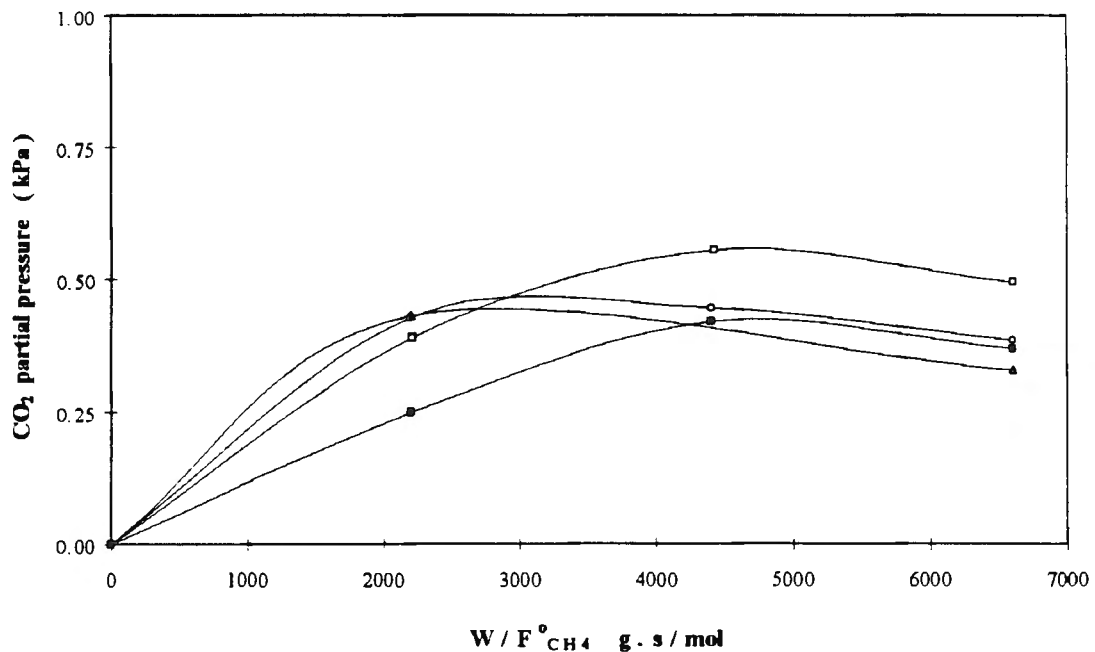
Figure 31-18   The effect of $P°_{H2}$ on P_{CO2} (T = 604°C, $P°_i$ in kPa: CH_4 = 2.96, O_2 = 1.34, H_2: □ = 0.00, ○ = 1.45, ▲ = 2.84, ■ = 5.61)

At the highest hydrogen partial pressure investigated, however, carbon dioxide partial pressure was substantially lower than the experiments without hydrogen in the feed. The latter is in agreement with the argument forwarded above, that the water-gas shift reaction was pushed to the right by the presence of hydrogen (see Figure 31-18). However, the slight

increase in P_{CO2} at low W/F°_{CH4} and low P°_{H2} cannot be explained readily in terms of the water-gas shift reaction.

Water partial pressure was enhanced significantly by the presence of hydrogen at the bed inlet as shown in Figure 31-19.
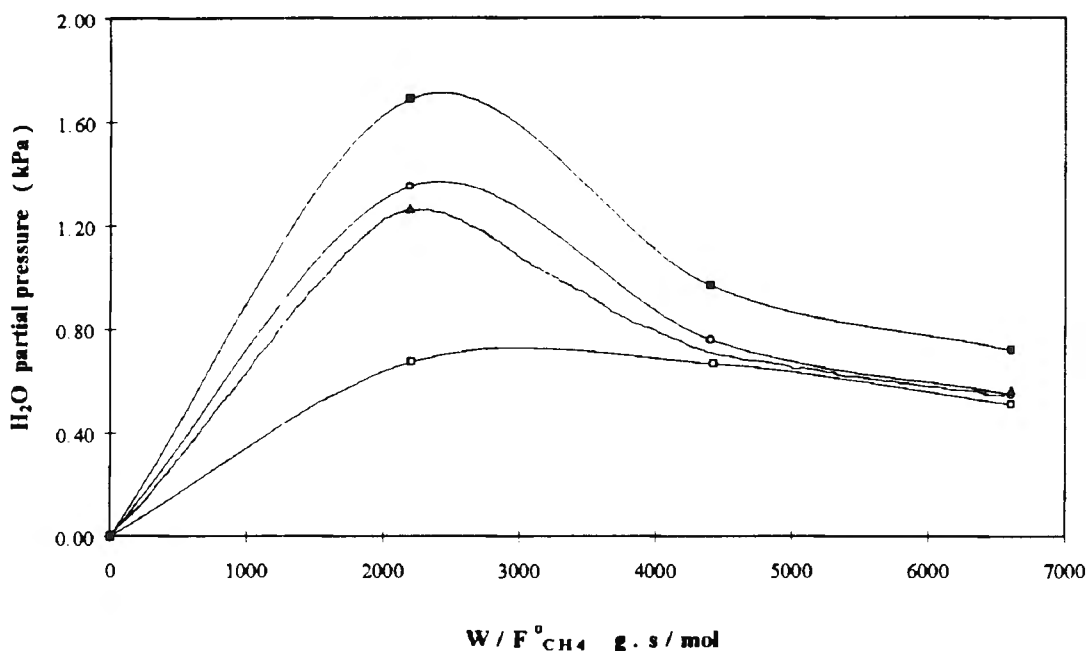
Figure 31-19 The effect of P°_{H2} on P_{H2O} (T = 604°C, P°_i in kPa: CH_4 = 2.96, O_2 = 1.34, H_2: $\square$ = 0.00, $\circ$ = 1.45, $\triangle$ = 2.84, $\blacksquare$ = 5.61)

This may be linked to the observation of rapid disappearance of oxygen shown in Figure 31-16. The highest P°_{H2} led to the highest water partial pressure. The rate of water consumption downstream of the peak in P_{H2O} also increased as the water pressure increased. The argument that the decrease in P_{H2O} after the peak may simply have been shifted to hydrogen by the water-gas shift reaction, does not hold water due to the fact that methane conversion increased even after total oxygen consumption was measured and that water (steam reforming of methane) and CO_2 (methane dry reforming) were the only compounds able to sustain the increase in methane conversion. This suggests that the steam reforming reaction occurred at a greater rate deeper into the catalyst bed. The fact that the slope of the P_{CO2} curves after the peak, as depicted in Figure 31-19, was not influenced by hydrogen partial pressure and therefore did not have a significant contribution towards methane

160

conversion, supports the contention that the rate of steam reforming- rather than dry (CO_2) reforming of methane was enhanced deeper into the catalyst bed.

Hydrogen partial pressure increased almost monotonously with increasing W/F°_{CH4}, except at the highest P°_{H2} where hydrogen passed through a minimum and then started to increase.
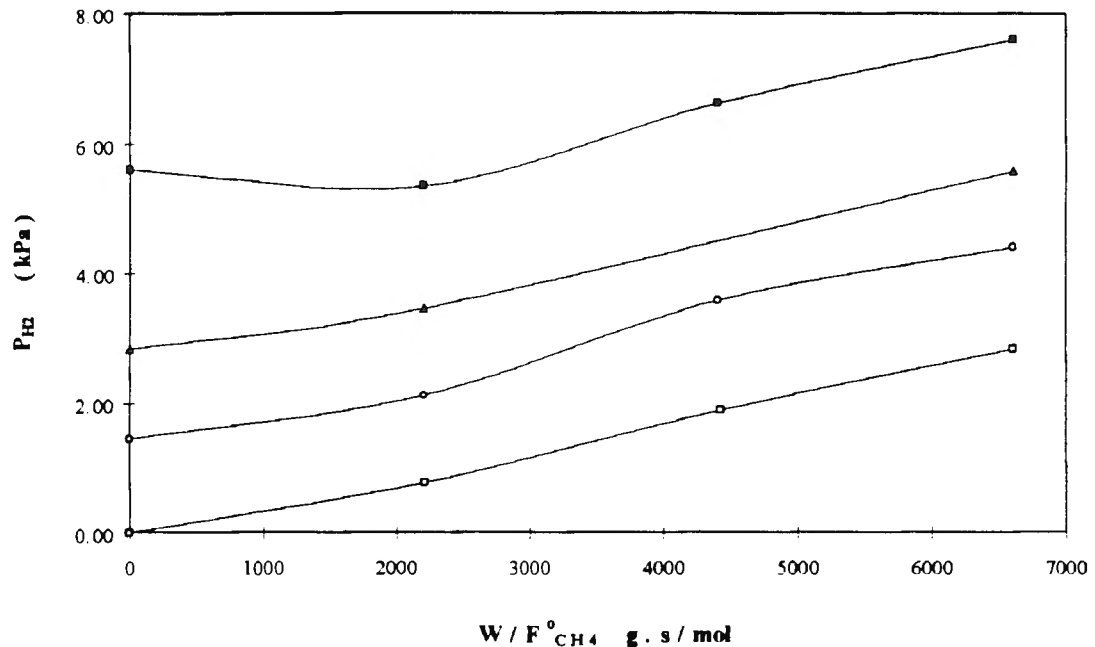
Figure 31-20 The effect of P°_{H2} on P_{H2} (T = 604°C, P°_i in kPa: CH_4 = 2.96, O_2 = 1.34, H_2: □ = 0.00, ○ = 1.45, ▲ = 2.84, ■ = 5.61)

In summary thus, hydrogen partial pressure enhanced the formation of water and carbon monoxide and suppressed the formation of carbon dioxide, supporting the conclusion that hydrogen forced the water-gas shift reaction to the left. Methane conversion was enhanced at low P°_{H2} (possibly due to enhanced methane adsorption in the light of a lower oxygen coverage and a higher vacant site concentration) and depressed at high P°_{H2} (probably due to adsorption of excess hydrogen on vacant sites previously available for methane adsorption). If these possible explanations hold for the effect of P°_{H2} on X_{CH4}, it has a supporting effect on the underlying assumption, namely that methane adsorption is the rate-determining step.

3.3.6.3.b.ii.   The effect of P_{H2} on reaction kinetics

A differential treatment of the integral kinetic data using a number of analytical curve-fitting expressions was used to calculate the reaction rate. The natural logarithm of the rate of methane consumption at zero conversion (ln $r°_{CH4}$) was plotted against the natural logarithm of the inlet hydrogen partial pressure (ln $P°_{H2}$) in order to determine the reaction order of methane with respect to hydrogen. The results are summarized in Table 3-16.

Table 3-16   Reaction orders with respect to hydrogen partial pressure (T = 604°C, $P°_{CH4}$ = 2.96 kPa, $P°_{O2}$ = 1.34 kPa)

Curve fitting procedure	Reaction order[a]	R^2
Method 3	-0.17 ± 0.06	0.8979
Method 7	-0.14 ± 0.02	0.9847
Method 8	-0.16 ± 0.01	0.9960

a   95% Confidence interval

A negative reaction order was calculated when using all three techniques. Clearly the rate of methane consumption was inhibited by the presence of hydrogen at the reactor inlet.

The rates of oxygen consumption and product formation were again calculated as described previously and plotted as a function of $P°_{H2}$ to determine the pseudo-reaction orders with respect to hydrogen partial pressure. Due to the fact that the rate of hydrogen consumption exceeded the rate of hydrogen production at $P°_{H2}$ = 5.61 kPa at the bed inlet, only two data points could be used to calculate the reaction order of the hydrogen formation rate. The influence of hydrogen on the the water-gas shift reaction may be inferred from the positive reaction orders of water and carbon monoxide and the negative order of carbon dioxide.

The finding that the rate of oxygen consumption was inhibited by adding hydrogen to the feed is counter-intuitive and does not agree with the observation (Figure 31-16) that oxygen conversion was significantly enhanced by the addition of hydrogen. Very high oxygen conversions (X_{O2} > 0.98) were used in the curve-fitting routine of method 7 to find the $r°_{O2}$ values. When such high conversions, virtually at the thermodynamic equilibrium, are used

in the curve-fitting technique, the errors in curve-fitting parameters become very large and the r°_{O2} from this set of data should therefore be considered with caution.

Table 3-17 Pseudo-reaction orders with respect to hydrogen partial pressure (T = 604°C, P°_{CH4} = 2.96 kPa, P°_{O2} = 1.34 kPa)

Compound	Reaction order	R^2
CH_4	-0.14 ± 0.02	0.9847
O_2	-0.10 ± 0.02	0.9775
CO	0.06 ± 0.16	0.1182
H_2^a	-0.09	1.0000
CO_2	-0.48 ± 0.43	0.5577
H_2O	0.24 ± 0.16	0.7093

a The line was fit to two data points

3.3.6.3.c. Carbon dioxide partial pressure

3.3.6.3.c.i. The effect of P°_{CO2} on reactant consumption and product formation

The effect of P°_{CO2} on the product composition is summarized in Table C-11 in the appendix. The data that were extracted from Table C-11 was used to generate a number of graphs of partial pressures and conversion as a function of W/F°_{CH4}. The effect of P°_{CO2} on methane and oxygen conversion is shown in Figure 31-21.

At low inlet carbon dioxide levels, (P°_{CO2} < 1.38 kPa) methane conversion was enhanced by the presence of carbon dioxide. The highest carbon dioxide partial pressure tested, however, led to a decrease in methane conversion. At the highest W/F°_{CH4} value tested, however, the presence of even the smallest amount of carbon dioxide led to a depression of methane conversion compared to the pure feed containing only methane and oxygen. A similar observation with respect to the effect of co-fed compound of methane conversion was earlier made in the case of hydrogen and CO co-feeding experiments.

While the absence of a clear trend in any of these cases may cast doubt on the accuracy of

the "zero co-feeding" data, the accuracy of the data in question was ensured by performing a replicate set of experiments as shown earlier in Table 3-2. The variation in X_{CH4} in the presence of CO_2 at the inlet (shown in Figure 31-21) were well outside the range in which the X_{CH4} varied during the replicate set of experiments (Table 3-2).
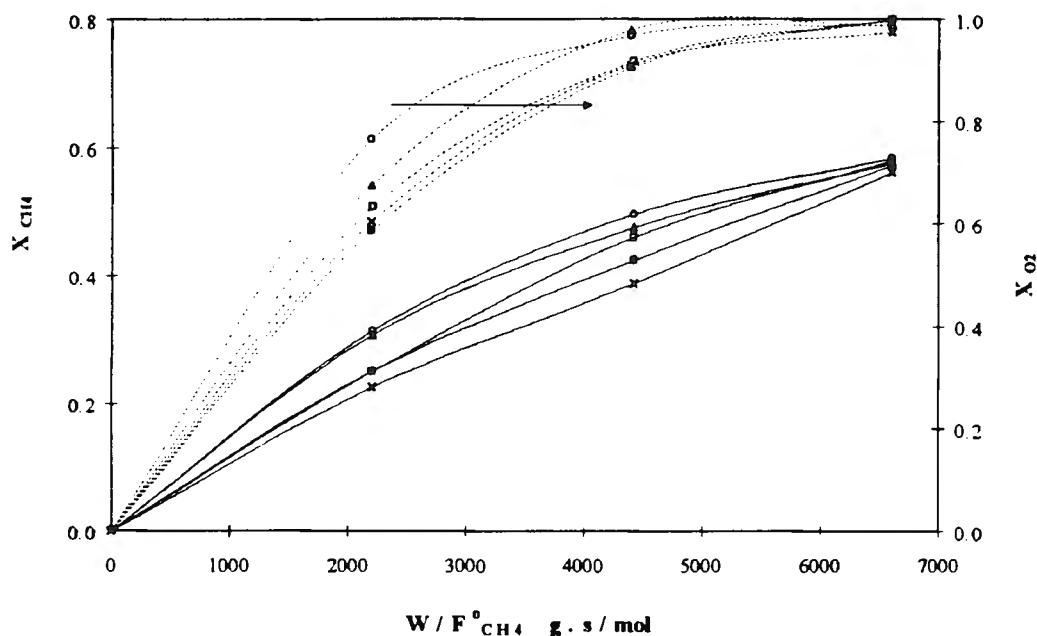
Figure 31-21 The effect of P°_{CO2} on X_1 (T = 604°C, P°_1 in kPa: CH_4 = 2.96, O_2 = 1.34, CO_2: □ = 0.00, ○ = 0.27, ▲ = 0.55, ■ = 1.38, x = 2.77)

The fact that methane conversion was not enhanced at all levels of P°_{CO2} tested and also the observation that the increase in methane conversion was mirrored by an increase in oxygen conversion suggests that the carbon dioxide reforming reaction did not contribute significantly to the conversion of methane. An explanation of the effect of the inlet carbon dioxide partial pressure on the conversion of both methane and oxygen perhaps needs to be sought in adsorption phenomena. Oxygen conversion was also enhanced at low values of carbon dioxide partial pressure (P°_{CO2} = < 0.55 kPa), but oxygen conversion was inhibited when the carbon dioxide partial pressure at the inlet exceeded 0.55 kPa.

The data presented in Figure 31-22 shows that carbon monoxide formation was enhanced by the presence of even the smallest amount of carbon dioxide in the feed. While there is no discernable trend in the magnitude of the enhancement of carbon monoxide formation at

low $W/F°_{CH4}$, the higher values of $W/F°_{CH4}$ investigated clearly showed that the higher the inlet partial pressure of carbon dioxide, the greater was the degree of carbon monoxide enhancement that was measured. One may conclude from this data that the water-gas shift reaction was forced to the left by the introduction of carbon dioxide to the feed.
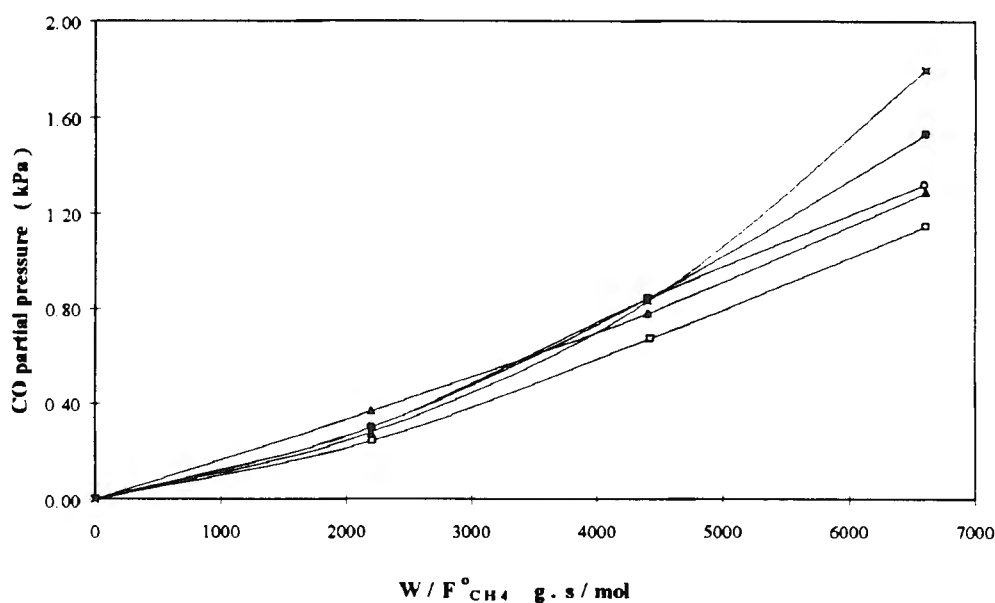
Figure 31-22 The effect of $P°_{CO2}$ on P_{CO} (T = 604°C, $P°_1$ in kPa: CH_4 = 2.96, O_2 = 1.34, CO_2: $\square$ = 0.00, $\circ$ = 0.27, $\triangle$ = 0.55, $\blacksquare$ = 1.38, x = 2.77)

With the exception of one data point on the line for $P°_{CO2}$ = 0.27 kPa, hydrogen partial pressure, on the other hand, was lowered significantly by the presence of carbon dioxide. The effect of $P°_{CH4}$ on the formation of hydrogen is shown in Figure 31-23.

Water partial pressure was enhanced by the presence of carbon dioxide in the feed (Figure 31-24). The highest carbon dioxide partial pressure investigated ($P°_{CO2}$ = 2.77 kPa) led to the greatest enhancement of water formation compared to the pure feed containing only methane and oxygen. These observations support the earlier claim that the water-gas shift reaction was forced to the left by the presence of CO_2 in the feed.

Carbon dioxide partial pressure did not pass through a minimum (Figure 31-25) as was seen for carbon monoxide during CO co-feeding and for hydrogen during H_2 co-feeding.
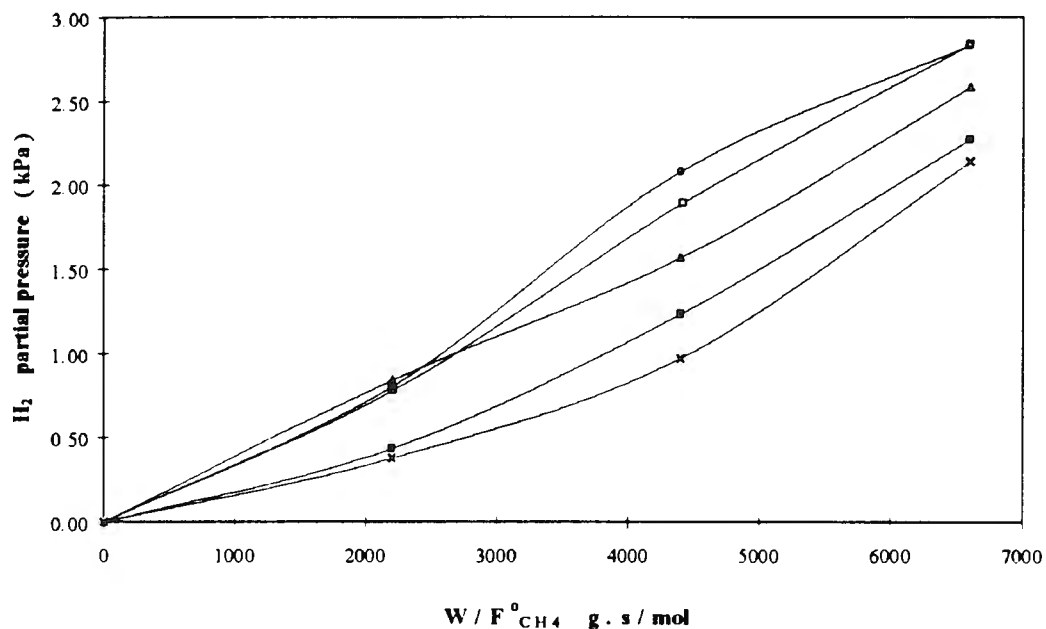
Figure 31-23 The effect of P°_{CO2} on P_{H2} (T = 604°C, P°_i in kPa: CH_4 = 2.96, O_2 = 1.34, CO_2: □ = 0.00, ○ = 0.27, ▵ = 0.55, ■ = 1.38, x = 2.77)
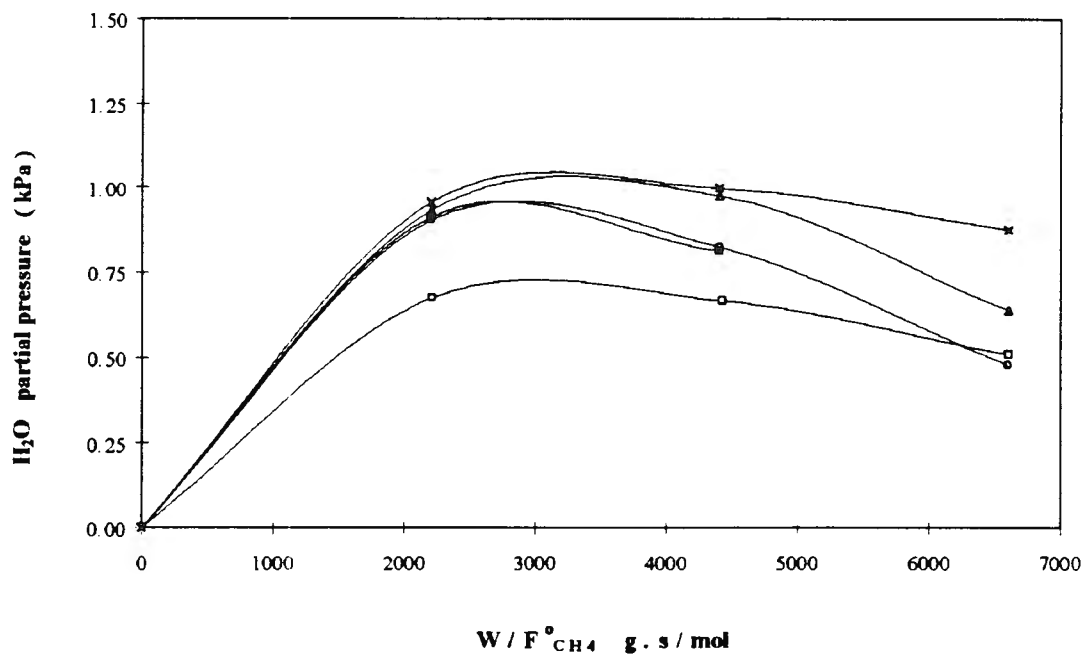
Figure 31-24 The effect of P°_{CO2} on P_{H2O} (T = 604°C, P°_i in kPa: CH_4 = 2.96, O_2 = 1.34, CO_2: □ = 0.00, ○ = 0.27, ▵ = 0.55, ■ = 1.38, x = 2.77)
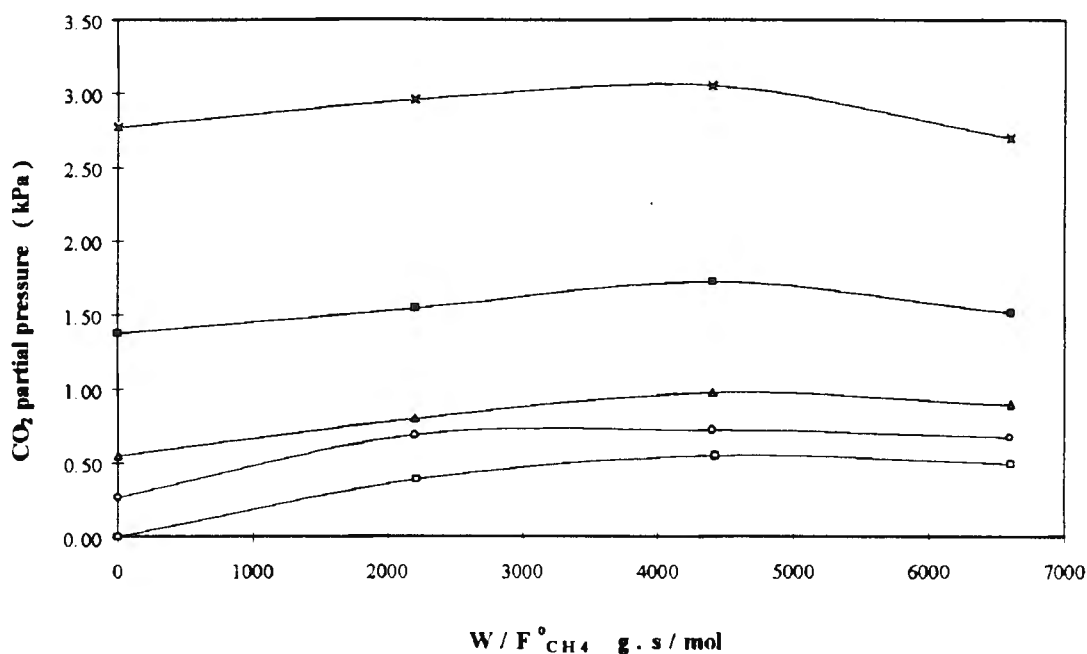
Figure 31-25 The effect of $P°_{CO2}$ on P_{CO2} (T = 604°C, $P°_1$ in kPa: CH_4 = 2.96, O_2 = 1.34, CO_2: □ = 0.00, ○ = 0.27, ▲ = 0.55, ■ = 1.38, x = 2.77)

3.3.6.3.c.ii. The effect of P_{CO2} on reaction kinetics

The integral data was differentiated after fitting a number of analytical curves to the experimental data and taking their first derivative at $W/F°_{CH4}$ = 0. The reaction rate thus obtained was used to construct logarithmic plots which were useful in obtaining the reaction order with respect to carbon dioxide. The results of the reaction order determination are summarized in Table 3-18.

Table 3-18 Reaction order of methane consumption with respect to carbon dioxide partial pressure (T = 604°C, $P°_{CH4}$ = 2.96 kPa, $P°_{O2}$ = 1.34 kPa)

Curve fitting procedure	Reaction order[a]	R^2
Method 3	-0.21 ± 0.03	0.9576
Method 7	-0.13 ± 0.01	0.9907
Method 8	-0.10 ± 0.01	0.9817

a   95% Confidence interval

The very similar values of the reaction order as well as the small values of the 95%

confidence intervals for the three selected methods confirm the applicability of any of the three methods in calculating the reaction rate ($r°_{CH4}$) at the bed inlet. The negative reaction orders imply that carbon dioxide depressed the rate of methane conversion at the bed inlet. Unfortunately it cannot be used to assess the effect of CO_2 on the rate of methane consumption deeper into the catalyst bed.

The influence of the inlet partial pressure of carbon dioxide on the initial rate of product formation and the rate of oxygen consumption was as before quantified by plotting the relevant initial rate of formation as a function of $P°_{CO2}$. The "pseudo reaction orders" obtained by calculating the slope of the best fit straight line through $\ln r°_i$ vs. $\ln P°_{CO2}$ data are presented in Table 3-19.

Table 3-19 Reaction orders with respect to carbon dioxide partial pressure (T = 604°C, $P°_{CH4}$ = 2.96 kPa, $P°_{O2}$ = 1.34 kPa)

Compound	Reaction order[a]	R^2
CH_4	-0.13 ± 0.01	0.9913
O_2	-0.17 ±	0.8920
CO	-0.09 ±	0.2313
H_2	-0.39 ±	0.7989
CO_2	-0.40 ±	0.6980
H_2O	0.01 ±	0.1257

a 95% Confidence interval

The pseudo reaction orders of all the reaction products are questionable because of the low R^2 values. However, it was shown previously (Figure 31-24 and Figure 31-22) that both carbon monoxide and water formation were enhanced by the presence of carbon dioxide. The quantitative proof for this, however, may not be apparent from the calculated reaction orders.

In contrast to the reaction products, the rate of oxygen consumption was much better correlated with $P°_{O2}$. The fact that the rate of both methane and oxygen consumption was lowered by the presence of CO_2 in the feed suggests that carbon dioxide occupied some

available active sites which would otherwise have been available for the chemisorption of methane or oxygen. Direct adsorption measurements need to be made to confirm this.

In summary therefore, the co-feeding of carbon dioxide did not provide direct evidence for the carbon dioxide reforming of methane reaction. Furthermore, clear evidence was provided to show that the water-gas shift reaction was forced to the left by the presence of carbon dioxide in the feed.

3.3.6.3.d.   Water partial pressure

3.3.6.3.d.i.   The effect of P_{H2O} on reactant conversion and product formation

The effect of water partial pressure was investigated at 604°C and with methane and oxygen inlet partial pressures of 2.96 kPa and 1.34 kPa respectively. The effect of water partial pressure at the reactor inlet on methane and oxygen conversion respectively is shown in Figure 31-26.
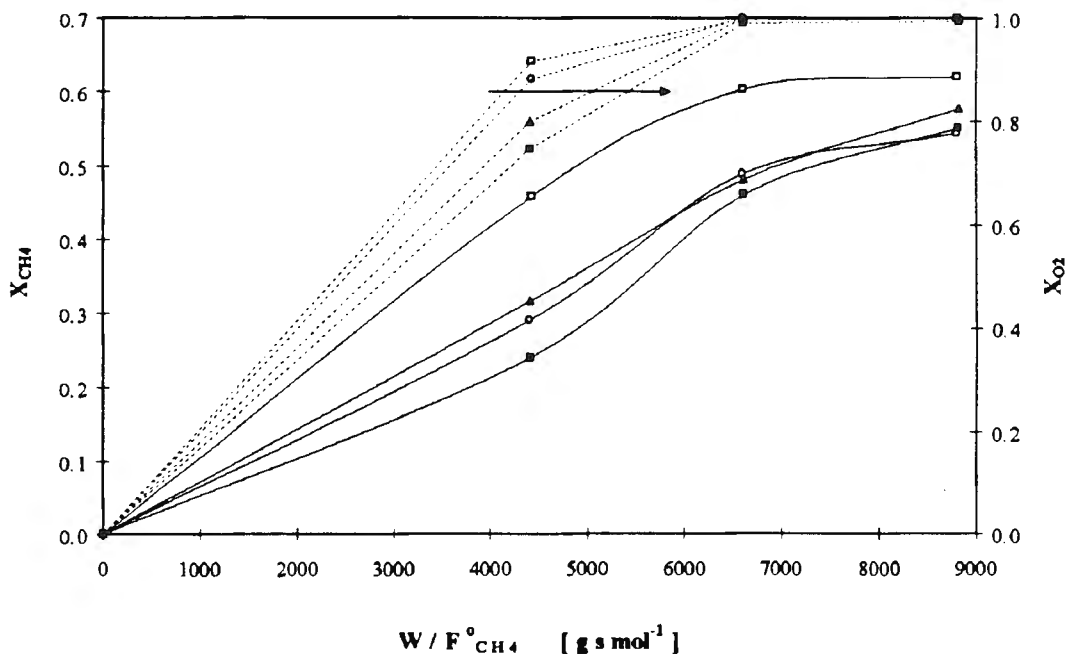
Figure 31-26   The effect of P°_{H2O} on X_i (T = 604°C, P°_i in kPa: CH_4 = 2.96, O_2 = 1.31, H_2O: □ = 0.00, ○ = 0.49, △ = 0.73, ■ = 1.20)

Methane conversion was significantly inhibited by the presence of water at the inlet. The expected trend on a commercial steam reforming catalyst such as G-90B studied here, is that the addition of water would enhance the methane conversion. However, this was clearly not the case in the data presented here. One possible explanation for this phenomenon is that the dissociation of adsorbed water was slow at the low temperature investigated (604°C). Commercial steam reformers with the concomitant fast dissociation of water, operate at temperatures that are more than 300°C higher than that studied here. Competitive, nondissociative adsorption of water therefore probably led to the lower methane conversion recorded in the presence of water. Oxygen conversion was also inhibited by water addition to the feed. If the previous contention is accepted, namely that water caused the blocking of sites available to methane adsorption, less methane fragments would be available to react with oxygen and therefore the oxygen conversion would be lower.

The formation of carbon monoxide was significantly inhibited by the presence of water in the feed (Figure 31-27), but because of a questionable data point on the $P^°_{H2O} = 0.73$ kPa line, a consistent trend could not be identified.
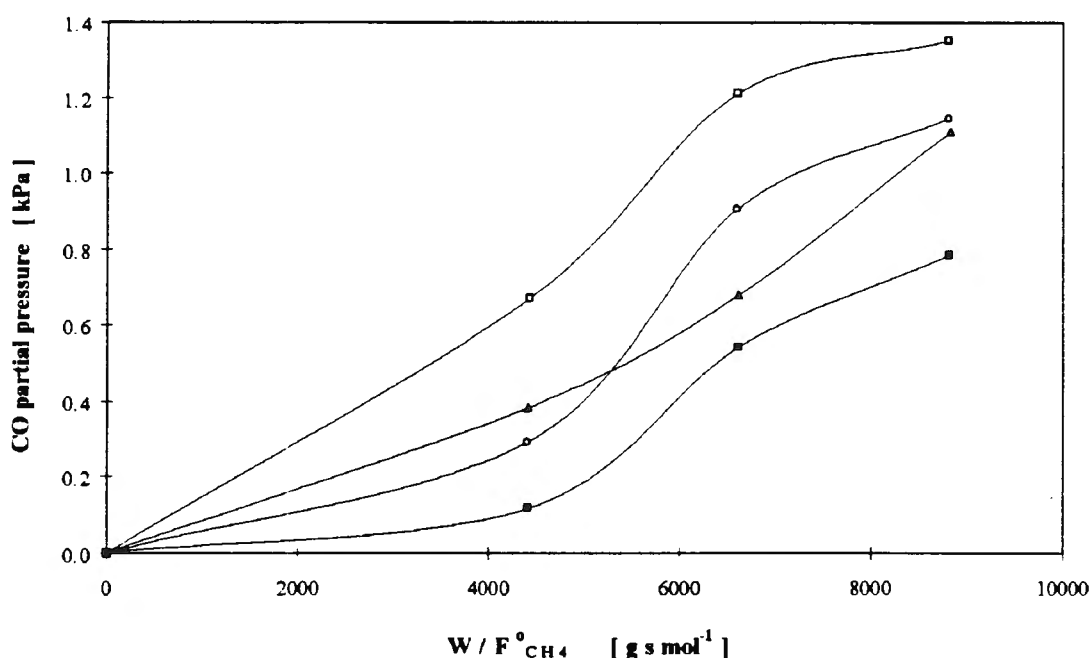
Figure 31-27 The effect of $P^°_{H2O}$ on P_{CO} (T = 604°C, $P^°_i$ in kPa: CH_4 = 2.96, O_2 = 1.31, H_2O: □ = 0.00, ○ = 0.49, ▲ = 0.73, ■ = 1.20)

The co-feeding of water had a positive effect on the formation of carbon dioxide, but as observed for the effect of $P°_{H2O}$ on P_{CO}, the data represented by the two lines corresponding to $P°_{H2O} = 0.49$ kPa and 0.73 kPa prevented one from concluding that there was a quantifiable trend (Figure 31-28).
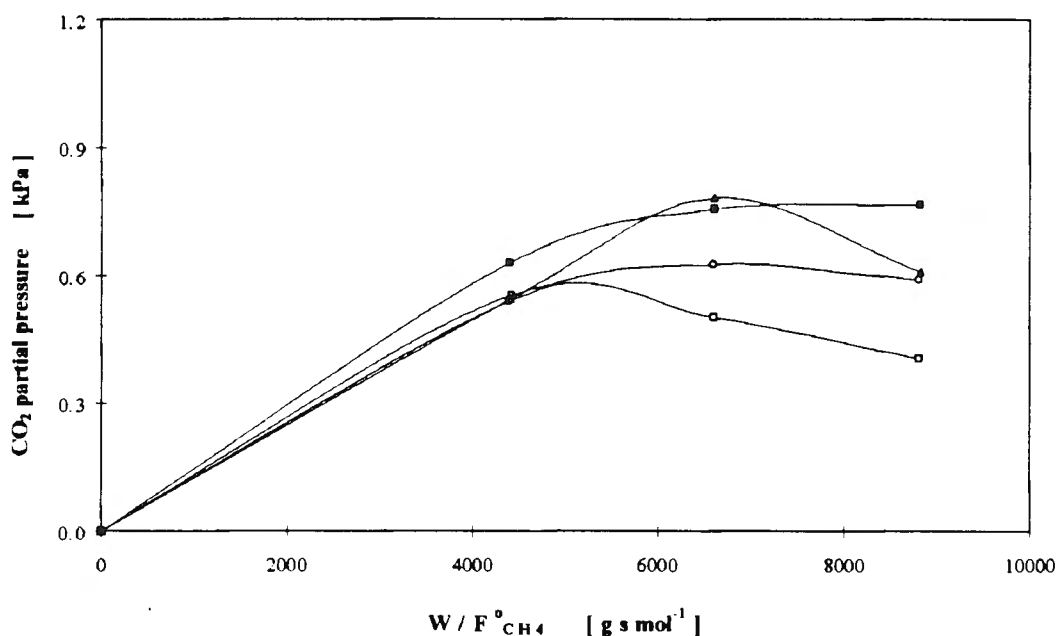
Figure 31-28 The effect of $P°_{H2O}$ on P_{CO2} (T = 604°C, $P°_i$ in kPa: CH_4 = 2.96, O_2 = 1.31, H_2O: □ = 0.00, ○ = 0.49, ▲ = 0.73, ■ = 1.20)

Hydrogen formation was also suppressed by the presence of water in the feed (see Figure 31-29).

This observation, taken together with the lower CO formation and lower methane and oxygen conversion provides strong evidence for competitive adsorption of water onto methane adsorption sites. The drastic decrease in methane conversion and the concomitant decrease in CO and H_2 partial pressures probably masked any effect of water co-feeding on the water-gas shift reaction which was previously shown, by the co-feeding of all the other products, to be shifted either to the left (CO_2 and H_2 co-feeding) or to the right (CO co-feeding). At the lower two $P°_{H2O}$ values investigated, these inexplicable trends may, in the light of the above, perhaps be attributed to a mixture of competitive water adsorption and the effect of water on the water-gas shift reaction.
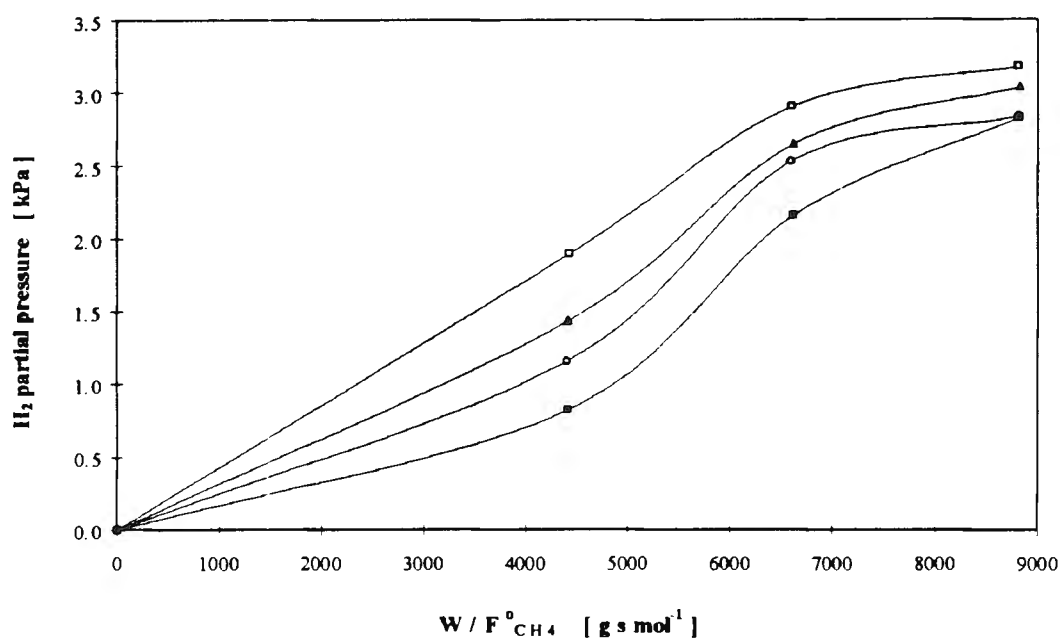
Figure 31-29 The effect of $P°_{H2O}$ on P_{H2} (T = 604°C, $P°_1$ in kPa: CH_4 = 2.96, O_2 = 1.31, H_2O: □ = 0.00, ○ = 0.49, △ = 0.73, ■ = 1.20)

The water partial pressure gradient over the catalyst bed is shown in Figure 31-30.
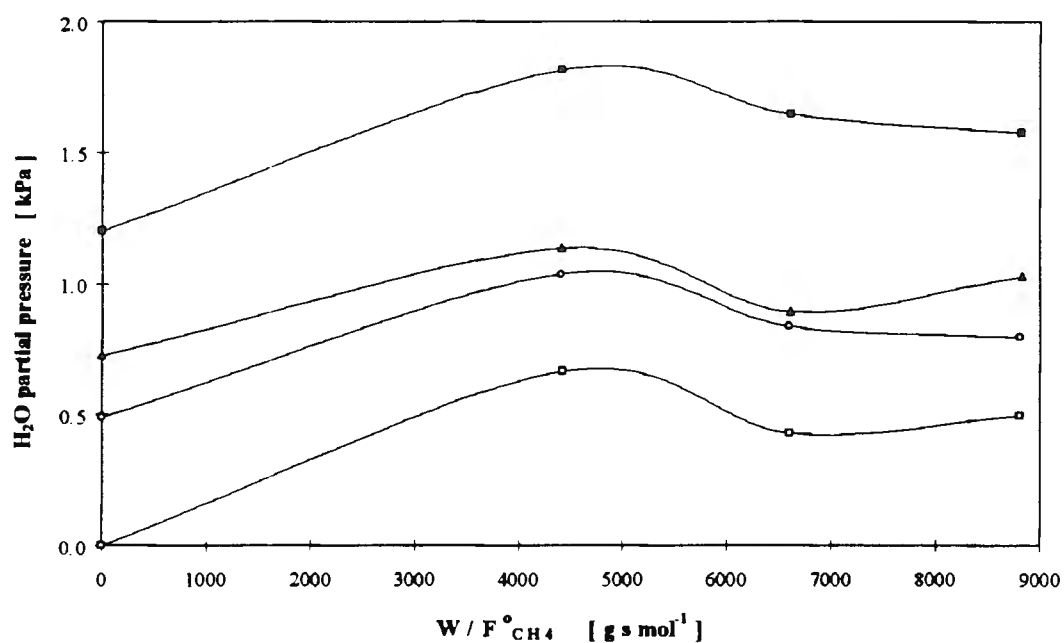
Figure 31-30 The effect of $P°_{H2O}$ on P_{CO2} (T = 604°C, $P°_1$ in kPa: CH_4 = 2.96, O_2 = 1.31, H_2O: □ = 0.00, ○ = 0.49, △ = 0.73, ■ = 1.20)

At low $W/F°_{CH4}$ values, the water partial pressure increased towards a peak value and then started to decline. A number of arguments have thus far been made against the role of the steam reforming reaction. However, the decline in water partial pressure after a peak was reached (observed **throughout** this work), should be considered as evidence **for** the existence of the steam reforming reaction. Except for experimental scatter and the error inherent in the **calculated** water partial pressure values, no explanation can be offered at this point for the slight increase in water partial pressure at the highest value of $W/F°_{CH4}$ investigated.

3.3.6.3.d.ii. The effect of P_{H2O} on reaction kinetics

The results of the reaction order determination of the rate of methane consumption with respect to water partial pressure are summarized in Table 3-20. The low correlation coefficients of the straight line fits to the experimental data, and therefore the scatter in the data, led to very wide confidence intervals for all three curve-fitting methods. While keeping in mind the low certainty in the data, it may be stated that the presence of water inhibited the rate of methane consumption.

Table 3-20 Reaction order of the rate of methane consumption with respect to water partial pressure (T = 604°C, $P°_{CH4}$ = 2.96 kPa, $P°_{O2}$ = 1.31 kPa)

Curve fitting procedure	Reaction order[a]	R^2
Method 3	-0.33 ± 0.23	0.6670
Method 7	-0.19 ± 0.17	0.6718
Method 8	-0.08 ± 0.10	0.3978

a   95% Confidence interval

The fact that the oxidative reforming of methane is clearly not a single reaction, but is made up of a network of possible reactions, will inevitably lead to problematic differential analyses of the experimental rate data.

In order to further elucidate the role of water vapor on the rate of methane consumption, additional values of $P°_{H2O}$ need to be tested, but this is beyond the scope of this work.

The pseudo reaction order of the rate of formation of all products and the rate of consumption of methane and oxygen with respect to water partial pressure were calculated as before and the results are shown in Table 3-21. Again the correlation coefficients were very low.

Table 3-21 Reaction orders with respect to water partial pressure (T = 604°C, P°_{CH4} = 2.96 kPa, P°_{O2} = 1.31 kPa)

Compound	Reaction order	R^2
CH_4	-0.17 ± 0.17	0.4865
O_2	-0.29 ± 0.07	0.9402
CO	-1.41 ± 1.18	0.5886
H_2	-0.54 ± 0.55	0.4850
CO_2	0.20 ± 0.15	0.6556
H_2O^*	0.21 ± 0.67	0.0869

a   The reaction order refers to the rate of water formation

Except for carbon dioxide and water formation, water partial pressure inhibited the rate of formation of all the products and the rate of consumption of both methane and oxygen. Except for the oxygen pseudo-reaction order, all the compounds displayed high uncertainty with respect the actual value of the reaction order.

3.3.7. Summary of the experimental findings of kinetic experiments

A normal Arrhenius-type dependence of the reaction rates were found with respect to temperature. The Arrhenius plots formed a straight line over the temperature range investigated (579°C - 650°C). This lent further support to the contention that pore diffusion was insignificant in the present experimental data, although it should be added that the activation energy of methane consumption was not very high (between 60 and 70 kJ mol⁻¹). The **apparent** activation energy for reactant consumption and product formation followed the trend:

$$CO > O_2 > H_2 > CH_4 > H_2O > CO_2$$

The rate of methane disappearance was found to be directly proportional to methane partial pressure, but a weaker function of oxygen partial pressure. Products were found to inhibit the rate of methane consumption to a varying degree.

When co-fed, carbon monoxide was consumed very early in the catalyst bed. Its presence enhanced the rate of oxygen consumption and the rate of carbon dioxide formation. CO also caused the water-gas shift reaction to be forced to the right.

Hydrogen co-feeding led to the even more rapid consumption of oxygen and the formation of significant amounts of water. The water formed in-situ was shown to enhance the steam reforming reaction. Hydrogen in the feed resulted in the water-gas shift reaction being forced to the left.

The presence of carbon dioxide led to enhanced water- and carbon monoxide formation and an inhibition in the formation of hydrogen. This suggests that the water-gas shift reaction was shifted to the left by the presence of carbon dioxide.

Water co-feeding experiments revealed that both methane conversion and oxygen conversion were reduced considerably by the presence of water at the bed inlet. The competitive adsorption of water onto the sites active for methane and oxygen adsorption was proposed to be the cause of the decrease in reactant conversion. The temperature was most probably too low to allow for the rapid dissociation of water on the nickel surface. On the other hand, it was clear from Figure 31-30 that water was indeed **consumed** at the same temperature, but deeper into the catalyst bed. This is in line with the observations made during hydrogen co-feeding.

The only explanation which is consistent with all the evidence with respect to steam reforming is that oxygen inhibited the dissociation of water on a nickel surface and that, when occurring together over a nickel catalyst, water and oxygen adsorb competitively, oxygen dissociatively and water non-dissociatively. If no oxygen is present, water adsorption

occurs dissociatively (as indicated by a peak in the P_{H2O} vs. $W/F°_{CH4}$ curves).

Considering the error that was introduced by applying curve-fitting techniques to integral kinetic data to obtain reaction rates, the qualitative features that were observed in integral partial pressure vs. $W/F°_{CH4}$ plots, were well correlated with the differential treatment of the data.

3.4. The catalyst

3.4.1. Catalyst morphology

The catalyst appeared to have a rough surface, both before and after kinetic testing. No gross differences between the used and unused catalyst could be detected by SEM. A SEM photograph of the unused catalyst is shown in Figure 31-31.
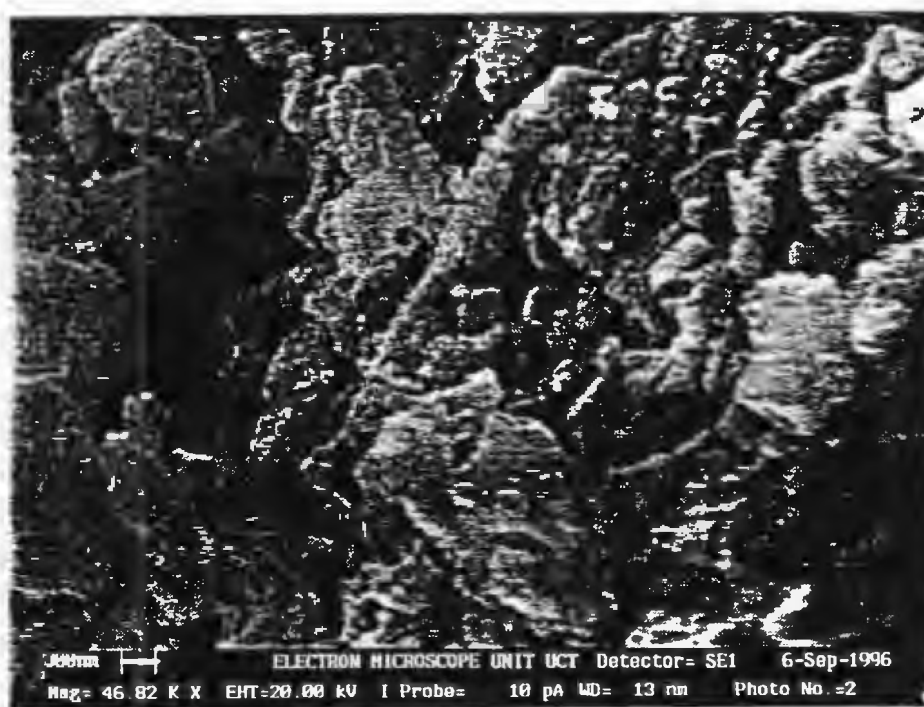
Figure 31-31 SEM photograph of the surface of the unused catalyst

3.4.2. Oxidation state of the catalyst

The catalyst was pre-reduced in flowing hydrogen prior to using it in oxidative reforming

experiments. However, because of the presence of oxygen, one would expect a degree of oxidation. Upon removing the catalyst from the reactor after an experiment, the top part of the catalyst bed was often much lighter in colour than the lower part of the bed. After one such experiment, the catalyst particles were separated by hand into a ligt and a dark fraction. These two fractions were subjected to X-Ray diffraction. The XRD spectra thus obtained were compared to the spectra of the unused, unreduced catalyst and that of the catalyst which was treated in a stream of flowing oxygen (TGA) after it was used for oxidative reforming experiments. The results are shown in Figure 32-1. The Miller indices corresponding to the marked peaks are also indicated above the spectra. The lower two spectra were slightly shifted towards lower 2θ values. This occurred because there was very little sample available and a shallow enough sample holder could not be fitted into the XRD chamber to ensure that the upper surface of the sample was at the reference level. From Figure 32-1 it is clear that the Ni(200) peak was higher in the dark particle spectrum than in the light particle spectrum. The opposite was observed for the NiO(200), NiO(220) and NiO(111) peaks. Two reference peaks were chosen and its ratio to an Al_2O_3 peak taken to illustrate this (see Table 3-22).
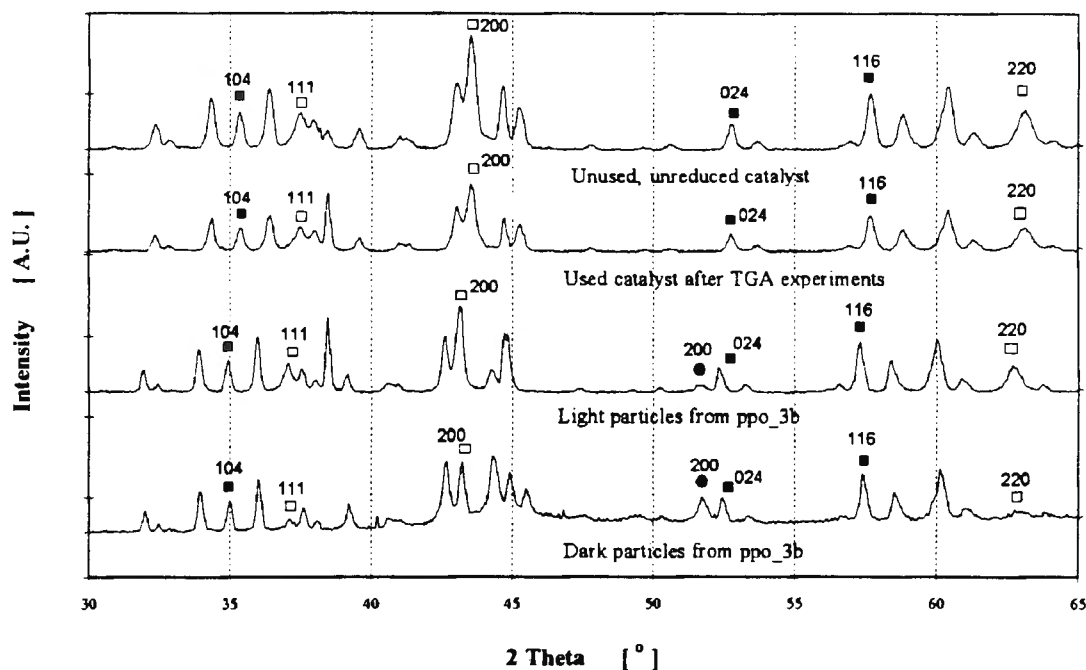
Figure 32-1   XRD spectra of unused catalyst, ligt and dark sections of a used catalyst bed and post-TGA samples (Peaks: ● = Ni, □ = NiO, ■ = Al_2O_3)

The XRD spectra of the unused, unreduced catalyst and the catalyst samples after TGA

treatment were similar in appearance. This was confirmed by the very similar peak ratios for the two cases given in Table 3-22.

Table 3-22 Nickel and alumina peak height ratios from XRD spectra

Sample description	Ratio of peak intensities	
	$\dfrac{NiO(111)}{Al_2O_3(104)}$	$\dfrac{Ni(200)}{Al_2O_3(104)}$
Unused and unreduced	1.00	0
Light section of ppo_3b	0.89	0.11
Dark section of ppo_3b	0.38	0.98
Post-TG-DTA sample	1.08	0

According to the Ni(200) reflection given in Table 3-22, there were no Ni$^\circ$ present in the unused catalyst or the post-TGA catalyst samples. There was furthermore much more nickel in the dark catalyst particles than in the light particles of the same catalyst sample. According to the NiO(111) reflection given in Table 3-22, the unused catalyst and post-TGA catalyst had very similar amounts of NiO present. This amount was more than either the light or dark sections of the catalyst sample. Furthermore, the NiO(111)/Al$_2$O$_3$(104) reflection ratio indicated that the light catalyst particles had more NiO than the dark particles. These findings are in agreement with previous evidence presented in the literature [88].

None of the three characteristic lines for NiAl$_2$O$_4$ were present in any of the spectra [162].

In light of the data presented here, one may conclude that the state of the active catalyst was a function of the position of the particles in the catalyst bed, i.e. the oxidizing/reducing ability of the gas in contact with the catalyst. Not only should the oxidation state of the catalyst be determined by the oxidizing ability of the gas mixture, but also by the duration for which the catalyst is exposed to a given gas mixture; chemisorbed oxygen forms metal-oxygen bonds and after some time an external NiO layer is transformed into a three-dimensional bulk oxide.

3.4.3. Catalyst deactivation

The deactivation of the catalyst and the need to use a fresh charge of catalyst for each experiment was described in section 2.4.1.5. Additional evidence is presented here in an attempt to shed some light on the mechanism of catalyst deactivation.

3.4.3.1. Thermogravimetric analysis

Various batches of used catalyst were subjected to TGA analysis in an oxidizing atmosphere. The experimental procedure of the thermogravimetric (TGA) experiments is described in section 2.5.3. Two features were evident from the TGA curves, namely an initial increase in the sample mass which was often followed by the second feature, namely a decrease in sample mass. In spite of very low heating rates ($1 °C$ min^{-1}) and low oxygen partial pressures ($P°O2 = 3$ kPa) in the gas flowing over the samples in the TGA apparatus, the abovementioned two TGA features could not be completely resolved from one another. This prevented a quantitative treatment of the TGA data. However, some qualitative curves are shown here to illustrate the information to be gleaned from the TGA experiments.

Time [s]
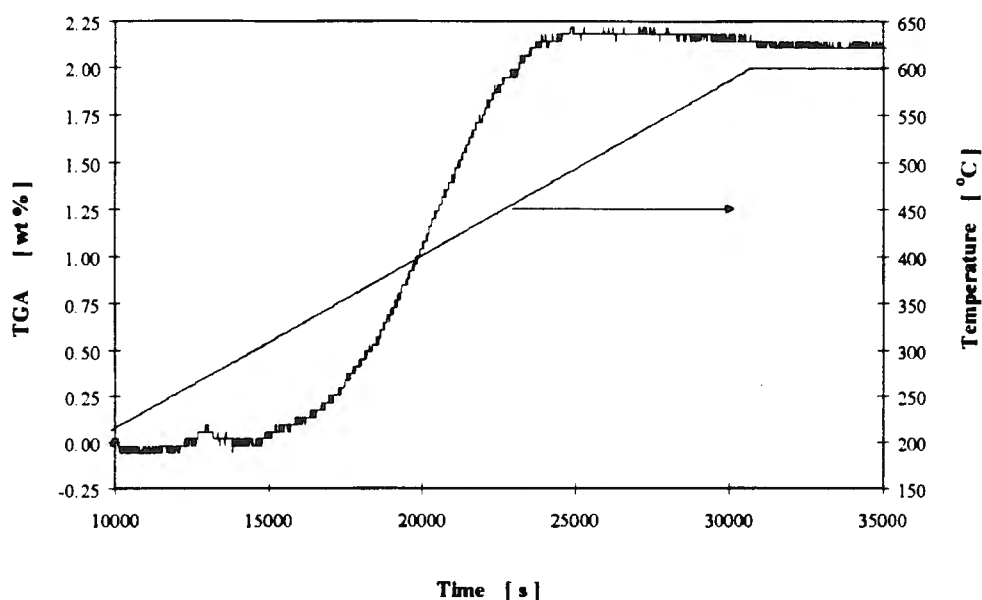
Figure 32-2 TGA curve for the catalyst exposed to $P°_{H2} = 2.84$ kPa during catalytic tests

In light of the TGA curve shown in Figure 32-2, no carbon was formed during the hydrogen co-feeding experiments. The only feature evident is an increase in mass which may be attributed to the oxidation of Ni° to NiO during the TGA experiment. Virtually identical curves were obtained for catalysts that had previously been exposed to different P°_{H2} values during kinetic experiments. While it is possible that mass loss due to carbon oxidation may have been masked by the marked mass gain during nickel oxidation, the amount of carbon corresponding to such a masked loss would be small enough to be negligible.

The second observation from TGA results stems from the shape of the TGA curves of the catalysts having previously been exposed to varying values of P°_{O2} during kinetic experiments. After an initial peak corresponding to the mass gain associated in this case to nickel oxidation, some of the TGA curves decreased markedly (indicating a mass loss which corresponds to carbon oxidation). The steady-state mass of the catalyst samples during TGA increased as the P°_{O2} values they had previously been exposed to, increased. This indicates that higher oxygen inlet partial pressures led to decreasing amounts of carbon on the catalysts. This is shown below in Figure 32-3.
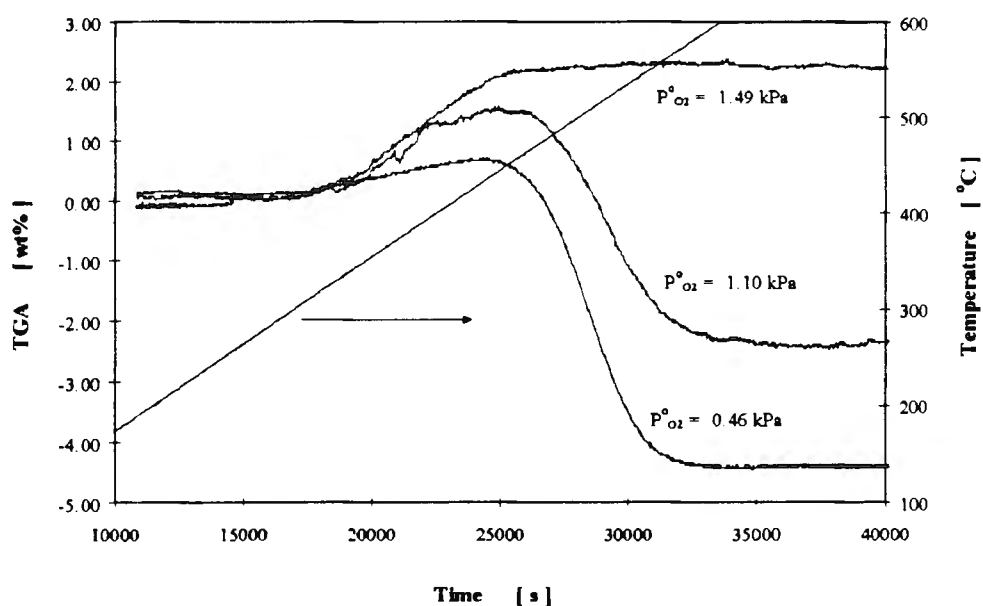
Figure 32-3   TGA curve for catalyst exposed to various oxygen partial pressures during prior catalytic tests

Three batches of catalyst that had been used in carbon monoxide co-feeding experiments were also subjected to TGA experiments (see Figure 32-4). The three catalysts had been

180

exposed to inlet carbon monoxide partial pressures of 1.42 kPa, 2.84 kPa and 6.3 kPa.
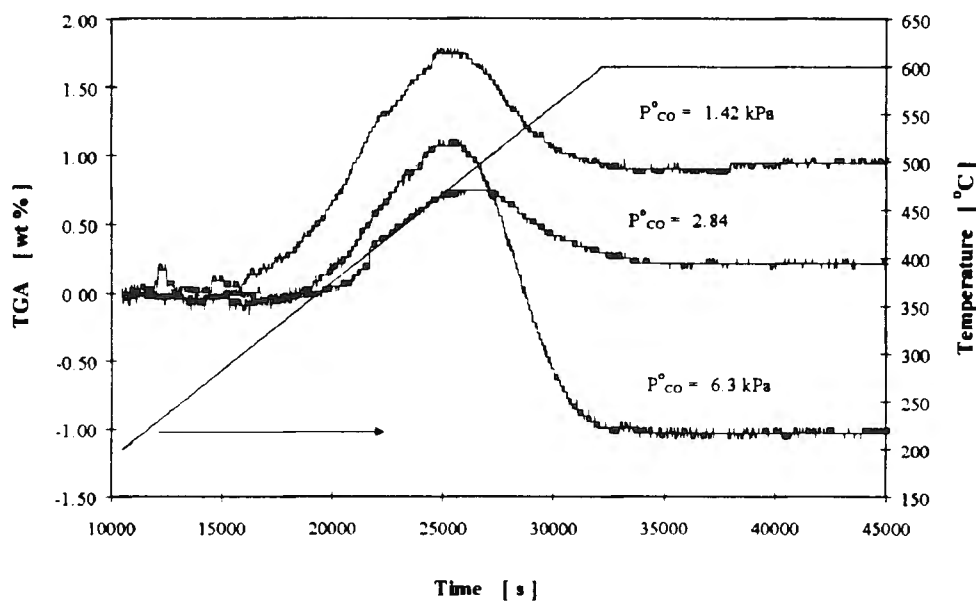
Figure 32-4 TGA curve for catalyst exposed to various carbon monoxide partial pressures during prior catalytic tests

The difference between initial mass and the final mass in the TGA experiments was directly related to the partial pressure of CO that the catalysts had previously been exposed to. The height of the initial peak was, however, not related in the same manner and no trend was evident. This leads to the conclusion that the amount of carbon deposited on the catalyst was directly related to the carbon monoxide partial pressure.

Carbon dioxide co-feeding resulted in very little carbon deposition (see Figure 32-5). An increase in the CO_2 partial pressure led to the presence of less oxidizable nickel in the used catalyst (lower TGA peaks). Thus it may be concluded that carbon dioxide caused the oxidation of the active zero-valent metal.

In summary, therefore, the following conclusions may be drawn from the information presented above. In the first instance it was shown that hydrogen co-feeding during kinetic experiments prevented, and that high oxygen inlet partial pressures inhibited, carbon formation. Thereafter it was demonstrated that CO co-feeding enhanced carbon formation and that CO_2 co-feeding resulted in enhanced oxidation of nickel metal during kinetic

experiments.
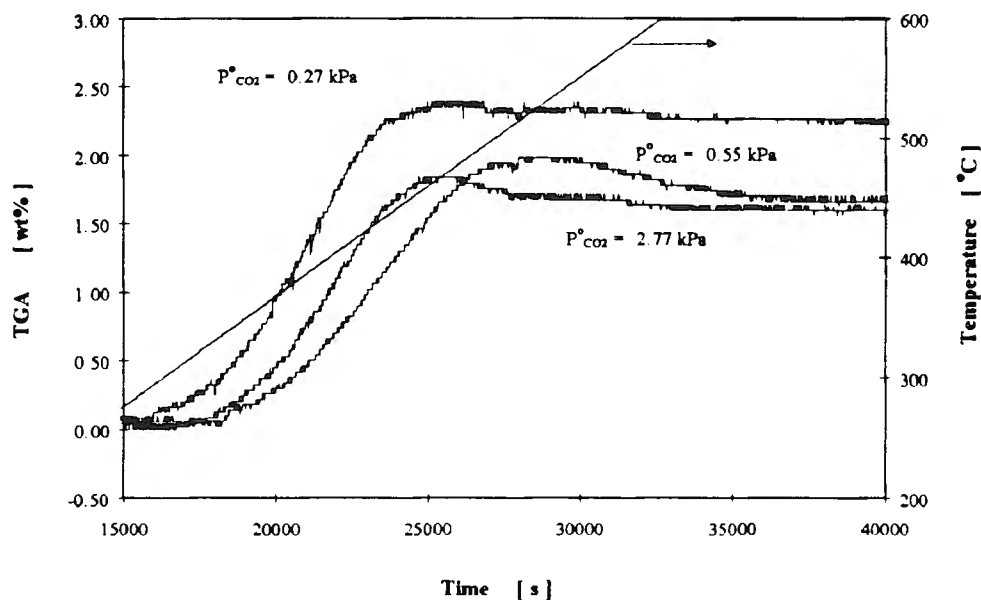
Figure 32-5   TGA curve for catalyst exposed to various carbon dioxide partial pressures during prior catalytic tests

3.4.3.2. Evidence from catalytic experiments

The time on-stream data was taken from all the kinetic experiments and collated in an attempt to isolate the conditions that were most conducive to catalyst deactivation. Three conditions were identified as the major causes of deactivation, namely temperatures lower than 600°C and higher than 625°C , high oxygen partial pressure and high water partial pressure. The effect of temperature on the catalyst deactivation at the **bed outlet** over a period of two hours is shown in Figure 32-6. Negative y-values indicate that the parameter decreased with time on-stream. The data were taken from different experiments and are therefore cumulative, i.e. the percentage decrease in conversion, for example, refers to the total decrease over the bed up to that point.

Methane conversion as well as the synthesis gas selectivities decreased more rapidly at low- and at high temperatures than at intermediate temperature. Oxygen conversion, however, decreased only at low temperature and was unchanged (and complete, i.e. $X_{O2} = 1$) at high temperature.

182
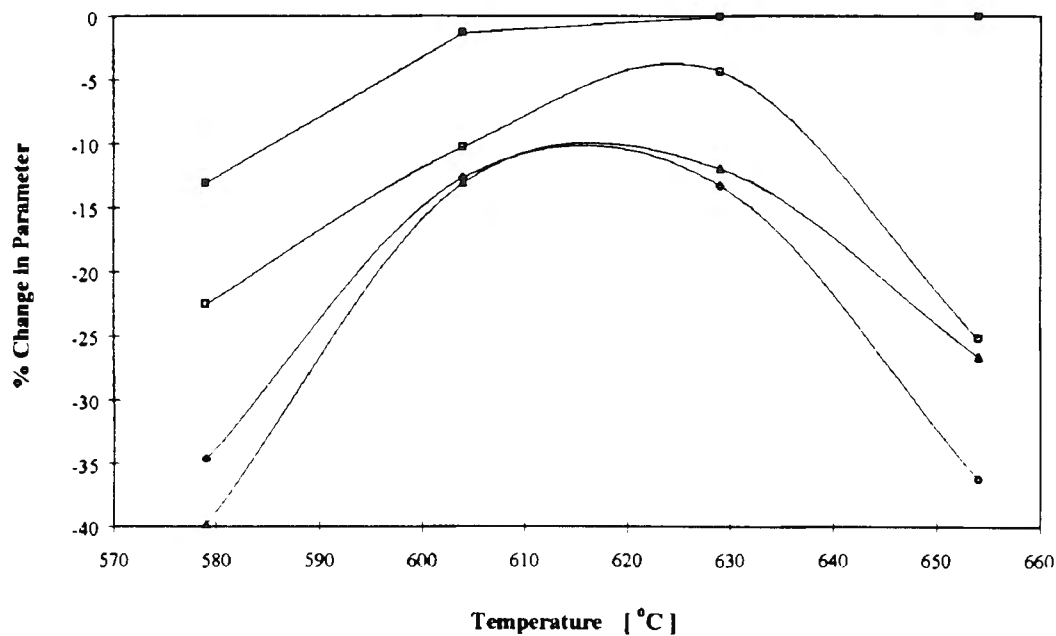
Figure 32-6 The effect of temperature on catalyst deactivation at the bed outlet ($\lozenge$ = X_{CH4}, $\blacksquare$ = X_{O2}, $\triangle$ = S_{CO}, $\square$ = S_{H2})

The active sites responsible for oxygen conversion thus disappeared faster at low temperature. Encapsulate carbon formation will be limited in the presence of oxygen and hence the most likely cause of a reduction in the number of active sites is the oxidation of nickel to nickel oxide. Therefore, nickel oxidation to nickel oxide is more predominant at low temperature than at high temperature.

The observation that oxygen conversion was unaffected while methane conversion and the syngas selectivities decreased **at high temperature** allows one to conclude that the number of sites responsible for methane conversion in the absence of gaseous oxygen decreased more rapidly at high temperature. It has been shown that the lower part of the catalyst bed (which contains the active sites responsible for methane conversion after oxygen conversion has been completed) consists of reduced nickel (see section 3.4.2). Furthermore, since no nickel aluminate peaks were detected by XRD, it may be concluded that nickel sintering was responsible for deactivation of the catalyst in the absence of oxygen at high temperature.

The small catalyst samples tested (always less than 100 mg) and the low metal surface area of the catalyst made it impossible to perform chemisorption on batches of the used catalyst.

Thus, no direct evidence in terms of the number of available sites can be offered as support for the above conclusion.

The trend in the decrease of X_{CH4} was not the same at the bed inlet and the bed outlet (as shown in Figure 32-7).
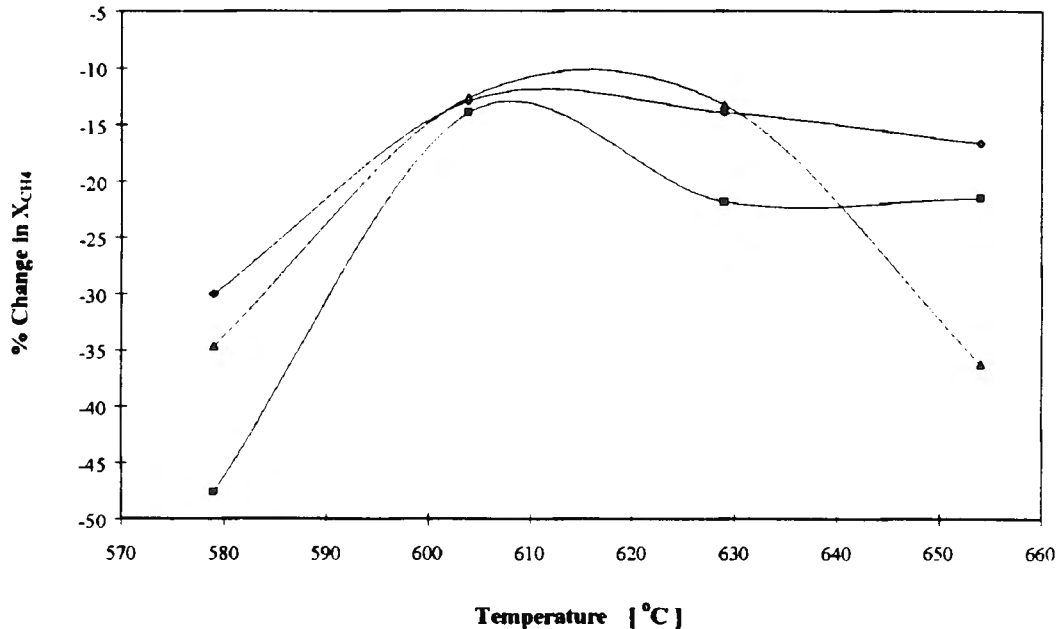
Figure 32-7   The effect of position in the catalyst bed on the decrease in X_{CH4} ($\diamond$ = Inlet, ■ = Centre, ▲ = Outlet)

The decline in methane conversion at high temperature at the bed outlet (as shown in Figure 32-7) was much less evident at the centre of the bed, and even less so at the bed inlet. Methane conversion at the bed inlet occurred in the presence of oxygen. At the centre of the bed, methane was converted both in the presence of oxygen and of water (a weaker oxidant). Hence, at both the inlet of the catalyst bed and the centre of the bed, methane conversion was effected to some degree by a strong oxidant able not only to oxidize methane, hydrogen and carbon monoxide, but also to convert metallic nickel to bulk nickel oxide. Therefore, if nickel sintering (enhanced by high temperatures) was responsible for the deactivation of the catalyst at high temperature and at the bed outlet, as alluded to above, one would observe a less significant decrease in methane conversion at the centre of the bed and at the inlet than at the bed outlet at high temperature. This was in fact observed (see the data presented in

Figure 32-7) and provides further evidence for the previous conclusion that nickel sintering caused catalyst deactivation at high temperature and in the region of the catalyst bed where oxygen was already converted.

Closer to the bed inlet - in the region of limited conversion of the reactants, one would expect the high oxygen partial pressure to result in enhanced nickel oxidation and a concomitant decrease in activity with time on-stream since the total available metallic nickel is reduced with the formation of nickel oxide. Therefore the decrease in methane conversion would be evident at any position of the catalyst bed located downstream of the position where the nickel oxidation had occurred since events at the bed inlet influence those deeper into the bed. If methane conversion was lower at the inlet, the methane conversion would be lower also at the outlet. This was true at all the temperatures investigated (Figure 32-7).

The effect of co-fed carbon monoxide on the catalyst deactivation characteristics did not exhibit any identifiable trend. Because TGA experiments revealed the presence of carbon on used catalysts that had previously been exposed to high partial pressures of carbon monoxide, this suggests that carbon deposition did not have a significant effect on the deactivation of the catalyst.

Early in the catalyst bed, the presence of hydrogen improved the methane conversion with time on-stream, but at the bed outlet, high P°_{H2} led to rapid decrease in X_{CH4}. This suggests that sintering (enhanced by high temperature in the presence of hydrogen [163]) was the cause of catalyst deactivation rather than carbon deposition or catalyst oxidation.

There was not any quantifiable trend in the decrease in X_{CH4} with respect to CO_2 partial pressure. However, deactivation at the bed inlet was faster than at the bed outlet when CO_2 was present in the feed. This latter fact was true of both X_{CH4} and X_{O2}. If the postulate holds that NiO is more predominant at the bed inlet, then the formation of nickel carbonate at the bed inlet could be the cause of the higher degree of deactivation.

In conclusion, thus, it may be stated that experiments at high temperature and during H_2 co-feeding provided evidence for sintering, although the hydrogen co-feeding argument is

based on only one data point. Direct evidence for sintering, i.e. chemisorption measurement of the nickel surface area and calculation of the nickel particle size was complicated by the small amount of catalyst used in each charge of catalyst. The low surface area of the catalyst necessitated much larger sample sizes to ensure accurate chemisorption results. The catalyst deactivation caused by high oxygen- and water partial pressures lends support to the metal oxidation- mechanism of catalyst deactivation. Carbon deposition was observed by TGA experiments on the used catalyst, but it is unclear from the (deactivation) kinetic experimental data to what extent carbon deposition contributed to the loss in catalyst activity.

3.4.3.3. Aspects of deactivation from electron microscopy

Transmission electron microscopy was used to probe the catalyst microstructure. At no stage was any evidence found for the presence of filamentous carbon. However, structures that may be assigned to either encapsulate carbon or a NiO film surrounding nickel metal particles, was observed on more than one occasion. An example of a TEM plate of a catalyst that was exposed for two hours to an atmosphere containing methane and oxygen at 604 °C is shown in Figure 32-8. The dark spots are nickel particles while the lighter areas around these spots may be either NiO or encapsulate carbon. From the previous discussion, the former scenario is the more likely of the two.
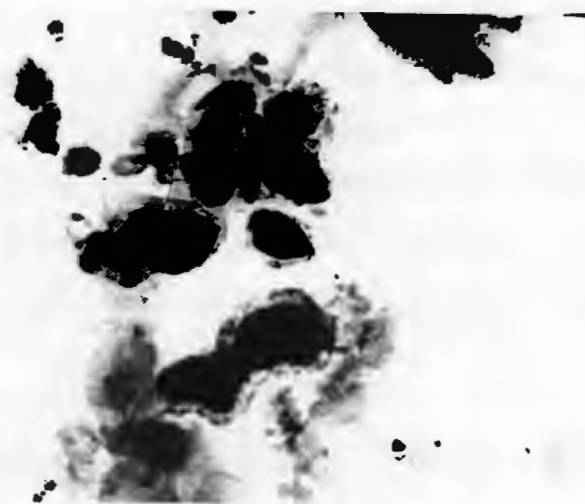
Figure 32-8   TEM plate of a used catalyst sample (Mag. = 73 000X (1mm = 13.7nm), $P°_{CH4}$ = 2.97 kPa, $P°_{O2}$ = 0.99 kPa, T = 604°C)

Chapter 4

4. DISCUSSION

Write against those who probe science too deeply (Blaise Pascal [164])

4.1. Implications of the results of initial catalytic tests

4.1.1. The influence of heat and mass transport

It was concluded earlier (see section 3.2.5) that the reactor used in this work was free from the effects of film transport and that there were no internal gradients. That conclusion is tested in this section by applying well-known theoretical criteria to the complete data set. The criteria require the use of an experimental reaction rate and in this case the rates calculated by method 7 (as discussed in section 3.3.1.4.b) were used.

4.1.1.1. External transport effects

After presenting a theoretical framework of film transport processes, the experimental data will be evaluated in terms of the importance of external heat and mass transport.

4.1.1.1.a. Theory of evaluating external transport effects

The effect of mass and heat transfer through the hydrodynamic layer around catalyst particles may be quantified by applying the method which was presented by Carberry [165]. In that work, external transfer processes were treated in terms of observable parameters and an external effectiveness factor for an nth order reaction was defined as the ratio of the reaction rate expressed in terms of surface conditions to the reaction rate expressed in terms of bulk conditions:

$$\eta_{ext} = \frac{k_s \cdot C^n_s}{k \cdot C^n} \tag{4-1}$$

and

$$\eta_{ext} = \frac{k_s}{k} \cdot \left(\frac{C_s}{C}\right)^n = exp\left[\frac{-E_a}{R \cdot T} \cdot \left(\frac{T}{T_s} - 1\right)\right] \cdot \left(\frac{C_s}{C}\right)^n \tag{4-2}$$

At steady state, the rate of mass transfer across the film with k_g the mass transfer coefficient ($m.s^{-1}$) and a_m the external surface area available for mass transfer expressed per unit mass of catalyst ($m^2.g^{-1}$), must be equal to the rate of the surface reaction:

$$r_{CH_4} = k_s C_s^n = k_g a_m (C - C_s) \tag{4-3}$$

One may re-arrange equation (4-3) to obtain an expression for the ratio of species concentration on the catalyst surface to the concentration in the bulk:

$$\frac{C_s}{C} = 1 - \frac{r_{CH_4}}{k_g \cdot a_m \cdot C} \tag{4-4}$$

If the Chilton-Colburn analogy is invoked which is based on the assumption that heat and mass transfer both occur by a convective mechanism and that there is no significant radiative heat transfer, J_D can be set equal to J_A. This may not be true at temperatures as high as 600°C, but because radiation offers an additional pathway for heat transfer between the catalyst surface and the gas, it contributes to the equalization of the bulk and surface temperatures. The assumption that radiation is absent ($J_D = J_H$) will therefore give a conservative estimate of the difference between surface and bulk temperatures.

$$J_A = J_D = \frac{h}{\rho \, u_o \, C_p} \, Pr^{2/3} = \frac{k_g}{u_o} \, Sc^{2/3} \qquad (4\text{-}5)$$

One may re-write this expression and thus find a relationship between the heat- and mass-transfer coefficients:

$$\frac{h}{k_g} = \rho \cdot C_p \cdot Le^{2/3} \qquad (4\text{-}6)$$

where the Lewis number is the ratio of the Schmidt and Prandtl numbers (Le = Sc/Pr). The assumption of steady state also allows one to equate the rate of film heat transfer to the rate of heat generation at the catalyst surface.

$$(-\Delta H) \cdot r_{CH_4} = h \, a_m (T_s - T) \qquad (4\text{-}7)$$

In the above expression, h is the heat transfer coefficient in units of $W.m^{-2}.K^{-1}$. The relationship between the temperature of the bulk and that of the catalyst surface is then calculated by re-arranging equation (4-7):

$$t = \frac{T_s}{T} = 1 + \frac{-\Delta H \cdot C}{\rho \cdot C_p \cdot T \cdot Le^{2/3}} \cdot \frac{r_{CH_4}}{k_g \cdot a_m \cdot C} \qquad (4\text{-}8)$$

The term on the right-hand side which also appears in equation (4-4), is a dimensionless variable which can be calculated from directly-measurable quantities and is designated by the symbol *Ob*:

190

$$Ob = \frac{r_{CH_4}}{k_g \, a_m \, C} \qquad \text{(4-9)}$$

Two additional constants which are also functions of measurable quantities only may be defined to further characterize the system, namely a heat-of-reaction term

$$\beta = \frac{-\Delta H \cdot C}{\rho \cdot C_p \cdot T \cdot Le^{2/3}} \qquad \text{(4-10)}$$

which allows one to re-write equations (4-4) and (4-8):

$$\frac{C_s}{C} = 1 - Ob \qquad \text{(4-11)}$$

$$t = \frac{T_s}{T} = 1 + \beta \cdot Ob \qquad \text{(4-12)}$$

and a term accounting for the apparent activation energy:

$$\gamma = \frac{E_a}{R \cdot T} \qquad \text{(4-13)}$$

If these two constants and the expression for *Ob* are back-substituted in equation (4-2), an analytical expression relating the external effectiveness factor in terms of observables parameters only, is obtained:

$$\eta_{ext} = (1 - Ob)^n \cdot exp\left[-\gamma \left(\frac{1}{1 + \beta \cdot Ob} - 1 \right) \right] \qquad \text{(4-14)}$$

4.1.1.1.b. Evaluation of experimental conditions with the criteria for checking external transport effects

The above correlations were applied to the experimental data by using the bulk properties of the gases at experimental conditions and the measured reaction rate to calculate the observable parameters in the Carberry correlation. The mass transfer coefficient (k_g) was estimated from a J_D correlation from the work of Williamson *et al.* [166] and the transport properties of gases were calculated using standard correlations [167, 168]. The reaction rate was determined by differentiating a curve that was fitted to the integral kinetic data (method 7 as shown in section 3.3.1.4.b). The methane partial pressure at the catalyst surface was calculated according to equation (4-4) and the result was plotted as a function of the methane partial pressure in the bulk (Figure 4-1).

The deviation from the bulk **partial pressure** of methane is more pronounced at high values of P_{CH4}. This effect was to be expected due to the proportional dependence of the rate of methane consumption (r_{CH4}) to methane partial pressure (see Table 3-11). At high r_{CH4}, more severe film gradients develop due to the rapid depletion of the reactant close to the catalyst surface.

P_{CH4} **In the Bulk** [kPa]
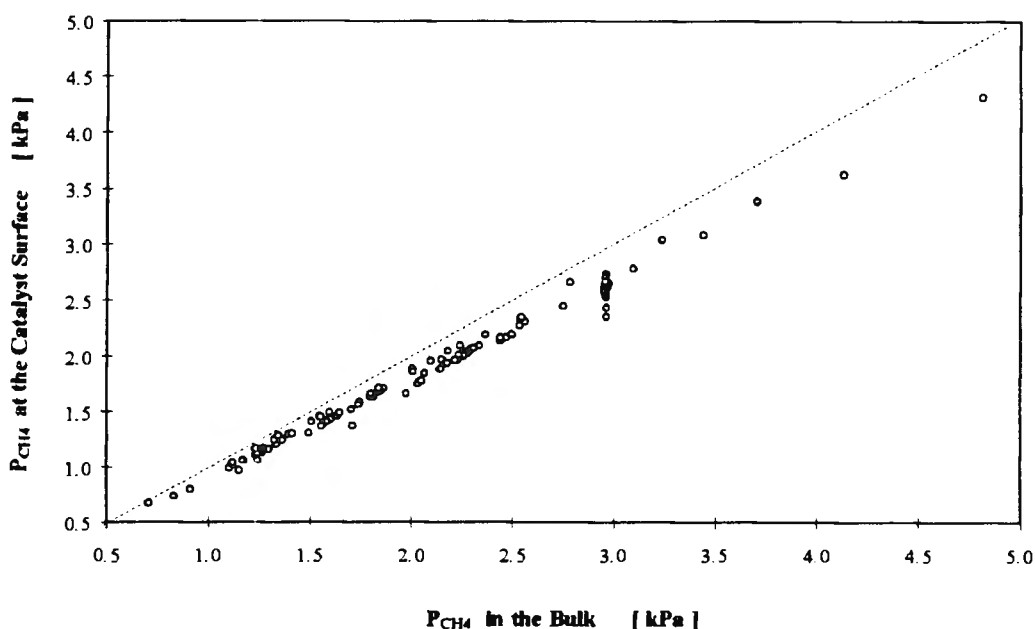
Figure 4-1 P_{CH4} at the catalyst surface as calculated from equation (4-4)

The difference between surface and bulk **temperatures** was estimated by equation (4-8). Three cases were considered, each with different heat of reaction. In the first case, it was assumed that total combustion was the predominant reaction (ΔH = -803 kJ mol^{-1}).
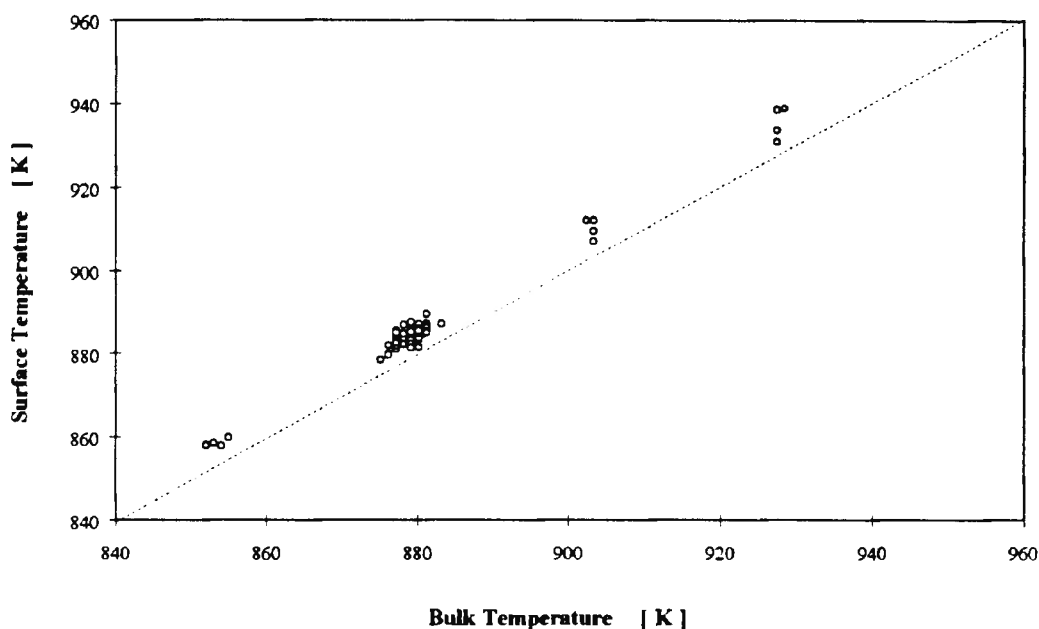
Figure 4-2 Temperature at the catalyst surface as calculated from equation (4-8). (ΔH = -803 kJ.mol^{-1})

As shown in Figure 4-2, this led to a positive deviation of the surface temperature from the bulk temperature, indicating that the rate of heat transfer would not be sufficiently high to remove all the heat from the catalyst surface if all the methane that was consumed, was converted into total oxidation products. When it was assumed that oxidative reforming was the predominant reaction (ΔH = -22.2 kJ mol^{-1}), the deviation was less pronounced than in the case when total combustion was assumed (see Figure 4-3).

Both total oxidation and oxidative reforming take place in conjunction with endothermic steam reforming which led to a negative deviation from the bulk temperature. This latter finding again suggests that if steam reforming were the only reaction responsible for all methane consumption, the rate of heat transfer would not be high enough to ensure uniformity in temperature between the catalyst surface and the bulk gas.
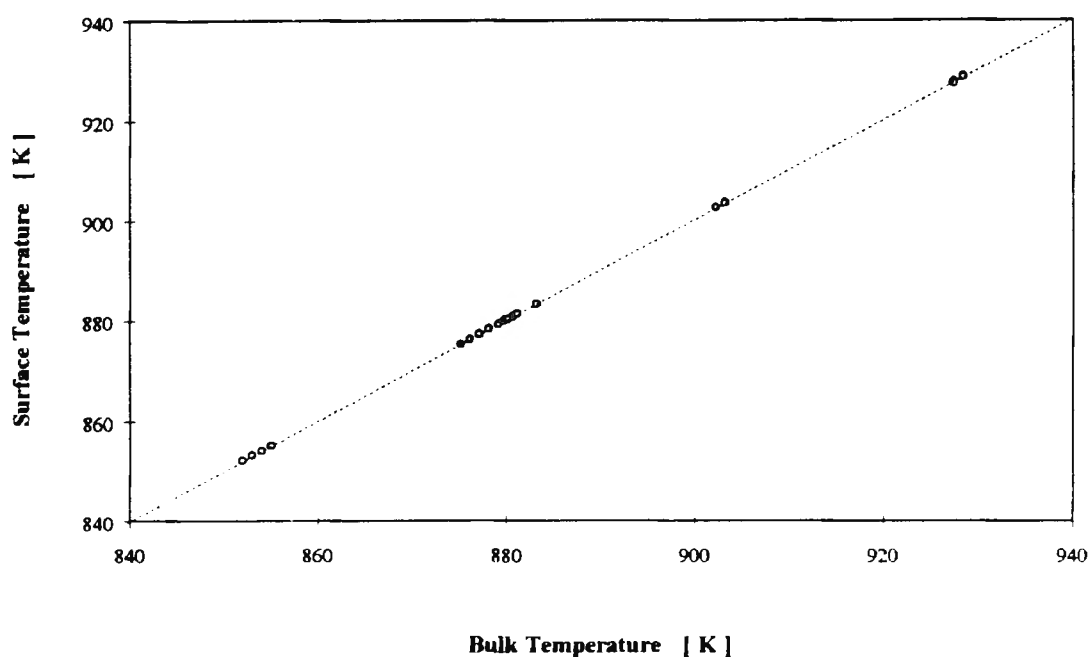
Figure 4-3 Temperature at the catalyst surface as calculated from equation (4-8). (ΔH = -22.2 kJ.mol^{-1})

Since both CO and CO_2 are formed at the bed inlet, T_S will most probably assume a value between the T_S for total oxidation (Figure 4-2) and T_S for oxidative reforming (Figure 4-3). As the bed outlet is approached, steam reforming becomes more important and T_S will be between that of steam reforming oxidative reforming.

In addition to the calculation of the temperature and methane partial pressure at the catalyst surface, the so-called external effectiveness factor (as previously defined in equation (4-1)) was calculated (see Figure 4-4). In order to do this, a value was needed for the activation energy. The Arrhenius plot (see Section 3.3.6.1) was used to calculate an apparent activation energy of approximately 60 kJ mol^{-1}.

Most of the data points were higher than η_{ext} = 0.90 which is an indication that the difference between the measured reaction rate and the intrinsic rate caused by external diffusion limitations if combustion was the rate-determining step, was less than 10%. The most significant deviation of η_{ext} was observed at high reaction rates. This was even more pronounced when the calculation of η_{ext} was based on the assumption that steam reforming (Figure 4-5) and oxidative reforming (Figure 4-6) were the respective rate-determining steps. An exothermic reaction in the presence of transport limitations may theoretically cause an

elevated catalyst surface temperature and thus lead to a reaction rate which is higher than the intrinsic rate at bulk conditions. This, however, does not seem to be the case in our system with the external effectiveness factor always less than unity, even when combustion was assumed to be the rate-determining step (Figure 4-4).
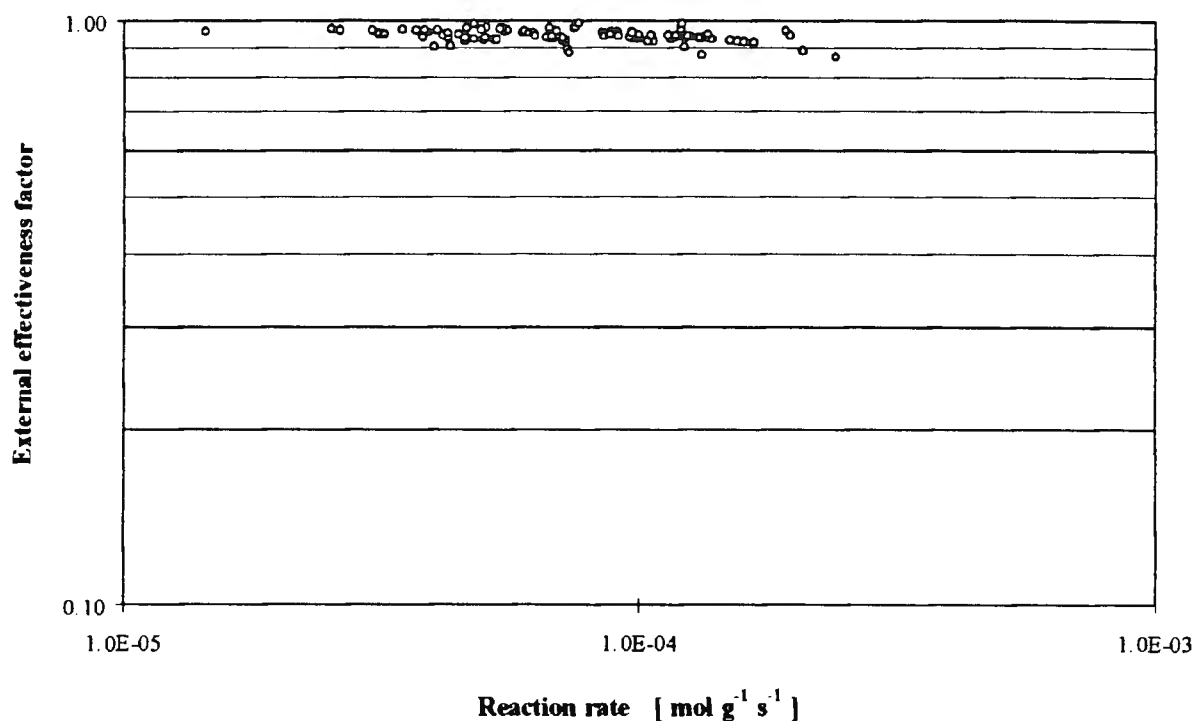
Figure 4-4 External effectiveness factor as a function of r_{CH4}. (E_a = 58 kJ mol^{-1}, ΔH = -890 kJ mol^{-1}))

As was to be expected, the higher the endothermicity of the rate-determining step, the more pronounced was the deviation of η_{ext} from unity. The decrease in reaction rate at the catalyst surface due to the starvation of reactants was compensated for in the case of an exothermic reaction by a higher temperature, and hence a higher reaction rate because of less efficient heat removal from the catalyst surface. The highest rate of methane consumption always occurred at, or close to the catalyst bed inlet. This was also the region where methane was converted mostly to total oxidation products. Because of the decrease in external effectiveness factor with increasing reaction rate, one may conclude that the highest deviation from η_{ext} occurred at the bed inlet and thus in the region of the bed where combustion was predominant. Therefore the maximum deviation between the intrinsic rate of methane consumption at the catalyst surface and the rate measured in the bulk gas was never higher

than about 10%.
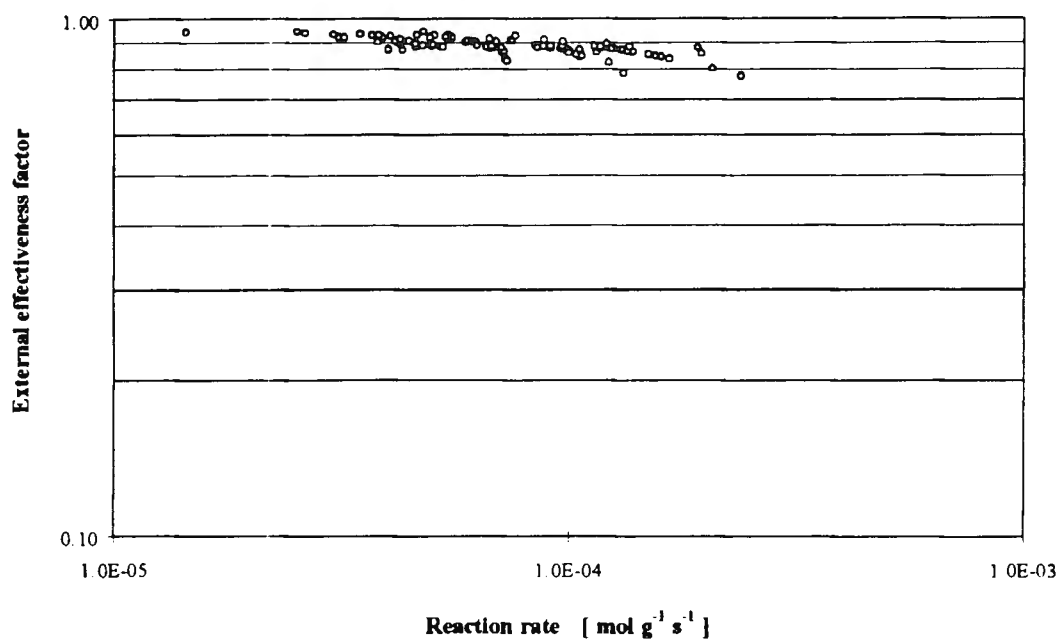
Figure 4-5 External effectiveness factor as a function of r_{CH4}. (E_a = 58 kJ mol^{-1}, ΔH = 250 kJ mol^{-1}))
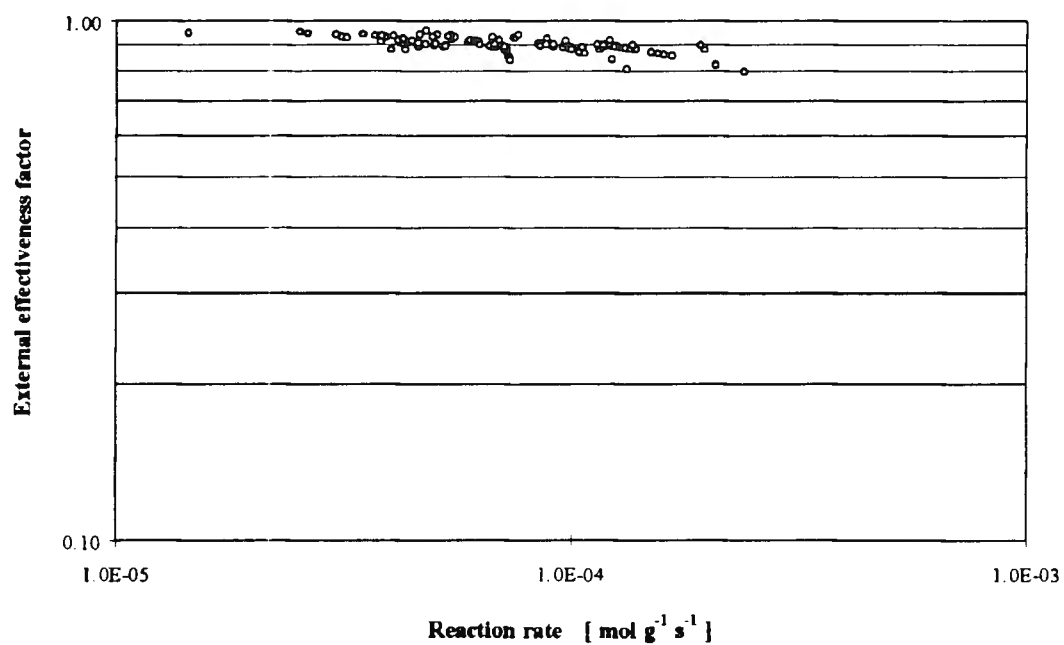
Figure 4-6 External effectiveness factor as a function of r_{CH4}. (E_a = 58 kJ mol^{-1}, ΔH = -56 kJ mol^{-1}))

4.1.1.2. Internal transport effects

The absence of internal transport effects was first demonstrated in section 3.2.5.2. This conclusion was based on the assumption that constant methane conversion at constant contact time over a range of catalyst particle sizes was indicative of the absence of pore diffusion resistance in the range of particle sizes investigated. The effect of pore diffusion is evaluated in the present section by applying two theoretical criteria to experimental rate data. The reaction rates were calculated from X_{CH4} vs. W/F°_{CH4} data by method 7.

In this work, Knudsen diffusivity was determined from the correlation suggested by Anderson [158]:

$$D_{K,E} = 1.94 \cdot \frac{\varepsilon_p}{\tau S \rho_p} \sqrt{\frac{T}{M_M}} \qquad (4\text{-}15)$$

where M_M is the molecular mass of methane (g.mol^{-1}), ρ_p the particle density determined by Hg porosimetry (g.cm^{-3}), ε_p the porosity of the catalyst (also from Hg porosimetry), τ the tortuosity factor (assumed to be 0.2) and S the catalyst surface area (4.9 cm^2.g^{-1} determined by BET). The molecular diffusivity of methane in the reactive mixture was calculated from the binary diffusivities using correlations proposed in the literature [167]. The binary diffusivities, in turn, were calculated with the Chapman-Enskog formula. Effective diffusivity was calculated by equation (4-16):

$$D_e = \left(\frac{1}{D_{CH4, Mix}} + \frac{1}{D_K} \right)^{-1} \qquad (4\text{-}16)$$

For the internal effectiveness factor to exceed 0.95 (thus ensuring that internal concentration gradients are absent) for a first-order reaction in the absence of substantial inhibition by products, Mears proposed [159] that the Weisz-Prater criterion should be applied to experimental data, ie. the Dahmköhler number (Da) must not exceed unity:

$$Da = \frac{r_{CH_4} \cdot r_p^2}{C_S \cdot D_e} < 1 \qquad (4\text{-}17)$$

with r_p the particle radius and C_S the reactant concentration at the catalyst surface. The Dahmköhler number represents a measure of the activity of the catalyst and is a modified form of the Thiele modulus. In order to ensure that the internal effectiveness factor is within 5% of unity, Mears [159] suggested the use of a correlation developed by Kubota et al. [169] for the non-isothermal case

$$\frac{r_{CH_4} \cdot r_p^2}{D_e \cdot C_s} < \frac{1}{\mid n - \gamma \beta \mid} \qquad (4\text{-}18)$$

where β is defined as $(-\Delta H) \, D_e \, C_s \, / \, (\lambda_s \, T_s)$, with λ_s the particle thermal conductivity [157] and γ an Arrhenius factor defined as E_a/RT.

In order to test whether the experimental data presented in this work was subject to intraparticle temperature and concentration gradients, the above two expressions ((4-17) and (4-18)) were applied to the experimental data. The Dahmköhler number was plotted as a function of the rate of methane consumption in Figure 4-7. The Dahmköhler number was significantly smaller than unity over the entire range of methane consumption rate investigated. This confirmed the absence of **concentration** gradients.

For the internal effectiveness factor to be within 5% of unity in the presence of a non-isothermal reaction, the adherence of experimental data to the expression derived by Kubota (equation (4-18)) was tested. Three heats of reaction were assumed, i.e. $\Delta H_{Combustion}$, $\Delta H_{Steam\ reforming}$ and $\Delta H_{Oxidative\ reforming}$. The effect of the rate of methane consumption on the adherence of the data to the Kubota criterion is shown in Figure 4-8. The values depicted on the y-axis refer to the ratio of the left-hand side (LHS) and right-hand side (RHS) of equation (4-18). A value exceeding unity is indicative that the Kubota criterion was not satisfied.
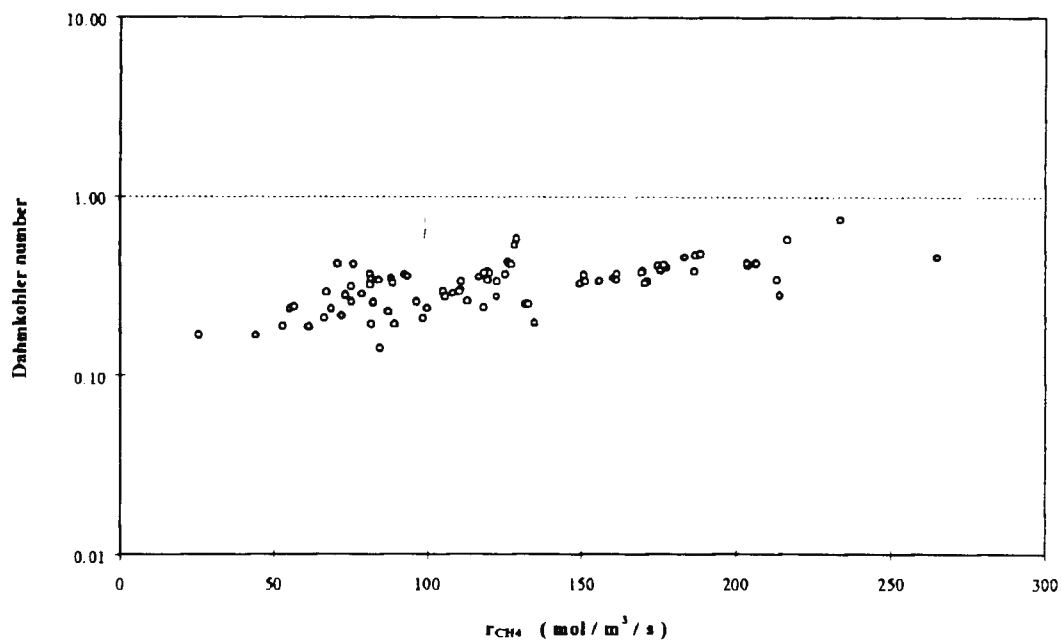
Figure 4-7 Dahmköhler number as a function of the rate of methane consumption
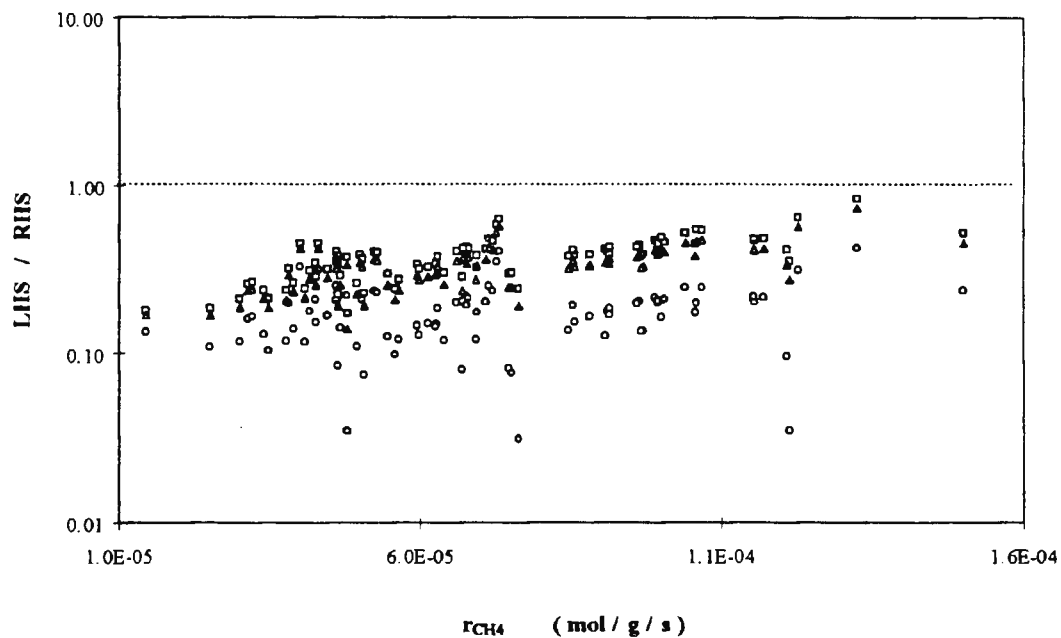
Figure 4-8 The effect of $W/F°_{CH_4}$ on internal diffusion (ΔH: O = Combustion, $\square$ = Steam reforming, $\triangle$ = Oxidative reforming)

From Figure 4-8 it is clear that the Kubota criterion was satisfied for all the assumed heats of reaction. Therefore it may be concluded that there were no internal temperature- or concentration gradients present.

4.2. Reaction mechanism/pathway

As discussed at some length in section 1.6, it has been proposed in the literature that the oxidative reforming of methane may follow one of two reaction pathways. Either carbon monoxide is formed directly from methane oxidation as a primary product or it may be formed as a secondary product by the reaction of methane with CO_2 and water produced *in-situ* early in the catalyst bed by the total oxidation of a fraction of the methane in the feed.

There are a number of findings in the present work which suggest that the pathway is more complex than either of these two scenarios.

Firstly, a typical product spectrum (P_i vs. $W/F^°_{CH4}$ shown in Figure 3-19) indicates that water and carbon dioxide were formed as primary products. Carbon monoxide and hydrogen were also produced at the inlet of the bed (in the presence of oxygen) as primary products. Therefore; either the rate of steam reforming and/or carbon dioxide reforming of methane in this part of the catalyst bed (close to the bed inlet and in the presence of oxygen) was fast enough to lead to the formation of substantial amounts of carbon monoxide and hydrogen, or carbon monoxide and hydrogen were formed as products of the oxidative reforming (partial oxidation) of methane.

Water co-feeding did not enhance the rate of CO and H_2 formation at the bed inlet; in fact the rate of methane consumption was significantly depressed (refer to section 3.3.6.3.d.i). Carbon dioxide co-feeding enhanced CO formation, but depressed H_2 formation which is more in line with the expected effect of CO_2 on the water-gas shift reaction (as discussed in section 3.3.6.3.c.i). When methane conversion was enhanced in the presence of co-fed carbon dioxide, oxygen conversion was also enhanced. Additionally, at the highest level of CO_2 partial pressure, methane conversion was lower than the level of methane conversion in the absence of CO_2. This suggests that neither the steam reforming- nor the carbon dioxide reforming of methane was operative at the bed inlet.

Hence, it follows that the CO and H_2 formation in the presence of oxygen and close to the bed inlet was the result of the direct oxidative reforming of methane.

As stated above, carbon dioxide and water were formed as primary products (*i.e.* methane combustion) at the bed inlet. However, given the rapid consumption of oxygen and enhanced formation of combustion products when hydrogen and carbon monoxide were co-fed with methane and oxygen, the formation of CO_2 and H_2O very early in the catalyst bed by the oxidation of primary oxidative reforming products (CO and H_2) cannot be excluded. Such a reaction would be very fast since at no time during the kinetic experiments was an inflection point in the CO_2 or H_2O partial pressure vs. W/F°_{CH4} observed which would have been indicative of the secondary formation of combustion products. The experimental setup did not allow for the investigation of the reaction pathway at very short contact times.

Within the accuracy of the current experimental setup, therefore, it may be concluded that carbon dioxide and water were formed as primary products of methane oxidation.

The rates of formation of water and carbon dioxide (slopes of the P_{H2O} vs. W/F°_{CH4} and P_{CO2} vs. W/F°_{CH4} curves) were always the highest at the bed inlet. The rate of formation of these two products declined deeper into the catalyst bed. In some cases the rate of formation was zero at some point deeper into the bed (as evidenced by a peak in P_i vs. W/F°_{CH4} curves) and became negative at the bed outlet. Furthermore, carbon dioxide consumption in the latter part of the bed was less pronounced than that of water. These findings indicate that water and carbon dioxide were not secondary products. In fact, these two primary products were the reactants for a secondary reaction.

The rates of hydrogen and carbon monoxide formation were never negative, except during co-feeding experiments when rapid consumption of CO and H_2 was observed in the presence of oxygen close to the bed inlet. Inflection points were common in the majority of P_{CO} vs. W/F°_{CH4} and P_{H2} vs. W/F°_{CH4} curves.

The conclusion thus follows that carbon monoxide and hydrogen are formed, in addition to the direct oxidative reforming of methane at the bed inlet, also by the steam reforming- and carbon dioxide reforming of methane deeper into the catalyst bed and thus in the absence of oxygen.

Methane was converted both in the presence of oxygen and when all the oxygen had disappeared. Lastly, the water-gas shift reaction was forced to the left or right, depending on the co-fed component. Based on the above information, the following reaction mechanism/scheme is proposed:

i   The reaction pathway of methane conversion consists of a series-parallel scheme.

ii All the products are formed as primary products; CO and H_2 by direct oxidative reforming and CO_2 and H_2O by total oxidation of methane.

iii Steam reforming- and CO_2 reforming of methane (with the former more pronounced) are responsible for methane conversion to carbon monoxide and hydrogen in the latter part of the bed.

iv The water-gas shift reaction is close to the equilibrium value for all reaction conditions.

From the above information, the following reaction pathway is proposed:

Primary products   Secondary products
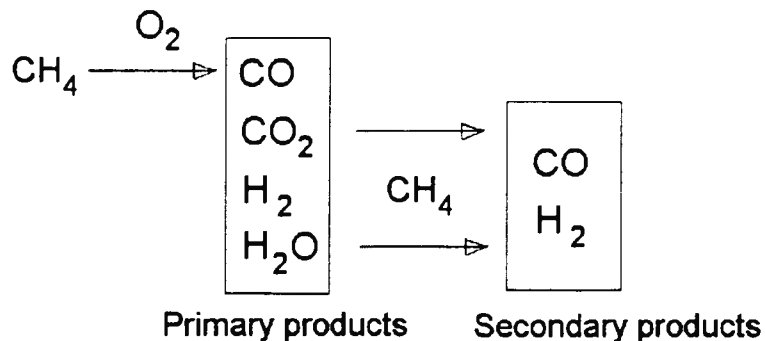
This proposed pathway was used in the construction of a kinetic model.

4.3. Reaction Kinetics

4.3.1. Aspects of the experimental kinetic data

It was shown previously that the catalyst deactivated with time on-stream (see

sections 2.4.1.5 and 3.4.3). In the first instance, this necessitated the use of a fresh charge of catalyst for each level of each of the operating conditions. Furthermore, the catalyst performance could not be evaluated at steady state. This led to the decision to evaluate the catalyst performance at zero time on-stream. The manner in which methane and oxygen conversion and product selectivities were determined have been discussed in the abovementioned sections.

In general, an experiment was always started with a charge of fresh catalyst, pre-reduced in H_2/He at 400°C (see the discussion in section 2.3.2). With time on-stream, the presence of oxygen at the bed inlet would result in the conversion of some of the nickel to nickel oxide. Since nickel oxide is less active than nickel for catalysing the methane oxidative reforming reaction, the conversion of methane would steadily decrease with time on-stream.

4.3.2. Differential treatment of integral kinetic data

As discussed previously, the integral kinetic data were converted to reaction rates by fitting analytical curves to the X_{CH4} vs. $W/F^°_{CH4}$ data and taking the first derivative of the curves. This section deals with attempts to find a kinetic model that would adequately describe the rate of methane consumption calculated from integral kinetic data. The two models that were considered, were based on certain assumptions of the reaction mechanism and the lack of fit of these models can be expected to yield some clues about improbable reaction pathways (rather than supporting a more likely mechanism).

4.3.2.1. Kinetic models tested

Two variations on a Langmuir-Hinshelwood model were evaluated by comparing the rate of methane consumption predicted by the models to the rate obatined experimentally from a differential treatment of integral kinetic data. Certain clues from the data presented in the previous chapter have been used in the development of these models. The rate of methane consumption (r_{CH4}) was shown earlier (see section 3.3.6.2) to be proportional to methane

partial pressure and a weak function of oxygen partial pressure. Furthermore, the products were found to inhibit the rate of methane consumption (r_{CH4}). It was therefore decided to evaluate two models, both of which were based on the assumption that some form of methane adsorption was the rate-limiting step in the oxidative reforming of methane. In the first model, methane adsorption on a single vacant site was assumed to be the slowest step while the derivation of the second model was based on the premise that the rate-determining step,, i.e. methane adsorption, required two adjacent vacant sites.

4.3.2.1.a. Methane adsorption on a single vacant site (Model 1)

For the development of the first model, methane adsorption was assumed to occur by the interaction of gaseous CH_4 with vacant sites (*) on the catalyst surface by the following mechanism:

$$CH_4 + * \rightarrow CH_4 - * \tag{41-1}$$

Reaction (41-1) was assumed to be the rate-limiting step and with the rate of the forward reaction being proportional to the methane partial pressure and the concentration of vacant sites, this approach led to the following expression for the rate of methane consumption:

$$- r_{CH_4} = k_1 \, P_{CH_4} \, \theta_v \tag{41-2}$$

with θ_v denoting the fraction of acant sites. It is furthermore assumed that the decomposition of adsorbed CH_4 into adsorbed C ia CH_3, CH_2 and CH fragments occurs rapidly and that the coverages of these intermediate adsorbed C1 species (θ_{CH3}, θ_{CH2}, θ_{CH} and θ_C) are negligible in the present setup. This is in line with the argument followed by Hickman and Schmidt [94].

Dissociative adsorption of oxygen (as can be assumed on the basis of work done by

Boreskov [154])

$$O_2 + 2 * \rightleftharpoons 2 O - * \tag{41-3}$$

as well as dissociative adsorption of hydrogen (as found by Lee and Schwarz [170]) is proposed for the present system,

$$H_2 + 2 * \rightleftharpoons 2 H - * \tag{41-4}$$

This leads to the equilibrium relationships:

$$\theta_O = \sqrt{K_{O_2} P_{O_2}} \; \theta_v \tag{41-5}$$

$$\theta_H = \sqrt{K_{H_2} P_{H_2}} \; \theta_v \tag{41-6}$$

whereas the adsorption of carbon monoxide, carbon dioxide and water are assumed to be non-dissociative and on single sites.

$$CO + * \rightleftharpoons CO - * \tag{41-7}$$

$$CO_2 + * \rightleftharpoons CO_2 - * \tag{41-8}$$

$$H_2O + * \rightleftharpoons H_2O - * \tag{41-9}$$

The coverage of these species could therefore be written as follows:

$$\theta_{CO} = K_{CO} \ P_{CO} \ \theta_v \qquad\qquad (41\text{-}10)$$

$$\theta_{CO_2} = K_{CO_2} \ P_{CO_2} \ \theta_v \qquad\qquad (41\text{-}11)$$

$$\theta_{H_2O} = K_{H_2O} \ P_{H_2O} \ \theta_v \qquad\qquad (41\text{-}12)$$

The subsequent dissociation of water into HO-* and H-* fragments and the dissociation of the HO-* fragments to yield adsorbed H and O species were accounted for by reaction (41-13)

$$O-* \ + \ H-* \ \rightleftharpoons \ HO-* \ + \ * \qquad\qquad (41\text{-}13)$$

and led to the relationship:

$$\theta_{OH} = \sqrt{K_{O_2} \ K_{H_2} \ P_{O_2} \ P_{H_2}} \ K_{OH} \ \theta_v \qquad\qquad (41\text{-}14)$$

The dissociation of adsorbed CO_2 and H_2O into adsorbed OH, H and O and adsorbed CO_2 into CO, O and C is therefore not disallowed.

The shape of a typical partial pressure vs. W/F°_{CH4} curve for water and carbon dioxide was shown in the previous chapter to frequently exhibit maxima. This is indicative of the consumption of CO_2 and H_2O deeper into the catalyst bed. Hence, the proposed model should account for these qualitative features. The abovementioned assumption with respect to the dissociation of adsorbed H_2O and CO_2 and their possible consumption is therefore consistent with the experimental observations.

From the above relationships, θ_v is given by equation (41-15):

$$\theta_v = 1 \div$$

$$(1 + \sqrt{K_{O_2} P_{O_2}} + K_{CO} P_{CO} + \sqrt{K_{H_2} P_{H_2}} + K_{CO_2} P_{CO_2} +$$

$$K_{H_2O} P_{H_2O} + \sqrt{K_{H_2} K_{O_2} P_{H_2} P_{O_2}} K_{OH})$$

(41-15)

The above expression for the vacant site coverage is written in terms of equilibrium constants and compound partial pressures. The expressions for the coverage of adsorbed CH_4, CH_3, CH_2, CH and C species are not included in the vacant site expression because of the stated assumption that the coverage of these species are negligible. Furthermore, the absence of equilibrium constants for the decomposition of adsorbed CO_2 and H_2O is consistent with the assumption that all surface reactions are at equilibrium. The inclusion of those species that take part in the water and carbon dioxide decomposition reactions in other equilibrium expressions, is sufficient to ensure that the system is completely represented.

Thus, by combining equations (41-15) and (41-2), an expression for the rate of methane consumption in terms of compound partial pressures and adsorption constants may be written. This is indicated in equation (41-18). The present model gives a fixed product distribution due to the assumption that all reactions are at equilibrium, except for the rate-determining step. The same is valid for the next model.

4.3.2.1.b. Methane adsorption on two adjacent vacant sites (Model 2)

An additional case was considered, namely the dissociative adsorption of methane on two adjacent vacant sites:

$$CH_4 + 2 * \rightarrow CH_3 - * + H - *$$

(41-16)

Therefore it follows that

$$- r_{CH_4} = k_1 \ P_{CH_4} \ \theta_v^2 \tag{41-17}$$

while all the assumptions outlined for model 1 are still valid for model 2. Therefore the denominator of the rate expression remains identical to that of model 1, with the exception that it would be squared. The resulting rate expression is shown in equation (41-19).

208

$$-r_{CH_4} = \frac{k_1 \, P_{CH_4}}{\left(1 + \sqrt{K_{O_2} \, P_{O_2}} + K_{CO} \, P_{CO} + \sqrt{K_{H_2} \, P_{H_2}} + K_{CO_2} \, P_{CO_2} + K_{H_2O} \, P_{H_2O} + \sqrt{K_{H_2} \, K_{O_2} \, P_{H_2} \, P_{O_2} \, K_{OH}} \right)}$$

(41-18)

$$-r_{CH_4} = \frac{k_1 \, P_{CH_4}}{\left(1 + \sqrt{K_{O_2} \, P_{O_2}} + K_{CO} \, P_{CO} + \sqrt{K_{H_2} \, P_{H_2}} + K_{CO_2} \, P_{CO_2} + K_{H_2O} \, P_{H_2O} + \sqrt{K_{H_2} \, K_{O_2} \, P_{H_2} \, P_{O_2} \, K_{OH}} \right)^2}$$

(41-19)

4.3.2.2. Fit of differential kinetic data to the rate expressions

The two rate expressions that were derived above were fitted to differential experimental kinetic data by a Nelder-Mead optimization routine written in Turbo Pascal [171]. The code for for program is included in Appendix E. The reaction rates obtained from three methods (methods 3, 7 and 8) of curve-fitting to $W/F°_{CH4}$ vs. X_{CH4} experimental data were used in the optimization routine for each of the two models. Therefore a total of six optimization runs were performed.

The rate constants were assumed to take the form:

$$K_i = A_i \, exp \left(\frac{-E_a}{R \cdot T} \right) \qquad (41\text{-}20)$$

and the adsorption constants

$$K_i = A_i \, exp \left(\frac{-B_i}{R \cdot T} \right) \qquad (41\text{-}21)$$

with B_i having been assigned no specific physical significance. B_i is essentially a lumped parameter that estimates the adsorption enthalpy and was chosen for mathematical convenience rather than for any physical or chemical significance. The adsorption entropy is incorporated in the pre-exponential factor and is in this instance, assumed to be independent of temperature. The values of A_i, E_a and B_i were determined by finding the best fit of the proposed model to 108 experimental data points. The data that were used were the partial pressures obtained by extrapolating the experimental data to zero time on-stream and therefore corresponded to the initial activity of the pre-reduced catalyst. The results of the optimization procedure are tabulated in Table 4-1.

The adequacy of the models were tested by invoking the so-called F-test which is discussed in appendix C.3.5 (as applied by Froment and Hosten [172] and Anderson and

Sclove [173]) while simultaneously considering the adherence of the optimized parameters to certain physical constraints, namely a negative adsorption enthalpy and positive pre-exponential terms. In all cases the stop criterion (5E-12) was satisfied within 10 000 iterations.

In only two instances did the modelling results fail the F-test. In both cases (for both models 1 and 2) the rate of methane consumption that was used to optimize the model parameters were calculated from a second-order polynomial fit to the data (Method 3).

Table 4-1 Forms of the rate expressions that were evaluated

Model number	Method[a]	Constraints[b]	RMSE[c] x 100	F_c	$F_{0.95}$	F[d]-test
1	3	✓	2.72	0.44	0.25	No
2	3	✓	2.74	0.45	0.25	No
1	7	✓	1.75	0.04	0.25	✓
2	7	✓	1.74	0.04	0.25	✓
1	8	✓	1.38	0.05	0.25	✓
2	8	✓	1.38	0.05	0.25	✓

a   The curve-fitting method that was used to calculate the reaction rate that was used in the optimization procedure.
b   Negative adsorption enthalpy and positive pre-exponential terms.
c   RMSE defined in equation (41-22)
d   The F-test was based on the Lack-of fit sum of squares from independent experiments and was evaluated at the 95% confidence level.

Clearly a polynomial fit to the data was an unsatisfactory representation of the measured reaction rate in spite of the fact that lower residuals resulted for its representation of X_{CH4}. The failure of the polynomial fit was already apparent by a visual inspection of the curve fits; at high W/F°_{CH4} the slope of the polynomial expression became negative and the rate of methane consumption was therefore incorrectly calculated. In this instance, the failure of method 3 to accurately predict the rate of methane consumption at high W/F°_{CH4} does not imply that the second-order polynomial fit to the integral data failed entirely. Because of the arbitrary nature of the selective removal of suspect data points from the data set, the finding of a better model fit to experimental data using method 3 was not pursued further.

The two exponential curve-fitting procedures (methods 7 and 8) both resulted in much

lower F_c values than method 3. When the rates calculated by method 8 were used in the optimization routine, the lowest RMSE and hence the best fits to the data resulted for both models tested.

The model which exhibited the lowest root mean square error (RMSE defined in equation (41-22)) was that derived from the assumption of methane adsorption on a single vacant site (model 1 using r_{CH4} calculated by method 8).

$$RMSE = \frac{\sqrt{r_{CH_4}^{Pred} - r_{CH_4}^{Meas}}}{N \cdot r_{CH_4}^{Meas, Average}}$$ (41-22)

The parity plots of the two models, using rates calculated by method 8, are shown in Figure 4-9 to Figure 4-10.
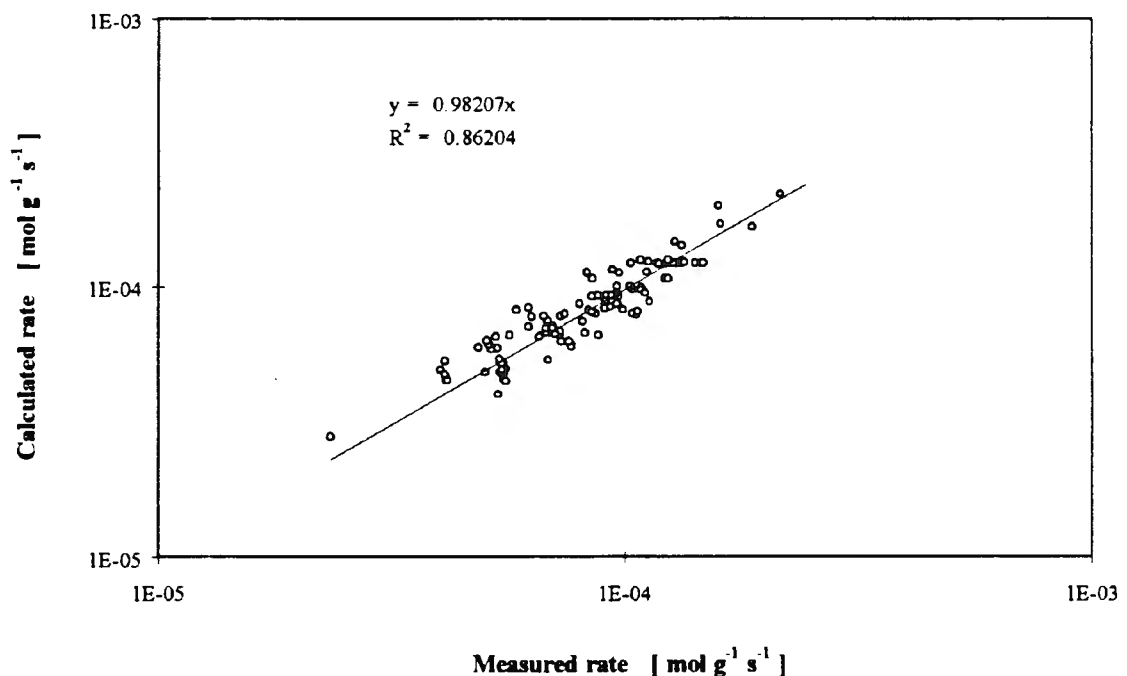
Figure 4-9 Parity plot of the best model fit to differential reaction rates from integral kinetic data (Model 1, r_{CH4} calculated by method 8)
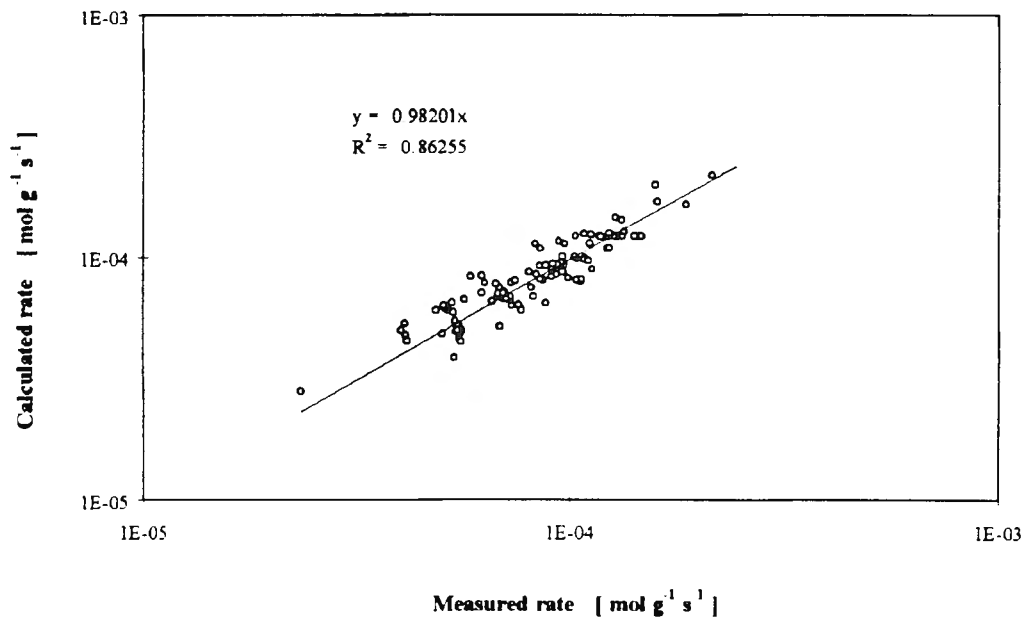
Figure 4-10 Parity plot of the best model fit to differential reaction rates from integral kinetic data (Model 2, r_{CH_4} calculated by method 8)

The kinetic constants from the optimization of model 1 are tabulated in Table 4-2. The activation energy calculated by the model was fairly similar to the experimentally-determined E_a value (E_a = 61 kJ mol^{-1} for method 8).

Table 4-2 Kinetic constants from the unconstrained optimization of model 1 to differential kinetic data obtained by method 8.

Parameter	Units of A_i	Pre-exponential	E_a or B_i kJ mol^{-1}	K^{877K}_i
k_1	[mol g^{-1} s^{-1}]	0.99	72.4	4.8E-5
K_{O2}	[kPa^{-1}]	8.6E-9	-107.0	8.6E-9
K_{CO}	[kPa^{-1}]	2.8E-5	-60.8	2.8E-5
K_{H2}	[kPa^{-1}]	1.3E-15	-90.0	1.3E-15
K_{CO2}	[kPa^{-1}]	1.1E-13	-136.5	1.2E-13
K_{H2O}	[kPa^{-1}]	1.4E-5	-67.3	1.4E-5
K_{OH}	[-]	3.4E-5	-74.3	3.4E-5

Also evident from the above results are the low values of the adsorption constants for carbon dioxide and hydrogen compared to carbon monoxide and water. This suggests that

these compounds have a very small effect on the rate of methane consumption compared to water and carbon monoxide. This does not correlate very well with the reaction orders that were calculated by the method of **initial rates** in the previous chapter (see Table 4-3). However, the lower propensity for carbon dioxide to adsorb and thus dissociate, sheds some light on the previous observation that dry (CO_2) reforming was less pronounced than steam reforming.

Table 4-3 Reaction order vs. adsorption constants of reaction products

Compound	Reaction order[a]	Adsorption constant[b]
CO	-0.28 ± 0.07	2.8E-5
H_2	-0.16 ± 0.01	1.3E-15
CO_2	-0.10 ± 0.01	1.2E-13
H_2O	-0.08 ± 0.10	1.4E-5

a   Determined by the method of initial rates - using rates calculated by method 8
b   From the optimization of model 1 - using rates calculated by method 8

It is interesting to note that, of the four reaction products, CO was found to have the most significant effect on the rate of methane consumption, in both the method of initial rates (leading to reactions orders) and the optimized model fit to differential kinetic data (resulting in adsorption constants).

In the process of deriving the differential models, the assumption was made that all reactions, except for the rate-determining step, were at equilibrium. Hence, the predicted product distribution should be identical to the product distribution calculated at thermodynamic equilibrium.

The ratio of the experimental water-gas shift expression to the theoretical WGS equilibrium ratio was plotted as a function of the methane conversion and the result is shown below in Figure 4-11. There was no trend with respect to the methane conversion, which indicates that the water-gas shift reaction was very fast and close to the equilibrium on the catalyst investigated and at the present operating conditions. While the proximity to equilibrium indicates that the models were adequate in predicting the actual product composition, any

other possible model that was derived on the basis of the rate-determining step would, in with the present set of experimental data, have been equally successful.
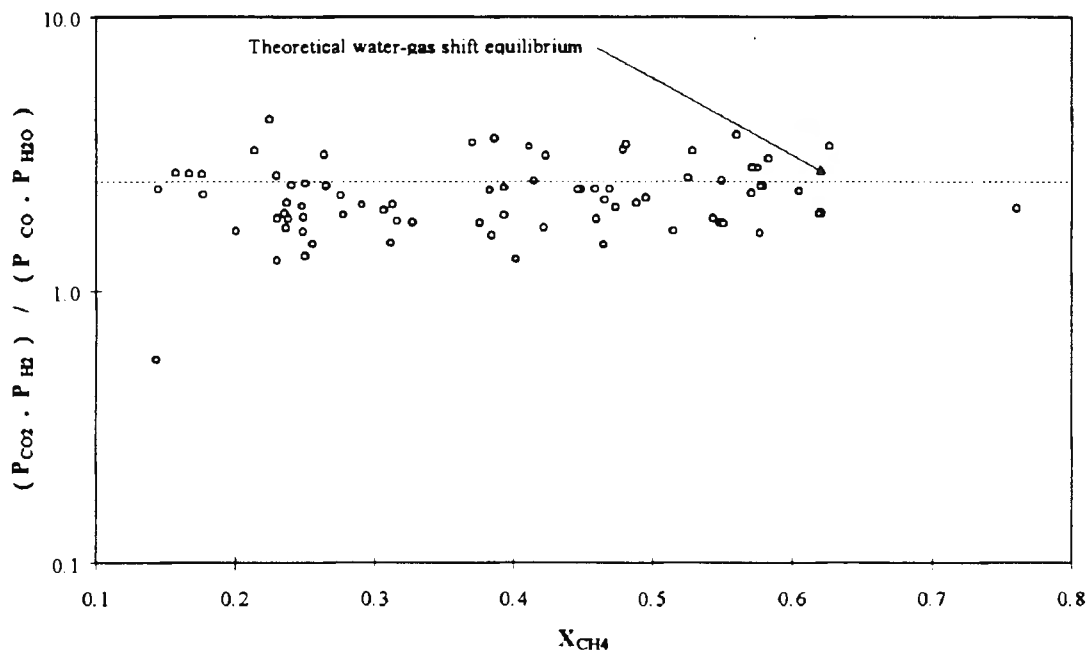
Figure 4-11 Ratio of experimental and theoretical WGS expressions as a function of X_{CH4}

In summary, therefore, method 8 proved to be the most appropriate form of the curve to use for calculating reaction rates from integral kinetic data. The difference in goodness-of-fit between the two models was not sufficient to either discard the one model or to accept the other; both displayed reasonable fits to the experimental data.

4.3.3. Integral analysis of kinetic data

A number of kinetic models were proposed to account for the oxidative conversion of methane (See Table 4-4 for a summary of the models). The kinetic models were combined with mass conservation equations of reactions in a plug flow reactor which were integrated by third- or fifth-order Runge-Kutta-Butcher numerical integration routines [174].

$$\frac{W}{F^{o}_{CH_4}} = \int_{X_{CH_4} = 0}^{X_{CH_4}} \frac{dX_{CH_4}}{- r_{CH_4}} \qquad (42\text{-}1)$$

The procedure were as follows: starting values of the kinetic constants were guessed; taken together with the inlet gas composition, temperature and pressure, the integration procedure was used to obtain 83 calculated/predicted values of methane conversion for each of the 83 inlet conditions of the kinetic experiments. These predicted X_{CH4} values were compared with the measured X_{CH4} and the initial values of the guessed kinetic constants were updated before re-integrating the entire set of 83 data points. The direction and magnitude with which the kinetic constants were adjusted between successive iterations of the data set were determined by a Nelder-Mead simplex routine (written in Turbo Pascal 6). This routine sought to minimize the objective function (n = 83 data points), using all species partial pressures (j = 6):

$$RMSE = \frac{\sum_{i=1}^{n} \sum_{j=1}^{6} (P_{j}^{Measured} - P_{j}^{Model})^{2}}{n \cdot P_{i,j}^{Measured \cdot Mean}} \qquad (42\text{-}2)$$

by adjusting the kinetic constants. Due to the splitting of the n kinetic constants into a pre-exponential factor and activation energy / B_i terms (as described above in equations (41-20) and (41-21)), 2*n number of parameters were optimized for any chosen model. In order to start the optimization procedure, 2*n + 1 so-called simplexes had to be set up from initial guesses of the rate constants / parameters. It has been shown that the choice of the initial simplexes affect the rate of convergence of the Nelder-Mead routine [175], but in our case the initial simplexes were constructed by taking numbers from the random number generator of Turbo Pascal 6 to expand the parameters around their initial guessed values. The initial guesses for E_a was 60 kJ mol^{-1}, B_i = 100 kJ mol^{-1} and the pre-exponential factors were expanded around values of 0.1.

The number of Runge-Kutta steps that were used for the integration of each data point with the guessed rate constants varied and had a significant influence on the time needed to

perform the optimization, but a typical value was always between 10 and 100.

4.3.3.1. The reactions that were considered

Four possible reactions were chosen to represent the kinetic data, namely total oxidation (reaction 1), oxidative reforming (reaction 2), steam reforming (reaction 3) and the water-gas shift reaction (reaction 4). These reactions were used in various combinations (as shown in Table 4-4) to make up a total of eight models. The form of the rate expressions of the four reactions were either taken from literature or from proposals in the present section.

$$CH_4 + 2 O_2 \rightarrow CO_2 + 2 H_2O \qquad\qquad \text{Reaction 1} \qquad \text{(42-3)}$$

$$CH_4 + 0.5 O_2 \rightarrow CO + 2 H_2 \qquad\qquad \text{Reaction 2} \qquad \text{(42-4)}$$

$$CH_4 + H_2O \rightarrow CO + 3 H_2 \qquad\qquad \text{Reaction 3} \qquad \text{(42-5)}$$

$$CO + H_2O \rightleftharpoons CO_2 + H_2 \qquad\qquad \text{Reaction 4} \qquad \text{(42-6)}$$

The reaction rate of the first two reactions, i.e. total oxidation and oxidative reforming, were represented by a number of empirical rate expressions which are discussed in section 4.3.3.2.

The rates of the last two reactions, i.e. steam reforming and water-gas shift, were taken from the literature [178]. If the model description in Table 4-4 denoted steam reforming /

water-gas shift as "opt", only the **form** of the rate expression was used and the **value** of the rate constant was calculated by nonlinear optimization. In the case where the model description was referred to as "lit", however, the **form** of the expression as well as the **value** of the rate constant were taken directly from the literature.

The rate expressions were combined with species conservation equations to relate the predicted species partial pressures to inlet partial pressure ratios ($R_i = P^\circ_i/P^\circ_{CH4}$) and conversions ($X_i$) of the relevant reactions. In the following set of expressions, the subscript 1 refers to total oxidation, 2 to oxidative reforming, 3 to steam reforming and 4 to the water-gas shift reaction. The species partial pressures at each integration step (n+1) were calculated from the partial pressure at the previous step (n) and the conversion of the reactions calculated from $r_i . dW/F^\circ_{CH4}$:

$$P_{CH_4}^{n+1} = P^o_{CH_4} (1 - X_1 - X_2 - X_3) \tag{42-7}$$

$$P_{O_2}^{n+1} = P^o_{CH_4} (R_{O_2} - 2 X_1 - 0.5 X_2) \tag{42-8}$$

$$P_{CO}^{n+1} = P^o_{CH_4} (R_{CO} + X_2 + X_3) - P_{CO}^n . X_4 \tag{42-9}$$

$$P_{H_2}^{n+1} = P^o_{CH_4} (R_{H_2} + 2 X_2 + 3 X_3) + P_{H_2}^n . X_4 \tag{42-10}$$

$$P_{CO_2}^{n+1} = P^o_{CH_4} . (R_{CO_2} + X_1) + P_{CO_2}^n . X_4 \tag{42-11}$$

$$P_{H_2O}^{n+1} = P^o_{CH_4} (R_{H_2O} + 2 X_1 - X_3) - P_{H_2O}^n . X_4 \tag{42-12}$$

4.3.3.2. Kinetic expressions for the four reactions

Mezaki and Watson proposed a number of kinetic models for the **total oxidation** of methane on a Pd/Al_2O_3 catalyst [176]. The model that gave the best representation of their measured data was based on the unlikely elementary reaction of a gaseous methane molecule impinging on three palladium sites covered in non-dissociatively adsorbed oxygen. In the case of a supported nickel catalyst as in the present case, oxygen is more likely to be dissociated upon adsorbing under reaction conditions. Therefore the rate expression proposed in the abovementioned work is not considered here.

Furthermore, Qin *et al.* [177] suggested that oxygen adatoms may desorb from a noble metal catalyst surface and exist in the gas phase without recombining. These free oxygen atoms were proposed to be highly active for the **total oxidation** of gaseous methane to carbon dioxide and water. It contrast to gaseous total oxidation, it was proposed by these authors that oxidative reforming (direct formation of CO and H_2), occurred catalytically between **adsorbed** oxygen atoms and CH_x fragments on the catalyst surface.

In the present work, the possibility of methane reacting with free oxygen atoms in a homogeneous reaction to yield total oxidation products was not considered explicitly. However, if a rate expression were to be developed for such a reaction, it would have to reflect the product of a rate constant with two terms, one accounting for the gaseous "partial pressure" of oxygen atoms and the other for the partial pressure of methane. Free oxygen atoms are produced by the flux of adsorbed oxygen atoms from the catalyst surface, the abundance of which are, in turn, a function to the square root of $(K_{O2}.P_{O2})$.

Therefore, an expression for total oxidation containing the product $k.P_{CH4}.P^{0.5}_{O2}$, includes the possibility of methane combustion occuring via gaseous O atoms as well as by a heterogeneous mechanism (methane reacting with dissociatively adsorbed O) as indeed included in the present work (equations (42-14) and (42-16)).

The rate expressions that were tested for reactions 1 and 2 were derived along the same lines as that in the discussion of the differential treament of kinetic data. A number of

numerators were proposed. The first was based on the adsorption of methane on a single vacant site, the second followed from the assumption that the reaction between gaseous or weakly adsorbed methane and dissociatively adsorbed oxygen was the rate-determining step and the third presumed that oxygen was non-dissociatively or weakly adsorbed. In an additional numerator, the term for oxygen adsorption was omitted.

$$NUM-1 = k \cdot P_{CH_4} \tag{42-13}$$

$$NUM-2 = k \cdot \sqrt{K_{O_2}} \cdot P_{CH_4} \cdot \sqrt{P_{O_2}} \tag{42-14}$$

$$NUM-3 = k \cdot P_{CH_4} \cdot P_{O_2} \tag{42-15}$$

$$NUM-4 = k \cdot P_{CH_4} \cdot \sqrt{P_{O_2}} \tag{42-16}$$

Two different denominators were used. The first was the same as that of the model previously proposed (equation (41-18)) and is denoted by DEN-1. In the second denominator, the terms for hydrogen and carbon dioxide were omitted because of the low adsorption constants previously shown in Table 4-2:

$$DEN-2 = 1 + \sqrt{K_{O_2} P_{O_2}} + K_{CO} P_{CO} + K_{H_2O} P_{H_2O} \tag{42-17}$$

The rate of methane consumption by total oxidation and oxidative reforming respectively, were constructed from these terms and the combinations that were evaluated are listed in Table 4-4.

The rate expression for the **steam reforming** reaction was taken from the literature [178]:

$$r_{CH_4} = k_{SR} \left(P_{CH_4} - \frac{P_{H_2} P_{CO}^3}{P_{H_2O} K_{Steam}} \right) \qquad \text{(42-18)}$$

where k was the forward rate constant and K_{Steam} refers to the equilibrium constant for the steam reforming reaction at reaction conditions. The rate of the **water-gas shift** (WGS) reaction was predicted by a similar expression (equation (42-19)). In all cases where WGS was allowed to take place, the value of the rate constant was calculated by the optimization procedure. The equilibrium constant of the water-gas shift reaction (K_{WGS}) was calculated by an expression from the literature [33].

$$r_i = k_{WGS} \left(P_{CO} - \frac{P_{H_2} P_{CO_2}}{P_{H_2O} K_{WGS}} \right) \qquad \text{(42-19)}$$

The models are shown in Table 4-4 and the comparative results tabulated in Table 4-5.

Table 4-4 Reaction models investigated by the integral method of analysis with kinetic constants either taken from the literature (lit) or optimized (opt)

Model number	Combustion	Oxidative reforming	Steam reforming	Water-gas shift	Number of constants
1	NUM-3	NUM-1	lit	-	2
2	NUM-4	NUM-1	opt	-	3
3	NUM-4	NUM-1	lit	opt	3
4	NUM-1	NUM-1	opt	opt	4
5	NUM-1/DEN-2	NUM-1/DEN-2	lit	opt	6
6	NUM-1/DEN-2	NUM-1/DEN-2	opt	opt	7
7	NUM-2/DEN-1	NUM-1/DEN-1	opt	-	9
8	NUM-2/DEN-1	NUM-2/DEN-1	lit	-	8

Table 4-5 Results of the integral analysis of kinetic data using a variety of rate expressions

Model number	Constraints[A]	RMSE[B] x 100	Number of constants
1	✓	1.41	2
2	✓	1.43	3
3	✓	1.43	3
4	✓	1.57	4
5	✓	1.16	6
6	✓	1.11	7
7	✓	1.27	9
8	✓	1.23	8

A   Physical constraints satisfied, ie. negative adsorption enthalpies and positive pre-exponentials.
B   RMSE calculated according to equation (42-2).

All the models tested satisfied the physical constraints, i.e. the adsorption enthalpies were negative and the pre-exponential factors positive. Model 6 was fitted with the lowest RMSE value and was therefore regarded as the best fit to the experimental data. The values of the kinetic constants of model 6 are listed in Table 4-6 and the results of the best model fit are furthermore shown graphically in Figure 4-12 to Figure 4-17.

Table 4-6 Kinetic constants from the unconstrained optimization fit of model 6 to integral data

Parameter	Units of A_i	Pre-exponential	E_a or B_i kJ mol^{-1}	K^{877K}_i
k_{Comb}	[mol kPa^{-1} g^{-1} s^{-1}]	3.29E-3	39 597	1.44E-5
k_{Oxref}	[mol kPa^{-1} g^{-1} s^{-1}]	9.78E-2	57 545	3.66E-5
k_{SR}	[mol atm^{-1} g^{-1} s^{-1}]	7.19E-2	44 885	1.53E-4
k_{WGS}	[mol atm^{-1} g^{-1} s^{-1}]	9.55E-2	35 967	6.89E-4
K_{O2}	[atm^{-1}]	1.99E-8	-66 321	1.77E-4
K_{CO}	[atm^{-1}]	9.55E-8	-106 594	0.21
K_{H2O}	[atm^{-1}]	1.42E-7	-110 247	0.52

Model 6 successfully predicted the experimental methane partial pressure. Oxygen partial

pressure, however, was overestimated by the model.
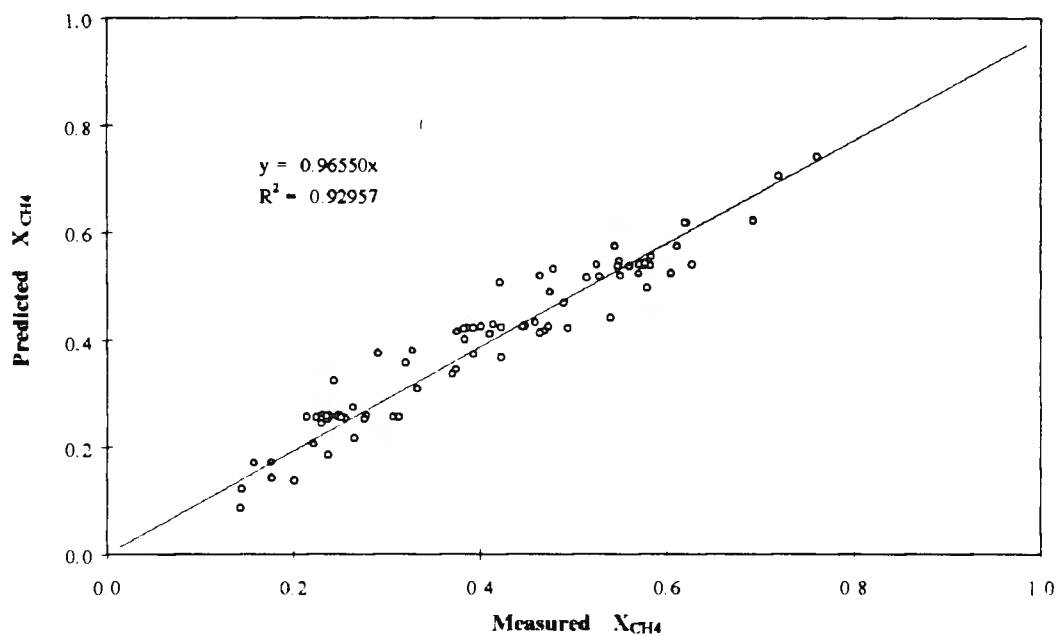
Figure 4-12 Parity plot of the results of model 6
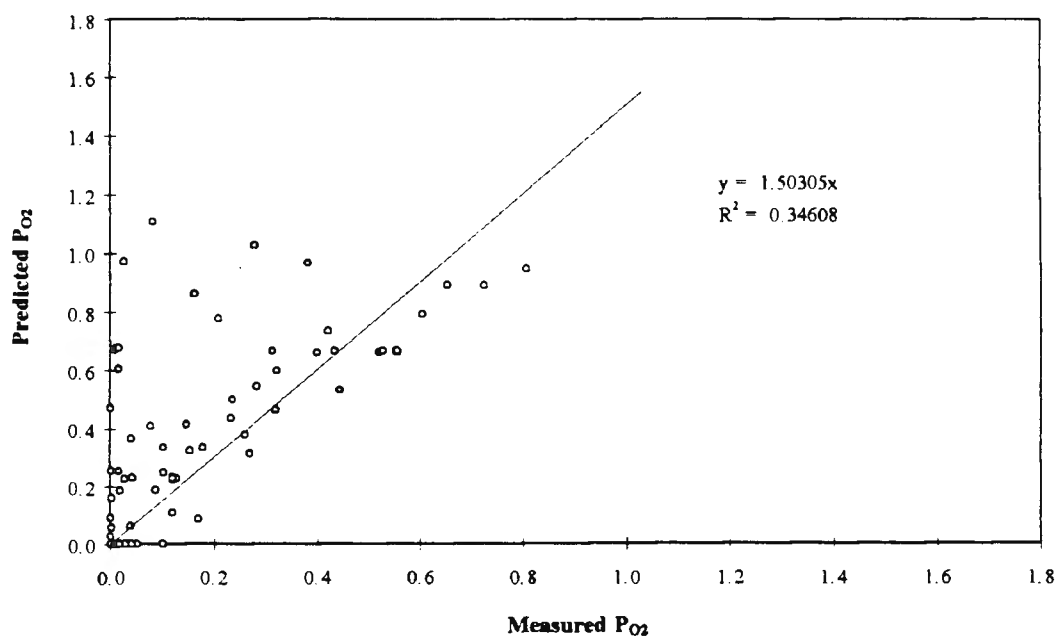
Figure 4-13 P_{O_2} parity plot predicted by model 6
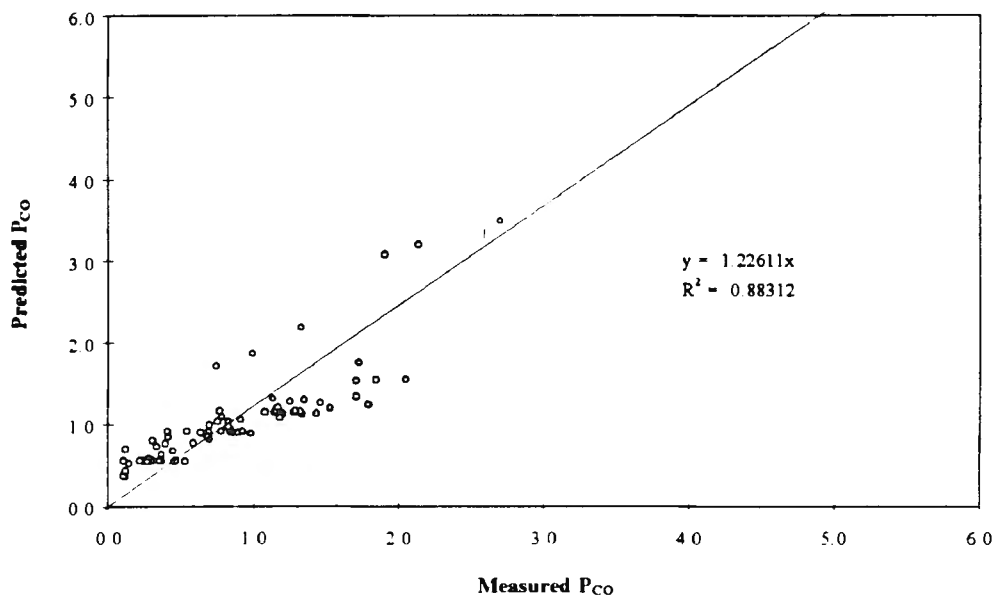
Figure 4-14 P_{CO} parity plot predicted by model 6
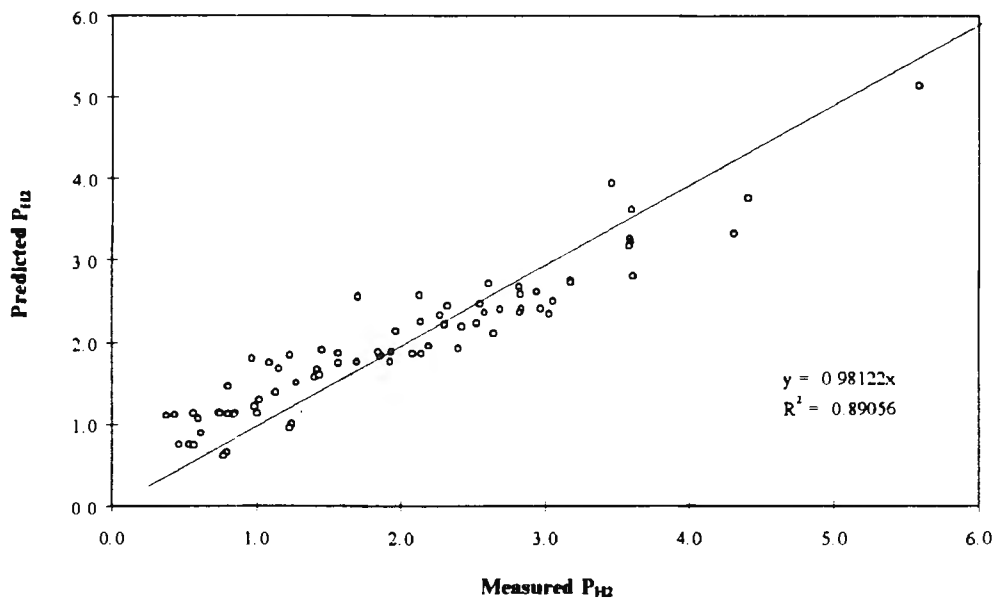
Figure 4-15 P_{H2} parity plot predicted by model 6

Both the values of the water and carbon dioxide partial pressures were underestimated by the model. Taken together with the earlier observation that the predicted oxygen partial pressure was too high, this leads to the conclusion that the optimized kinetic constant of the total oxidation reaction (reaction 1) was possibly too low.
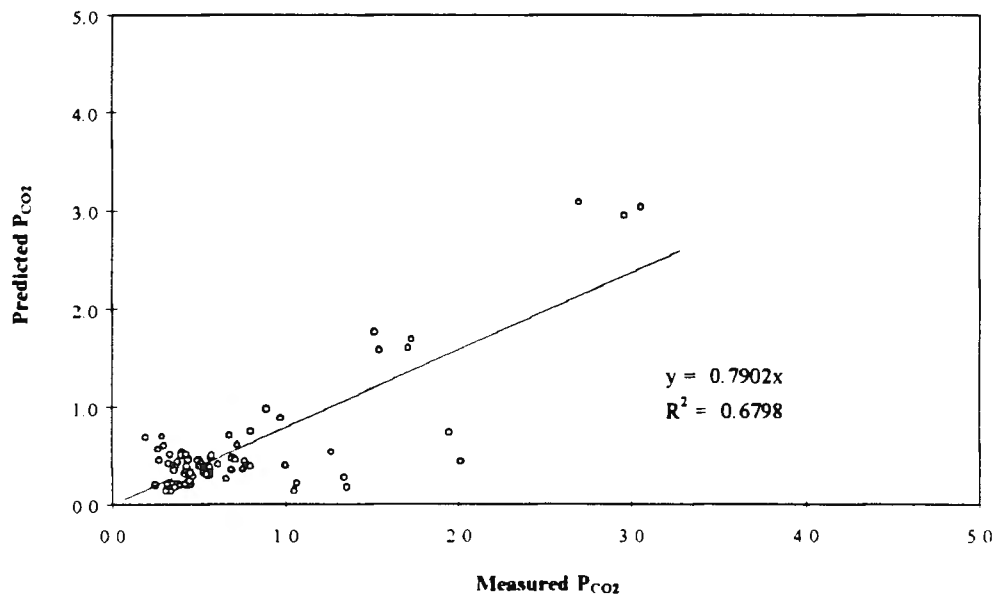
Figure 4-16 P_{CO2} parity plot predicted by model 6
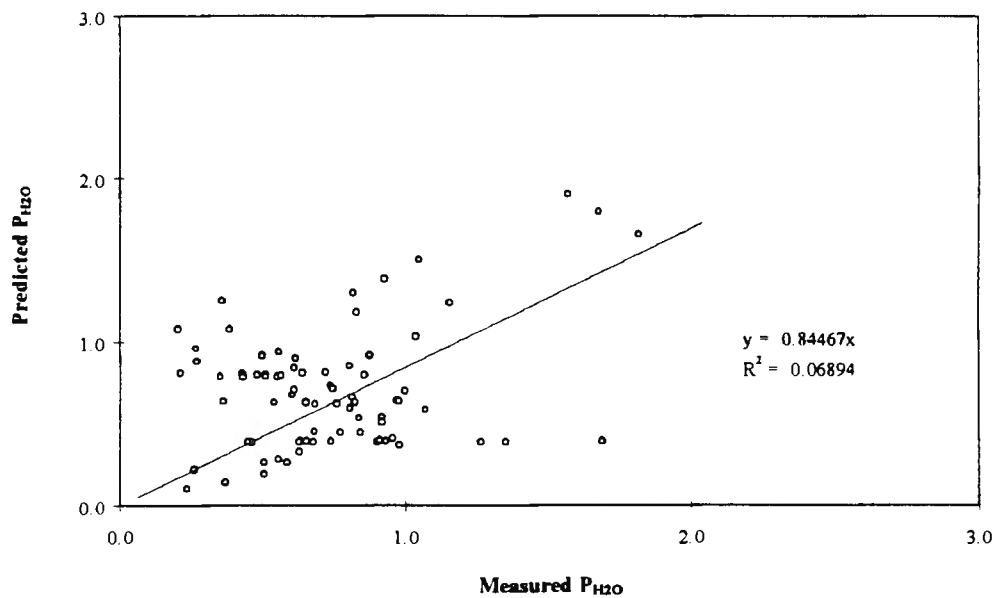
Figure 4-17 P_{H2O} parity plot predicted by model 6

From the optimized values of the kinetic constants shown in Table 4-6 it is clear that the adsorption constant for water was the highest. This finding corresponds well with the observation that water co-feeding had a significant effect on the conversion of methane and oxygen (see Figure 31-26).

The integral model thus did not fail in its entirety and provided some quantitative confirmation of general trends that were identified by means of a differential treatment of the data and from a qualitative analysis of the integral results. The weak point in the integral model is its failure to accurately account for the experimentally-measured product distribution. While this fact detracts from its utility in scale-up calculations, it does provide a starting point for a more in-depth kinetic probe into the oxidative reforming of methane.

Conclusions

For the moment it is impossible to push our investigation further (Jean-Paul Sartre [179])

An extensive survey of the available literature highlighted some of the similarities between oxidative reforming and other fields of heterogeneous catalysis. The thermodynamics of the reaction was treated, as well as most of the available reported experimental results. In addition to this, the effect of transport phenomena and the choice of catalytic material were discussed. The under-researched areas of this reaction were shown to be mostly concerned with heat- and mass transfer and reaction kinetics of the reaction. Some of the aspects of one of the approaches to oxidative reforming, namely the use of monolith reactors, was shown to have more than a passing similarity with porous radiant burners and catalytically-stabilized burners which are more well known in the combustion sciences. In spite of claims to the contrary, the importance of gas-phase reactions in these devices have in the opinion of this author been underestimated. It is proposed that further advances towards the commercialization of methane oxidative reforming are highly likely if this approach to the reaction is further pursued.

The oxidative reforming of methane to predominantly carbon monoxide and hydrogen was studied over a commercial steam reforming catalyst (Südchemie G-90B). The said reaction was performed in an integral fixed-bed reactor at temperatures between 575°C and 650°C at a total pressure of 200 kPa(a). The primary objective of the study was the design and construction of equipment to facilitate firstly, the measurement of axial bed temperature profiles, and secondly, the investigation of transport effects during the oxidative reforming of methane.

The absence of external transport resistance was confirmed by measuring the methane conversion at constant temperature (604°C), reactant partial pressures (P°_{CH4} = 2.69 kPa and P°_{O2} = 1.34 kPa), total pressure (P_T = 201.3 kPa), particle size range (425μm < d_p < 710μm) and contact time (W/F°_{CH4} = 1.9 E4 g s mol⁻¹), but varying the

linear velocity between 3 m s⁻¹ and 18 m s⁻¹. The absence of internal gradients were confirmed by measuring the methane conversion over different particle size ranges (125μm < d_p < 710μm) with all other parameters being constant (T = 604°C, u_o = 14.1 cm s⁻¹, $P°_{CH4}$ = 2.69 kPa, $P°_{O2}$ = 1.33 kPa, P_T = 201.3 kPa and W = 200 mg).

The absence of internal or external temperature- and concentration gradients were tested by subjecting the experimental results to theoretical criteria that had previously been derived to check for transport limitations. The value of the external effectiveness factor was calculated to be between 0.85 and 1.0. The Dahmköhler number was less than unity for all the data, confirming the absence of internal concentration gradients. The absence of internal temperature gradients was checked by the Kubota criterion, which all the experimental data adhered to.

A kinetic study was performed under conditions of negligible transport limitations. Methane partial pressures at the bed inlet was varied between 2.75 kPa and 4.82 kPa and that of oxygen between 0.99 kPa and 1.63 kPa. All the reaction products were co-fed at constant (inlet) methane and oxygen partial pressures. The ranges of product partial pressures at the reactor inlet was: $P°_{CO}$ = 1.34 to 6.29 kPa, $P°_{H2}$ = 1.45 to 5.61 kPa, $P°_{CO2}$ = 0.27 to 2.77 kPa and $P°_{H2O}$ = 0.49 to 1.20 kPa.

The integral data thus obtained was first analyzed by the method of initial rates (at zero conversion) by taking the slopes of the X_{CH4} vs. $W/F°_{CH4}$ data at the origin. This indicated that the rate of methane consumption was first-order with respect to methane partial pressure and independent of oxygen partial pressure. The reaction products were found to inhibit the rate of methane consumption. The activation energy of methane consumption agreed closely with the activation energy of methane chemisorption on Ni(111) surfaces. Various curves were fitted to the data to enable the calculation of the slopes of the X_{CH4} vs. $W/F°_{CH4}$ data at different values of $W/F°_{CH4}$. In spite of yielding the lowest deviation in general between measured- and predicted X_{CH4}, the second-order polynomial curves failed to predict the slopes of the curves at high methane conversion because of excessive curvature. A set of ten hand-drawn curves to a model data set also showed a good correlation between predicted X_{CH4} and measured X_{CH4}. Two exponential curves were also fitted to the data, with one of the curves

taking account of the methane conversion at thermodynamic equilibrium $(W/F^{\circ}_{CH4} \rightarrow \infty)$. The relative success of these curves were assessed in terms of a selected model data set.

Having obtained differential reaction rates from the integral data, two Langmuir-Hinshelwood models were developed and fitted to the data. The model which was derived from the assumption that methane adsorption on a single active site was the rate-determining step, gave the best fit to the experimental data. This is in line with the previous finding that the activation energy of the reaction was very similar to the activation energy of methane chemisorption on Ni(111) surfaces. Adsorption constants correlated in broad terms with the reaction orders of the species which were previously determined by the method of initial rates. The differential kinetic data that were obtained from the fitting of exponential curves to the integral data gave the best correlation between predicted and measured reaction rates.

In the next step of the kinetic analysis, the integral data was correlated by means of an integral reaction model. A combination of the total oxidation-, oxidative reforming- and steam reforming of methane, as well as the water-gas shift reaction, resulted in the best fit between measured- and predicted data. The predicted methane, carbon monoxide- and hydrogen partial pressures correlated well with experimental data, but that of oxygen, carbon dioxide and water were less accurately predicted by the model. The lack of any comparable study in the literature made it impossible to compare adsorption- and rate constants to other work.

X-ray diffraction results showed that the active catalyst bed consisted of a top layer of nickel oxide on alumina and zero-valent nickel on alumina deeper into the bed. Evidence from thermogravimetric experiments revealed that carbon formation was inhibited by hydrogen co-feeding and high oxygen inlet partial pressures, but that it was enhanced by carbon monoxide co-feeding.

In summary thus, the aims of the project as far as the experimental study of transport phenomena is concerned, were satisfied. The kinetic study shed some light onto the reaction pathway and the modelling of the experimental kinetic results paved the way for further work into this industrially-promising reaction.

APPENDIX A

Properties of the compounds

A. Properties of the compounds

Table A-1   Properties of methane

Property	Value
Triple point	-182.5°C
Critical temperature	-82.5°C
Normal boiling point	-161.5°C
Melting point	-182.6°C
Critical pressure	45.8 atm
Standard heat of formation	-17.889 kcal/mol
Free energy of formation	-12.140 kcal/mol
Net heat of combustion	191.76 kcal/mol
Gross heat of combustion	212.80 kcal/mol
Upper flammability limit	15.4 vol%
Lower flammability limit	5.0 vol%

Table A-2 Gibbs free energy in units of kcal/mol for the reaction components

T (K)	CH$_4$	C$_2$H$_4$	C$_2$H$_4$	CO	CO$_2$	H$_2$O
300	-12.11	-7.79	16.31	-32.85	-94.26	-54.57
400	-10.07	-3.45	17.69	-35.01	-94.33	-53.45
500	-7.85	1.16	19.25	-37.19	-94.39	-52.29
600	-5.51	5.96	20.92	-39.36	-94.45	-51.09
700	-3.06	10.90	22.68	-41.53	-94.50	-49.86
800	-0.56	15.91	24.49	-43.68	-94.54	-48.59
900	1.99	21.00	26.35	-45.82	-94.58	-47.29
1000	4.58	26.13	28.25	-47.95	-94.61	-45.98
1200*	9.89	36	32.33		-94.68	-43.28
1500*	17.86	51	38.27		-94.73	-39.14

* Data from CRC Handbook and Gas Encyclopaedia and Stull
• Water data from Kyle

Appendix B

Calibration, gas analysis and sample calculation

B. Calibration and gas analysis

B.1. Mass flow controller calibration

Gas flow rate was measured with a bubble meter and stopwatch. The flow rate at ambient conditions could be determined by dividing the volume between two points on the cylinder (burette) by the time that it took a soap film to move through that volume. The measured flow rate was then converted to a standard flow rate at STP (0°C and 101.325 kPa) for a number of mass flow controller setpoints and a line was fitted to the data by least-squares regression. This allowed one to calculate the flow at STP from a given mass flow controller setpoint at a later stage. In all cases the R^2 value of the lines that was fit to the data was better than 0.998. Constants to fit the expressions for the lines that were derived from calibration data have been summarized in Table 2-1.

Water was produced in-situ upstream of the reactor by passing the required amounts of hydrogen and oxygen over 5.2278 grams of an industrial Pt-Ni/Al_2O_3 oxidation catalyst (Südchemie catalyst EX-1621). The catalyst was packed in a ¼" tube which was well insulated and maintained at 275°C by a mantle heater. The catalyst was pre-reduced at 275°C for one hour before each experiment. The ability of the oxidation catalyst to convert all hydrogen in a hydrogen-poor gas stream for the duration of an experiment was confirmed prior to the water co-feeding kinetic experiments.

B.2. Recycle vessel calibration

The recycle vessel was calibrated in order to determine the recycle ratio. A flame ionization detector was used in conjunction with a data logging device to measure the response of the jetloop mixer when a propane pulse was introduced to the vessel. The recycle ratio was calculated from the difference between the first and second pass peaks:

$$\frac{t}{\tau} = \frac{1}{1 + R} \tag{B-1}$$

where τ was the residence time (volume/volumetric flow rate), t the time difference between pass peaks and R the recycle ratio.
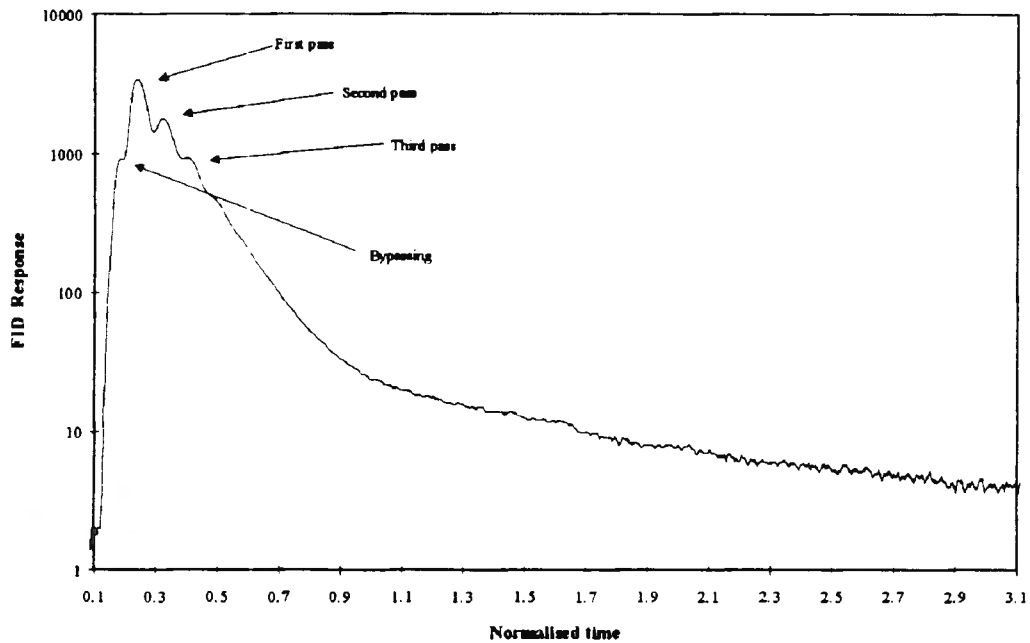
Figure B-1 Pulse response measurement of the C_3H_8 concentration in the outlet of the jetloop mixer. (V°_T = 230 cm³/min, T = 20°C, τ = 7 cm³)

B.3. Thermocouple calibration

A K-type thermocouple (chromel-alumel) was used to measure the axial bed temperature profile. The temperature indicator was calibrated with an electronic calibration and simulation device (Time electronics - Thermocouple simulator 1088). The instrument has an accuracy of 0.25°C in the range -200 to 600°C and 0.5°C between 600 and 1250°C. The result of the calibration procedure is depicted in Figure B-2.

B.4. Gas Analysis

Prior to response factor calibration, the optimum carrier gas flow rate was determined by
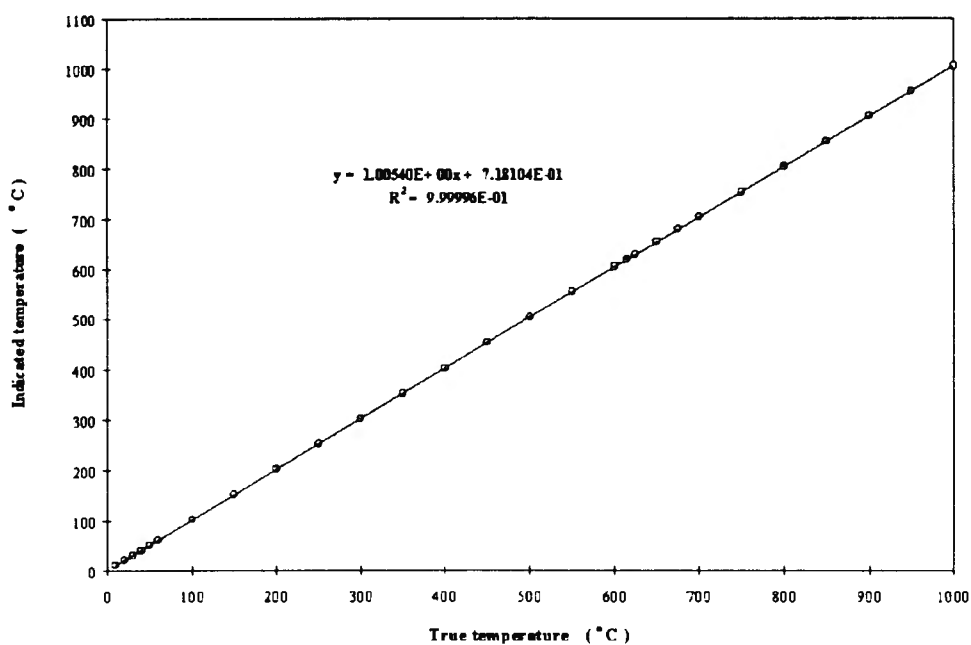
Figure B-2 Temperature indicator calibration (Cold junction temperature = 23.1°C and ambient temperature = 20.2°C)

injecting a known amount of oxygen into the column with varying carrier gas flow rates. The optimum flow rate was determined by plotting the height of an equivalent theoretical plate against the carrier gas flow rate. The height of a theoretical plate (HETP) was calculated from the column length and the number of theoretical plates (N). The latter was in turn calculated with equation (B-2):

$$N = 16 \left(\frac{t_R}{w} \right)^2 \qquad\qquad \text{(B-2)}$$

with t_R the residence time of the peak and w the width of the peak at the base 180. From the van Deemter curve that was fitted to the data:

$$HETP = A + \frac{B}{u} + C \cdot u \qquad\qquad \text{(B-3)}$$

the optimum carrier gas flow rate (u) was calculated by taking the first derivative of equation (B-3). The optimum flow rate was 42.1 cm³/min 181.

Fit of experimental data to the van Deemter equation
$y = 0.425 + 2.281E\text{-}3 . x + 4.0388 / x$
$R^2 = 0.99911$

Carrier gas flow rate (cm^3 / min)
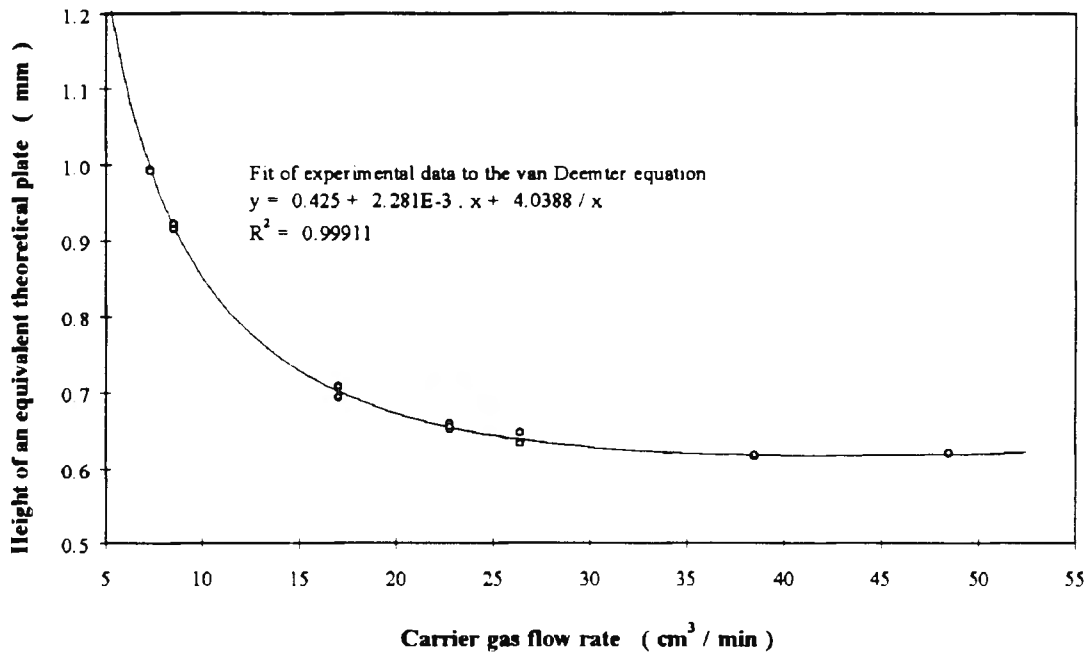
Figure B-3 Optimizing the efficiency of the chromatographic column

The temperature program that was used for chromatographic seperation of the permanent gases is shown in Figure B-4.

225 °C

32 °C / min

5 minutes
45 °C
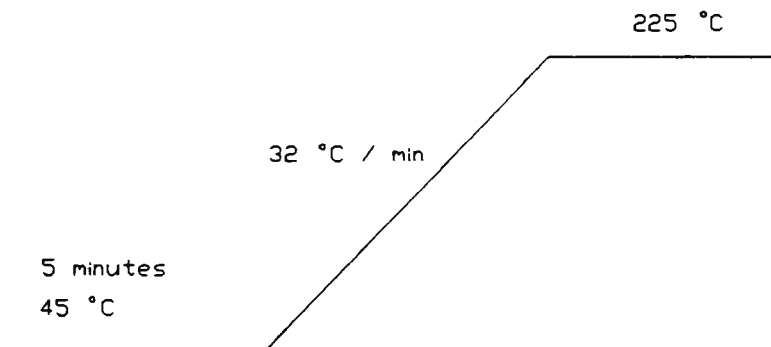
Figure B-4 GC temperature program

B.5. Response factor determination

Nitrogen was used as an internal standard to quantify the amount of each species present in a given gas sample. The response factor of a species, relative to nitrogen, is defined as:

$$RRF_{species} = \frac{\left(\dfrac{Area_{species}}{Area_{N_2}}\right)}{\left(\dfrac{Moles_{species}}{Moles_{N_2}}\right)} \qquad \text{(B-4)}$$

The relative response factor for a given species was determined by passing a mixture with known composition through the GC sample loop. The area response of the compound relative to the area response of N_2 was determined by integrating the area under the species peak and the nitrogen peak repsectively. This procedure was repeated several times for a variety of feed gas compositions. The relationship of the area ratios and molar ratios was then plotted and a straight line passing through the origin was fitted to the data. As indicated on the graphs below, the relative response factors were valid over quite a wide range of concentrations.

The calibration data for all the compounds of interest is graphically depicted in Figure B-5 to Figure B-9 and the response factors have been summarized in Table 2-3.
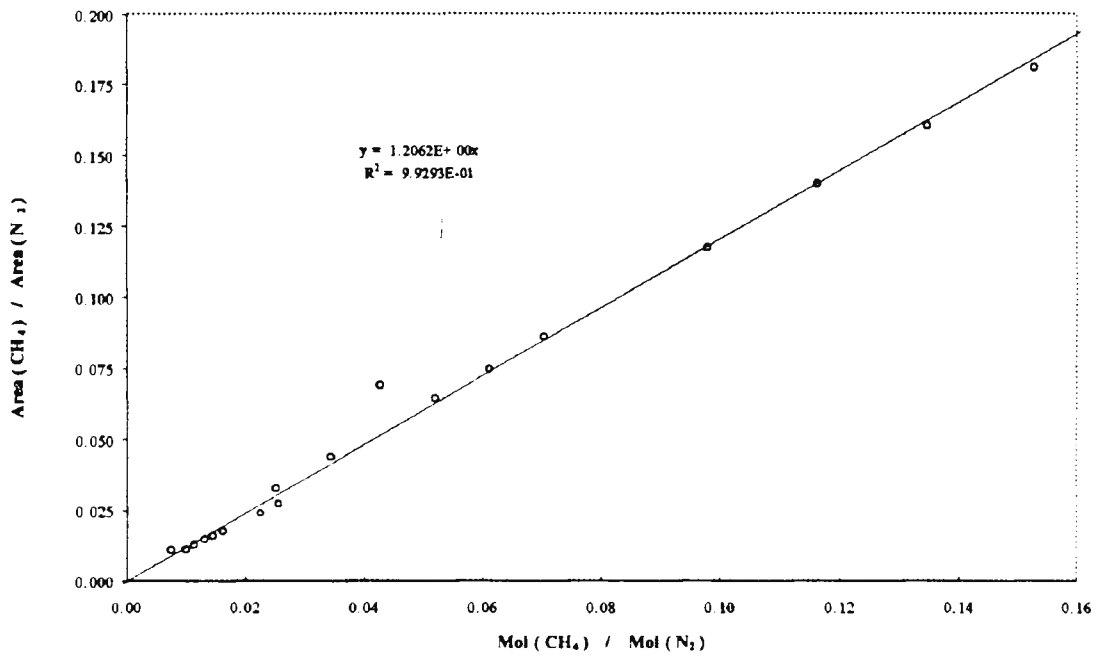
Figure B-5 Methane relative response factor
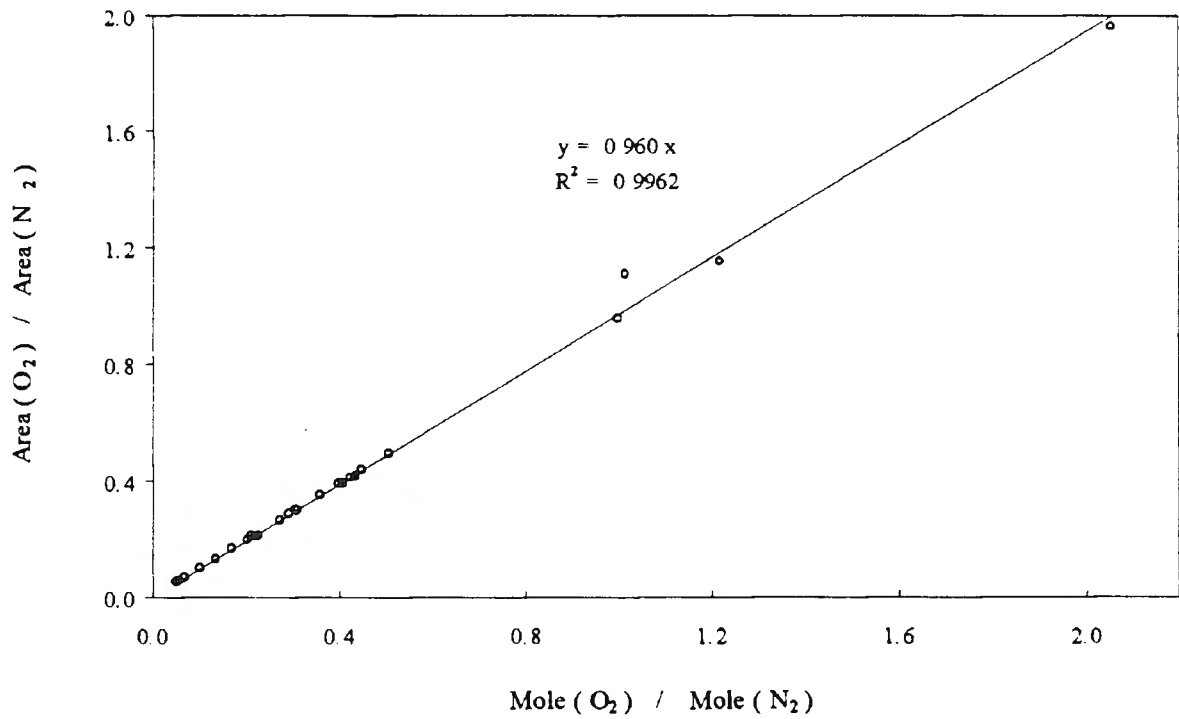
Figure B-6 Oxygen relative response factor
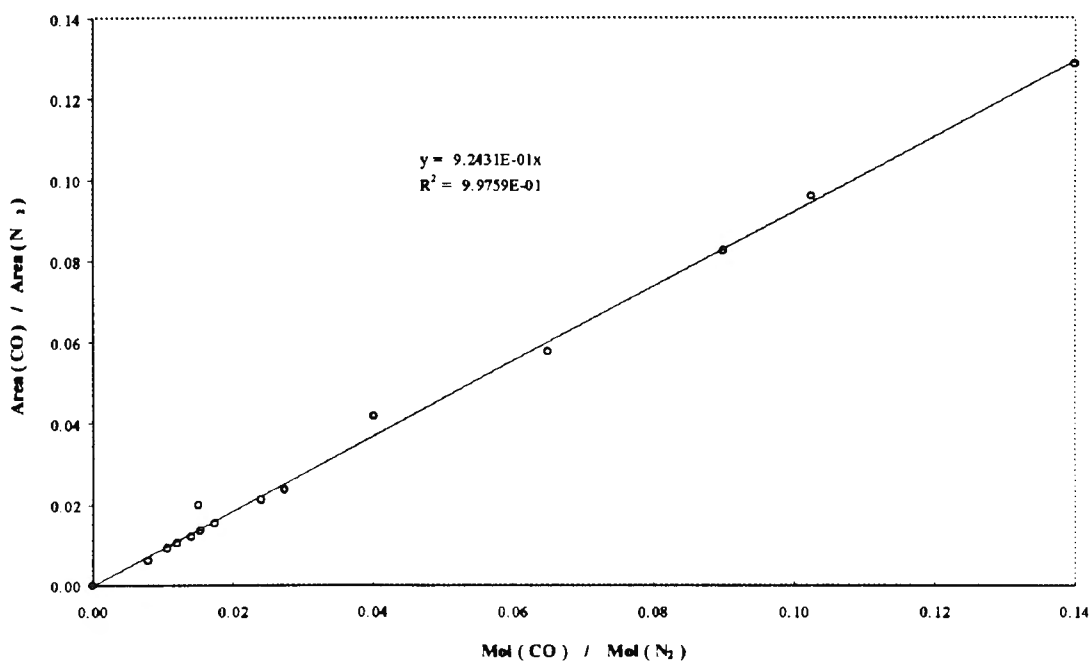
Figure B-7 Carbon monoxide relative response factor
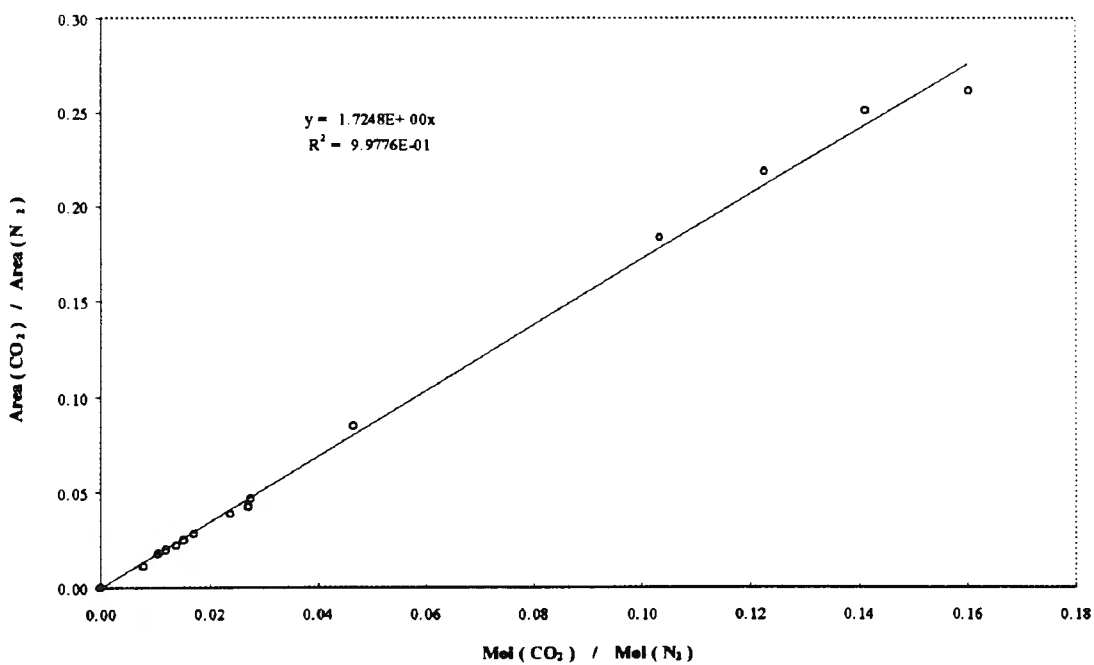
Figure B-8 Carbon dioxide relative response factor
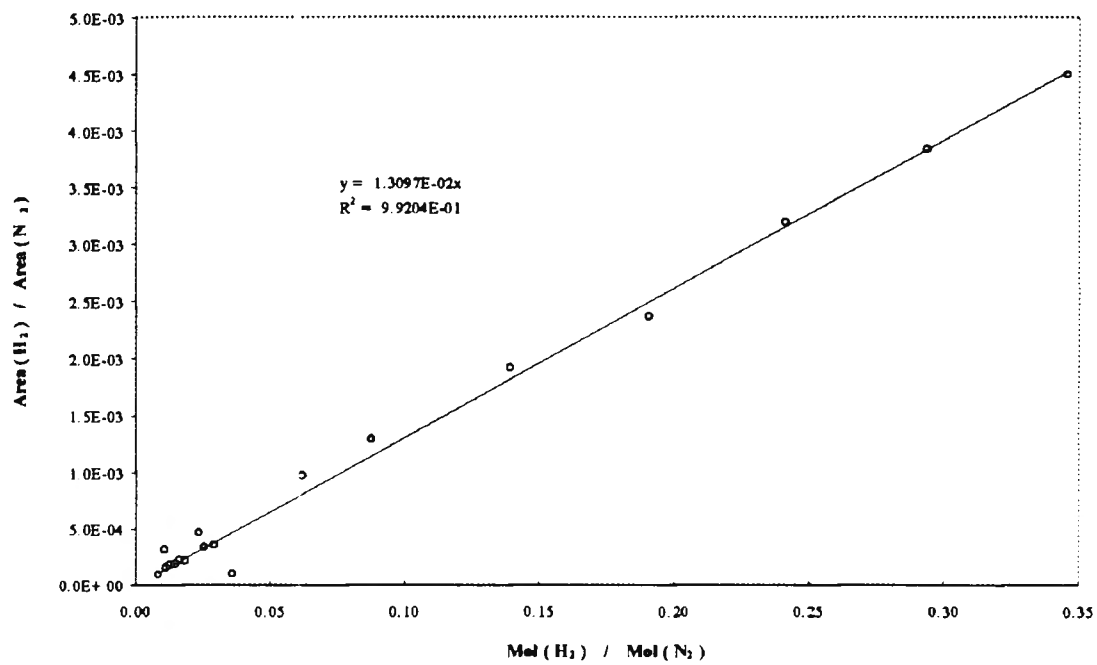
Figure B-9 Hydrogen relative response factor

B.6. Gases used

The purity and source of the gases that were used for catalytic testing are contained in Table B-1. All gases were used as-received and no further purification or drying was performed.

Table B-1 Purity and source of gases used for catalytic testing

Gas	Purity (mol %)	Source
CH_4	99.9	Air Products (Messer Griesheim)
O_2	99.5	Air Products
He	99.995	Air Products
N_2	99.999	Fedgas
CO	99.3	Air Products
CO_2	99.9	Air Products
H_2	99.995	Air Products

B.7. Sample calculation

From the molar flowrates calculated above, the mol fractions and therefore the partial pressure of each species was determined (the molar flow rate of water calculated by the first method was used). The reactor was at 100 kPa (gauge).

Table B-2 Partial pressures at the inlet and outlet of the reactor

Species	$F^{IN}_{Species}$ mmol/min	$F^{OUT}_{Species}$ mmol/min	$P^{IN}_{Species}$ kPa	$P^{OUT}_{Species}$ kPa
CH_4	0.68255	3.02706	2.9618	1.9161
O_2	0.30928	0.44410	1.3421	0.2293
CO	0	0.12645	0	0.5456
H_2	0	0.35836	0	1.5462
CO_2	0	0.11083	0	0.4782
H_2O	0.66648	0.83066	2.8920	3.5840
N_2	3.02706	3.02706	13.1352	13.0606
He	41.71075	41.71075	180.9939	179.9653
Total	46.39612	46.66130	201.3250	201.3250

The methane conversion and product selectivities were calculated from the above data:

-

$$X_{CH_4} = 1 - \frac{F^{OUT}_{CH_4}}{F^{IN}_{CH_4}} \qquad \text{(B-5)}$$

$$S_{CO} = \frac{F^{OUT}_{CO}}{F^{OUT}_{CO} + F^{OUT}_{CO_2}} * 100 \qquad \text{(B-6)}$$

$$S_{H_2} = \frac{F^{OUT}_{H_2}}{F^{OUT}_{H_2} + F^{OUT}_{H_2O}} * 100 \qquad \text{(B-7)}$$

The conversion and partial pressures at zero time on-stream were not directly determined, but calculated by linear regression. The results of experiment PPW_12 are listed in Table B-3 and graphically depicted in Figure B-10.

Table B-3 Results of gas analysis for the first four samples of Run PPW_12

Time	X_{CH4}	P_{CH4}	P_{O2}	P_{CO}	P_{H2}	P_{CO2}	P_{H2O}	C_{Bal}
0	0.379	1.8317	0.1729	0.5883	1.7055	0.5129	3.3773	-
4	0.3788	1.8321	0.1751	0.5846	1.7092	0.5219	3.3584	99.637
43	0.3494	1.9201	0.2298	0.5467	1.5494	0.4792	3.3755	99.828
76	0.3374	1.9553	0.2606	0.5155	1.5059	0.5040	3.2956	100.805
98	0.3313	1.9737	0.2845	0.4905	1.4248	0.5033	3.2745	100.548
154	0.3213	2.0039	0.2984	0.4657	1.4258	0.4589	3.3629	99.180

The values at zero time on-stream were calculated by means of linear regression

Linear regression was performed on the first three values of this data set, using time as the independent variable, to find the intercept of each species partial pressure with the y axis (time = 0 min).
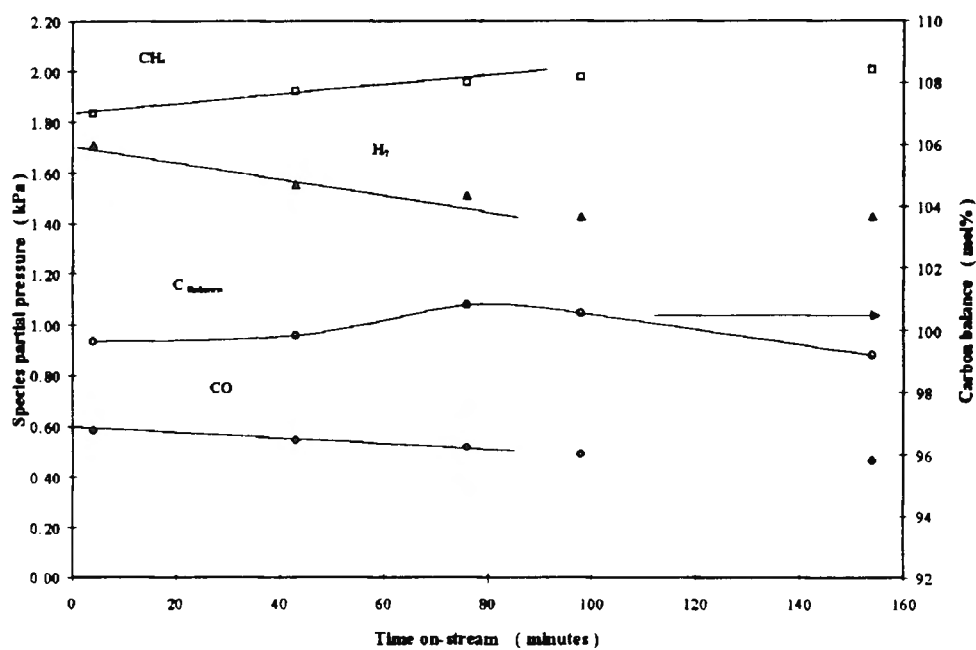
Figure B-10 Time on-stream behaviour of experiment PPW_12

This approach was considered justified in light of the steady deactivation of the catalyst, as evident from the close fit between the experimental data and the lines drawn on Figure B-10.

Appendix C

Results

C. Results of kinetic experiments

C.1. Temperature

The effect of temperature on the product composition is given in Table C-1 while the effect of temperature on the differential rates is shown in Table C-2. In order to avoid repeating data, the data at 604°C are contained in Table C-5. The experiment labels have been explained in Table 2-5.

Table C-1 The effect of temperature on the product composition

Run ID	W	Temperature	Partial pressure at the reactor outlet (kPa)					
	mg	°C	CH_4	O_2	CO	H_2	CO_2	H_2O
T575_6a	25.4	579	2.305	0.605	0.121	0.618	0.361	0.627
T575_1	50.2	579	1.852	0.148	0.334	1.274	0.564	0.917
T575_0	74.9	579	1.363	0.002	0.928	2.399	0.565	0.602
T625_6	25.0	629	1.975	0.283	0.446	1.131	0.446	0.772
T625_1	49.9	629	1.245	0.003	1.183	2.530	0.431	0.607
T625_0	74.8	629	0.911	0	1.711	3.612	0.334	0.270
T650_6	25.0	654	1.710	0.078	0.699	1.420	0.449	0.918
T650_1	49.9	654	1.152	0.003	1.463	2.945	0.377	0.432
T650_0	75.1	654	0.831	0	1.847	3.593	0.267	0.266

All the above experiments were conducted at P_T = 200 kPa(a), $P^°_{CH4}$ = 2.964 kPa and $P^°_{O2}$ = 1.343 kPa

Table C-2 The effect of Temperature on the rate of methane and oxygen consumption and the rates of product formation

Run ID	r_{CH_4} x 1E5 [mol g^{-1} s^{-1}]			Reaction Rate[a] x 1E5 [mol g^{-1} s^{-1}]				
	Method 3	Method 7	Method 8	O_2	CO	H_2	CO_2	H_2O
Origin_1[b]	10.16	12.42	11.30	19.31	1.521	9.685	5.786	10.37
T575_6	8.795	8.826	8.811	7.557	2.265	9.509	4.300	6.966
T575_1	7.422	6.252	6.857	2.934	5.718	13.27	1.597	-0.107
T575_0	6.077	4.460	5.363	1.161	10.72	19.08	-0.385	-6.199
Origin_2[b]	17.98	20.75	18.72	33.59	5.953	16.43	7.636	14.54
T625_6	13.01	12.27	12.40	6.568	8.530	19.11	3.270	5.079
T625_1	8.068	7.269	8.223	1.293	10.12	19.10	-1.223	-5.991
T625_0	3.123	4.307	5.455	0.255	7.700	16.12	-1.517	-4.959
Origin_3[b]	21.79	24.03	21.51	58.72	9.641	21.07	7.874	16.87
T650_6	14.45	13.24	13.40	3.387	7.732	22.80	1.744	2.258
T650_1	7.133	7.310	8.359	0.198	8.832	16.96	-1.766	-5.605
T650_0	-2.689	4.008	5.186	0.011	5.112	8.012	-1.597	-1.227

a   Rate of oxygen consumption calculated by method 8
Rate of product formation calculated from tangents to hand-drawn curves through W/F°$_{CH_4}$ vs X$_{CH_4}$ data.
b   Rate at W/F°$_{CH_4}$ = 0
All the above experiments were conducted at P$_T$ = 200 kPa(a)

C.2. Reactant partial pressure

C.2.1. Methane partial pressure

The present section is concerned with the effect of methane partial pressure on the product composition (see Table C-3) and reaction rates (given in Table C-4) at constant oxygen partial pressure and bed temperature. The experiment labels have been explained in Table 2-5.

Table C-3 The effect of $P°_{CH4}$ on the product composition

Run ID	W	$P°_{CH4}$	Partial pressure at the reactor outlet (kPa)					
	mg	kPa	CH_4	O_2	CO	H_2	CO_2	H_2O
ppc_65	25.3	2.752	2.067	0.421	0.145	0.596	0.392	0.979
ppc_15	49.9	2.752	1.646	0.102	0.415	1.086	0.530	1.070
ppo_0x	75.0	2.752	1.243	0.038	0.914	2.305	0.513	0.737
FW03	250.1	2.752	0.548	0.053	1.864	4.544	0.305	0.224
ppc_62	25.3	3.442	2.562	0.323	0.367	1.017	0.449	0.841
ppc_12A	49.9	3.442	2.149	0.120	0.755	1.967	0.504	0.746
ppc_02a	74.9	3.442	1.841	0.040	1.255	2.824	0.401	0.614
ppc_63	25.4	4.132	3.097	0.233	0.584	1.402	0.465	0.838
ppc_13	50.2	4.132	2.544	0.051	1.159	2.553	0.440	0.609
ppc_03	75.5	4.132	2.005	0.029	1.710	3.584	0.300	0.383
ppc_64	25.0	4.816	3.706	0.179	0.684	1.568	0.451	0.805
ppc_14	50.0	4.816	3.239	0.101	1.135	2.612	0.429	0.556
ppc_04b	75.2	4.816	2.783	0.041	1.731	3.602	0.290	0.358
ppc_34	150.0	4.816	1.871	0.045	2.220	4.241	0.184	0.073

All the above experiments were conducted at 604°C, P_T = 200 kPa(a) and $P°_{O2}$ = 1.375 kPa

Table C-4 The effect of $P°_{CH4}$ on the rate of methane and oxygen consumption and the rates of product formation

Run ID	r_{CH4} x 1E5 [mol g^{-1} s^{-1}]			Reaction Rate[a] x 1E5 [mol g^{-1} s^{-1}]				
	Method 3	Method 7	Method 8	O_2	CO	H_2	CO_2	H_2O
Origin_1[b]	10.94	11.70	11.15	25.27	1.512	9.308	6.366	18.47
ppc_65	8.708	8.541	8.527	7.489	2.962	6.731	4.152	6.240
ppc_15	6.536	6.289	6.570	2.296	5.561	12.30	0.930	-3.235
ppc_0x	4.320	4.602	5.035	0.687	8.158	20.40	-0.502	-5.583
Origin_2[b]	14.76	13.62	13.27	28.89	5.191	15.55	7.370	14.11
ppc_62	10.25	9.675	10.28	7.193	5.766	15.07	3.841	4.551
ppc_12A	5.860	6.935	8.023	1.861	6.920	13.93	-0.629	-2.419
ppc_02A	1.400	4.945	6.235	0.472	8.027	12.63	-1.708	-1.688
Origin_3[b]	16.52	19.65	16.05	36.31	8.835	22.19	7.991	16.06
ppc_63	12.58	12.09	12.40	6.282	8.835	19.42	3.533	3.208
ppc_13	8.722	7.519	9.637	1.133	8.478	16.45	-1.580	-4.106
ppc_03	4.792	4.633	7.452	0.197	8.121	15.21	-2.274	-3.374
Origin_4[b]	18.07	19.27	15.87	40.25	11.01	25.33	7.985	14.39
ppc_64	12.82	12.13	12.79	5.934	8.640	19.04	3.177	3.103
ppc_14	7.561	7.64	10.31	0.875	7.916	15.14	-1.499	-4.141
ppc_04b	2.264	4.794	8.299	0.127	9.709	14.77	-2.132	-2.909

a   Rate of oxygen consumption calculated by method 8
    Rate of product formation calculated from tangents to hand-drawn curves through $W/F°_{CH4}$ vs X_{CH4} data.
b   Rate at $W/F°_{CH4}$ = 0
All the above experiments were conducted at 604°C and P_T = 200 kPa(a)

C.2.2. Oxygen partial pressure

The effect of oxygen partial pressure on the product composition is given in Table C-5 while the differential reaction rates are shown in Table C-6. The experiment labels have been explained in Table 2-5.

Table C-5 The effect of $P^°_{O2}$ on the product composition

Run ID	W	$P^°_{CH4}$	$P^°_{O2}$	Partial pressure at the reactor outlet (kPa)					
	mg	kPa		CH_4	O_2	CO	H_2	CO_2	H_2O
ppo2_65	25.1	2.969	0.991	2.332	0.270	0.352	1.005	0.318	0.448
ppo2_15	50.0	2.969	0.991	1.814	0.005	0.893	2.153	0.355	0.355
ppo2_05	75.0	2.969	0.991	1.547	0	1.193	3.032	0.272	0.213
ppo2_64	24.9	2.977	1.202	2.292	0.446	0.270	0.847	0.387	0.463
ppo2_14	50.1	2.977	1.202	1.837	0.171	0.641	1.843	0.435	0.539
ppo2_04	75.2	2.977	1.202	1.413	0	1.081	2.691	0.445	0.430
pph_70	15.3	2.964	1.343	2.496	0.654	0.115	0.535	0.338	0.584
ppo2_71	15.4	2.964	1.343	2.440	0.725	0.108	0.463	0.311	0.504
ppcm_60	25.0	2.964	1.343	2.281	0.522	0.272	0.858	0.366	0.632
ppcd_60	25.3	2.964	1.343	2.140	0.401	0.239	0.735	0.454	0.739
ppo2_61	25.0	2.964	1.343	2.257	0.557	0.217	0.747	0.348	0.653
ppcd_10	49.9	2.964	1.343	1.573	0.102	0.653	1.855	0.564	0.683
ppo2_11	50.6	2.964	1.343	1.635	0.120	0.691	1.934	0.543	0.651
ppcd_00	75.0	2.964	1.343	1.106	0.005	1.279	2.972	0.508	0.352
ppo2_01	75.0	2.964	1.343	1.248	0	1.146	2.840	0.494	0.510
ppo2_21	100.0	2.964	1.343	1.123	0	1.352	3.179	0.404	0.497
pph_30	150.2	2.964	1.343	0.710	0	2.051	4.309	0.194	0.205
ppo2_62	25.0	2.970	1.626	2.335	0.807	0.109	0.564	0.423	0.677
ppo2_12	50.4	2.970	1.626	1.739	0.237	0.410	1.452	0.688	0.976
ppo2_02	75.6	2.970	1.626	1.337	0.087	0.771	2.325	0.712	0.856

All the above experiments were conducted at 604°C and $P^°_T$ = 200 kPa(a)

Table C-6 The effect of P°_{O2} on the rate of methane and oxygen consumption and the rates of product formation

Run ID	r_{CH4} x 1E5 [mol g^{-1} s^{-1}]			Reaction Rate[a] x 1E5 [mol g^{-1} s^{-1}]				
	Method 3	Method 7	Method 8	O_2	CO	H_2	CO_2	H_2O
Origin_1[b]	12.79	13.49	10.81	12.35	4.976	15.19	5.385	7.771
ppo2_65	9.062	8.572	8.512	7.883	6.874	16.60	2.696	2.793
ppo2_15	5.360	5.465	6.716	1.317	6.553	15.59	-0.523	-2.396
ppo2_05	1.643	3.478	5.294	0.000	4.177	13.09	-1.497	-2.271
Origin_2[b]	11.03	12.63	11.24	12.60	3.878	12.71	6.576	7.836
ppo2_64	8.941	8.817	8.782	7.887	4.897	14.23	3.225	4.285
ppo2_14	6.830	6.129	6.844	3.028	6.201	13.71	0.090	-0.728
ppo2_04	4.727	4.267	5.339	2.085	6.930	12.67	0.090	-1.898
Origin_3[b]	12.87	13.83	12.29	12.89	2.811	10.74	5.630	10.74
ppo2_61	9.994	9.600	9.378	9.688	5.209	14.93	4.241	5.170
ppo2_11	7.044	6.607	7.108	4.229	7.342	16.58	1.145	-1.762
ppo2_01	4.232	4.628	5.458	1.243	7.175	13.82	-1.242	-2.382
Origin_4[b]	10.93	12.29	11.85	13.22	1.281	8.055	6.764	11.36
ppo2_62	9.186	9.143	9.130	10.70	2.938	11.39	5.269	7.527
ppo2_12	7.418	6.773	7.004	5.681	5.166	13.59	2.134	1.266
ppo2_02	5.663	5.030	5.384	1.329	5.626	13.23	-0.077	-2.634

a   Rate of oxygen consumption calculated by method 8
    Rate of product formation calculated from tangents to hand-drawn curves through W/F°_{CH4} vs X_{CH4} data.
b   Rate at W/F°_{CH4} = 0
All the above experiments were conducted at 604°C and P_T = 200 kPa(a)

C.3. Product partial pressure

C.3.1. Carbon monoxide partial pressure

The effect of $P°_{CO}$ on the product composition is given in Table C-7 and the effect on the reaction rates in Table C-8. The experiment labels have been explained in Table 2-5.

Table C-7 The effect of $P°_{CO}$ on the product composition

Run ID	W	$P°_{CH4}$	$P°_{O2}$	$P°_{CO}$	Partial pressure at the reactor outlet (kPa)					
	mg		kPa		CH_4	O_2	CO	H_2	CO_2	H_2O
ppcm_72	15.1	2.963	1.343	1.343	2.438	0.383	0.742	0.794	1.051	0.504
ppcm_62	25.1	2.963	1.343	1.343	2.177	0.209	0.993	1.245	1.065	0.555
ppcm_12	51.2	2.963	1.343	1.343	1.798	0.040	1.330	1.694	1.002	0.680
ppcm_73	15.1	2.963	1.342	2.837	2.534	0.280	1.908	0.771	1.357	0.235
ppcm_63	25.0	2.963	1.342	2.837	2.260	0.162	2.141	1.231	1.341	0.370
ppcm_13	50.2	2.963	1.342	2.837	1.865	0	2.703	1.925	1.267	0.261
ppcm_74	15.4	2.952	1.338	6.294	2.537	0.082	4.337	0.568	2.017	0.470
ppcm_64	25.0	2.952	1.338	6.294	2.367	0.026	4.790	0.987	1.949	0.243
ppcm_14	49.9	2.952	1.338	6.294	2.180	0.017	4.935	1.705	1.710	0.332

All above experiments were conducted at 604°C, P_T = 200 kPa(a).

Table C-8 The effect of $P°_{CO}$ on the rate of methane and oxygen consumption and the rates of product formation

Run ID	r_{CH_4} x 1E5 [mol g^{-1} s^{-1}]			Reaction Rate^a x 1E5 [mol g^{-1} s^{-1}]				
	Method 3	Method 7	Method 8	O_2	CO	H_2	CO_2	H_2O
Origin_1^b	15.20	13.15	12.23	40.81	-22.18	20.38	29.77	13.62
ppcm_72	11.38	10.57	10.39	12.32	-5.070	20.79	10.59	8.409
ppcm_62	8.848	9.145	9.330	5.575	5.856	11.63	-2.806	1.420
ppcm_12	2.241	6.270	7.044	0.704	4.684	5.729	-0.790	1.883
Origin_2^b	12.66	11.95	11.07	50.22	-29.95	19.21	37.85	5.868
ppcm_73	10.09	9.706	9.557	11.50	-4.958	19.95	16.23	6.889
ppcm_63	8.413	8.472	8.678	4.377	11.55	11.38	-5.189	0.180
ppcm_13	4.136	5.992	6.787	0.374	8.507	9.677	-1.428	-1.885
Origin_3^b	12.28	8.845	8.127	93.99	-4.493	14.16	58.28	13.62
ppcm_74	8.449	7.480	7.294	5.959	-22.63	16.97	13.37	2.808
ppcm_64	5.936	6.701	6.795	0.977	6.162	13.27	-7.643	-4.060
ppcm_14	**-0.463**	5.066	5.674	0.010	1.656	10.56	-3.957	-0.530

a   Rate of oxygen consumption calculated by method 8
    Rate of product formation calculated from tangents to hand-drawn curves through W/F°$_{CH_4}$ vs X$_{CH_4}$ data.
b   Rate at W/F°$_{CH_4}$ = 0
All the above experiments were conducted at 604°C and P_T = 200 kPa(a)

C.3.2. Hydrogen partial pressure

The effect of P°_{H2} on the product composition is given in Table C-9 and the effect on reaction rates in Table C-10. The experiment labels have been explained in Table 2-5.

Table C-9 The effect of P°_{H2} on the product composition

Run ID	W	P°_{H2}	Partial pressure at the reactor outlet (kPa)					
	mg	kPa	CH_4	O_2	CO	H_2	CO_2	H_2O
pph_63	24.9	1.449	2.038	0.009	0.453	2.129	0.428	1.352
pph_13a	50.5	1.449	1.584	0.017	0.982	3.586	0.446	0.759
pph_03	75.3	1.449	1.170	0	1.340	4.405	0.384	0.549
pph_64	25.0	2.836	2.145	0.011	0.533	3.462	0.430	1.264
pph_04	75.0	2.836	1.272	0	1.438	5.590	0.327	0.564
pph_65	24.9	5.609	2.260	0.016	0.467	5.358	0.248	1.690
pph_15	50.3	5.609	1.744	0.001	0.858	6.632	0.420	0.970
pph_05	75.4	5.609	1.396	0	1.204	7.602	0.369	0.720

All above experiments were conducted at 604°C, P_T = 200 kPa(a), P°_{CH4} = 2.963 and P°_{O2} = 1.342

Table C-10 The effect of P°_{H2} on the rate of methane and oxygen consumption and the rates of product formation

| Run ID | r_{CH4} x 1E5 [mol g^{-1} s^{-1}] | | | Reaction Rate^a x 1E5 [mol g^{-1} s^{-1}] | | | | |
	Method 3	Method 7	Method 8	O_2	CO	H_2	CO_2	H_2O
Origin_1^b	15.19	16.70	14.63	105.4	6.815	8.672	7.418	26.57
pph_63	11.10	10.59	10.60	0.630	7.461	15.90	3.598	3.036
pph_13a	6.997	6.712	7.682	0.004	6.898	17.79	-0.885	-7.932
pph_03	2.898	4.256	5.567	0.000	5.137	11.58	-0.954	-2.652
Origin_2^b	14.5	15.54	13.29	100.1	8.550	8.153	8.885	26.06
pph_64	10.60	10.01	9.917	0.773	7.301	14.02	1.630	4.704
pph_04	2.783	4.159	5.524	0.000	6.795	16.68	-1.179	-6.744
Origin_3^b	12.09	13.87	11.76	91.53	7.383	-8.361	3.880	36.89
pph_65	9.366	9.083	9.075	1.072	6.505	6.361	3.647	2.144
pph_15	6.640	5.949	7.006	0.013	5.576	17.74	0.886	-8.243
pph_05	3.914	3.897	5.408	0.000	5.177	14.23	-1.471	-2.790

a   Rate of oxygen consumption calculated by method 8
    Rate of product formation calculated from tangents to hand-drawn curves through W/F$^\circ_{CH4}$ vs X_{CH4} data.
b   Rate at W/F$^\circ_{CH4}$ = 0
All the above experiments were conducted at 604°C and P_T = 200 kPa(a)

C.3.3. Carbon dioxide partial pressure

The effect of P°_{CO2} on the product composition is given in Table C-11 and the effect on the reaction rates in Table C-12. The experiment labels have been explained in Table 2-5.

Table C-11 The effect of P°_{CO2} on the product composition

Run ID	W	P°_{CH4}	P°_{O2}	P°_{CO2}	Partial pressure at the reactor outlet (kPa)					
	mg	kPa	kPa	kPa	CH_4	O_2	CO	H_2	CO_2	H_2O
ppcd_61	25.0	2.960	1.341	0.269	2.033	0.313	0.300	0.804	0.691	0.901
ppcd_11	50.0	2.960	1.341	0.269	1.494	0.043	0.841	2.083	0.723	0.823
ppcd_01	74.9	2.960	1.341	0.269	1.235	0.015	1.322	2.835	0.677	0.479
ppcd_62	25.0	2.955	1.339	0.551	2.049	0.434	0.368	0.840	0.801	0.931
ppcd_12	50.0	2.955	1.339	0.551	1.555	0.027	0.779	1.566	0.975	0.975
ppcd_02	75.0	2.955	1.339	0.551	1.256	0.014	1.289	2.582	0.893	0.638
ppcd_63	25.0	2.954	1.338	1.371	2.214	0.553	0.300	0.434	1.546	0.911
ppcd_13	50.2	2.954	1.338	1.371	1.704	0.127	0.844	1.232	1.728	0.813
ppcd_03	74.8	2.954	1.338	1.371	1.266	0	1.530	2.275	1.516	0.804
ppcd_64	24.9	2.953	1.338	2.768	2.289	0.528	0.279	0.378	2.954	0.955
ppcd_14	49.9	2.953	1.338	2.768	1.812	0.120	0.830	0.970	3.052	0.998
ppcd_04	75.0	2.953	1.338	2.768	1.299	0.034	1.794	2.140	2.695	0.875

All the above expeiments were conducted at 604°C and $P_T = 200$ kPa(a)

Table C-12 The effect of P°_{CO2} on the rate of methane and oxygen consumption and the rates of product formation

Run ID	r_{CH4} x 1E5 [mol g^{-1} s^{-1}]			Reaction Rate[a] x 1E5 [mol g^{-1} s^{-1}]				
	Method 3	Method 7	Method 8	O_2	CO	H_2	CO_2	H_2O
Origin_1[b]	16.54	15.98	14.74	30.69	4.082	11.45	7.227	19.79
ppcd_61	11.38	10.68	10.66	6.910	6.481	16.09	3.613	5.291
ppcd_11	6.211	7.142	7.703	1.556	7.980	15.80	-0.591	-5.900
ppcd_01	1.065	4.783	5.575	0.353	7.295	10.60	-0.779	-4.993
Origin_2[b]	15.79	15.01	14.17	25.78	5.637	13.32	3.892	19.22
ppcd_62	11.03	10.40	10.37	7.368	5.860	12.08	3.663	6.397
ppcd_12	6.264	7.21	7.593	2.106	6.955	13.00	0.766	-4.006
ppcd_02	1.501	4.998	5.558	0.602	8.253	16.34	-2.271	-5.241
Origin_3[b]	12.18	13.08	12.74	20.72	4.090	6.147	2.273	19.83
ppcd_63	9.799	9.635	9.626	7.572	6.220	8.893	3.599	5.302
ppcd_13	7.414	7.101	7.271	2.767	9.509	14.21	-0.396	-5.464
ppcd_03	5.029	5.233	5.492	1.011	10.95	16.70	-3.908	-4.376
Origin_4[b]	10.31	11.96	11.81	21.10	3.645	5.440	3.036	19.83
ppcd_64	9.052	9.111	9.107	7.569	6.192	6.929	2.637	6.397
ppcd_14	7.790	6.942	7.022	2.715	11.75	13.11	-1.744	-2.191
ppcd_04	6.528	5.289	5.414	0.974	15.87	19.17	-6.346	-1.502

a   Rate of oxygen consumption calculated by method 8
      Rate of product formation calculated from tangents to hand-drawn curves through W/F°_{CH4} vs X_{CH4} data.
b   Rate at $W/F^\circ_{CH4} = 0$
All the above experiments were conducted at 604°C and $P_T = 200$ kPa(a)

C.3.4. Water partial pressure

The effect of P°_{H2O} on the product composition is given in Table C-13 and the effect on differential reaction rates in Table C-14. The experiment labels have been explained in Table 2-5.

Table C-13 The effect of P°_{H2O} on the product composition

Run ID	W	P°_{CH4}	P°_{O2}	P°_{H2O}	Partial pressure at the reactor outlet (kPa)					
	mg		kPa		CH_4	O_2	CO	H_2	CO_2	H_2O
ppwa_13	50.0	2.957	1.305	0.489	2.096	0.154	0.292	1.156	0.539	1.039
ppwa_03a	74.9	2.957	1.305	0.489	1.513	-	0.905	2.531	0.626	0.889
ppwa_23	100.0	2.957	1.305	0.489	1.350	-	1.146	2.840	0.590	0.799
ppwa_11	50.3	2.956	1.309	0.726	2.021	0.263	0.384	1.434	0.544	1.135
ppwa_01	75.1	2.956	1.309	0.726	1.535	-	0.680	2.649	0.781	0.896
ppwa_21	100.1	2.956	1.309	0.726	1.250	-	1.110	3.040	0.609	1.029
ppwa_12	50.1	2.957	1.301	1.200	2.246	0.331	0.118	0.822	0.630	1.816
ppwa_02	75.1	2.957	1.301	1.200	1.597	0.014	0.543	2.160	0.755	1.647
ppwa_22	100.1	2.957	1.301	1.200	1.328	0.008	0.785	2.832	0.766	1.577

All the above experiments were conducted at 604°C and P_T = 200 kPa(a)

Table C-14 The effect of P°_{H2O} on the rate of methane and oxygen consumption and the rates of product formation

Run ID	r_{CH_4} x 1E5 [mol g^{-1} s^{-1}]			Reaction Rate[a] x 1E5 [mol g^{-1} s^{-1}]				
	Method 3	Method 7	Method 8	O_2	CO	H_2	CO_2	H_2O
Origin_3[b]	7.970	11.40	9.069	30.39	2.007	8.280	4.381	4.706
ppwa_13	6.323	5.371	6.083	1.465	4.354	12.42	3.198	1.742
ppwa_03a	5.502	3.692	4.986	0.324	6.912	13.99	-0.304	-2.127
ppwa_23	4.675	2.531	4.081	0.071	4.893	4.752	-0.638	3.850
Origin_1[b]	8.448	11.77	9.523	25.52	2.980	10.47	5.335	2.978
ppwa_11	6.696	5.549	6.246	1.987	3.426	13.95	4.227	1.027
ppwa_01	5.832	3.830	5.073	0.564	5.840	12.55	-7.235	-0.238
ppwa_21	4.957	2.632	4.110	0.158	7.515	4.724	-4.112	2.585
Origin_2[b]	6.004	9.718	8.482	23.32	0.611	5.297	5.294	5.435
ppwa_12	6.435	5.432	5.834	2.250	2.824	10.92	3.591	1.712
ppwa_02	6.649	4.063	4.840	0.701	5.522	16.54	0.286	-3.362
ppwa_22	6.864	3.039	4.016	0.218	3.419	8.660	0.149	-1.456

a   Rate of oxygen consumption calculated by method 8
    Rate of product formation calculated from tangents to hand-drawn curves through $W/F^{\circ}_{CH_4}$ vs X_{CH_4} data.
b   Rate at $W/F^{\circ}_{CH_4} = 0$
All the above experiments were conducted at 604°C and $P_T = 200$ kPa(a)

C.3.5. Replicate experiment for the lack-of fit test

A set of experiments were repeated under identical conditions to determine the pure error sum of squares (PE - SS). The results of the repeat experiments are shown below (see Table C-16). The lack-of-fit sum of squares (LOF - SS) was calculated by subtracting the pure error sum of squares (equation (C-4)) from the residual sum of squares (RES calculated by equation (C-1)).

$$RES = \sum_{i=1}^{n} (r_{CH_4} - r_{CH_4}^{Model})^2 \qquad \text{(C-1)}$$

The analysis of the replicate experiments and the calculation of the PE - SS values for each of the three curve-fitting methods is given in appendix C.3.5. The F-value that was compared to the $F_{0.95}(n-p-n_e+1, n_e-1)$ value was calculated from [172]:

$$F_c = \cfrac{\cfrac{LOF - SS}{n - p - n_e + 1}}{\cfrac{PE - SS}{n_e - 1}} \qquad \text{(C-2)}$$

where n was the number of data points, p the number of parameters used in the model fit and n_e the number of replicate experiments. If $F_c > F_{0.95}(n-p-n_e+1, n_e-1)$, it was concluded that there was a 95% chance that the model was inadequate. When the F-test was adhered to, it was indicated in Table 4-1 by a ✓ sign. The $F_{0.95}(n-p-n_e+1, n_e-1)$ values were taken from standard tables [173] and was calculated as:

$$F_{0.95} (n - p - n_e + 1 , n_e - 1) = \frac{1}{F_{0.05} (n_e - 1 , n - p - n_e + 1)} \qquad \text{(C-3)}$$

Two sets of kinetic experiments were conducted under identical conditions of temperature, pressure and feed composition ($n_e = 1$). The measured methane conversion values were then

used to calculate the rate of methane consumption. The methane feed rate (W/F°_{CH4}), methane conversion and the calculated rates of methane consumption are tabulated below. Methods 3, 7 and 8 were used to calculate the rate of methane consumption (as described in detail in section 3.3.1). The pure error sum of squares (PE - SS) was based on the initial rate of reaction (r°_{CH4}) and was defined as

$$PE - SS = \sum_{n_i = 1}^{2} (r^{o}_{CH_4} - r^{o}_{CH_4, Average})^2 \qquad \text{(C-4)}$$

The PE - SS values for the three curve-fitting methods are shown below in Table C-15.

Table C-15 Pure error sum of squares of the initial rate of methane consumption from replicate experiments

Curve-fitting method	Pure error sum of squares	Mean r°_{CH4}
3	1.427E-9	1.234E-4
7	5.386E-9	1.482E-4
8	3.199E-9	1.362E-4

These sum of square values were used in the F-test to evaluate the goodness-of-fit of the chosen rate models.

Table C-16 Results of replicate experiments. ($P°_i$ in kPa: CH_4 = 2.96, O_2 = 1.34, T = 604°C, P_T = 201.3 kPa, $F°_{CH4}$ = 1.136 mol.s⁻¹)

Run number	W_{cat} mg	$W/F°_{CH4}$ g.s.mol⁻¹	P_{CH4} kPa	X_{CH4}	r_{CH4} Method 3 mol.g.s⁻¹	r_{CH4} Method 7 mol.g.s⁻¹	r_{CH4} Method 8 mol.g.s⁻¹
	0	0	2.96	0	1.239E-4	1.547E-4	1.420E-4
ppo2_71	15.3	1347.3	2.44	0.18	1.221E-4	1.206E-4	1.173E-4
ppcm_60	25.0	2201.5	2.28	0.23	1.048E-4	1.029E-4	1.039E-4
ppcd_10	49.9	4394.3	1.57	0.47	8.577E-5	6.855E-5	7.609E-5
ppo2_01	75.0	6604.6	1.11	0.63	6.658E-5	4.551E-5	5.559E-5
	0	0	2.96	0	1.229E-4	1.416E-4	1.305E-4
pph_70	15.4	1356.2	2.50	0.16	1.085E-4	1.125E-4	1.093E-4
ppo2_61	25.0	2201.5	2.26	0.24	9.960E-5	9.747E-5	9.788E-5
ppo2_11	50.6	4455.9	1.63	0.45	7.579E-5	6.651E-5	7.295E-5
ppcd_00	75.0	6604.6	1.25	0.58	5.309E-5	4.621E-5	5.511E-5

Appendix D

Catalyst characterization

D. Catalyst characterization

D.1. Chemisorption

Chemisorption results of the unused, reduced catalyst is shown in Figure D-1.
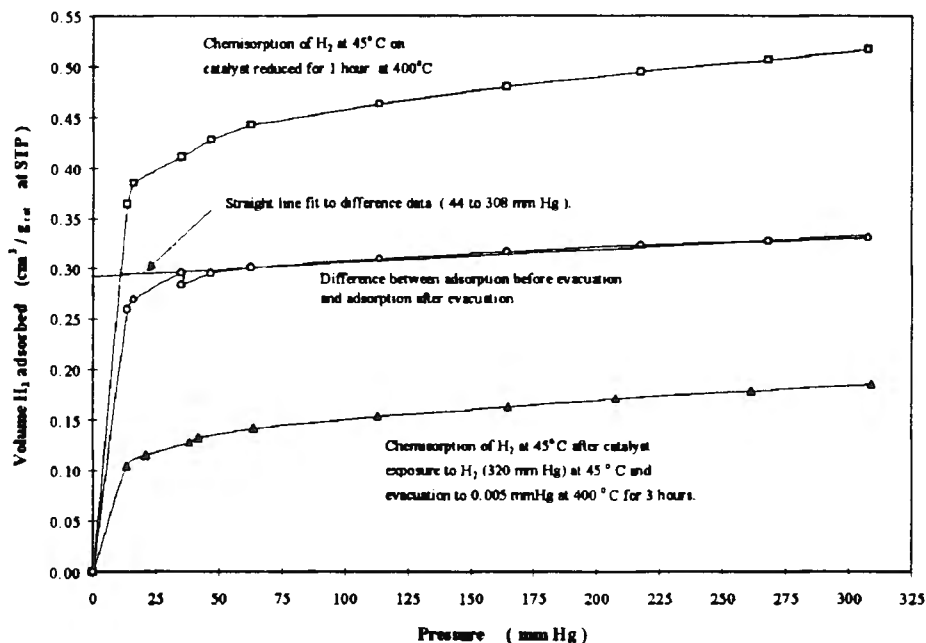
Figure D-1 Result of hydrogen chemisorption (at 45°C) of the unused catalyst

The analysis (upper) curve represents chemisorbed hydrogen as well as physisorbed hydrogen, while the repeat (lower) curve represents only the physisorbed hydrogen. The volume adsorbed at zero pressure may be obtained by extrapolating the linear section of each curve to the y-axis and reading off the intercept. The difference in adsorbed volume between the analysis and repeat runs then enables one to calculate the volume of hydrogen that was chemisorbed by the sample.

A sample calculation is given below:

Volume difference	0.3154 cm^3/g$_{cat}$
H$_2$ adsorbed	3.582 E-5 mol
Number of H atoms adsorbed	4.315 E+19 atoms
Mass of nickel in catalyst	0.2703 g
Total number of Ni atoms	2.773 E+21 atoms
Nickel atom surface density	1.54 E+19 atoms/m^2
Nickel surface area	1.1013 m^2/g$_{cat}$
Particle size	65.04 E-9 m
Dispersion	1.56 %

D.2. Atomic absorption

To ensure that possible differences in nickel loading between the size fractions due to the impregnation procedure were negligible, two of the size fractions were subjected to AA analysis to determine the nickel content. The nickel content of these two size fractions were identical to within 5% (average value of 10.63 wt%) and therefore it may be assumed that the different size fractions are identical, at least in terms of nickel loading. A repeat analysis was also performed a few months later, and the value of 10.37 wt% was in good agreement with the first value of 10.63 wt%.

Appendix E

Code for the optimization program

Differential Model Optimization Routine

```pascal
Program Differential_1;
Uses Crt;


CONST
R  = 8.314;
Pstd  =  101.325;
Tstd  =  273.15;
number_of_constants  =  7;
np    =  2*number_of_constants;
mp    =  np  +  1;
data  =  108;
ftol  =  1e-12;


TYPE
Sixbydata      =  Array[1..6,1..data]        of REAL;
glmpnp         =  Array[1..mp,1..np]         of REAL;
glmp           =  Array[1..mp]               of REAL;
glnp           =  Array[1..np]               of REAL;
onebycon       =  Array[1..number_of_constants]  of REAL;


VAR
Pexp           : Sixbydata;
Consts         : Array[1..2,1..number_of_constants]  of REAL;
K              : Array[1..number_of_constants]       of REAL;
pr, solut      : glnp;
y              : glmp;
p              : glmpnp;
WFPT           : Array[1..24,1..data]        of REAL;
Rate3          : Array[1..data]              of REAL;
Rate7          : Array[1..data]              of REAL;
Rate8          : Array[1..data]              of REAL;
R_array        : Array[1..data]              of REAL;

{Input values to be read from a file}
Txtvar,Txtvar1                              : TEXT;
trap, step, trap1, ndim, iter,input_int1, input_int2  : INTEGER;
{P_CH4, P_O2, P_CO, P_H2, P_CO2, P_H2O, XCH4,}
Temp, dWF, FoCH4, W,
R_deviate, R_sum, Rate_calc, RMSE           : REAL;



Function Rate(P_CH4, P_O2, P_CO, P_H2, P_CO2, P_H2O,
          K1, K2, K3, K4, K5, K6, K7        : Real) :Real;

Begin

Rate   :=  K1*P_CH4 /
        (1 + sqrt(K2*P_O2) + K3*P_CO  + sqrt(K4*P_H2) + K5*P_CO2
         + K6*P_H2O + sqrt(K2*K4*P_O2*P_H2)*K7 );

End;   {Endfunc}



PROCEDURE READ_INPUT_DATA;

BEGIN
Assign (Txtvar,  'D_INPUT.txt');
RESET (Txtvar);
```

```pascal
{Now read file}
For trap := 1 to data do
 Begin

    Readln(Txtvar, WFPT[1,trap], WFPT[2,trap], WFPT[3,trap], WFPT[4,trap],
            WFPT[5,trap], WFPT[6,trap], WFPT[7,trap], WFPT[8,trap],
            WFPT[9,trap], WFPT[10,trap], WFPT[11,trap], WFPT[12,trap],
            WFPT[13,trap], WFPT[14,trap]);

 End; {End_trap}

CLOSE (Txtvar);

{ Fill the experimental partial pressure and rate arrays }
For trap1 := 1 to data do
 Begin
  For trap := 1 to 6 do
    Begin
     Pexp[trap,trap1] := WFPT[trap+2,trap1];
    End;
  Rate7[trap1] := WFPT[12,trap1];
  Rate8[trap1] := WFPT[13,trap1];
  Rate3[trap1] := WFPT[14,trap1];
 End; {End_trap1}

END; {End of procedure}


PROCEDURE WRITE_OUTPUT_DATA;
BEGIN
Assign(Txtvar1,'Outputdf.txt');
REWRITE(Txtvar1);

For trap := 1 to data do
 Begin
 Temp     := WFPT[9,trap];

   For trap1 := 1 to number_of_constants do
    Begin
     K[trap1] := solut[trap1] * exp (-solut[trap1+number_of_constants]/(R*Temp));
    End;

   R_array[trap] := Rate(Pexp[1,trap],Pexp[2,trap],Pexp[3,trap],
                    Pexp[4,trap],Pexp[5,trap],Pexp[6,trap],
                    K[1],K[2],K[3],K[4],K[5],K[6],K[7]);
   Writeln(Txtvar1, Rate8[trap], R_array[trap]);
 End;

Writeln(Txtvar1,' ');

For trap := 1 to np do
Begin
 Writeln(Txtvar1, solut[trap]);
End;

CLOSE(Txtvar1);

END; {Endproc}


Function func(pr:glnp) :REAL;
Begin
```

```
For trap := 1 to number_of_constants do
Begin
    Gotoxy(1,trap+2);
    Writeln('A',trap,'   =   ',pr[trap]:12:10);
    Gotoxy(1,trap+2+number_of_constants);
    Writeln('Ea/dH',trap,'   =   ',pr[trap+number_of_constants]:9:3);
End;


{Now calculate the root mean square error}
RMSE       := 0;
R_deviate  := 0;
R_sum      := 0;

  For trap1 := 1 to number_of_constants do
    Begin
      Temp        := WFPT[9,trap];
      K[trap1] := pr[trap1] * exp (-pr[trap1+number_of_constants]/(R*Temp));
    End;


For trap := 1 to data do
  Begin

    Rate_calc := Rate(Pexp[1,trap],Pexp[2,trap],Pexp[3,trap],
                 Pexp[4,trap],Pexp[5,trap],Pexp[6,trap],
                 K[1],K[2],K[3],K[4],K[5],K[6],K[7]);

    {Sum of squares:}
    R_deviate     := R_deviate + SQR( Rate_calc - Rate8[trap]);
    R_sum         := R_sum     + Rate8[trap];

  End;


RMSE := sqrt(R_deviate) / (data*R_sum);
func := RMSE;

Gotoxy(1,23);
Writeln('Root mean square error  =  ', RMSE:20:17);


END; {END_PROCEDURE}



PROCEDURE amoeba(VAR p: glmpnp; VAR y: glmp; ndim: integer;
     ftol: real; VAR iter: integer);

(* Programs using routine AMOEBA must supply an external function
func(pr:glnp):real whose minimum is to be found. They must
also define types
TYPE
   glmpnp = ARRAY [1..mp,1..np] OF real;
   glmp = ARRAY [1..mp] OF real;
   glnp = ARRAY [1..np] OF real;
where mp and np are physical dimensions *)

LABEL 99;
CONST
   alpha = 1.0;
   beta  = 0.5;
   gamma = 2.0;
   itmax = 10000;
```

```
VAR
   mpts,j,inhi,ilo,ihi,i        : INTEGER;
   ytry,ysave,sum,rtol          : REAL;
   psum                         : ^glnp;


Function evaluate(VAR p         : glmpnp;
              VAR y       : glmp;
              VAR sum     : glnp;
              ndim, ihi   : integer;
              VAR iter    : integer;
              fac         : REAL)  : REAL;
VAR
j                      : Integer;
fac1, fac2, ytry       : REAL;
ptry                   : ^glnp;

BEGIN

new(ptry);
fac1      := (1-fac)/ndim;
fac2      := fac1 - fac;

{ Write routine to set boundary conditions for the constants }
{ and to expand, contract etc the values }

For j := 1 to ndim DO
  BEGIN

      ptry^[j] := sum[j]*fac1 - p[ihi,j]*fac2;

      IF (j < number_of_constants+2)  THEN
      BEGIN
        IF ptry^[j] < 0 then ptry^[j] := abs(ptry^[j]);
      END

      else
      IF ptry^[j] > 0 then ptry^[j] := -(ptry^[j]);

  END;


ytry := func(ptry^);    {Evaluate the function at the trial point}
iter := iter + 1;

Gotoxy(1,24);
Writeln('Iteration number : ', iter);

IF ytry < y[ihi] then
BEGIN
   y[ihi] := ytry;
   FOR j := 1 to ndim DO BEGIN
     sum[j]   := sum[j]+ptry^[j] - p[ihi,j];
     p[ihi,j] := ptry^[j]
   END
END;

evaluate := ytry;
dispose(ptry)

END; {end of function}
```

```
BEGIN  {Begin procedure amoeba}

Gotoxy(1,23);
Writeln('Optimizing...please be VERY patient...');

new(psum);

  mpts := ndim+1;
  iter := 0;

  For j := 1 to ndim do BEGIN
    sum := 0;
    For i := 1 to mpts do
      sum := sum + p[i,j];
    psum^[j] := sum
  End;

  WHILE true DO
  BEGIN
    ilo := 1;
    IF (y[1] > y[2]) THEN
    BEGIN
      ihi := 1;
      inhi := 2
    END {End_if}
    ELSE
    BEGIN
      ihi := 2;
      inhi := 1
    END; {End_else}

    FOR i := 1 to mpts DO
    BEGIN
      IF (y[i] < y[ilo]) THEN  ilo := i;
      IF (y[i] > y[ihi]) THEN
      BEGIN
        inhi := ihi;
        ihi := i
      END {End_if}
      ELSE
      IF (y[i] > y[inhi]) THEN
        IF (i < > ihi) THEN  inhi := i
    END; {End_for i}
```

{Compute the fractional range from highest to lowest}

```
    rtol := 2.0*abs(y[ihi]-y[ilo])/(abs(y[ihi])+abs(y[ilo]));

    IF (rtol < ftol) THEN GOTO 99;  {return if rtol satisfactory}
    IF (iter > itmax) THEN
      BEGIN
        writeln('A BREATHER...there are too many iterations');
        Readln;
        GOTO 99
      END;

    ytry := evaluate(p,y,psum^,ndim,ihi,iter,-alpha);

    IF (ytry < = y[ilo]) THEN
```

{ Gives a result better than the previous point, so try an additional }
{ extrapolation by a factor gamma: }

```
        ytry := evaluate(p,y,psum^,ndim,ihi,iter,gamma)

        ELSE IF  (ytry > = y[inhi]) THEN BEGIN

{ Reflected point is worse than the second-highest, so look for an }
{ intermediate lower point, ie. do a one-dimensional contraction  }

        ysave := y[ihi];
        ytry  := evaluate(p,y,psum^,ndim,ihi,iter,beta);
        IF (ytry > = ysave) THEN BEGIN

{ Can't get rid of high point; contract around the lowest point }

            FOR i := 1 to mpts DO
                IF (i < > ilo) THEN BEGIN
                    FOR j := 1 to ndim DO BEGIN
                        psum^[j] := 0.5*(p[i,j]+p[ilo,j]);
                        p[i,j]   := psum^[j]
                    END;
                    y[i] := func(psum^)
                END; {end_if}
            iter := iter + 1;
            FOR j := 1 to ndim DO BEGIN
                sum := 0;
                FOR i := 1 to mpts DO
                    sum := sum + p[i,j];
                psum^[j] := sum
            END {j}
        END {if ytry > =ysave}
    END {else if ytry}

END;
99:  dispose(psum);

For trap := 1 to np do
    Begin
    solut[trap] := p[mp,trap];
    End;

END; {End_PROCEDURE}


{“““““““““““““““““MAIN   PROGRAM“““““““““““““““““““}
BEGIN
Clrscr;

READ_INPUT_DATA;  {Read text file with inlet conditions}


{Starting guess for kinetic constants}
For input_int1 := 1 to mp do
Begin

Randomize;

    For input_int2 := 1 to number_of_constants do
    Begin

        pr[input_int2]                     := 1e-8   *    (20+Random(10))/(10+Random(15));
        pr[input_int2+number_of_constants] := -100000  - 50000*(20+Random(10))/(10+Random(15));
        pr[1]                              := 5e-1   *    (20+Random(10))/(10+Random(15));
        pr[number_of_constants+1]          := 60000    + 40000*(20+Random(10))/(10+Random(15));
```

```
      p[input_int1,input_int2]                      := pr[input_int2];
      p[input_int1,number_of_constants+input_int2] := pr[input_int2+number_of_constants];


   End; {End_int2}


y[input_int1]  := func(pr);
Gotoxy(1,22);
Writeln('Input row number : ',input_int1);



End; {End_input_int1}

ndim := np;

Gotoxy(1,22);
Writeln('                                  ');


AMOEBA(p,y,ndim,ftol,iter);



Gotoxy(15,40);
Write('...ALL  DONE!...');
Gotoxy(16,30);
Write('   Press SPACEBAR to continue    ');
Repeat until READKEY = ' ';

WRITE_OUTPUT_DATA;


END. {End of the main program}
```

Integral Model Optimization Routine

```pascal
{N+}
Program Simplex_Integrate_WGS;
Uses Crt;

CONST
R    = 8.314;
Pstd = 101.325;
Tstd = 273.15;
P_t  = 201.325;
number_of_steps = 5;
number_of_constants = 7;
np   = 2*number_of_constants;
mp   = np + 1;
data = 83;
ftol = 5e-10;


TYPE
Sixbydata              = Array[1..6,1..data]      of REAL;
glmpnp                 = Array[1..mp,1..np]       of REAL;
glmp                   = Array[1..mp]             of REAL;
glnp                   = Array[1..np]             of REAL;


VAR
Po,Pexp,Ppred   : Sixbydata;
Consts          : Array[1..2,1..number_of_constants]  of REAL;
K               : Array[1..number_of_constants]       of REAL;
pr              : glnp;
y               : glmp;
p, solutions    : glmpnp;
WFPT            : Array[1..21,1..data]           of REAL;
X_deviate, Temp : Array[1..data]                 of REAL;

{Input values to be read from a file}
Txtvar,Txtvar1                         : TEXT;
trap, step, trap1, ndim, iter,input_int1, input_int2,
teller,jan                             : INTEGER;
P_CH4, P_O2, P_CO, P_H2, P_CO2, P_H2O, XCH4,
A, B, C, D, E, XCH4_n_1, XCH4_n_2, XCH4_n_3, XCH4_n_4,
dWF, FoCH4, W, X_dev_sum, X_exp_ave, RMSE, P_dev_sum  : REAL;
k_1, k_3, K_3_eq, XCH4_n, K_4_eq, k_4                 : REAL;


Function Rate1(X1, X2, X3, X4 : Real)    :REAL;
{Total oxidation}

Begin

    P_CH4  := Po[1,step]*( 1 - X1 - X2 - X3);
    P_O2   := Po[1,step]*( Po[2,step]/Po[1,step]   - 2*X1 - 0.5*X2 );
    If P_O2 < 0 then P_O2 := 0;
    P_CO   := (Po[1,step])*( Po[3,step]/Po[1,step]  +   X2 +   X3 );
    P_CO   := P_CO * (1 - X4);
    P_H2   := (Po[1,step])*( Po[4,step]/Po[1,step]  + 2*X2 + 3*X3 ) + P_CO*X4;
    P_CO2  := (Po[1,step])*( Po[5,step]/Po[1,step]  +   X1       ) + P_CO*X4;
    P_H2O  := (Po[1,step])*( Po[6,step]/Po[1,step]  + 2*X1 -   X3 ) - P_CO*X4;

    Rate1  := K[1] * P_CH4 /
         (1 + sqrt(K[5]*P_O2) + K[6]*P_CO + K[7]*P_H2O );

End;    {Endfunc}
```

```pascal
Function Rate2(X1, X2, X3, X4 : Real)        :Real;
{Oxidative reforming}

Begin

    P_CH4  := Po[1,step]*( 1 - X1 - X2 - X3);
    P_O2   := Po[1,step]*( Po[2,step]/Po[1,step]   - 2*X1 - 0.5*X2 );
    If P_O2 < 0 then P_O2 := 0;
    P_CO   := (Po[1,step])*( Po[3,step]/Po[1,step]  +  X2 +  X3 );
    P_CO   := P_CO * (1 - X4);
    P_H2   := (Po[1,step])*( Po[4,step]/Po[1,step]  + 2*X2 + 3*X3 ) + P_CO*X4;
    P_CO2  := (Po[1,step])*( Po[5,step]/Po[1,step]  +  X1      ) + P_CO*X4;
    P_H2O  := (Po[1,step])*( Po[6,step]/Po[1,step]  + 2*X1 -  X3 ) - P_CO*X4;


    Rate2  := K[2] * P_CH4 /
        (1 + sqrt(K[5]*P_O2) + K[6]*P_CO + K[7]*P_H2O );


End;   {Endfunc}



Function Rate3(X1, X2, X3, X4 : Real)        :Real;


{Steam reforming}
Begin

    P_CH4  := (Po[1,step]/Pstd)*( 1 - X1 - X2 - X3);
    P_O2   := Po[1,step]*( Po[2,step]/Po[1,step]   - 2*X1 - 0.5*X2 );
    If P_O2 < 0 then P_O2 := 0;
    P_CO   := (Po[1,step]/Pstd)*( Po[3,step]/Po[1,step]  +  X2 +  X3 );
    P_CO   := P_CO * (1 - X4);
    P_H2   := (Po[1,step]/Pstd)*( Po[4,step]/Po[1,step]  + 2*X2 + 3*X3 ) + P_CO*X4;
    P_CO2  := (Po[1,step]/Pstd)*( Po[5,step]/Po[1,step]  +  X1      ) + P_CO*X4;
    P_H2O  := (Po[1,step]/Pstd)*( Po[6,step]/Po[1,step]  + 2*X1 -  X3 ) - P_CO*X4;


{   k_3    := 3.48165E-4 * P_t * exp (-36750.326/(R*Temp[step]));}


    K_3_eq := exp( (- 10308/Temp[step] + 4.87*ln(Temp[step])/ln(10) +
            6.6E-5*Temp[step]  - 8.1E-8 * sqr(Temp[step]) - 3.04) * ln(10) );  {H.M. Stanley}


    If (P_H2O < = 0) OR (P_O2 = 0) then Rate3 := 0 else


    Rate3  := K[3]{k_3} * (P_CH4 - (P_H2*P_H2*P_H2 * P_CO)/(K_3_eq * P_H2O));

End;   {Endfunc}



Function Rate4(X1, X2, X3, X4 : Real)        :Real;
{Water-Gas Shift Reaction}
Begin

    P_CO   := (Po[1,step]/Pstd)*( Po[3,step]/Po[1,step]  +  X2 +  X3 );
    P_CO   := P_CO * (1 - X4);
    P_H2   := (Po[1,step]/Pstd)*( Po[4,step]/Po[1,step]  + 2*X2 + 3*X3 ) + P_CO*X4;
    P_H2O  := (Po[1,step]/Pstd)*( Po[6,step]/Po[1,step]  + 2*X1 -  X3 ) - P_CO*X4;
    P_CO2  := (Po[1,step]/Pstd)*( Po[5,step]/Po[1,step]  +  X1      ) + P_CO*X4;


    k_4    := 8.337246E-3 * P_t * exp (-58149.250/(R*Temp[step]));
    K_4_eq := exp( ( 2210/Temp[step] - 0.9103*ln(Temp[step])/ln(10) + 9.74E-4*Temp[step]
            - 1.49E-7 * sqr(Temp[step]) - 0.118) * ln(10) );  {H.M. Stanley}
    If P_H2O = 0 then Rate4 := 0 else
    Rate4  := {k_4}K[4] * (P_CO - (P_H2 * P_CO2)/(K_4_eq * P_H2O));

End;   {Endfunc}
```

```pascal
PROCEDURE RUNGE_KUTTA;

Var
Rk1_1, Rk2_1, Rk3_1, Rk4_1, Rk5_1, Rk6_1,
Rk1_2, Rk2_2, Rk3_2, Rk4_2, Rk5_2, Rk6_2,
Rk1_3, Rk2_3, Rk3_3, Rk4_3, Rk5_3, Rk6_3,
Rk1_4, Rk2_4, Rk3_4, Rk4_4, Rk5_4, Rk6_4,
XCH4_1_1, XCH4_2_1, XCH4_3_1, XCH4_4_1, XCH4_5_1, XCH4_6_1,
XCH4_1_2, XCH4_2_2, XCH4_3_2, XCH4_4_2, XCH4_5_2, XCH4_6_2,
XCH4_1_3, XCH4_2_3, XCH4_3_3, XCH4_4_3, XCH4_5_3, XCH4_6_3,
XCH4_1_4, XCH4_2_4, XCH4_3_4, XCH4_4_4, XCH4_5_4, XCH4_6_4  : REAL;

BEGIN

For trap1 := 1 to number_of_steps do
Begin
      {First constant}
      XCH4_1_1 := XCH4_n_1;
      XCH4_1_2 := XCH4_n_2;
      XCH4_1_3 := XCH4_n_3;
      XCH4_1_4 := XCH4_n_4;
      Rk1_1    := rate1(XCH4_1_1, XCH4_1_2, XCH4_1_3, XCH4_1_4);
      Rk1_2    := rate2(XCH4_1_1, XCH4_1_2, XCH4_1_3, XCH4_1_4);
      Rk1_3    := rate3(XCH4_1_1, XCH4_1_2, XCH4_1_3, XCH4_1_4);
      Rk1_4    := rate4(XCH4_1_1, XCH4_1_2, XCH4_1_3, XCH4_1_4);

      {Second constant}
      XCH4_2_1 := XCH4_1_1 + 0.5*dWF*Rk1_1;
      XCH4_2_2 := XCH4_1_2 + 0.5*dWF*Rk1_2;
      XCH4_2_3 := XCH4_1_3 + 0.5*dWF*Rk1_3;
      XCH4_2_4 := XCH4_1_4 + 0.5*dWF*Rk1_4;
      Rk2_1    := rate1(XCH4_2_1, XCH4_2_2, XCH4_2_3, XCH4_1_4);
      Rk2_2    := rate2(XCH4_2_1, XCH4_2_2, XCH4_2_3, XCH4_1_4);
      Rk2_3    := rate3(XCH4_2_1, XCH4_2_2, XCH4_2_3, XCH4_1_4);
      Rk2_4    := rate4(XCH4_2_1, XCH4_2_2, XCH4_2_3, XCH4_1_4);

      {Third constant}
      XCH4_3_1 := XCH4_1_1 - dWF*(Rk1_1 - 2*Rk2_1);
      XCH4_3_2 := XCH4_1_2 - dWF*(Rk1_2 - 2*Rk2_2);
      XCH4_3_3 := XCH4_1_3 - dWF*(Rk1_3 - 2*Rk2_3);
      XCH4_3_4 := XCH4_1_4 - dWF*(Rk1_4 - 2*Rk2_4);
      Rk3_1    := rate1(XCH4_3_1, XCH4_3_2, XCH4_3_3, XCH4_1_4);
      Rk3_2    := rate2(XCH4_3_1, XCH4_3_2, XCH4_3_3, XCH4_1_4);
      Rk3_3    := rate3(XCH4_3_1, XCH4_3_2, XCH4_3_3, XCH4_1_4);
      Rk3_4    := rate4(XCH4_3_1, XCH4_3_2, XCH4_3_3, XCH4_1_4);

      XCH4_n_1 := XCH4_1_1 + dWF*( Rk1_1 + 4* Rk2_1 + Rk3_1 )/6;
      XCH4_n_2 := XCH4_1_2 + dWF*( Rk1_2 + 4* Rk2_2 + Rk3_2 )/6;
      XCH4_n_3 := XCH4_1_3 + dWF*( Rk1_3 + 4* Rk2_3 + Rk3_3 )/6;
      XCH4_n_4 := XCH4_1_4 + dWF*( Rk1_4 + 4* Rk2_4 + Rk3_4 )/6;
      XCH4_n   := XCH4_n_1 + XCH4_n_2 + XCH4_n_3;

End;

{Update predicted partial pressures}
Ppred[1,step] := Po[1,step]*(1 - XCH4_n);
Ppred[2,step] := Po[1,step]*(Po[2,step]/Po[1,step]  - 2*XCH4_n_1 -   XCH4_n_2/2);
If Ppred[2,step] < 0 then Ppred[2,step] := 0;

If trap = 1 then
Ppred[3,step] := Po[1,step]*(Po[3,step]/Po[1,step]  +   XCH4_n_2 +   XCH4_n_3)
else
```

```
Ppred[3,step] := Po[1,step]*(Po[3,step]/Po[1,step]  +   XCH4_n_2 +   XCH4_n_3)
                  - Ppred[3,trap]*XCH4_n_4;


Ppred[4,step] := Po[1,step]*(Po[4,step]/Po[1,step]  + 2*XCH4_n_2 + 3*XCH4_n_3)
                  + Ppred[3,step]*XCH4_n_4;


Ppred[5,step] := Po[1,step]*(Po[5,step]/Po[1,step]  +   XCH4_n_1              )
                  + Ppred[3,step]*XCH4_n_4;


Ppred[6,step] := Po[1,step]*(Po[6,step]/Po[1,step]  + 2*XCH4_n_1 - XCH4_n_3)
                  - Ppred[3,step]*XCH4_n_4;
{End of partial pressure update}


END; {Endproc}



PROCEDURE READ_INPUT_DATA;

BEGIN

Assign (Txtvar, 'Input.txt');
RESET (Txtvar);

{Now read file}
For trap := 1 to data do
 Begin

   Readln(Txtvar, WFPT[1, trap], WFPT[2,trap], WFPT[3, trap], WFPT[4,trap],
             WFPT[5, trap], WFPT[6,trap], WFPT[7, trap], WFPT[8,trap],
             WFPT[9, trap], WFPT[10,trap], WFPT[11, trap], WFPT[12,trap],
             WFPT[13, trap], WFPT[14,trap], WFPT[15, trap], WFPT[16,trap],
             WFPT[17, trap], WFPT[18,trap], WFPT[19, trap], WFPT[20,trap],
             WFPT[21, trap]);

 End; {End_trap}

CLOSE (Txtvar);

{""""""Fill the inlet and experimental partial pressure array""""""}
For trap1 := 1 to data do
 Begin
    For trap := 1 to 6 do
    Begin
    Po [trap,trap1] := WFPT[trap+3,trap1];
    Pexp[trap,trap1] := WFPT[trap+9,trap1];
    End;
 Temp[trap1] := WFPT[21,trap1];
 End; {End_trap1}

END; {End of procedure}



PROCEDURE WRITE_OUTPUT_DATA;

BEGIN

Assign(Txtvar1,'Output.txt');
REWRITE(Txtvar1);
```

```pascal
For trap := 1 to data do
  Begin
    Writeln(Txtvar1, Po  [1,trap], Po  [2,trap], Po  [3,trap],
                Po  [4,trap], Po  [5,trap], Po  [6,trap],
                Po  [4,trap], Po  [5,trap], Po  [6,trap],
                Pexp [1,trap], Pexp [2,trap], Pexp [3,trap],
                Pexp [4,trap], Pexp [5,trap], Pexp [6,trap],
                Ppred[1,trap], Ppred[2,trap], Ppred[3,trap],
                Ppred[4,trap], Ppred[5,trap], Ppred[6,trap]);
  End;

Writeln(Txtvar1,' ');

For trap := 1 to mp do
Begin
  For teller := 1 to np do
  Begin
   Writeln(Txtvar1, solutions[trap,teller]);
  End;
   Writeln(Txtvar1,' ');
End;

CLOSE(Txtvar1);

END; {Endproc}


Function func(pr:glnp) :REAL;
BEGIN

RMSE       := 0;
X_dev_sum  := 0;
X_exp_ave  := 0;
P_dev_sum  := 0;
X_deviate[step]  := 0;

For step := 1 to data do
Begin

   XCH4_n   := 0;
   XCH4_n_1 := 0;
   XCH4_n_2 := 0;
   XCH4_n_3 := 0;
   XCH4_n_4 := 0;
   W        := WFPT[1,step];
   FoCH4    := WFPT[2,step];
   dWF      := (W/FoCH4) / number_of_steps;

For trap := 1 to number_of_constants do
 Begin
 K[trap] := pr[trap] * exp( - pr[trap+number_of_constants] / (R*Temp[step]) );
 End;

RUNGE_KUTTA;

For jan := 1 to 6 do {Loop to calc RMSE for all partial pressures}
Begin
   X_deviate[step] := SQR( Pexp[jan,step]  -  Ppred[jan,step] );
   X_dev_sum       := X_dev_sum + X_deviate[step];   {Sum of error^ of X}
   X_exp_ave       := X_exp_ave + Pexp[jan,step];    {Ave Pi(exp) }
End;

   X_exp_ave       := X_exp_ave / (data*6);
```

```
Gotoxy(1,1);
Writeln('Data point number  : ',step:2);

End; {End_step}

RMSE := SQRT(X_dev_sum) / (X_exp_ave*data);

func := RMSE;

   For trap := 1 to number_of_constants do
   Begin                                         i
     Gotoxy(1,trap+2);
     Writeln('A',trap,'       = ',pr[trap]:15:10);
     Gotoxy(1,trap+2+number_of_constants);
     Writeln('Ea/dH',trap,'   = ',pr[trap+number_of_constants]:15:5);
   End;

Gotoxy(1,19);
Writeln('                              ');
Gotoxy(1,19);
Writeln('Root mean square error =  ', RMSE:15:10);

END; {END_FUNCTION}


PROCEDURE amoeba(VAR p: glmpnp; VAR y: glmp; ndim: integer;
     ftol: real; VAR iter: integer);

(* Programs using routine AMOEBA must supply an external function
func(pr:glnp):real whose minimum is to be found. They must
also define types
TYPE
   glmpnp = ARRAY [1..mp,1..np] OF real;
   glmp = ARRAY [1..mp] OF real;
   glnp = ARRAY [1..np] OF real;
where mp and np are physical dimensions *)


LABEL 99;
CONST
   alpha = 1.0;
   beta  = 0.5;
   gamma = 2.0;
   itmax = 5000;

VAR
   mpts,j,inhi,ilo,ihi,i      : INTEGER;
   ytry,ysave,sum,rtol        : REAL;
   psum                       : ^glnp;


Function evaluate(VAR p       : glmpnp;
            VAR y       : glmp;
            VAR sum     : glnp;
            ndim, ihi   : integer;
            VAR iter    : integer;
            fac         : REAL)  : REAL;

VAR
j                   : Integer;
fac1, fac2, ytry    : REAL;
ptry                : ^glnp;
```

```
BEGIN

new(ptry);
fac1      := (1-fac)/ndim;
fac2      := fac1 - fac;

{  Write routine to set boundary conditions for the constants  }
{  and to expand, contract etc the values  }

For j := 1 to ndim DO
  BEGIN

      ptry^[j] := sum[j]*fac1 - p[ihi,j]*fac2;

      IF {((j < 4) OR (j > 4)) and} (j < 12) then
      BEGIN
        IF ptry^[j] < 0 then ptry^[j] := abs(ptry^[j]);
      END

  END;

ytry := func(ptry^);     {Evaluate the function at the trial point}
iter := iter + 1;

Gotoxy(1,17);
Writeln('Iteration number :  '. iter);

IF ytry < y[ihi] then
BEGIN
   y[ihi] := ytry;
   FOR j := 1 to ndim DO BEGIN
    sum[j]   := sum[j]+ptry^[j] - p[ihi,j];
    p[ihi,j] := ptry^[j]
   END
END;

evaluate := ytry;
dispose(ptry)

END;  {end of function}


BEGIN  {Begin procedure amoeba}

Gotoxy(1,23);
Writeln('Optimizing...please be VERY patient...');

new(psum);

  mpts := ndim+1;
  iter := 0;

  For j := 1 to ndim do BEGIN
   sum := 0;
   For i := 1 to mpts do
    sum := sum + p[i,j];
   psum^[j] := sum
  End;
```

```
WHILE true DO
BEGIN
  ilo := 1;
  IF (y[1] > y[2]) THEN
  BEGIN
    ihi := 1;
    inhi := 2
  END {End_if}
  ELSE
  BEGIN
    ihi := 2;
    inhi := 1
  END; {End_else}

  FOR i := 1 to mpts DO
  BEGIN
    IF (y[i] < y[ilo]) THEN  ilo := i;
    IF (y[i] > y[ihi]) THEN
    BEGIN
      inhi := ihi;
      ihi := i
    END {End_if}
    ELSE
    IF  (y[i] > y[inhi]) THEN
      IF (i < > ihi) THEN  inhi := i
  END; {End_for i}
```

{Compute the fractional range from highest to lowest}

```
rtol := 2.0*abs(y[ihi]-y[ilo])/(abs(y[ihi])+abs(y[ilo]));

IF (rtol < ftol) THEN GOTO 99; {return if rtol satisfactory}
IF (iter > = itmax) THEN
  BEGIN
    Writeln('pause in AMOEBA - too many iterations');
    Readln;
    Goto 99;
  END;

ytry := evaluate(p,y,psum^,ndim,ihi,iter,-alpha);

IF (ytry < = y[ilo]) THEN
```

{ Gives a result better than the previous point, so try an additional }
{ extrapolation by a factor gamma: }

```
ytry := evaluate(p,y,psum^,ndim,ihi,iter,gamma)

ELSE IF  (ytry > = y[inhi]) THEN BEGIN
```

{ Reflected point is worse than the second-highest, so look for an }
{ intermediate lower point, ie. do a one-dimensional contraction }

```
ysave := y[ihi];
ytry  := evaluate(p,y,psum^,ndim,ihi,iter,beta);
IF (ytry > = ysave) THEN BEGIN
```

{ Can't get rid of high point; contract around the lowest point }

```
        FOR i := 1 to mpts DO
            IF (i < > ilo) THEN BEGIN
                FOR j := 1 to ndim DO BEGIN
                    psum^[j] := 0.5*(p[i,j]+p[ilo,j]);
                    p[i,j]   := psum^[j]
                END;
                y[i] := func(psum^)
            END; {end_if}
            iter := iter + 1;
            FOR j := 1 to ndim DO BEGIN
                sum := 0;
                FOR i := 1 to mpts DO
                    sum := sum + p[i,j];
                psum^[j] := sum
            END {j}
        END {if ytry > =ysave}
    END {else if ytry}

END;
99:
For trap := 1 to mp do
Begin
    For teller := 1 to np do
    Begin
    solutions[trap,teller]      := p[trap,teller];
    End;
    Writeln;
End;

Clrscr;
dispose(psum)

END; {End_PROCEDURE}


{'''''''''''''''''''''''MAIN   PROGRAM'''''''''''''''''''''''}
BEGIN

Clrscr;
P_CH4:= 0;
P_O2 := 0;
P_CO := 0;
P_H2 := 0;
P_CO2:= 0;
P_H2O:= 0;

READ_INPUT_DATA; {Read text file with inlet conditions}

{Starting guess for kinetic constants}

For input_int1 := 1 to mp do
Begin
    Randomize;
    For trap := 1 to number_of_constants do
    Begin

    pr[trap]                      := 1e-8  *        (20+Random(10))/(5+Random(10));
    pr[trap + number_of_constants]  := -90000  -    4000*(20+Random(10))/(5+Random(10));
    pr[1]                         := 1e-2  *        (20+Random(10))/(5+Random(10));
    pr[8]                         := 50000  +    5000*(20+Random(10))/(5+Random(10));
    pr[2]                         := 1e-2  *        (20+Random(10))/(5+Random(10));
```

```
pr[9]                              :=  50000  +    5000*(20+Random(10))/(5+Random(10));
pr[3]                              :=  1e-2   *      (20+Random(10))/(5+Random(10));
pr[10]                             :=  50000  +    5000*(20+Random(10))/(5+Random(10));
pr[4]                              :=  1e-2   *      (20+Random(10))/(5+Random(10));
pr[11]                             :=  50000  +    5000*(20+Random(10))/(5+Random(10));
p[input_int1,trap]                    :=  pr[trap];
p[input_int1,trap + number_of_constants]  := pr[trap + number_of_constants];
End;


y[input_int1]  := func(pr);


Gotoxy(1,22);
Writeln('Input row number : ',input_int1);

End; {End_input_int1}

ndim := np;
Gotoxy(1,22);
Writeln('                              ');

{Now call the optimizition routine}
iter := 1;

AMOEBA(p,y,ndim,ftol,iter);

Gotoxy(15,40);
Write('...FINITO!...');
Gotoxy(16,30);
Write('  Press SPACEBAR to continue   ');
Repeat until READKEY = ' ';
WRITE_OUTPUT_DATA;

END. {End of the main program}
```

REFERENCES

1. From: Human, all too human (Vol. 1 - 251) in: The philosophy of Nietzsche, G. Clive (ed.), Meridian, New York (1984)

2. J.R. Partington, A History of Chemistry, MacMillan, London, 1962

3. P.J. Meynell, Methane: Planning a digester, Prism Press, Dorset, 1976

4. M.V. Twigg (ed.), Catalyst Handbook (2nd ed.) Wolfe Publishing Ltd., London (1989)

5. BP Statistical Review of World Energy, 1985

6. A.V.G. Hahn, The Petrochemical Industry: Market and Economics, McGraw-Hill, New York (1970)

7. M.A. Peña, J.P. Gómez and J.L.G. Fierro, Appl. Catal., 144(1996), 7

8. J.M. Fox (III), Catal. Rev.- Sci. Eng., 35(1993)169

9. J.R. Rostrup-Nielsen in J.R. Anderson and M. Boudart (Editors), Catalysis Science and Technology, Vol. 5, Springer-Verlag, Berlin, 1984, p. 1

10. A.B. Stiles, F. Chen, J.B. Harrison, X. Hu, D.A. Storm and H.X. Yang, Ind. Eng. Chem. Res., 30(1991), 811

11. A. Solbakken, Natural Gas Conversion (Studies in Surface Science and Catalysis, Vol. 61), Elsevier, Amsterdam, 1991, p. 447

12. The catalytic oxidation of organic compounds in the vapor phase, L.F. Marek and D.A. Hahn, The Chemical Catalog Company, Inc., New York(1932), p. 158

13. G.E. Keller and M.M. Bhasin, J. Catal., 72(1982)9

14. J.A. Labinger, Catal. Lett., 1(1988)371

15. Y. Amenomiya, V.I. Birss, M. Goledzinowski, J. Galuszka and A.R. Sanger, Catal. Rev.- Sci. Eng., 32(1990)163

16. J.R. Anderson, Appl. Catal., 47(1989)177

17. G.J. Hutchings, M.S. Scurrell and J.R. Woodhouse Chem. Soc. Rev., 18(1989)251

18. V.D. Sokolovski and E.A. Mamedov, Catal. Today, 14(1992)415

19. R. Pitchai and K. Klier Catal. Rev.- Sci. Eng., 28(1986)13

20. M.J. Brown and N.D. Parkyns, Catal. Today, 8(1991)305

21. Proceedings of the Fourth International Natural Gas Conversion Symposium, Kruger National Park, South Africa, 19-23 November 1995, <u>Studies in Surface Science and Catalysis</u> (Elsevier), In press.

22. L.D. Schmidt, M. Huff and S.S. Bharadwaj, Chem. Eng. Sci., 49(1994)3981

23. M. Prettre, Ch. Eichner and M. Perrin, Trans. Faraday Soc., 43(1946)335

24. H. Liander, Trans. Far. Soc., 25(1929)462

25. W.A. Bone and H.F. Coward, J. Chem. Soc. (Trans.), 93(1908)1197

26. Badische Anilin -u. Soda-Fabrik, B.P. 266,410 (23 February 1927)
    Coke-oven gas containing 2% CO_2, 7% CO, 53% H_2, 30% CH_4, 7% N_2, 2% higher hydrocarbons and 23% O_2 was converted at 1000°C over a Ni-impregnated magnesia catalyst to yield a gas stream containing 1.5% CO_2, 26% CO, 64% H_2, 3.5% CH_4 and 5% N_2.

27. A.T. Ashcroft, A.K. Cheetham, J.S. Foord, M.L.H. Green, C.P. Grey, A.J. Murrell and P.D.F. Vernon, Nature, 344(1990)319

28. HYSIM, Version C1.50, Hyprotech, Calgary, 1991

29. V.R. Choudhary, A.M. Rajput and B. Prabhakar, Catal. Lett., 15(1992)363

30. V.R. Choudhary, A.M. Rajput and B. Prabhakar, J. Catal., 139(1993)326

31. M.G. Poirier, J. Trudel and D. Guay, Catal. Lett., 21(1993)99

32. P.D.F. Vernon, M.L.H. Green, A.K. Cheetham and A.T. Ashcroft, Catal. Lett., 6(1990)181

33. H.M. Stanley in The Science of Petroleum, A.E. Dunstan, A.W. Nash, B.T. Brooks and H. Tizard (eds.), Oxford University Press, (London,1938), vol. 3, p. 2164

34. W.J.M. Vermeiren, E. Blomsma and P.A. Jacobs, Catal. Today, 13(1992)427

35. H.W. Haynes (Jr.), Diffusion and Reaction in Porous Media, in AIChEMI modular instruction: series E, Kinetics, p. 24

36. R.J. Berger, G.B. Marin, Private Communication, 1994

37. D.A. Hickman and L.D. Schmidt, J. Catal., 138(1992)267

38. D.A. Hickman and L.D. Schmidt, J. Catal., 136(1992)300

39. O. Levenspiel, Chemical Reaction Engineering, John Wiley & Sons, New York, 1972, p. 473

40. G.F. Froment and K.B. Bischoff, Chemical Reactor Analysis and Design, John Wiley & Sons, New York, 1979, p. 151

41. A. Santos, M. Menéndez, A. Monzón, J. Santamaria, E.E. Miró and E.A. Lombardo, J. Catal., 157(1995)1015

42. R.M. Contractor, H.E. Bergna, U. Chowdhry and A.W. Sleight in: Proceedings of the 6th Engineering Foundation International Conference on Fluidization, J.R. Grace, L.W. Shemilt and M.A. Bergougnou (eds.), 7-12 May 1989, Banff (Alberta, Canada) p. 589

43. S.S. Bharadwaj and L.D. Schmidt, J. Catal., 146(1994), 11

44. Gas Encyclopedia, Elsevier, 1976

45. B. Lewis and G. von Elbe, Combustion, flames and explosions of gases, 3rd ed., Academic Press, Orlando, 1987

46. A. Santos, M. Menéndez and J. Santamaría, Catal. Today, 21(1994)481

47. Fischer and Pichler, Brennstoff Chem., 11(1930)501

48. K. Heitnes, S. Lindberg, O.A. Rokstad and A. Holmen, Catal. Today, 24(1995)211

49. K. Heitnes Hofstad, O.A. Rokstad and A. Holmen, Catal. Lett., 36(1996)25

50. Kirk-Othmer Encyclopedia of Chemical Technology, Vol. 11, 3rd ed., Wiley-Interscience, New York, p. 1098

51. D. Eng and M. Stoukides, Catal. Rev. -Sci. Eng., 33(1991)375

52. A. Santos, J. Coronas, M. Menédez and J. Santamaría, Catal. Lett., 30(1995)189

53. T. Ioannides and X.E. Verykios, Catal. Lett., 36(1996)165

54. S. Pei, M.S. Kleefisch, T.P. Kobylinski, J. Faber, C.A. Udovich, V. Zhang-McCoy, B. Dabrowski, U. Balachandran, R.L. Mieville and R.B. Poeppel, Catal. Lett., 30(1995)201

55. R. Burch and P.K. Loader, Appl. Catal., 122(1995)169

56. C.T. Au, H.Y. Wang and H.L. Wan, J. Catal., 158(1996)349

57. C.T. Au, Y.H. Hu and H.L. Wan, Catal. Lett., 36(1996)159

58. C.T. Au, Y.H. Hu and H.L. Wan, Catal. Lett., 27(1994)199

59. O.V. Buyevskaya, D. Wolf and M. Baerns, Catal. Lett., 29(1994)249

60. O.V. Buyevskaya, D. Wolf and M. Baerns, Catal. Lett., 38(1996), 81

61. Y.H. Hu and E. Ruckenstein, Catal. Lett., 34(1995)41

62. V.R. Choudhary, A.S. Mamman and S.D. Sansare, Angew. Chem. - Int. Ed. Engl., 31(1992)1189

63. D. Wang, O. Dewaele, A.M. De Groote and G.F. Froment, J. Catal., 159(1996), 418

64. S.B. Sathe, R.E. Peck and T.W. Tong, Int. J. Heat Mass Transfer, 33(1990)1331

65. F. Escobedo and H.J. Viljoen, AIChE Journal, 39(1993)1680

66. A.A. Barresi, S.L. Hung and L.D. Pfefferle, J. Chem. Eng., 50(1992)123

67. L.D. Pfefferle and W.C. Pfefferle, Catal. Rev.-Sci. Eng., 29(1987)219

68. C. van Heerden, Ind. Eng. Chem., 45(1953)1242

69. H. Kramers and K.R. Westerterp, Elelments of Chemical Reactor Design and Operation, Chapman and Hall Ltd., London, 1963, p. 118

70. R. Aris, Introduction to the Analysis of Chemical Reactors, Prentice-Hall Inc., Eaglewood Cliffs, 1965, p. 286

71. S.C. Reyes, E. Iglesia and C.P. Kelkar, Chem. Eng. Sci., xx(1993)2643

72. A. M. de Groote and G. F. Froment, Rev. in Chem. Eng., 11(1995)145

73. D.L. Trimm, and C.-W. Lam, Chem. Eng. Sci., 35(1980)1405

74. J.K. Hochmuth, Appl. Catal.: B, 1(1992)89

75. F. van Looij, The catalytic partial oxidation of methane to synthesis gas, PhD. Thesis, University of Utrecht, The Netherlands, October 1994

76. A. Slagtern and U. Olsbye, Appl. Catal., 110(1994)99

77. Y. Matsumura and J.B. Moffat, Catal. Lett., 24(1994)59

78. Y. Boucouvalas, Z. Zhang and X.E. Verykios, Catal. Lett., 27(1994)131

79. J.N. Theron, M.E. Dry and C.T. O'Connor, Unpublished results, 1994

80. D. Dissanayake, M.P. Rosynek and J.H. Lunsford, J. Phys. Chem., 97(1993)3644

81. Y.-F. Chang and H. Heinemann, Catal. Lett., 21(1993)215

82. W.R. Williams, M.T. Stenzel, X. Song and L.D. Schmidt, Comb. and Flame, 84(1991)277

83. D.A. Hickman and L.D. Schmidt, Science, 259(1993)343

84. D.A. Hickman, E.A. Haupfear and L.D. Schmidt, Catal. Lett., 17(1993)223

85. M. Huff, P.M. Torniainen and L.D. Schmidt, Catal Today, 21(1994)113

86. N. Mouaddib, C. Feumi-Jantou, E. Garbowski and M. Primet, Appl. Catal., 87(1992)129

87. P.D.F. Vernon, M.L.H. Green, A.K. Cheetham and A.T. Ashcroft, Catal. Today, 13(1992)417

88. D. Dissanayake, M.P. Rosynek, K.C.C. Kharas and J.H.Lunsford, J. Catal., 132(1991)117

89. J.C. Slaa, R.J. Berger and G.B. Marin, Preprints of the 211th National Meeting of the American Chemical Society, New Orleans, LA, March 24-29 (1996), p. 126

90. S.H. Oh, P.J. Mitchell and R.M. Siewert, J. Catal., 132(1991)287

91. F.H. Ribeiro, M. Chow and R.A. Dalla Betta, J. Catal., 146(1994)537

92. D. Klvana, J. Vaillancourt, J. Kirchnerova and J. Chaouki, Appl. Catal.:A, 109(1994)181

93. Y. Li and J.N. Armor, Appl. Catal.:B, 3(1994)275 - And references therein

94. D.A. Hickman and L.D. Schmidt, J. AIChE, 39(1993)1164

95. R.F. Blanks, T.S. Wittrig and A.A. Peterson, Chem. Eng. Sci., 45(1990)2407

96. J.W. Veldsink, G.F. Versteeg and W.P.M. van Swaaij, Chem. Eng. Journal, 57(1995)273

97. Y. Boucouvalas, Z. Zhang and X.E. Verykios, Catal. Lett., 27(1994)131

98. F. Van Looi, J. C van Giezen, E.R. Stobbe and J.W. Geus, Catal. Today, 21(1994)495

99. H. Wise and J. Oudar, Material Concepts in Surface Science and Reactivity of Catalysis, Academic Press Inc., San Diego, 1990, p. 203

100. T.Inui, K. Saigo, Y. Fujii and K. Fujioka, Catal. Today, 26(1995)295

101. H. Matsumoto, J. Phys. Chem., 98(1994)5180

102. E. Ruckenstein and Y.H. Hu, Catal. Lett., 35(1995)265

103. Y. Chu, S. Li, J. Lin, J. Gu and Y. Yang, Appl. Catal., 134(1996)67

104. A.K. Bhattacharya, J.A. Breach, S. Chand, D.K. Ghorai, A. Hartridge, J. Keary and K.K. Mallick, Appl. Catal., 80(1992)L1

105. J.A. Lapszewicz, A. Ekstrom, Q. Daiyi, X.-Z. Jiang, Proc. Int. Conf. Catalysis and Catalytic Processing, Cape Town, South Africa, October 24-27, 1993

106. E.P.J. Mallens, J.H.B.J. Hoebink and G.B. Marin, Catal. Lett., 33(1995)291

107. T. Hayakawa, K. Sato, T. Tsunoda, S. Hamakawa, K. Suzuki, J. Nakamura, K. Takehira and T. Uchijima, J. Chem. Soc. Chem. Commun., 1994, 1899

108. K. Walter, O.V. Buyevskaya, D. Wolf and M. Baerns, Catal. Lett., 29(1994)261

109. F. Solymosi and J. Cserényi, Catal. Today, 21(1994)561

110. M. Baerns, O.V. Buyevskaya, L. Mleczko and D. Wolf, Proceedings of the Fourth International Natural Gas Conversion Symposium, Kruger National Park, South Africa, 19-23 November 1995, Studies in Surface Science and Catalysis (Elsevier), In press.

111. M. Berg, S. Järås, Appl. Catal.: A, 114(1994)227

112. A.G. Steghuis, J.G. van Ommen, K. Seshan and J.A. Lercher, Proceedings of the Fourth International Natural Gas Conversion Symposium, Kruger National Park, South Africa, 10-23 November 1995, to be published by Elsevier as part of the Studies in Surface Science and Catalysis series.

113. R.H. Jones, A.T. Ashcroft, D. Waller, A.K. Cheetham and J.M. Thomas, Catal. Lett., 8(1991)169

114. M.G. Poirier, G. Jean and M.P. Poirier, Stud. Surf. Sci. Catal., 73(1992)359

115. T. Hayakawa, A.G. Andersen, M. Shimizu, K. Suzuki and K. Takehira. Catal. Lett., 22(1993)307

116. O. Deutschmann, F. Behrendt and J. Warnatz, Catal. Today, 21(1994)461

117. D. König, W.H. Weber, B.D. Poindexter, J.R. McBride, G.W. Graham, K. Otto, Catal. Lett., 29(1994)329

118. J.G. McCarty, Catal. Today, 26(1995)283

119. K. Otsuka, E. Sunada, T. Ushiyama and I. Yamanaka, Kidorui, 24(1994)66

120. K. Otsuka, E. Sunada, T. Ushiyama and I. Yamanaka, Proceedings of the Fourth International Natural Gas Conversion Symposium, Kruger National Park, South Africa, 19-23 November 1995, Studies in Surface Science and Catalysis (Elsevier), In press.

121. Y. Matsumura and J.B. Moffat, J. Catal., 148(1994)323

122. V.R. Choudhary, S.D. Sansare and A.S. Mamman, Appl. Catal., 90(1992)L1

123. J.B. Claridge, M.L.H. Green and S.C. Tsang, Catal. Today, 12(1994), 455

124. D.A. Dowden, Chem. Eng. Prog. Symp. Ser., 63(1973)90

125. V.R. Choudhary, B. Prabhakar and A.M. Rajput, J. Catal., 157(1995)752

126. S.H. Oh and P.J. Mitchell, Appl. Catal. B, 5(1994)165

127. E. Garbowski, C. Feumi-Jantou, N. Mouaddib and M. Primet, Appl. Catal. A; 109(1994)277

128. P. Briot, A. Auroux, D. Jones and M. Primet, Appl. Catal., 59(1990)141

129. R.A. Van Santen, Catal. Lett., 16(1992)59

130. J.N. Theron, J.C.Q. Fletcher and C.T. O'Connor, Catal. Today, 21(1994)489

131. V.R. Choudhary, A.M. Rajput, and V.H. Rane, Catal. Lett., 16(1992)269

132. V.R. Choudhary, V.H. Rane and A.M. Rajput, Catal. Lett., 22(1993)289

133. J. Nakamura, S. Umeda, K. Kubushiro, K. Kunimori and T. Uchijima, Sekiyu Gakkaishi, 36(1993)97

134. J.B. Claridge, M.L.H. Green, S.C. Tsang, A.P.E York, A.T. Ashcroft and P.D. Battle, Catal. Lett., 22(1993)299

135. D.L. Trimm, Appl. Catal., 5(1983)263

136. P.M. Torniainen, X. Chu and L.D. Schmidt, J. Catal., 146(1994)1

137. K. Heitnes, S. Lindberg, O. A. Rokstad, A. Holmen, Catal. Today, 21(1994)471

138. N. Dave and G.A. Foulds, Ind. Eng. Chem. Res., 34(1995)1037

139. T. Sundset, J. Sogge and T. Strøm, Catal Today, 21(1994)269

140. P.D. Battle, J.B. Claridge, F.A. Copplestone, S.W. Carr and S.C. Tsang, Appl. Catal. A, 118(1994)217

141. M. Najbar, M. Barańska and W. Jura, Catal. Today, 17(1993)201

142. The catalytic oxidation of organic compounds in the vapor phase, L.F. Marek and D. A. Hahn, The Chemical Catalog Company, Inc. (New York, 1932)

143. M.B. Lee, Q. Y. Yang, S.L. Tang and S.T. Ceyer, J. Chem. Phys., 85(1986)1693

144. G.L. Haller, G.W. Coulston, in J.R. Anderson and M. Boudart (Editors), Catalysis Science and Technology, Vol. 5, Springer-Verlag, Berlin, 1984, p. 154

145. H.F. Winters, J. Chem. Phys., 62 (1975)2454

146. B.O. Nielsen, A.C. Luntz, P.M. Holmblad and I. Chorkendorff, Catal. Lett., 32(1995)15

147. I. Alstrup, I. Chorkendorff and S. Ullmann, Surf. Sci., 234(1990), 79

148. I. Panas, P. Siegbahn and U. Wahlgren, J. Chem. Phys., 90(1989)6791

149. P.G. Wright, P.G. Ashmore and C. Kemball, Trans. Faraday Soc., 54(1958)1692

150. T.P. Beebe, D.W. Goodman, B.D. Kay and J.T. Yates, J. Chem. Phys., 87(1987)2305

151. A.B. Anderson and J.J. Maloney, J. Phys. Chem., 92(1988)809

152. H. Yang and J.L. Whitten, J. Chem. Phys., 96(1992)5529

153. H. Burggraef, A.P.J. Jansen and R.A. van Santen, J. Chem. Phys., 101(1994)11012

154. G.K. Boreskov, in J.R. Anderson and M. Boudart (Editors), Catalysis: Science and Technology, Vol. 3, Springer-Verlag, Berlin, 1982

155. E.E. Wolf (Editor), Methane Conversion By Oxidative Processes: Fundamental and Engineering Aspects, Van Nostrand Reinhold, New York, 1992, p. ix

156. M.G. Zabetakis, Flammability characteristics of combustible gases and vapors, U.S. Bureau of Mines Bulletin 627, 1965

157. Perry's Chemical Engineer's Handbook, 6th ed., McGraw-Hill, New York (1984) - 36 W/m/K

158. J.R. Anderson and K.C. Pratt, Introduction to characterization and testing of catalysts, Academic Press, Syndey (1985)

159. D.E. Mears, Ind. Eng. Chem. Process Des. Develop., 10(1971)541

160. Microsoft Excel for Windows (version 5.1)

161. Yu. I. Pyatnitsky, Appl. Catal. A, 113(1994)9

162. A. Al-Ubaid and E.E. Wolf, Appl. Catal., 40(1988)73

163. P.H. Bolt, F.H.P.M. Habraken and J.W. Geus, J. Catal., 151(1995)300 and T. Numaguchi, K. Shoji and S. Yoshida, Appl. Catal.(A), 133(1995)241

164. Blaise Pascal, Pensées (#553), Penguin, Middlesex (1966)

165. J.J. Carberry in J.R. Anderson and M. Boudart (Editors), Catalysis Science and Technology, Vol. 8, Springer, Berlin (1984), p. 131

166. J.E. Williamson, K.E. Bazaire and C.J. Geankoplis, Ind. Eng. Chem. Fund., 2(1963)126

167. R.C. Reid, J.M. Prausnitz and T.K. Sherwood, The Properties of Gases and Liquids, McGraw-Hill, New York (1977)

168. Welty, J.R., Wicks, C.E. and Wilson, R.E., Fundamentals of Momentum, Heat and Mass Transfer, John Wiley and Sons, New York (1984), p. 443

169. H. Kubota and Y. Yamanaka, J. Chem. Eng. (Japan), 2(1969)238

170. P.I. Lee and J.A. Schwarz, J. Catal., 73(1982)272

171. Numerical Recipes Example Book, W.T. Vetterling, S.A. Teukolsky, W.H. Press and B.P. Flannery, Cambridge University Press, Cambridge (1990)

172. G.F. Froment and L.H. Hosten in: Catalysis Science and Technology, J.R. Anderson and M. Boudart (eds.), p. 106, Vol. 2, Springer-Verlag, Berlin (1981)

173. T.W. Anderson and S. L. Sclove, Statistical analysis of data, Houghton Mifflin Company, Boston (1978)

174. Numerical methods for engineers with computer applications, S.C. Chapra and R.P. Canale, McGraw-Hill, New York, 1985

175. Numerical Methods for unconstrained optimization - an introduction, M.A. Wolfe, Van Nostrand Reinhold Company, New York(1978)

176. R. Mezaki and C.C. Watson, Ind. Eng. Chem. Process Des. Dev., 5(1966)62

177. D. Qin, J. Lapszewicz and X. Jiang, J. Catal., 150(1996), 140

178. C.P.P. Singh and D.N. Saraf, Ind. Eng. Chem. Process Des. Dev., 18(1979)1

179. Jean-Paul Sartre, Being and Nothingness (p. 29), Washington Square Press, New York (1966)

180. Chromatography fundamentals and applications of chromatographic and electrophoretic methods, Part A: Fundamentals and techniques, E. Heftmann (ed.), Elsevier, Amsterdam (1983), p. A45

181. J.J. van Deemter, F.J. Zuiderweg and A. Klinkenberg, Chem. Eng. Sci., 5(1956)271